

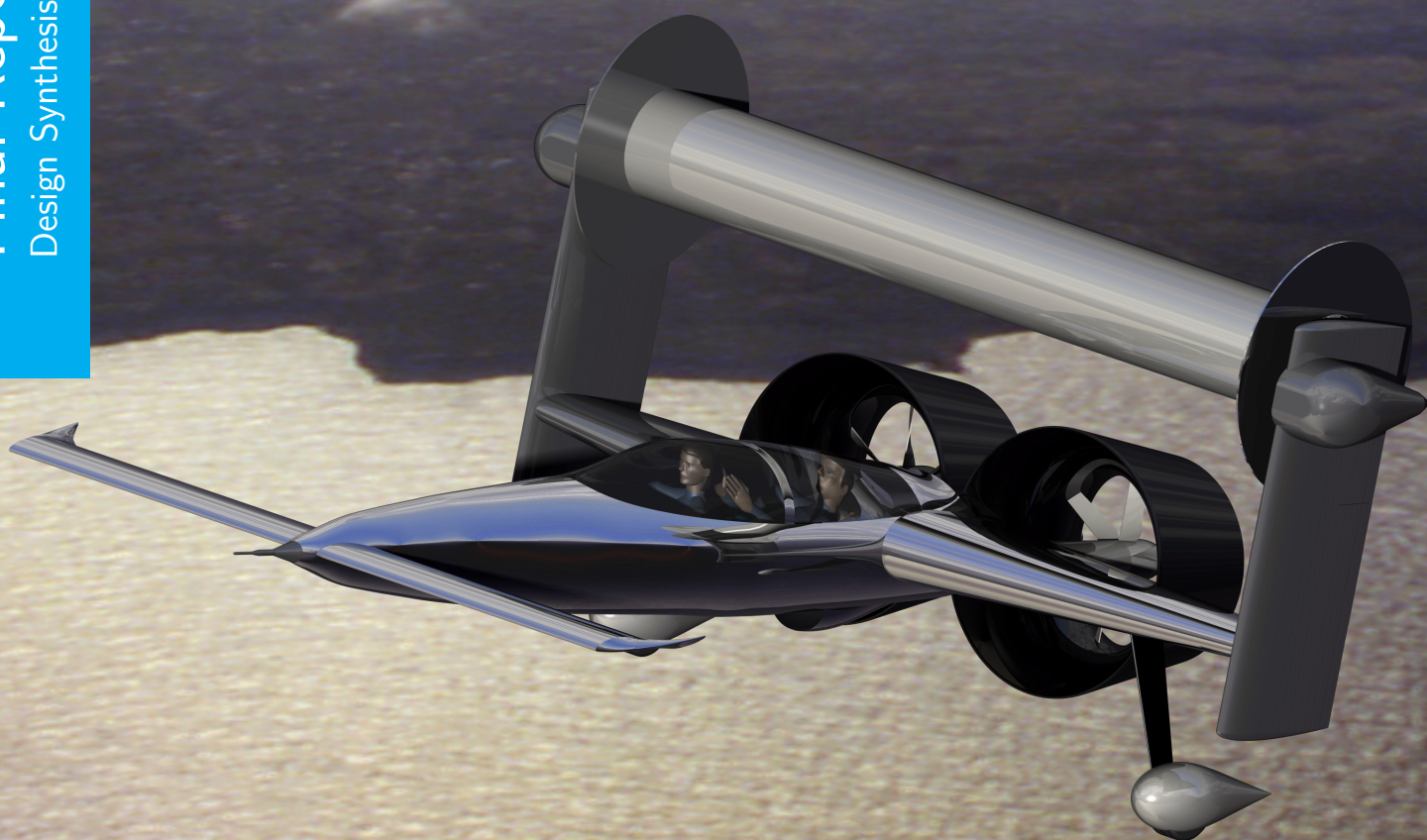
# Rediscovering the Magnus Effect in Aeronautics

## Final Report

H.R. Abdolhay	4301544	S.A. van Schouwenburg	4149394
T. Cappuyns	4290135	A.R. Speur	4090047
K.A. Gkirgkis	4273001	E.B. Todorov	4273389
D.M.E. de Jong	4294580	H.K.L. Verdonck	4298195
L.J. Kootte	4299167	L.J.A. Voet	4299868

Final Report

Design Synthesis Exercise



*Page intentionally left blank*

---

# Preface

This report treats the implementation of the Magnus effect in aeronautics. It has been written by Group 18, a group of 10 bachelor students at the Faculty of Aerospace Engineering at the Delft University of Technology, The Netherlands. It covers the assignment for the Design Synthesis Exercise finalizing the Bachelor Programme.

The report describes the design of an experimental aerial vehicle serving as a proof of concept to fly with the Magnus effect as the main lift providing force. Anyone with an interest in innovation, in unconventional vehicles in aviation, or in a Magnus aircraft in particular will benefit from reading this report.

Group 18 would like to thank Dr. S. Garcia Espallargas for suggesting this challenging idea, for his professional guiding and for giving constructive criticism during the project. It has been of great value to the group. We are also grateful to Dr. B. Santos and Ir. T. Pestana for coaching us, for giving valuable advice and for steering the group in the right direction. Our gratitude also goes to the Delft University of Technology involved in making this Design Synthesis Exercise possible. It created an educative opportunity to let us explore what teamwork is about and to let us convert our theoretical knowledge gathered during the Bachelor curriculum into practice.

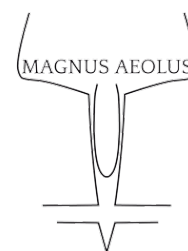
Furthermore we would like to thank all staff members of the Delft University of Technology who aided us during the design. For Aerodynamics: Ir. N. Timmer for providing us with windtunnel possibilities, Dr. Ir. M. Gerritsma and Prof. Dr. S. Hickel for sharing their experiences on computational fluid dynamics models. Special thanks to Ir. T. Pestana for always being available for a discussion related to aerodynamics and especially for his help while making the computational fluid dynamics model. For Structures and Mechanics: Dr. Ir. R. van Ostayen for consulting us on bearings and provide contact with SKF, Prof. Dr. C. Bisagni for sharing her view on the buckling modes of rotating cylinders. For Control: Dr. Ir. C. de Visser to help us with the simulation for control, consult us on the gyroscopic effect and more. For Power & Propulsion: Ir. J. Melkert for giving his view on the ducted fan and F. Scarano for providing us with his knowledge of thermodynamics.

Thanks to our contacts from outside the Faculty of Aerospace Engineering, namely Mr A. Altmikus from Enercon for sharing their knowledge on the Magnus effect, Mr P. Baart from SKF for a consultation on bearings and Mr B. Mury from Mistral Engines for providing us with the engine data. These representatives have given us useful advice at various stages in the design phase and they have given the design an extra dimension.

Similarly we would like to express our sincerest gratitude to Mr I. Cappuyns and Mr J. Huygen. They have given us the possibility to create an RC model of our design and to test its performance. For us this was an exceptional opportunity for which we are most grateful.

Finally we would like to express our thanks to the Delft University of Technology for providing excellent facilities and a unique environment to develop our talents and to explore our capabilities beyond boundaries.

**Delft, 28th June 2016**  
**Group 18**



# Summary

The main purpose of this project is to design an aerial vehicle that illustrates the potential of using the Magnus effect as the main lift provider. The design process of this aerial vehicle, named Magnus Aeolus is described in this report. The design of the different subsystems is based on a set of requirements set by the stakeholders. These requirements are set to fulfill the mission to transport one passenger from Rotterdam to Heathrow in less than 10 hours in an aerial vehicle using the Magnus effect as main lift providing force. The design meets these requirements and even surpasses them, as shown in Table 1.

The aircraft will produce its lift with a smooth cylinder having a 0.27 m radius and a span of 4.2 m. The design features rotating endplates to increase the lift-to-drag ratio of the cylinder. The cylinder is supported by a L-shaped structure, divided into a vertical support and a horizontal support. Within the vertical support providing structural integrity, the Simonini IC-engine rotating the cylinder and the driving chain are placed. It also functions as a vertical tail for stability and provides room for the rudders of 0.36 m<sup>2</sup> in total. The horizontal support is shaped as a symmetric airfoil and contains a wingbox that carries the loads from the cylinder. It also provides space for the fuel for the engines. Self-aligning ball bearings connect the shaft of the cylinder to the vertical support. This shaft is driven by the 26 hp Simonini engine. The propulsion is provided by two ducted fans, driven by a 200 hp Mistral engine. Interaction between the ducts and the aerodynamic wake of the cylinder is minimized by both optimizing the relative position of the cylinder and the shape of the ducts. Rolling the aircraft is enabled by the ailerons of 0.3 m<sup>2</sup> positioned on the horizontal support. Longitudinal control and stability is provided by a fully movable canard with a span of 3.7 m and a chord length of 0.52 m. The control will be executed by a fly-by-wire control system, optimizing the performance of the aircraft at all times. An optimization algorithm will be utilized to control the power setting of both engines depending on the airspeed.

The performance of the aircraft shows that the take-off distance at MTOW is 504 m, while the landing distance at Heathrow is 405 m. It also shows that the aircraft is able to adhere to the descent and landing procedures required by Heathrow. The range is 970 km which means the mission can be fulfilled, and even surpassed. For safety, the aircraft can also perform an unpowered descent and landing at MTOW. To the same extent, a ballistic recovery system is included in the design to save both the aircraft and the passengers in case of detrimental failure. The end-of-life solution for a mass produced aircraft shows that 73% of the aircraft weight can be reused or recycled. Finally, the compliance matrix indicates most of the requirements have been met. The emissions of the propulsion systems could not be achieved, but these are points of improvement for the future implementation of the project. This future of the project consists of a number of different phases. Preferably, a number of wind tunnel tests concerning modifications for the cylinder will be executed to improve the cylinder performance further. The design can then be further optimized before the validation and manufacturing is started. This data together with the aircraft test data can then be used to certify the aircraft. There is room for improvement of the design, but with the current one the mission is satisfied and surpassed. Research into both the applications for the Magnus effect and modifications to the design could highlight the potential of this concept even more. Therefore one can conclude that the Magnus effect could prove to be a viable alternative or supplement to the conventional way of providing lift. The mission is surpassed and the Magnus effect is finally receiving the attention it deserves.

Table 1: Overall summary: mission requirements compared to final design performance

Parameter	Mission	Final Design
Payload	100 kg	200 kg
Range	320 km	970 km
Time LHR-RTM	10h	2h45
Size	Two-seater aircraft	Span 4.2 m, Length 6 m
Stops	Allowed	No stops

---

# Contents

Preface	i
Summary	ii
Nomenclature	vii
<b>1 Introduction</b>	<b>1</b>
<b>2 Starting point</b>	<b>2</b>
<b>2.1 Mission Statement and Mission Requirements</b>	<b>2</b>
<b>2.2 Design Philosophy</b>	<b>3</b>
<b>2.3 Systems Engineering Process</b>	<b>4</b>
2.3.1 Preparing the design process	4
2.3.2 The design process	5
2.3.3 Additional considerations	5
<b>2.4 Preliminary Configuration</b>	<b>6</b>
<b>2.5 Subsystem Functions</b>	<b>6</b>
<b>2.6 Budget Breakdown</b>	<b>7</b>
2.6.1 Mass budget	7
2.6.2 Power budget	8
<b>3 Subsystem Design</b>	<b>9</b>
<b>3.1 Rotor</b>	<b>9</b>
3.1.1 Aerodynamic considerations	9
3.1.2 Structural considerations	20
3.1.3 Rotor propulsion	31
3.1.4 Summary rotor	32
<b>3.2 Rotor support</b>	<b>33</b>
3.2.1 Vertical support	33
3.2.2 Wingbox in horizontal support	36
3.2.3 Aerodynamic considerations	42
3.2.4 Summary rotor support	43
<b>3.3 Propulsion</b>	<b>44</b>
3.3.1 Ducted fan	44
3.3.2 Verification and validation	47

---

3.3.3	Propeller . . . . .	47
3.3.4	Engine . . . . .	47
3.3.5	Gearing . . . . .	49
3.3.6	Batteries and alternator . . . . .	49
3.3.7	Engine cooling and exhaust . . . . .	50
3.3.8	Summary propulsion . . . . .	51
<b>3.4</b>	<b>Stability and Control . . . . .</b>	<b>51</b>
3.4.1	Stability surfaces sizing . . . . .	51
3.4.2	Control surfaces sizing . . . . .	53
3.4.3	Pilot controls . . . . .	55
3.4.4	Avionics and instrumentation . . . . .	55
3.4.5	Throttle control . . . . .	56
3.4.6	Electronic Flight Control System . . . . .	56
3.4.7	Flight control modes/ laws . . . . .	57
3.4.8	Surface deflection mechanism . . . . .	59
3.4.9	Manual and automatic control segregation . . . . .	59
3.4.10	Cockpit elements . . . . .	60
3.4.11	Summary stability and control . . . . .	60
<b>3.5</b>	<b>Fuselage . . . . .</b>	<b>61</b>
3.5.1	Structural considerations . . . . .	61
3.5.2	Aerodynamic considerations . . . . .	64
3.5.3	Ergonomics . . . . .	65
3.5.4	Summary fuselage . . . . .	66
<b>3.6</b>	<b>Landing Gear . . . . .</b>	<b>66</b>
3.6.1	Location . . . . .	67
3.6.2	Struts . . . . .	68
3.6.3	Wheels . . . . .	68
3.6.4	Wheel pants . . . . .	69
3.6.5	Summary landing gear . . . . .	69
<b>3.7</b>	<b>Fuel System . . . . .</b>	<b>70</b>
3.7.1	Mistral engine fuelling . . . . .	70
3.7.2	Simonini engine fuelling . . . . .	70
3.7.3	Fuel tank size . . . . .	70
3.7.4	Fuel management system . . . . .	71
<b>3.8</b>	<b>Ballistic Recovery System . . . . .</b>	<b>72</b>
<b>3.9</b>	<b>Operations and Logistics . . . . .</b>	<b>73</b>
3.9.1	Aircraft testing . . . . .	73
3.9.2	Mission operations . . . . .	74
3.9.3	Surpassing the mission . . . . .	74
3.9.4	Pilot operations . . . . .	75
3.9.5	Logistics . . . . .	76
3.9.6	Ground support . . . . .	77

---

3.9.7	Summary operations and logistics	77
<b>3.10</b>	<b>Summary Design</b>	<b>78</b>
<b>4</b>	<b>Design Performance</b>	<b>81</b>
<b>4.1</b>	<b>Flight Performance Analysis</b>	<b>81</b>
4.1.1	Take-off performance	81
4.1.2	Flight profile	82
4.1.3	Landing performance	84
4.1.4	Verification flight trajectory performance	85
4.1.5	Flight envelope	86
4.1.6	Turn performance	88
4.1.7	Noise characteristics	89
4.1.8	Emission characteristics	91
<b>4.2</b>	<b>Flight dynamics</b>	<b>94</b>
4.2.1	Dynamic model of the aircraft	95
4.2.2	Results flight dynamics	97
4.2.3	Verification of dynamic model of the aircraft	100
4.2.4	Summary flight dynamics	102
<b>4.3</b>	<b>Sustainability Analysis</b>	<b>103</b>
4.3.1	Lifetime characteristics	103
4.3.2	End-of-life solution	105
<b>4.4</b>	<b>Sensitivity Analysis</b>	<b>106</b>
4.4.1	Increase in mass	106
4.4.2	Increase in drag	108
4.4.3	Change in center of gravity location	108
4.4.4	Conclusion	108
<b>4.5</b>	<b>RAMS Characteristics</b>	<b>109</b>
4.5.1	Reliability	109
4.5.2	Availability	110
4.5.3	Maintainability	110
4.5.4	Safety	111
<b>4.6</b>	<b>Risk Evaluation</b>	<b>111</b>
4.6.1	Risk map	111
4.6.2	Risk mitigation	113
<b>4.7</b>	<b>Market Analysis</b>	<b>114</b>
4.7.1	Scientific Market	114
4.7.2	PAV market	114
4.7.3	RC model market	116
<b>4.8</b>	<b>Compliance Matrix</b>	<b>117</b>
<b>5</b>	<b>Project Implementation</b>	<b>119</b>
<b>5.1</b>	<b>Project Development &amp; Design Logic</b>	<b>119</b>

---

5.1.1	Experimental data gathering . . . . .	119
5.1.2	Design optimization . . . . .	120
5.1.3	Validation of the design . . . . .	120
5.1.4	Prepare operations and logistics . . . . .	121
5.1.5	Production and assembly . . . . .	121
5.1.6	Testing the product . . . . .	121
5.1.7	Certification . . . . .	121
5.1.8	Performing the mission . . . . .	122
<b>5.2</b>	<b>Project Gantt Chart . . . . .</b>	<b>122</b>
<b>5.3</b>	<b>Experimental testing . . . . .</b>	<b>123</b>
5.3.1	Exploration of cylinder modifications . . . . .	123
5.3.2	Laboratory stand test . . . . .	125
5.3.3	The Iron Bird . . . . .	125
5.3.4	Remote-Controlled Magnus Aeolus model . . . . .	125
5.3.5	Simulation . . . . .	128
<b>5.4</b>	<b>Production Plan . . . . .</b>	<b>129</b>
5.4.1	Manufacturing . . . . .	129
5.4.2	Assembly & integration . . . . .	130
<b>5.5</b>	<b>Cost Analysis . . . . .</b>	<b>131</b>
5.5.1	Cost breakdown . . . . .	131
5.5.2	Cost estimation aircraft . . . . .	132
<b>5.6</b>	<b>Future of the Magnus effect . . . . .</b>	<b>134</b>
<b>6</b>	<b>Conclusion</b>	<b>136</b>
	<b>Bibliography</b>	<b>139</b>
<b>A</b>	<b>Material Characteristics</b>	<b>140</b>

# Nomenclature

$\alpha$	Effective angle of attack	[–]
$\Delta$	Maximum deflection	m
$\delta_a$	Aileron deflection	rad
$\dot{m}$	Mass flow	kg/s
$\frac{a}{c}$	Constant of the potential flow model	[–]
$\Gamma$	Vorticity	m <sup>2</sup> /s
$\gamma$	Constant of the potential flow model	[–]
$\lambda$	Air to fuel ratio in an internal combustion engine	–
$\mu_g$	Aircraft mass parameter	[–]
$\omega$	Cylinder rotational speed	rad/s
$\phi$	Bank angle	deg
$\phi$	Pitch of the blades	rad
$\rho$	Density	kg/m <sup>2</sup>
$\sigma_{allow}$	Maximum allowable stress	Pa
$\sigma$	Stress	Pa
$\tau$	Chord effectiveness factor	[–]
$\tau$	Shear stress	N/m <sup>2</sup>
$\varepsilon$	Strain	[–]
$A$	Enclosed Area	m <sup>2</sup>
$a$	Acceleration	m/s <sup>2</sup>
$a$	Wing lift curve slope during gust	[–]
$A_i$	Inlet area	m <sup>2</sup>
$C$	Complimentary Energy	J
$c_0$	Speed of sound	m/s
$C_D$	Drag coefficient	[–]
$C_L$	Lift coefficient	[–]
$C_{L\alpha_w}$	Wing lift coefficient	[–]
$C_{l\delta_a}$	Aileron rolling moment coefficient	[–]
$C_{n\delta_r}$	Yawing moment change due to rudder deflection	[–]
$C_{y\beta}$	Lateral force change due to side slip	[–]
$C_{y\delta_r}$	Lateral force change due to rudder deflection	[–]
$dt$	Difference in time	s
$dV$	Difference in velocity	m/s
$E$	Youngs Modulus	N/m <sup>2</sup>
$F_x$	Force in x-direction	N
$F_z$	Force in z-direction	N

---

$g$	gravitational acceleration on Earth	$\text{m/s}^2$
$I_{mass}$	Mass moment of inertia	$\text{kgm}^2$
$I_{xx}$	Area moment of inertia about x-axis	$\text{m}^4$
$I_{zz}$	Area moment of inertia about z-axis	$\text{m}^4$
$K$	Swirl	$\text{m}^2/\text{s}$
$k_g$	Gust coefficient	$[-]$
$K_\alpha$	Constant of the potential flow model	$[-]$
$L$	Length of a beam	$\text{m}$
$l_{vt}$	Distance from vertical tail's aerodynamic center to c.g.	$\text{m}$
$m$	Mass	$\text{kg}$
$M_x$	Moment around the x-axis	$\text{Nm}$
$M_z$	Moment around the z-axis	$\text{Nm}$
$M_{drag}$	Drag rolling moments from lifting surfaces	$\text{N} \cdot \text{m}$
$M_{max}$	Maximum moment	$\text{Nm}$
$MTOW$	Maximum take-off weight	$\text{kg}$
$n$	Load factor	$[-]$
$n$	rotations of the fanblades per minute	$\text{rpm}$
$P$	Power	$\text{Watt}$
$P_{cr}$	Critical Buckling load	$\text{N}$
$q$	Distributed load	$\text{N}$
$q_b$	Shear flow open cross section	$\text{N/m}$
$q_s$	Total shear flow	$\text{N/m}$
$q_t$	Torsional shear flow	$\text{N/m}$
$q_{s0}$	Shear flow closed cross section	$\text{N/m}$
$R$	Turn radius	$\text{m}$
$r$	Cylinder radius	$\text{m}$
$r_f$	Radius of the fan blades	$\text{m}$
$r_h$	Radius of the fan hub	$\text{m}$
$R_{inner}$	Inner diameter hollow shaft	$\text{m}$
$R_{outer}$	Outer diameter hollow shaft	$\text{m}$
$s_f$	Safety factor	$[-]$
$s_i$	gap between blade section	$\text{m}$
$S_{ref}$	Cylinder reference area	$\text{m}^2$
$T$	Thrust	$\text{N}$
$T$	Turn time	$[-]$
$t$	Thickness	$\text{m}$
$V_g$	Gust speed	$\text{m} \cdot \text{s}^{-1}$
$W$	Sound power	$\text{W}$
$y$	Distance from centroid	$\text{m}$

---

# Chapter 1

## Introduction

The aerospace industry has always been driven by innovation. It introduces new concepts, some of which have been successfully implemented while others have silently disappeared. The latter however, contains a number of interesting ideas which might - with the current high-end technology - lead to new designs. One of these concepts is the use of the Magnus effect as lift providing force for aerial vehicles suggested in the thirties. The Magnus effect relies on the generation of an aerodynamic force perpendicular to the free stream velocity and the axis of rotation of rotating cylinders or spheres. So far only a few examples of vehicles exist that have implemented the Magnus effect commercially, for example the E-Ship 1 [1]. Although considered in the past, it has not been applied with great success in aeronautics yet [2]. An aerial vehicle using this Magnus effect as the main lift provider is designed for this report. This innovative idea of about 80 years ago is now further explored in this project, to investigate whether it can transport someone from Rotterdam-The Hague to London-Heathrow.

The main purpose of this report is to give an overview of the detailed design of this aerial vehicle, named Magnus Aeolus or “ruler of the winds”. It describes the design choices made for the subsystems and their subsequent sizing. However, not only the subsystems are considered but also the aircraft system as a whole. Systems engineering techniques are applied to manage the interaction between those subsystems to finally come to an optimized design of the vehicle as such. The design of Magnus Aeolus is based on the primary mission stated as follows: “Transport one passenger from Rotterdam-The Hague airport (RTM) to London-Heathrow (LHR) in an aerial vehicle demonstrating the viability of the Magnus effect as a main lift provider”. Finally this report provides an insight in possible further implementations of the design.

The structure is as follows. The report is divided in four main parts: These parts are the starting point, the subsystem design, the design performance and the project implementation. The first part, chapter 2, is the base of the detailed design process. It contains mission requirements, design philosophy, system engineering methods, function descriptions and both the mass and power budget. When these are established, detailed designs can be developed of all the subsystems, discussed in chapter 3. The subsystems will be discussed after each other. First the cylinder will be discussed, next the rotor support, then propulsion, control, body and finally operations and logistics. For each subsystem all the necessary fields will be discussed. When the detailed design is finished, the design is proved feasible and the main characteristics are fixed, the performance analysis is done in chapter 4. It contains an analysis of flight performance of the aircraft, flight dynamics, sustainability, sensitivity and RAMS characteristics. It also contains the compliance matrix, to check for the requirements, a risk map and a market analysis. The project implementation is discussed in chapter 5. In this chapter, the future planning until the mission containing further design options, design optimization, validation, production plan and cost breakdown are discussed. Additionally, the recommendations for future implications of the Magnus effect are discussed in section 5.6.

---

## Chapter 2

# Starting point

The final design follows from the preliminary design. It evaluates the requirements set and designs the subsystems to fulfill these requirements. This chapter is the preparation for the final design and the closure of the preliminary design. It starts by restating the mission which has to be performed and the requirements for this mission. The design philosophy for this phase is then discussed in section 2.2. Then the incorporation of system engineering in the design process is evaluated. Also, the preliminary design is shown and the functions of its subsystems are discussed. The budget breakdown for the power and mass, as well as the evaluation of the markets then complete the starting point for this final design.

## 2.1 Mission Statement and Mission Requirements

A clear and definitive mission statement needs to be determined before determining the functions of the aircraft and designing it. This statement is derived by the customers' and stakeholders' needs and is formulated as follows:

**To transport one passenger from The Hague-Rotterdam airport to London-Heathrow  
in an aerial vehicle demonstrating the viability of the Magnus effect  
as main lift providing force.**

On top of this mission, it is set as a study goal to gather experimental data, such as aerodynamic, stability and flight performance characteristics, while the mission is being executed. This will result in better understanding of the behaviour of Magnus aircraft. This study goal is set by the group due to lack of available data on Magnus aircraft. Therefore, this group decided to set this as an additional goal in order to contribute towards filling this void.

A set of mission requirements that are derived from the mission statement are formulated as follows:

**RMEA-MIS-1** The range shall be at least 350 km.

**RMEA-MIS-2** The mission shall be accomplished in less than 10 hours.

**RMEA-MIS-3** The Magnus effect shall be the main lift provider.

**RMEA-MIS-4** There shall exist an end-of-life solution for the product.

**RMEA-MIS-5** The size of the product shall be comparable to a 2-seater conventional aircraft.

**RMEA-MIS-5.1** The product shall be able to carry a minimum payload of 100 kg.

These mission requirements are those set by the customer. However, the group wishes to surpass them by a margin. Therefore the design is performed in order to fulfill designers' wishes and goals. This statement is elaborated in section 2.2.

---

## 2.2 Design Philosophy

At the core of this project lies the mission to assess the feasibility of using the Magnus effect as a main lift provider for an aircraft. Applying the Magnus effect on such a large scale is a fairly unexplored field of study, and therefore a great challenge to use as a means of providing lift for an actual aerial vehicle.

Around this core a more specific mission was designed to give direction to the design process. This mission is to fly one passenger including luggage from The Hague to London in 10 hours. The mission served as a starting point for the preliminary design. During this phase it was found that the aircraft as designed was capable of more than the proposed mission. Therefore for the detailed design a new set of characteristics was selected as a goal for the final design. By using the Breguet range equation [3] combined with statistical data, an optimization is performed for the range and the maximum take-off weight (MTOW). This is done by determining the minimum MTOW-to-range ratio from a list of values of ranges and their corresponding MTOW. From this optimization, goal characteristics for the range and MTOW were found.

To make sure that the aircraft is able to compete in any aeronautical market, the goal for the payload was set to be that of a two person aerial vehicle. An overview of the characteristics of the original mission, the preliminary design and the goal for the final detailed design is given in Table 2.1.

Table 2.1: The original mission characteristics, the preliminary design characteristics and the goal for the detailed design characteristics.

Characteristic	Original	Preliminary	Goal
Maximum take-off mass	-	7500 N	11,960 N
Payload	100 kg	100 kg	200 kg
Size	Two-seater aircraft	Wingspan of 4.7 m	Two-seater aircraft
Range	350 km	635 km	1000 km
Flight time RTM-LHR	10 h	2:45 h	2:45 h
Stops	Stops are allowed	No stops	No stops

Diving from the preliminary design into the detailed design, the contingency management plays a crucial role in making sure the original mission requirements are kept in mind during the design phase and that the design converges towards the goal that is set to complete the mission. A contingency factor is set up for each of the different engineering specialities.

For the concept at the starting point of the preliminary design an analysis was done for which markets the concept would be most applicable. From this analysis it followed that the concept would best suit the Personal Areal Vehicle (PAV) and Farmer Areal Vehicle (FAV) markets. From these markets certain requirements were discovered which were additions to the mission requirements. These requirements were taken into account during the preliminary design phase. However, when these requirements caused conflicts with the mission requirements, the mission requirements were deemed to be more important than the market requirements. This prioritization will be further implemented during the detailed design phase to the extent that a market analysis will be done after the detailed design is finished. An assessment will then be made to determine in which market the final product will be most feasible. During the detailed design phase the requirements for different markets will therefore be of minor importance.

The range at which the design is aimed at the moment, 1000 km, is illustrated in Figure 2.1<sup>1</sup>. The aircraft can surpass the mission by flying to Heathrow and back to Rotterdam. Or it can fly to a city further away like Berlin or Copenhagen. In the performance analysis in section 4.1, the actual performance of the aircraft and therefore also the range will be discussed. This will show if the aircraft is able to reach the range of 1000 km and return to Rotterdam after flying to Heathrow.

<sup>1</sup><http://www.greatcirclemapper.net/en/great-circle-mapper.html>



Figure 2.1: Range [1000 km] possibilities of the aircraft starting at Rotterdam-The Hague airport (RTM)

## 2.3 Systems Engineering Process

Systems engineering enables the successful integration and functioning of systems. It encompasses a number of important aspects of design processes, like documentation and balancing requirements. The systems engineer, or in this case chief engineer, cooperates with the different engineering teams to incorporate all systems into one design. This section describes the different ways in which systems engineering is integrated into the design and evaluation of this aircraft.

### 2.3.1 Preparing the design process

An important aspect of systems engineering is the generation and evaluation of requirements. The project begins with a mission statement and mission requirements, shown in section 2.1. From these mission requirements, system and subsystem requirements are generated. These requirements are set with respect to functioning of the (sub)systems, but also with respect to sustainability, reliability and safety. The requirements have all been validated, which means that adhering to the requirements results in the product desired by the stakeholders. Throughout the design process, the requirements are observed to make sure the design adheres to them. At the end of the design, a compliance matrix is made to illustrate which requirements are met. This compliance matrix can be found in section 4.8.

Systems engineering is all about keeping an overview of the process as a whole. An important aspect therefore is the exploration of the project. This can be done in a number of ways. First of all, a work breakdown structure and work flow diagram gives an overview of the different aspects of the design. This breakdown of work can be traced to the structure of this report. The project as a whole is divided into the starting point, the detailed design, evaluating the design and exploring the future. Within each of these work packages, different aspects have to be considered as well as the interaction between these aspects.

---

### 2.3.2 The design process

Systems engineering is a useful tool to optimize the design process. One of the most important aspects of the implementation of systems engineering is information management. This emphasizes the careful documentation of the design process and the design itself. Key elements in this documentation include the availability and clarity of the requirements for the design, as well as its specifications. Visualization of the design can aid determining the consistency and interaction of the different components. So next to only sizing the elements, they are visualized in Catia. This gives an overview of the growing product and helps to keep track of interactions and interference of different systems. Also, appropriate documentation provides a good picture of the state of the design, the interaction between different systems and the work that still has to be performed. An important tool here is the information management which is used. All of the aircraft design parameters and performance parameters are kept up-to-date in a common file illustrating the current design and the most recent changes made. This ensures that the correct data is used all the time to optimize the design process.

Another tool for the actual design process is the usage of concurrent engineering. The focus is on simultaneous designing and proper communication to efficiently design the product. The information management discussed previously therefore is an integrated part of this approach. Different design teams were used with a systems engineer or chief engineering keeping an overview of the design as a whole. This chief engineer ensures the design is consistent by amongst others evaluating the information management, the Catia and progress of the different subsystems.

### 2.3.3 Additional considerations

There are a number of important systems engineering approaches which are an integral part of the design process and therefore performed parallel to designing the actual aircraft. These include the evaluation of the risks, the reliability, availability, maintainability and safety characteristics, the producibility and the future of the project. The primary importance of these elements of the design process is often underestimated. Making them part of the overall design process prevents this and ensures the aircraft lives up to the expectations. Besides the breakdown of work, the risks have to be determined and mitigated. This is a continuous process as new risks can rise during the design process and its preparation. Continuous risk mitigation prevents problems at the end of the design process.

Reliability, availability, maintainability and safety are characteristics of the design which are continuously evaluated during the design phase. Requirements are set in advance to ensure especially reliability and safety are an integral part of the design of the aircraft. The fulfillment of these requirements and the final reliability, availability, maintainability and safety characteristics is shown in section 4.5.

Throughout the detailed design, the producibility is a criteria which is also considered. A production plan is made parallel to the design process, which can be found in section 5.4. This ensures that the design can actually be produced and fulfills the five criteria. These are product quality according to specification, delivery reliability, production within cost limits, volume flexibility and obedience to law and regulations [4]. This aircraft is primarily designed as a single, experimental product.

A plan for the future of the project is also produced, ensuring an organized continuation of the project. Planning in advance throughout the design process provides a clear indication of the deadlines for certain packages and possible delays early on in the project. This planning for the continuation of the project is included in section 5.1. Taking into consideration all of the aspects of systems engineering discussed in this section ensures the proper design of the aircraft and the quality of the final product.

---

## 2.4 Preliminary Configuration

After the performing the trade-off between various configurations in the Midterm Report [5], a final configuration was selected. This configuration serves as a starting point for the detailed design phase. A general layout of this configuration is presented in Figure 2.2. A set of decisions related to each subsystem is stated below.

- The support structure (5) is used to carry fuel.
- The lateral control surfaces will be installed on support structure (5).
- The canard (1) is fully movable.
- The landing gears (6) are not retractable.
- The rotor engines are placed at the tip of support structure (5).
- The propulsion system uses Internal Combustion engine (7) with a ducted fan (3).
- The rotor (4) will be supported at both ends and/or other locations if necessary.

This is a preliminary configuration and during the detailed design, described in chapter 3, these subsystems are subject to change in size or location. This means the preliminary configuration is used as a starting point. There will be room for payload increase in order to achieve the additional goal of carrying two passengers instead of one.

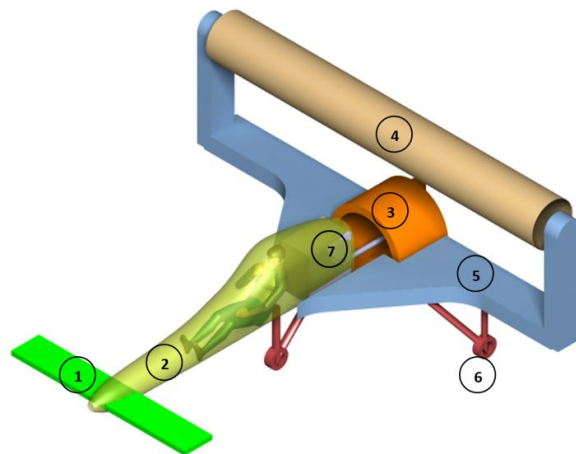


Figure 2.2: Schematic of the preliminary design configuration: canard (1), fuselage (2), duct (3), rotor (4), rotor support (5), landing gear (6), engine (7) and a pilot are placed with respect to the fuselage.

## 2.5 Subsystem Functions

Before the actual design and sizing of the aircraft can be started, the functions to be performed by the aircraft need to be determined. The main function of the aircraft as a whole is performing the mission, as described in section 2.2. To be able to do that, all of the subsystems have to perform certain functions. This section gives an overview of the different functions for each subsystems. The subsystems are the lift generating subsystem, the load transferring subsystem, the stability and control subsystem and the power and propulsion subsystem. For the lift generating subsystem, no functional breakdown was made because it has only one function: providing lift to the aircraft. The breakdown for the power and propulsion system can be found in Figure 2.3, for the load transferring subsystem in Figure 2.4 and for the stability and control in Figure 2.5. The requirements following the subsystem functions can be

found in section 4.8 in Table 4.12 and Table 4.13, where the compliance of the design to the requirements is checked.

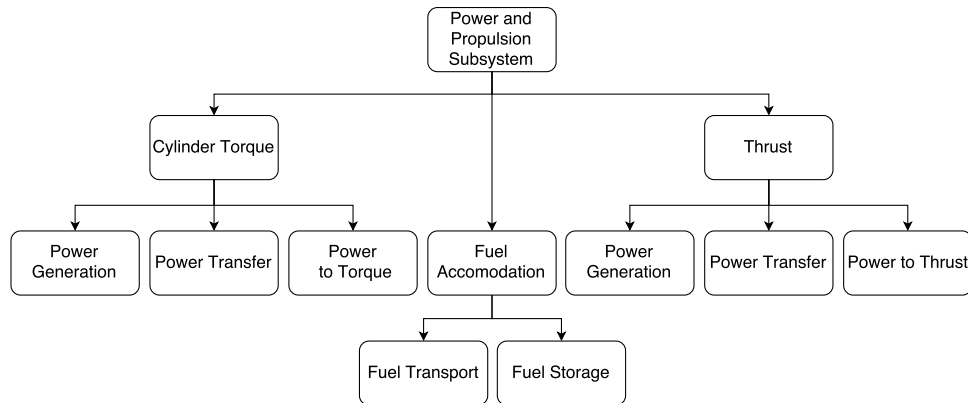


Figure 2.3: Functional breakdown structure of the power and propulsion subsystem

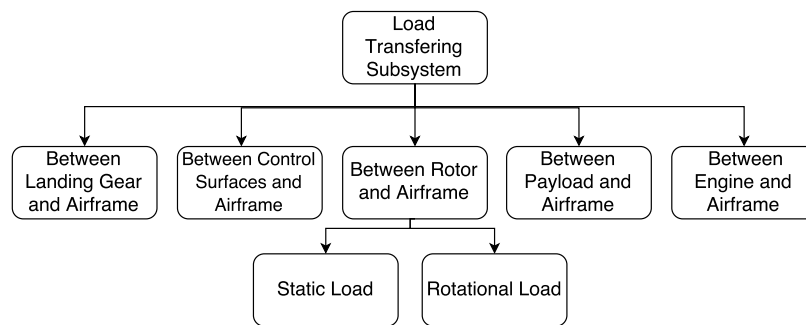


Figure 2.4: Functional breakdown structure of the load transferring subsystem

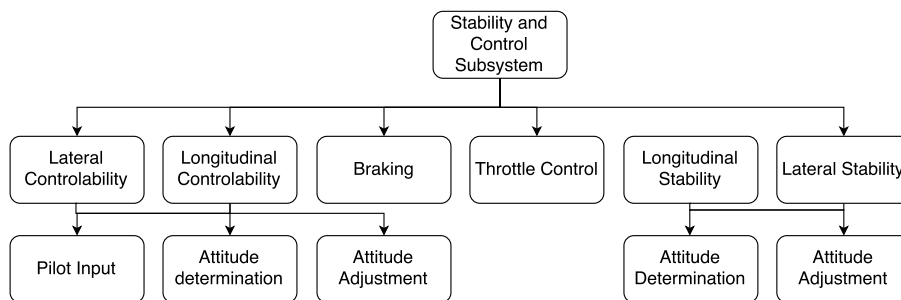


Figure 2.5: Functional breakdown structure of the stability and control subsystem

## 2.6 Budget Breakdown

The budget breakdown gives an overview of the power and mass budgets. These show the power and budget distributions as they were determined after the preliminary design.

### 2.6.1 Mass budget

The mass budget is a result of the preliminary design. These budgets were taken into account as design boundaries during the detailed design.

Table 2.2: Mass budget: overview of the components weights and c.g. location

	Mass [kg]		Mass [kg]
<b>Lift providing system</b>		<b>Structures</b>	
Rotor	40.0	Rotor winglets	20.0
Auxiliary engines	20.0	Airframe in front of payload	30.0
Gears and bearings	30.0	Airframe payload to engine	30.0
<b>P&amp;P</b>		Airframe to the sides	70.0
Engine	140.0	Main landing gear	70.0
Duct fan	5.0	Secondary landing gear	20.0
Fan blade	1.0	<b>Control</b>	
Fuel system	30.0	Avionics	30.0
Fuel	210.0/0	Canard	40.0
<b>Payload</b>		Aileron	12.0
Payload	200.0	Rudder	12.0
Pilot accommodation	20.0		
Maximum Take-off Weight			1030.0
Empty Weight			620
Useful Load			200

## 2.6.2 Power budget

The power budget breakdown tackles the power distribution of different subsystems. The budget is divided in two main parts: the first part is the power produced by the main engine and the rotor engine and the second part is the electrical power required for the avionics and electrical systems. An overview of the power generated by the engines is presented in Table 2.4 and Table 2.3 shows each subsystem with its respective power required.

Table 2.3: Power required by the avionics elements

Element	Maximum power [W]	Continuous power [W]
Integrated EFIS/EMS/Navigator	4.3	4.3
Backup Cylinder rpm indicator	0.6	0.6
Fuel tank indicator	30.0	30.0
Landing gear switch	96.0	96.0
Circuit breaker panel	126.0	42.0
Starter, magneto panel	approx. 0	approx. 0
Warning/failure panel lights	approx. 0	approx. 0
Servos	168.0	97.0
GPS antenna	50.0	50.0
Total	474.9	319.9

Table 2.4: Power generated by the IC-engines installed in the aircraft

Element	Maximum power [kW]	Continuous power [kW]
Mistral G200	143.0	143.0
Simonini mini 2 plus	19.4	14.6

---

## Chapter 3

# Subsystem Design

After the starting point has been explored and explained, the detailed design is started. This chapter gives an overview of the detailed design phase by describing the design of the different subsystems. First of all the rotor is analyzed and sized. The next component is the support of the rotor, which can be split into the vertical and horizontal support. Afterwards the power and propulsion system is shown, which includes the main engine and the design of the ducted fans. Then the stability and control of the aircraft is explored, resulting in the sizing and positioning of the control surfaces. Next the landing gear and fuel system are designed, after which the ballistic recovery system is placed. Then the operations and logistics for the design are determined, as well as the operations for the pilot during flight. Every section of the chapter contains an individual summary, and the chapter as a whole ends with a summary of the entire design.

### 3.1 Rotor

The first step in the detailed design is the design of the rotor. For its design, there are a number of different considerations. First of all the sizing is primarily based on the aerodynamic characteristics of the rotating cylinder. Several additional features are investigated to enhance its performance. Afterwards, the structure of the cylinder and its propulsion is described.

#### 3.1.1 Aerodynamic considerations

To be able to size the rotating cylinder, first the aerodynamic performance aspects of the Magnus effect have to be investigated. This means that lift, drag, torque and revolutions per minute have to be determined. Thereafter, these parameters of performance are used to size the dimensions of the cylinder, namely the radius and the span.

##### 2D potential flow model

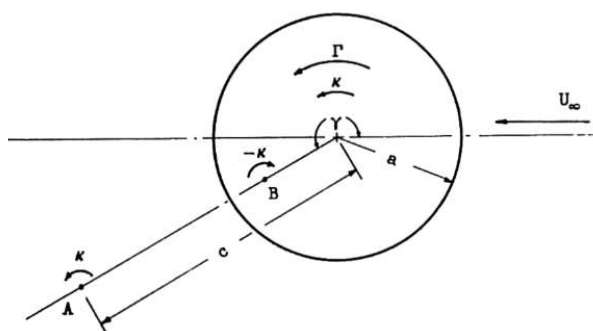


Figure 3.1: Representation of the potential flow model describing the flow over a rotating cylinder [6].

An ideal flow analysis based on potential flow theory is used as a theoretical model to describe the flow over a rotating cylinder. The potential flow pattern is obtained by superimposing several singularity-solutions of the potential flow equation [7]. The basic model combines three singularities to model the

flow over the rotating cylinder: a uniform parallel flow solution is used to account for the freestream; a doublet is used to account for the geometry of the cylinder; a potential vortex is used to account for the rotation of the cylinder according to the Kutta-Joukowski theorem.

Additionally, a vortex is placed downstream to represent the vorticity in the wake of the cylinder. A representation of this model can be seen in Figure 3.1. W.G.Bickley has developed a mathematical model using the complex potential flow function [8], from which the equations for the lift ( $C_L$ ) and drag ( $C_D$ ) coefficients are determined. These equations are given in Equation 3.1 and Equation 3.2 respectively.

$$C_L = \left[ 1 - \left(\frac{a}{c}\right)^2 \right] K_\alpha \alpha + \frac{\sin(\gamma)}{2\pi} \left(\frac{a}{c}\right) (K_\alpha \alpha)^2 \quad (3.1)$$

$$C_D = -\frac{\cos \gamma}{2\pi} \left(\frac{a}{c}\right) (K_\alpha \alpha)^2 \quad (3.2)$$

These equations describe the lift and drag coefficient as a function of effective angle of attack  $\alpha$ . This angle is defined as described in Equation 3.3.

$$\alpha = \frac{\omega r}{V_\infty} \quad (3.3)$$

This model is fully determined up to three constants that still need to be defined. According to W.M. Swanson [6], these coefficients are also a function of the effective angle of attack  $\alpha$ , namely  $\frac{a}{c}(\alpha)$ ,  $K_\alpha(\alpha)$  and  $\gamma(\alpha)$ . However, there is no analytical way to determine these relationships.

Therefore a set of experimental data of A. Thom [9] is used to determine these coefficients as a function of  $\alpha$ . This procedure serves two purposes, namely both generating the model and validating the potential flow model. By using the experimental data, one validates that the analytical model is able to describe the trendline of the data set. The procedure of fitting the experimental data on the model is described in the subsection describing the validation procedures of the model.

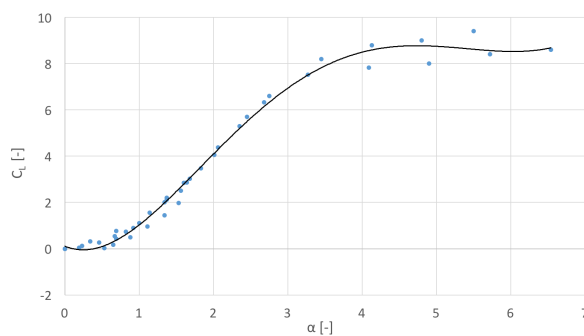


Figure 3.2:  $C_L$ - $\alpha$  data according to A. Thom [9]

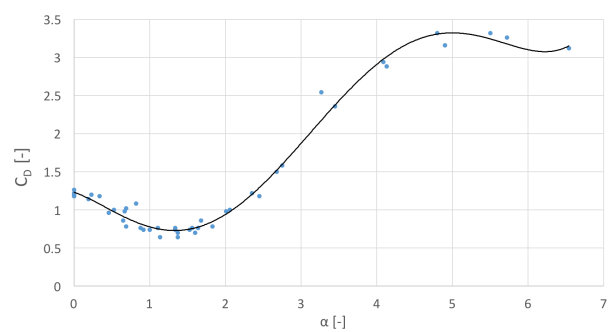


Figure 3.3:  $C_D$ - $\alpha$  data according to A. Thom [9]

To select this correct set of experimental data, a first estimate of the aspect ratio has to be made since this parameter has a significant influence on the values of the lift and drag coefficient. A higher aspect ratio resembles the infinite 2D wing better and is aerodynamically more efficient because of the increase in  $C_{L_{max}}$  and the decrease in  $C_D$ [10]. This is because the vortices at the tips of the wing have a relatively smaller influence. However, from a structural point of view, a higher aspect ratio increases the loads and increases the necessary rotational rate of the cylinder which is not desirable. The data set providing  $C_L$ ,  $C_D$  and  $C_T$  corresponds to a 2D measurement [9]. Since endplates will be dealt with later on in this chapter, first a model for a such a cylinder without endplates is discussed. The data for  $C_L(\alpha)$  and  $C_D(\alpha)$  can be seen in Figure 3.2 and Figure 3.3 respectively. The figures consist of a trend line through the measurement points of Thom's rotating cylinder.

Fitting the analytical model on the experimental data results in a set of  $\frac{a}{c}(\alpha)$ ,  $K_\alpha(\alpha)$  and  $\gamma(\alpha)$  for every  $\alpha$ . Having obtained these coefficients completes the analytical model to describe the flow around the rotating cylinder.

A flow visualization is made to illustrate the flow pattern around the rotating cylinder using ANSYS Fluent [11]. This illustration is shown in Figure 3.4.

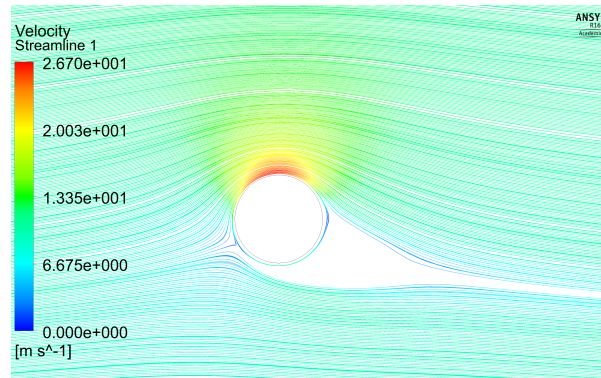


Figure 3.4: Steamline velocity pattern around a rotating cylinder at  $\alpha = 2$  at  $Re = 1000$ . In the picture one can clearly see the region of high velocity (and so low pressure) on the top of the cylinder. Also note the wake being pushed down and so generating lift.

### Verification of 2D potential flow model

Three verification techniques are applied to verify the potential flow model used to determine the lift and drag coefficients.

First of all the simple analytical ‘Kutta-Joukowski’ model is used to verify the more elaborate potential flow model. This model combines the singularity solutions of a freestream, doublet and vortex to model the flow around a rotating cylinder. The lift coefficient following from this model is calculated as described in Equation 3.4.

$$L = \rho V \Gamma \quad \text{where} \quad \Gamma = \oint V ds = 2\pi r^2 \omega \quad \Leftrightarrow \quad C_L = \frac{\rho V 2\pi r^2 \omega}{\frac{1}{2} \rho V^2 (2r)} = 2\pi \alpha \quad (3.4)$$

The equation for  $C_L$  of the Kutta-Joukowski model can be used as an upper boundary for the attainable lift coefficient. Theoretically it is the highest lift coefficient that can be obtained at a certain effective angle of attack. From Figure 3.5 one can see that the potential flow model is always below the Kutta-Joukowski model, which serves as a first verification of the potential flow model.

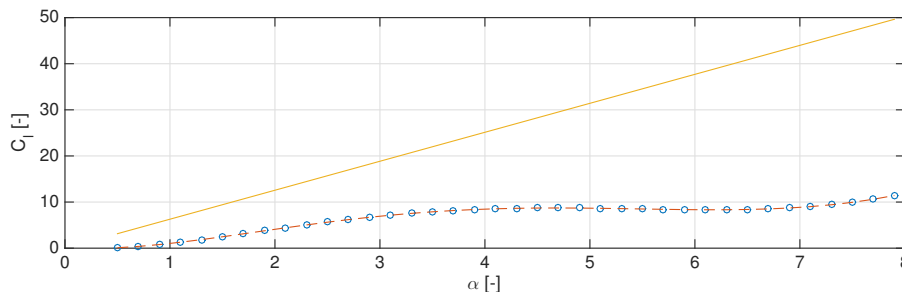


Figure 3.5: Comparison between Kutta-Joukowski model (solid) and potential flow model (dashed). Note that the potential flow model is fitted here on the experimental data set of A. Thom (points) [9].

For the drag coefficient calculation only pressure contributes since body and viscous forces are neglected. After integrating the pressure distribution over the cylinder surface, the drag coefficient is found to be zero because of the body being symmetric. This means that the drag coefficient of the potential flow model cannot be verified with the Kutta-Joukowski model.

Secondly, from Figure 3.5 one can see the linear region of the lift curve of the potential flow model between  $\alpha$  of about 1 to 4. This also serves as a verification for the potential flow model. One can also see that the gradient of the curve is smaller than the gradient of the Kutta-Joukowski curve [7]. Also a region of negative lift is predicted for small effective angles of attack by J. Seifert [2]. This behaviour is also seen in the potential flow model graph in Figure 3.5.

Finally, a computational fluid dynamics (CFD) simulation in Ansys Fluent [11] on the 2D rotating cylinder is performed to verify the potential flow model with a numerical model. This CFD model of the rotating cylinder is set up as follows:

- **Geometry:** The geometry for this model is a 1m diameter cylinder in a fluid domain of 100x50m<sup>2</sup>. The geometry can be seen in Figure 3.6.
- **Mesh:** The mesh is composed of triangular elements with a maximum face size of 0.3m. The boundary layer of the cylinder is modeled using both an edge sizing of 0.01m and an inflation around the cylinder surface with first layer height of 0.01m, number of layers of 40 and a growth rate of 2.5. The inflation mesh is used to be able to better model the boundary layer around the rotating cylinder. An extra refinement region in the wake of the cylinder is applied with a face sizing of 0.1m. The mesh applied on the previously described geometry can be seen in Figure 3.7.
- **Solution method:** A steady pressure-based solver is applied to solve the Reynolds-averaged Navier-Stokes (RANS) equations with a k- $\omega$  SST turbulence model. The following boundary conditions are applied: a velocity inlet of 10m/s, a pressure outlet of 0 Pa gauge pressure, zero shear far-field walls, a non-slip rotationally moving cylinder wall with radial velocity of -40rad/s corresponding to an effective angle of attack of 2. Note that the minus sign indicating a clockwise rotation direction is necessary to generate a positive lift force. The pressure-velocity coupling is set to coupled and the spatial discretisation is solved with a second-order upwind scheme high-order term relaxation for flow variables only with a relaxation factor of 0.25. The convergence limit regarding the residuals of the equations is set to 0.0001 for the continuity, momentum, k and  $\omega$  variables.

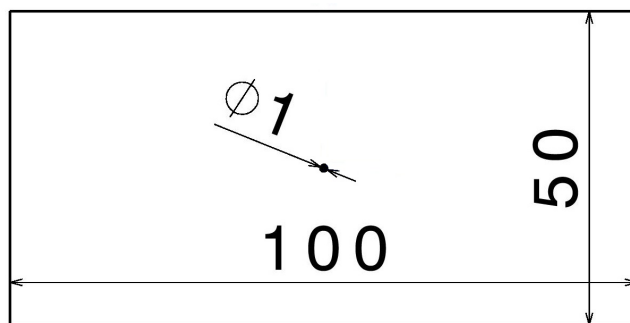


Figure 3.6: Geometry of the CFD model indicating the fluid domain around the cylinder (dimensions in meters).

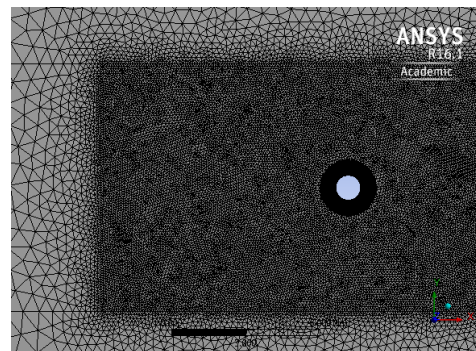


Figure 3.7: Mesh of the CFD model indicating three regions of refinement around the cylinder

After having reached convergence, meaning the residuals of the calculation drop below 0.0001, the lift coefficient  $C_l$  and drag coefficient  $C_d$  are plotted as a function of the number of iterations. The results can be seen in Figure 3.8. The lift coefficient converged to a value of 4.84; the drag coefficient converged to 0.235.

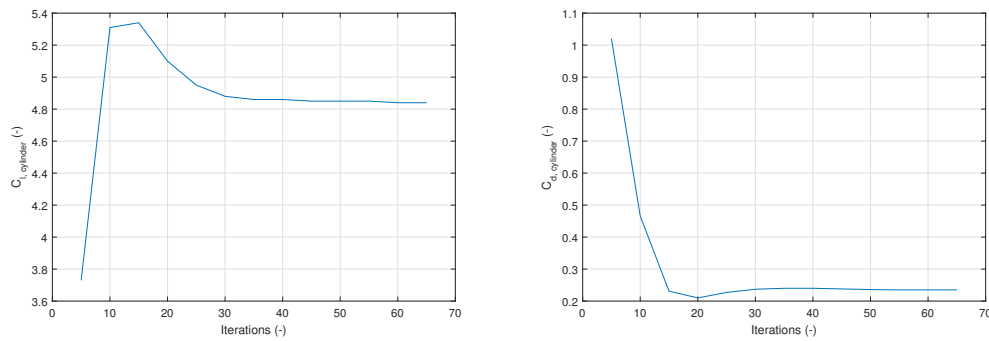


Figure 3.8: Results for cylinder  $C_l$  (left) and  $C_d$  (right) of the CFD-calculation as function of the number of iterations. Converged values:  $C_l = 4.84$ ;  $C_d = 0.235$ .

The following notes have to be made on the CFD model:

- The CFD model is able to correctly predict the values for the lift coefficients at low Reynolds numbers. However, the results for simulations at increasing Reynolds numbers diverged from measurements [12]. Therefore the simulations are executed at lower Reynolds number.
- Comparing the values of the drag coefficient of the rotating cylinder with measurements [12], one can see that  $C_{d,simulation} \approx 0.2 C_{d,measurements}$ .
- The flow around the rotating cylinder is predominated by turbulent flow. This turbulent flow is heavily influenced by the presence of walls, such as the cylinder surface. A strategy in turbulent flow modeling is looking at the wall  $y^+$  value at the cylinder surface. To accurately predict near-wall flows the statement  $y^+ \approx 1$  should hold [13]. The  $y^+$  value on the cylinder surface in the CFD simulation stays below 1.6.

To be able to better predict the drag generated by the cylinder, a second simulation is performed using different, more structured mesh generated using ANSYS ICEM instead of the standard ANSYS meshing tool. After having obtained almost the same results ( $C_{L,cylinder} = 5.07$  instead of 4.84 and  $C_{D,cylinder} = 0.232$  instead of 0.235), one could conclude that changing the mesh did not have an influence on the results. Therefore it was decided to use the CFD simulation to verify the trends of  $C_L - \alpha$  and  $C_D - \alpha$ . A number of simulations at various effective angles of attack  $\alpha$  have been executed at a fixed Reynolds number  $Re = 1000$ . The lift and drag coefficients are plotted versus  $\alpha$  in Figure 3.9.

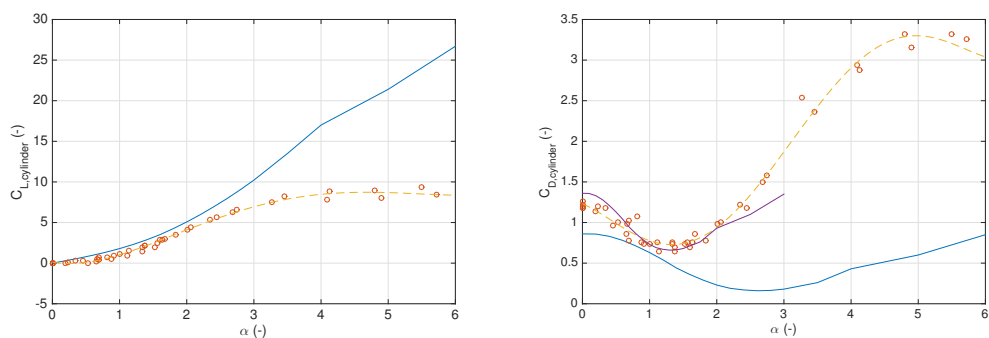


Figure 3.9: Verification of the  $C_L - \alpha$  and  $C_D - \alpha$  trend. CFD computations (solid line) ; scaled CFD computations (dotted line); measurements by A. Thom [9] (points); trendline of measurements (dashed line).

By comparing the CFD calculations with the measurements of A. Thom [9], the following conclusions were made:

- The CFD calculations are able to precisely predict the lift at low angles of attack as can be seen in the left graph of Figure 3.9. The graphs of the trendline of the measurements and the CFD calculations diverge from an angle of attack of 2.5 onwards; this is due to overestimating the lifting performance of the cylinder. A possible explanation for this is that at higher angles of attack, meaning at higher Reynolds numbers, there is more turbulence requiring a better definition of the mesh. Therefore at these higher  $\alpha$ , worse accuracy is expected. However, from this graph one can see that the trend of the lift is modeled correctly.
- The CFD calculations are not able to accurately describe the  $C_d - \alpha$  curve, as can be seen in the right graph of Figure 3.9. However, when scaling the CFD calculations and replacing them upwards, one can see the similarity in the trends of the CFD calculations and the measurements. This scaling is defined by placing the minima of the two curves at the same place. Note that this scaling is only done for illustrative purposes. Looking at the graph and noticing that scaling preserves the trend, one can see that the trend of the drag coefficient is modelled in the CFD.

From Figure 3.9, one can conclude that the trend of the CFD calculations is similar to the trend of the measurements. Comparing the trends serves as a verification step of the potential flow model.

### Validation of 2D potential flow model

The potential flow model is fully determined apart from three coefficients. To validate if the model is able to represent the flow characteristics of the rotating cylinder, the following procedure is applied. The model will be fitted on a set of experimental data of A. Thom [9]. Being able to fit the model on top of the experimental curves for lift and drag proves that the model is suitable for representing the flow around a rotating cylinder. It shows that the model can fit the trend of experimental data and this procedure thus serves as a validation.

The potential flow model consists of Equation 3.1 and Equation 3.2. Fitting the model on the experimental data set means that for every effective angle of attack  $\alpha$  a set of constants  $K_\alpha$ ,  $\gamma$  and  $\frac{a}{c}$  has to be found such that the model and experimental curves for both lift and drag are as close as possible. Note that this one set of constants has to fit the model curve of both lift and drag on the experimental data. The optimisation function *fminsearch* of Matlab is used to find the set of values for these constants such that the distance between the model and experimental curve is minimal for every angle of attack. This is described in Equation 3.5.

$$\begin{aligned} error_{C_L} &= |C_{L_{data}} - C_{L_{model}}| \\ error_{C_D} &= |C_{D_{data}} - C_{D_{model}}| \\ error_{total} &= error_{C_L} + error_{C_D} \end{aligned} \quad (3.5)$$

As suggested by W.M. Swanson [6], the set of parameters  $\left(\frac{a}{c}\right)(\alpha)$ ,  $K_\alpha(\alpha)$  and  $\gamma(\alpha)$  are a function of  $\alpha$  [6]. This is also confirmed by the investigation. The parameters are found to be a function of the angle of attack  $\alpha$ . The relations for the trend lines can be seen in Equation 3.6. Note that for the relation of the trend line of  $\gamma$  only the data points between an  $\alpha$  of 2 and 6 are used.

$$\begin{aligned} K_\alpha &= 0.07 \alpha^2 - 0.9 \alpha + 3.8 \\ \gamma &= -3 \alpha^3 + 29.15 \alpha + 81.5 \text{ for } \alpha \in [2, 6] \\ \frac{a}{c} &= 0.36 \end{aligned} \quad (3.6)$$

Note that for the data of the variable  $\left(\frac{a}{c}\right)$  in the range of  $\alpha \in [2, 4]$  demonstrates relatively large scatter compared to the other data. Keeping in mind that the data were obtained by measurements. Therefore, the relation is assumed to be constant. Both being able to fit the potential flow model on the experimental

---

data and finding these relations of the constants  $K_\alpha$ ,  $\gamma$  and  $\frac{a}{c}$  as a function of angle of attack  $\alpha$  proves the usability and the validity of the model and so that it can be used to describe lift and drag of the rotating cylinder.

Validation of the experimental aerodynamic data is an important step to size the rotating cylinder. Several issues with the available experimental data are listed below:

- First of all there is a lack of aerodynamic data. The Magnus effect has not been exhaustively investigated like e.g. airfoils. No database such as for the NACA airfoils exists.
- Most of the data that is available is taken at a different range of Reynolds numbers. The Magnus effect was already applied in Flettner ships [1], which sail at a different speed range.
- As C. Batalamenti and S.A. Prince stated: “... Thom freely admitted that, due to the limitations of the force balance, he placed no great confidence in the accuracy of the results at the Reynolds numbers and velocity ratios in question...” [10]. This means that the confidence in the data is low.
- No simple mathematical model exists that is able to describe the torque on the rotating cylinder.

Because of these issues, the following method is proposed to validate the aerodynamic data: by doing a wind tunnel experiment on the plain cylinder, the aerodynamic characteristics of the cylinder can be investigated. This would result in proper data being available such that the confidence level would increase. In the Midterm Report [5] the aspects of the wind tunnel experiment related to aerodynamics are discussed.

### 3D correction

The results of modeling the flow over the cylinder using the potential flow model are the two-dimensional  $C_l - \alpha$  and  $C_d - \alpha$  curves. In order to use the model to size a 3D cylinder, correction factors have to be applied. The effect of a finite length is decrease in lift and an increase in drag to the vortices generated at either end of the cylinder.

The correction factors were obtained by gathering experimental measurement points for both the 2D and 3D  $C_L$  and  $C_D$  for the range of operational alpha's, with a step (in alpha) of 0.25. The 3D datapoints were then divided by the respective 2D points. The small variance among the ratios ( 0.01 or 3% of the average value(s)), allowed for their average to be used as the correction factor. The correction factors are presented in Table 3.1.

Table 3.1: 2D to 3D correction factors for the drag and lift coefficients

Parameter	$C_L$	$C_D$
Correction factor	0.58	1.3

Another correction factor has to be applied to transform the model from cylinder-only to aircraft. Since the body is assumed not to generate lift, this correction only comprises a drag increase, which causes the Lift-to-Drag ratio to decrease. It was assumed that this decrease would be 10%.

### Endplates

Potentially the biggest disadvantage of the Magnus effect when compared to conventional lift-providing mechanisms, is the low Lift-to-Drag ratio (and, therefore, the low efficiency). A solution to increase the Lift-to-Drag ratio (L/D), is adding so-called “endplates” (thin discs) with larger diameter at both ends, rotating at the same speed. The effect of the endplates is to split the tip vortices into two parts (inner and outer), significantly increasing the lift and also (but less significantly) decreasing the drag[10]. An analogous solution for conventional aircraft would be the use of winglets.

Badalamenti [10] presents experimental results for the effect of endplates of various sizes on L/D. The size of the endplates is expressed in terms of  $D_e/D$  (the endplates-to-cylinder diameter ratio). The results

show that the L/D significantly increases with an increase in endplate diameter, up to a  $D_e/D=2.5$ . At this point, L/D has a value of 5.6. Further increase in endplate diameter does not offer significant improvements but does increase the power required to operate the rotor.

In order to correct the theoretical model for the effect of the endplates, another correction factor was applied in addition to the 2D to 3D correction factors given in subsection 3.1.1. The procedure used was the same as described in the aforementioned section and the results for a  $D_e/D$  of 2.5 are given in Table 3.2.

Table 3.2: 3D to Endplates correction factors for the drag and lift coefficients

Parameter	$C_L$	$C_D$
Correction factor	2.1	0.9

The power required to operate the rotor depends on the so-called torque coefficient ( $C_T$ ). For a plain cylinder, the value of this torque coefficient is 0.02 [2]. In order to calculate the contribution of the endplates, the “exact” solution of the Navier-Stokes equations for a thin rotating disk is used, as found by Schlichting [14]. Equation 3.7 gives the above mentioned torque coefficient for a thin rotating disk at laminar ( $Re < 300,000$ ) and turbulent ( $Re > 300,000$ ) flow conditions. Schlichting compared these solutions to experimental data and both were found to have a good fit.

$$C_T = 3.87 \text{ Re}^{-1/2} \text{ (laminar)} \quad \text{and} \quad C_T = 0.146 \text{ Re}^{-1/5} \text{ (turbulent)} \quad (3.7)$$

To calculate the total  $C_T$ , the contribution of the endplates is added to the  $C_T$  of the cylinder based on their wetted area. A safety factor is applied to the  $C_T$  of the endplates to take into account the fact that the fluid (air) is not stationary (an assumption that was made when solving the Navier-Stokes equations). Data from various authors presented in the “Review of the Magnus effect in Aeronautics [2] show a maximum increase of 100% between  $C_T$ s in stationary and non-stationary air and thus a safety factor ( $n_{spin}$ ) of 2 was used. As a final consideration, one has to take into account that the Reynolds number of the endplates differs from the one of the cylinders because of the difference in characteristic length (i.e. diameter) and should thus be corrected in accordance with Equation 3.8. The resulting equation for the total torque coefficient is given by Equation 3.9.

$$\text{Re}_{endplates} = \text{Re}_{cylinder} \frac{D_e}{D} \quad (3.8)$$

$$C_{T,total} = \left( C_{T,cylinder} \frac{S_{cylinder}}{S_{cylinder} + 2 S_{endplate}} \right) + \left( C_{T,endplate} \frac{S_{endplate}}{S_{cylinder} + 2 S_{endplates}} \right) n_{spin} \quad (3.9)$$

Results for the  $C_{T,total}$  with respect to the Reynolds number for a  $D_e/D$  of 2.5 are plotted in Figure 3.10. For the Range of Reynolds numbers covered during operations ( $1 \cdot 10^6 - 1.3 \cdot 10^6$ ) an appropriate  $C_T$  was then deemed to be 0.035. Table 3.3 summarizes the effect of the added endplates on the performance of the cylinder.

Table 3.3: Performance parameters for the cylinder with and without endplates where  $D_e/D$  is the ratio between the endplate diameter and the cylinder diameter

Parameter	With Endplates	Without endplates
$D_e/D$	2.5	1
L/D	5.6	2.2
$C_{T,total}$	0.035	0.02

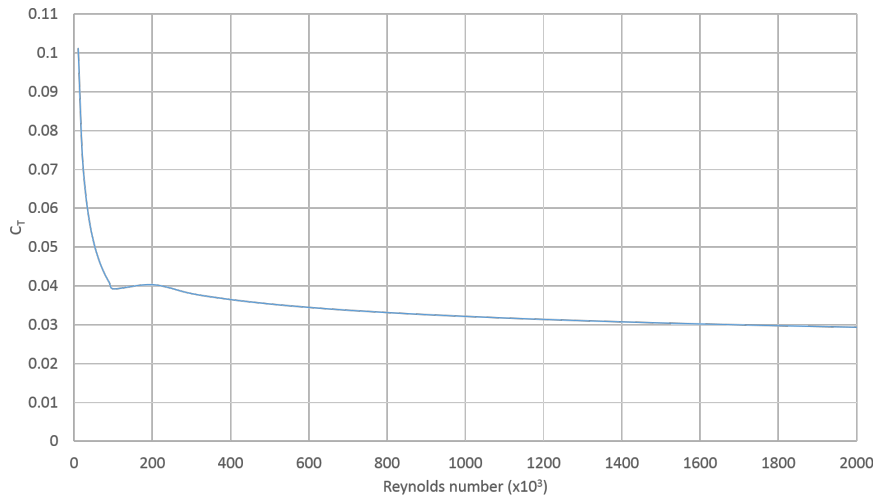


Figure 3.10: Results for the torque coefficient of the cylinder with added endplates with a diameter of 2.5 times the cylinder diameter with respect to the Reynolds number

### Skin Topology

Varying the surface roughness of the rotating cylinder will change its aerodynamic performance. When adding increased surface roughness on the cylinder, the separation of its boundary layer is delayed by inducing transition to turbulent flow. This has the following advantages and disadvantages. Pressure drag decreases because of the decrease in separated area. However, one has to note that the aircraft will cruise at a Reynolds number in the range of  $1.1 - 1.3 \cdot 10^6$ , which is already in the turbulent region. Therefore it is expected that the decrease in drag will be minor. Slightly higher lift coefficients are experienced at higher angles of attack (higher than the angle of attack at cruise) and the negative lift coefficient zone is less likely to be experienced, which is advantageous for operations. This can be seen in Figure 3.11. Note that in the graph a sanded cylinder means a cylinder to which sand is glued to increase surface roughness [2]. However, the main disadvantage is that the air torque required at least doubles [2]. This can be seen in Figure 3.12. Trading off these aspects, one can see that the increase in required air torque is the biggest disadvantage. This means the surface roughness of the cylinder is chosen to be smooth.

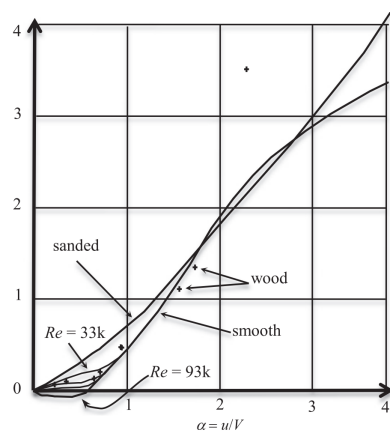


Figure 3.11: Comparison of lift coefficient for a smooth and a sanded cylinder [2].

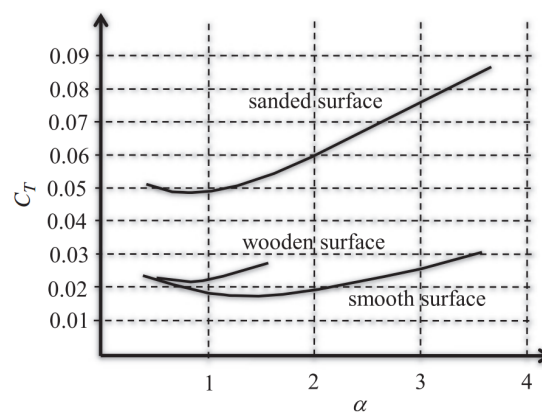


Figure 3.12: Comparison of torque coefficient for a smooth and a sanded cylinder [2].

When looking at skin topology, another feature can be added to the plain cylinder apart from just surface roughness. In 1924, the National Advisory Committee for Aeronautics (NACA) did tests on a cross-cylinder as shown in Figure 3.13 [15], which is in fact an exaggerated form of surface roughness.

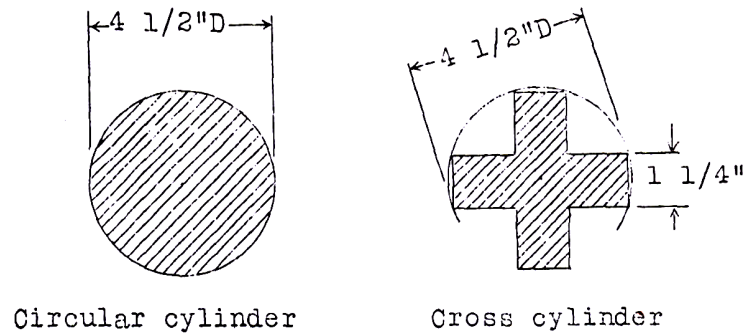


Figure 3.13: Geometry of a circular and a cross-cylinder as described by NACA [15].

The characteristics of this type of rotating cylinder were, as NACA measured, very irregular. According to [15]: *"...it would not be at all surprising if the maximum  $L/D$  ratio for this cylinder were found to be larger than that for the circular one..."*. However, the too high power required to rotate this cylinder prevented them from being able to spin it at high effective angles of attack. Considering the lack of aerodynamic data describing the performance of this type of cross-section and the extensive torque increase, it is also decided not to apply this cross-sectional shape for the cross-section. This principle also holds for addition of vortex generators which could be placed on the surface of the cylinder. Therefore also this feature is not applied.

### Cylinder positioning

The principle of conservation of momentum is used to explain the generation of the downwash downstream of the rotating cylinder. The cylinder generates lift by pushing air down and so according to Newton's 3rd law the air exerts an equal but opposite force back on the cylinder. The amount of downwash is thus heavily dependent on the amount of lift generated by the cylinder. Since the lift coefficient of the cylinder is large compared to this of regular airfoils[2], the amount of downwash is considered to be significant. Therefore the position of the rotating cylinder has to be carefully selected when designing the configuration of the aircraft.

The rotating cylinder is chosen to be placed at the back of the aircraft configuration. This to avoid the otherwise too high influence of the downwash on e.g. horizontal stabilizers and control surfaces. The choice to place the cylinder in the back is thus made to limit the size of these stabilizers and control surfaces.

However, by placing the cylinder in the back of the aircraft, there still will be an influence on the ducted fan, which is also placed in the back (the configuration is described in section 2.4). The influence of the cylinder on the ducted fan is investigated making sure that the downwash of the cylinder does not generate a too high downward force on the duct. To investigate this behaviour, a computational fluid dynamics (CFD) simulation is conducted using the ANSYS Fluent[11] program.

The position of the cylinder with respect to the duct is iterated up to the point at which the vertical force coefficient on the entire duct is less than  $1/50$  of that of the rotor. This choice is made because of the reasons listed below. The goal is to place the cylinder as close as possible to the duct without exceeding the limit of the downwash.

- The investigation is performed in 2D to obtain a first estimate. A 3D simulation would increase the complexity and required computational power tremendously.
- The model is simplified to decrease the complexity. The duct is replaced by two flat plates, placed at the angle selected in the duct design, modeling the outside of the cylinder.
- The influence of the Reynolds number on the results is neglected to decrease the computational complexity of the calculation. Therefore the simulation is performed at a low Reynolds number of 1000 at a freestream velocity of 10 m/s. This can be seen in the colour bar of Figure 3.15.

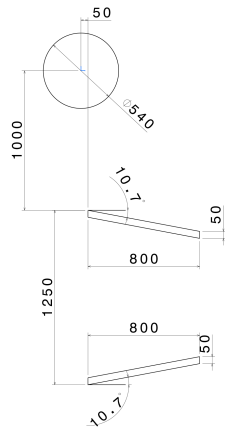


Figure 3.14: Technical drawing of the geometry used in the CFD analysis to analyse the location of the cylinder with respect to the ducted fans (dimensions in mm).

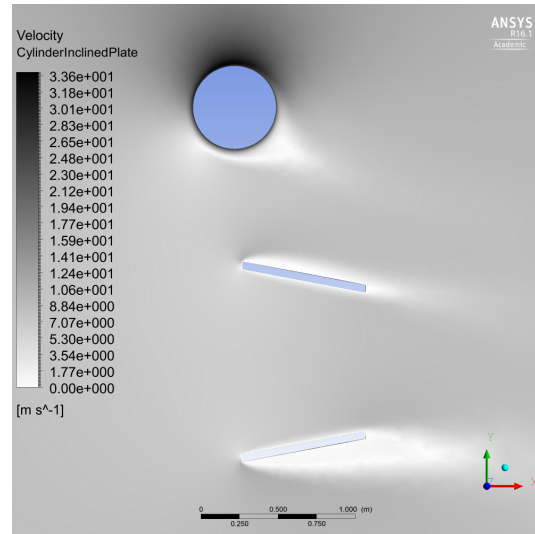


Figure 3.15: Velocity pattern around rotating cylinder and simplified ducted fan. The downwash of the cylinder is parallel w.r.t. the duct.

The geometry used to analyse this problem in ANSYS Fluent can be seen in Figure 3.14. Note that the dimensions indicated in Figure 3.14 are those of the converged design solution. The fluid domain is chosen to be a rectangular 2D plane with  $100 \times 50 \text{ m}^2$  dimensions. To solve the problem using CFD, a standard triangular mesh with a maximum face size of 0.3 m is chosen. An edge sizing with element size of 0.001 m is used at both cylinder and duct surfaces. A steady pressure-based solver is applied to solve the Reynolds-averaged Navier-Stokes (RANS) equations with the standard k- $\omega$  SST turbulence model. A velocity inlet of 10 m/s, a pressure outlet of 0 Pa Gauge pressure and zero-shear walls are used as boundary conditions for the fluid domain. The duct surfaces have a stationary non-slip boundary condition; the cylinder surface has a rotationally moving wall with a non-slip boundary condition. The pressure-velocity coupling is set to "coupled" and the spatial discretisation is solved with a second-order upwind scheme high-order term relaxation for flow variables only with a relaxation factor of 0.25.

The progression of the lift coefficient on both the cylinder and the entire duct are shown in Figure 3.16. The analysis is conducted keeping the lift coefficient of the cylinder at its cruise operating value, namely  $C_{L,cylinder} = 4.8$ . The iteration of the cylinder location is converged when  $C_{L,duct}$  drops below 0.1. One can also reason that the influence of the downwash on the duct can be read from the value of  $C_{L,duct}$ . Because the duct is symmetric, the normal  $C_{L,duct}$  is zero and every value different from zero comes from the downwash.

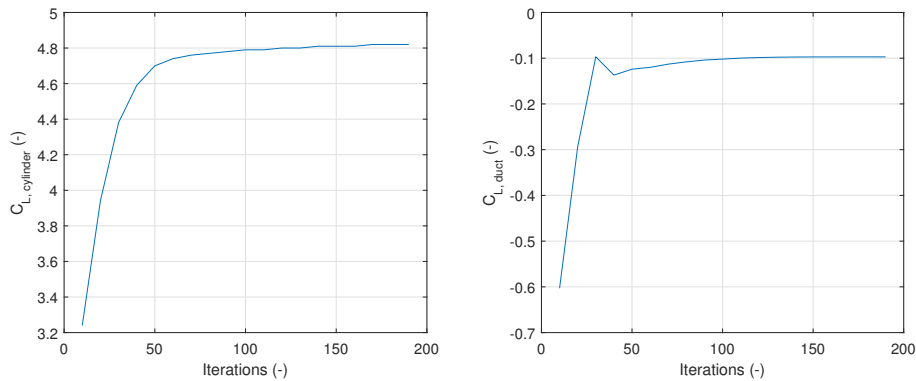


Figure 3.16: Progression of the lift coefficient of the rotating cylinder (left) and duct (right) as a function of the number of iterations. Converged values: Cylinder  $C_l = 4.82$ , Duct  $C_l = 0.097$ .

The velocity heat map that is obtained for the final configuration at cruise operating conditions is shown in Figure 3.15. This heat map clearly indicates the region of increased velocity on the top of the cylinder corresponding to a region of under pressure according to the Bernoulli principle. One can also see that the downwash is approximately aligned with the upper surface of the duct.

### Cylinder Sizing

After determining the aerodynamic performance of the cylinder, its sizing can be executed. Sizing the cylinder is an iterative process. It depends on the aerodynamic coefficients determined earlier in this chapter, on the total weight of the aircraft and also on the flight conditions. With an increasing cylinder size, the aircraft weight increases too. This means that the lift of the cylinder again has to increase to be able to lift the weight. This process converges to a weight of the aircraft and a sized cylinder.

The cylinder was sized to be most efficient in cruise, which means that the optimal  $C_L/C_D$  is maintained throughout the cruise flight, an operation that will be discussed in section 3.9. The aircraft flies at an altitude of 7000 ft with a speed of 40 m/s at the beginning of cruise. These numbers can then be used to obtain the area of the cylinder and together with the aspect ratio the span and the radius can be determined. All of the resulting parameters can be found in Table 3.4. Using the  $\alpha$  necessary to fly at this maximum  $C_L/C_D$ , the rotational speed for the cylinder can be obtained. Other parameters which follow include the drag produced by the cylinder and the power to overcome both the drag and the torque. These are summarized in Table 3.5.

Parameters	Value	Unit
Cylinder Area	2.27	$m^2$
Aspect Ratio	7.8	–
Span	4.2	m
Radius	0.27	m
Clearance to Ducts	0.73	m

Table 3.4: Main dimension characteristics of the cylinder

As the weight of the aircraft decreases during flight because of the decreasing fuel weight, the aircraft has to decelerate to keep flying at the optimal  $C_L/C_D$ . This results in a slower final speed and different power requirements. The final flight condition determines the minimum speed at which the aircraft can fly, which again differs for the beginning and the end of flight. This speed and the required power can be determined using the  $C_{L_{max}}$ . These data are also summarised in Table 3.5.

Parameters	Begin Cruise	End Cruise	$V_{min}$ , with Fuel	$V_{min}$ , no Fuel
Speed [m/s]	40	35	24	20
Weight [kg]	1030	820	1030	820
Drag [N]	1631	1228	3922	2952
Rotational Speed [rpm]	2940	2550	4110	3570
Thrust Power [kW]	65	57	92	60
Torque Power [kW]	14	9	20	13

Table 3.5: Cylinder performance parameters for different operating conditions

### 3.1.2 Structural considerations

The structural considerations of the rotor design consist of different parts. The first step is analyzing the loading case on the rotor. When the loading case is assessed the cylinder itself is designed. Hereafter the end-caps are designed, followed by the cylinder drive shafts and finally the bearing system.

---

## Loadcase and failure modes

### *Stresses*

To determine the loading case on the cylinder, the cylinder is regarded as a simply supported low-aspect-ratio beam loaded by a distributed load. This distributed load is the resultant force of the pressure distribution over cross-section of the cylinder and is assumed to be evenly distributed over the entire span of the cylinder. The maximum total resultant force, the lift force, is determined by taking the maximum take-off weight, multiplied by the gravitational acceleration, the maximum load factor and a safety margin. This force is found as in Equation 3.10 (see Requirement **RMEA-SS-LT-1**, Requirement **RMEA-SS-LT-2**):

$$P = MTOW \cdot g \cdot n \cdot s_f = 60kN \quad (3.10)$$

Where  $g = 9.81 \text{ m/s}^2$  is the gravitational acceleration,  $n = (-1.5; 3.8)$  is the maximum load factor and  $s_f = 1.5$  is a safety factor. This force is assumed to be evenly distributed along the span of the cylinder, so dividing the load calculated in Equation 3.10 gives the lift distribution over the cylinder. The reaction forces to this distributed load are determined using the solution regarding a beam that is simply supported on both ends of the cylinder. The magnitude of each reaction force at the support point is the lift force divided by two.

The lift force causes the cylinder to deflect in the direction of the load, and taking into account the simply supported beam solution, causing a rotation at ends. The maximum deflection angle can be calculated using the formula for the simply supported beam [16] as presented in Equation 3.11.

Another loading case to be considered is the centrifugal force caused by the rotation of the cylinder on the cross-section of the cylinder as discussed in subsection 3.1.2. This centrifugal force translates to a strain of the radius of the cylinder calculated using Equation 3.12.

$$\theta = \frac{qL^3}{24EI} \quad (3.11) \quad \varepsilon = \frac{\sigma}{E} = \frac{\rho \cdot \omega^2 \cdot r^2}{E} \quad (3.12)$$

The pressure distribution on the cross-section also causes a elongation of the radius of the cylinder, but the magnitude of this strain is a factor of 650 times smaller than the strain caused by the centrifugal force. The scale of the elongation of the centrifugal force is in the order of micrometers and therefore the strain due to the pressure distribution is not significant for the sizing of the cylinder and its subsystems.

### *Vibrations*

As discussed previously [5], the whirling vibrations are not expected to pose significant threat to the structure, since its natural frequency is very high. Nevertheless, vibrations in general are an important consideration of the structure. Although they do not threaten the integrity of the structure, vibration might have other negative effects. Their investigation is related to a close coupling between structural elasticity and aerodynamic effects. Aeroelasticity of rotating cylinders is a completely unexplored field, and some significant background needs to be established before vibrations can be analyzed in any meaningful way. At this state of the art, only qualitative design measures can be taken to mitigate the effects of vibrations, by designing for highly stiff structures and introducing damping and decoupling whenever it is possible. In terms of the current design, decoupling of the lower frequency is accomplished by the self-aligning bearings. The higher frequency problem is however exacerbated by this solution. Lower frequency initiation is decreased by reducing the out-of-plane membrane displacements of the cylinder. Future developments in the theory of rotating cylinder aeroelastic behaviour is necessary to provide quantitative response in terms of emitted noise.

### *Instabilities*

A more elaborate analysis was carried out on the instabilities (buckling and collapse) of the cylinder. As experience from aircraft fuselages suggest, instability is often present in thin circular shells. Although

the preliminary investigation concluded that the critical buckling and collapse loads on the structure are much higher than the loads present, a different investigative approach was taken. A third, well-established, but limited to isotropic materials method by Brezier [17] was used to verify the Matlab [18] implementation. Experimental data from [19] was used for validation of the main method, part of the NASA space vehicle design criteria [20].

The model followed is a design tool, which doesn't aim to accurately analyse the mechanics, but provides the designer with limiting critical loads. For bending of orthotropic, thin-walled cylinder, such as the thin laminated shell considered here, the critical load  $N_{cr} = \frac{M_{cr}}{2r}$  is given by Equation 3.13, where  $m$  and  $n$  are the buckling wave numbers. For the design, the wave numbers resulting in lowest critical load were used. For definitions of  $\bar{D}_i$  and  $\bar{E}_i$  the reader is referred to [20]. Their physical meaning is of corrected materials constants, similar to the ones derived in Appendix A.

$$\frac{N_{cr}L^2}{\pi^2\bar{D}_x} = m^2 \left( 1 + 2\frac{\bar{D}_{xy}}{\bar{D}_x}\beta^2 \right) + \frac{\gamma^2 L^4}{\pi^4 m^2 \bar{D}_x r^2} \frac{\bar{E}_x \bar{E}_y - \bar{E}_{xy}}{\bar{E}_x + \left( \frac{\bar{E}_x \bar{E}_y - \bar{E}_{xy}}{G_{xy}} - 2\bar{E}_{xy} \right) \beta^2 + \bar{E}_y \beta^4} \quad (3.13)$$

$$\gamma = 1 - 0.901(1 - \exp -\phi) \quad \beta = \frac{nL}{\pi r m} \quad \phi = \frac{1}{29.8} \left[ \frac{r}{\sqrt[4]{\frac{\bar{D}_x \bar{D}_y}{\bar{E}_x \bar{E}_y}}} \right]^{0.5} \quad (3.14)$$

## Cylinder Design

The design of the cylinder was approached from a perspective of lay-up optimization, since preliminary estimations suggested that instability would not be a critical failure mode, and topology optimization is unnecessary.

### Analytical optimization

During the design process, failure modes considered were: bending compression, bending tension, shear flow (torsion and force), longitudinal and transverse buckling loads, whirling vibration and centrifugal hoop stress.

The critical load case considered in the initial phase of design was bending, and the most relevant failure mode was the rotation of the end supports. If the rotation was within the limits of the self-aligning bearings, the stresses in the structure were checked. Optimization was ran over the lay-up of the cylinder. The material engineering constants were determined as thoroughly elaborated in Appendix A. The Tsai-Hill [21] stress failure criterion was used. To accommodate for its shortcomings, a warning was issued if this failure criterion was above 0.8, to get further investigation in possible alternative failure modes. Finally, Equation 3.13 was used to determine whether the bending moment is higher than the critical for collapse.

The outcome of the optimization was an optimum layup  $[\pm 45 \ 0/90 \ 0SP \ 90IM]_s$  with total thickness of 2.8 mm, corresponding to 32 kg of cylinder weight. The weave plies are 0.2 mm each, made out of spread-tow Hexcel G904 60% volume ratio with M20 resin system, the SP reinforcement is the 0.6 mm thick SparPreg<sup>TM</sup>, which is necessary to achieve such a thickness, and finally the intermediate-modulus fibre is the T1000G. (For specifics, please see Appendix A). The engineering constant resulting were:  $E_1 = 103$  GPa,  $E_2 = 47$  GPa. This resulted in 1.37 degrees of deflection at the bearings, and 0.16 mm radial expansion from the rotation.

The maximum stresses reached about 500 MPa, or a Tsai-Hill number of 0.23. The critical instability moment were estimated to be at least 220 kNm, far above the existing maximum of 31.5 kNm. By all accounts, a significant margin is present, which resulted from the necessity to use a realistic layup. Here realistic layup refers to the presence of symmetric  $\pm 45 \ 0/90$  surface layers, necessary for the toughness and impact strength of the laminate, and the SparPreg layers, without which no prepreg curing at such high thickness is realistic.

---

### Use of composite stress couplings

A certain amount of effort was given to using the benefits of composites to their full extent, designing an asymmetric laminate which uses coupling between loads present in the structure to increase its structural rigidity. Unfortunately, after significant investigation the idea was discarded, since it proved unrealistic, for several reasons.

1. The loads are only rarely present in the exact same ratio, for which the structure can be optimized
2. The effects of couplings that can be achieved with prepregs is small, since small freedom in the thickness of the layers is present
3. When sufficient coupling is forced in the structure, concerns for initiating internal loads during curing or temperature change arise
4. The structure is to such an extent dominated by the bending and pressure load, between which no coupling is possible, that coupling with the much smaller torque does not generally yield decrease in mass

### Validation

To validate the results of the analytical analysis, an Abaqus [22] finite-element model was constructed, and subjected to the limiting load case. This was done in order to obtain some measure of the validity of the analytical model used for the design procedure.

The model itself was validated using examples from the Abaqus Example and Verification guides [23], which had assumptions similar to what is necessary. Specifically, analysis of composite structures and analysis of pressure vessels in bending was studied. The cylinder, end plates and the simplified hub were modelled as a thin-shelled structure, with S4R shell element, as can be seen on Figure 3.17. A mesh refinement investigation (Table 3.6) was also carried out with the original layup to determine the convergence of the solution and the most efficient mesh size for further investigation.

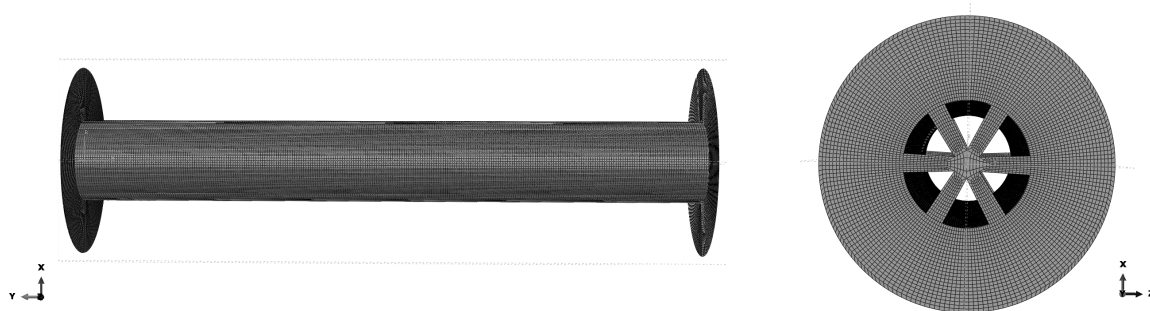


Figure 3.17: An intermediate mesh, with 56 598 shell S4R elements, was used for validation of the effect of lay-up and later core thickness. The cylinder has a structured mesh, as does the hub. The endplates use a swept quadrilateral mesh.

Table 3.6: Mesh convergence study of the rotor. The mesh with 56598 elements of type S4R was chosen as good compromise between accuracy and computational time. In the table, the values for displacements and stress factor under the different element numbers are presented.

Element type	S4R	S4R	S4R	S4	S4R	S4R
Element number	17 348	27 315	56 598	56 598	106 264	178 048
Umax [mm]	72.1	71.0	71.6	71.9	71.7	71.7
U3max [mm]	48.1	47.5	47.7	48.2	47.6	47.6
TSAIH	0.40	0.37	0.38	0.38	0.38	0.38
TSAIW	0.47	0.42	0.43	0.43	0.43	0.43

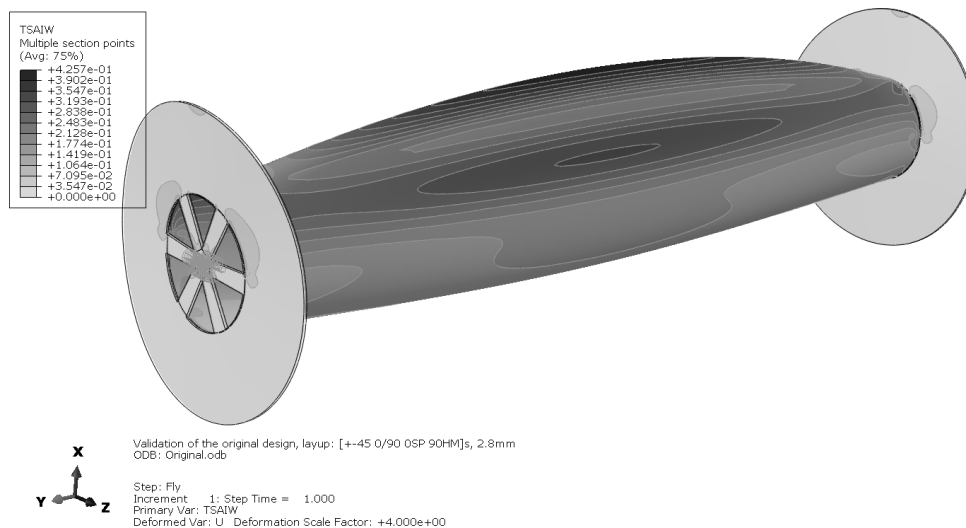


Figure 3.18: The stress distribution plotted on the deformed shape. The deformation is scaled 4 times, however it is obviously significant. The stresses are still below critical.

The results of this validation (see Figure 3.18) were alarming to the design. Although the lack of material failure was confirmed, such significant deformations can reduce the lifting force of the cylinder significantly, lead to small-scale vibrations and all-in-all decrease the performance.

While some design equations that determine buckling eigenvalues, and thus corresponding stresses and loads before loss of stress carrying capabilities, there are few developments in determining deformation due to instabilities. In this case, since the load carrying capability of the structure is not lost, evaluations of the design by analytical methods is next to impossible. On the other hand, the use of final-element simulations for optimization purposes is a slow, tedious and error-prone process.

#### *Further iteration*

Without the capability for analytical optimization and considering the approaching deadlines, a new goal was set: to find a valid cylinder structure, which, even if not optimized, fits within the initial weight estimate and does not impose unnecessarily high penalty the production methods. To keep the aerodynamics analysis valid, a requirement of 1% shape deviation was set, which can be translated to maximum decrease in the radius of 2.7 mm.

The stabilizing methods considered were changing the layup of the laminate, making the cylinder out of sandwich material, structural reinforcement (frame and stringers) or a corrugated concept. After a brief investigation, the foam-core sandwich cylinder strategy was chosen, because:

1. Changing the fibre orientation can not influence the buckling behaviour significantly enough.
2. Increasing the thickness of the laminate will only further increase the weight.
3. Corrugated concepts are very difficult to analyze and also present a major production challenge.
4. External frames ruin the aerodynamics, while installation of internal frames is impossible in a monocoque (single-piece) cylinder. While making the cylinder out of multiple parts is in fact easier, their final assembly will introduce a lot of inconsistencies over the circumference and the length, which will be lead to deterioration in balance.
5. Even if the manufacturing problem is solved, for example using laminated-in frames in specially prepared slots in the mandrel mold for the cylinder, there is still a huge design space of different sizes of frames and frame pitch to be explored.
6. Classical honey-comb core cannot be formed in tight curvatures. Alternatives such as Flex Core have their drawbacks in terms of internal stresses during curing and plastic deformation during production, which will again affect the balance.

7. Foam cores come in a relatively narrow band of thicknesses and densities. They can be easily explored in a FEM model, since only a material change is necessary, and the mesh and model can remain the same.

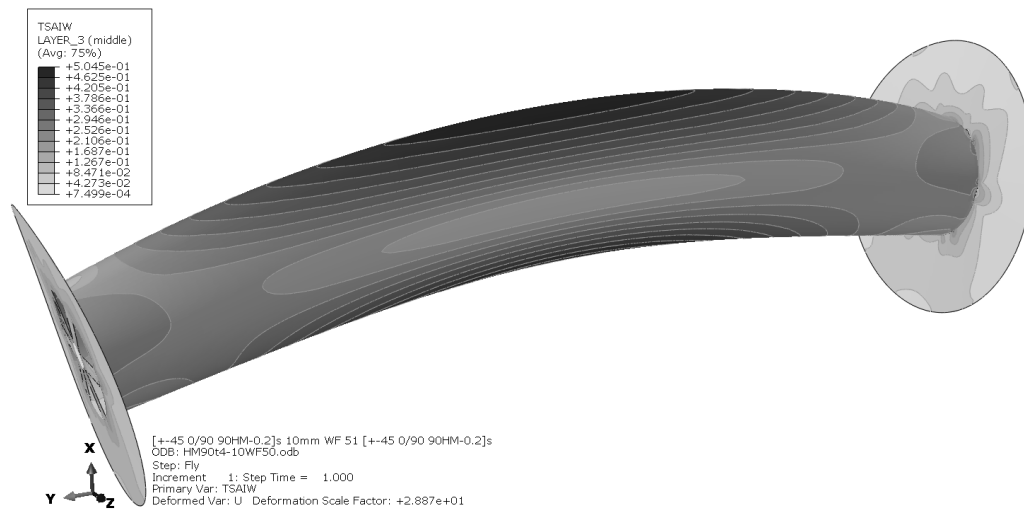


Figure 3.19: The stress distribution plotted on the deformed shape for the valid design. The deformation is scaled almost 30 times, however it is obviously smaller than before. The stresses are still below critical.

The first order optimization was carried out until a good enough solution was obtained (Table 3.7). Further analysis is expected to decrease the weight even further, however this solution is still 1.2 kg lighter than the analytical estimate. The total thickness is 12.4 mm, a 10 mm core and two laminates symmetric around an 0.4 mm thick ply of high-modulus Toray M60J 60% with Toray 250F resin system. An overview of the displacement is present on figure Figure 3.19

Table 3.7: First order optimization of sandwich panel cylinder. Only the last solution satisfies  $m \leq 35$  kg and  $U_{3max} < 27.6$  mm.  $U_{max}$  is the maximum deflection,  $U_{1NA}$  is the deflection the neutral axis upwards,  $U_{3max}$  is the maximum inward deflection of the sides, TSAIW is the Tsai-Wu failure criterion for the most loaded layer and MSTRN is the maximum strain criterion for the core. The carbon fibre weave is spread-tow Hexcel G904, while HM is the high-modulus uni-directional M60J (see Appendix A for details on the materials).

Layup	Core	Mass	$U_{max}$	$U_{1NA}$	$U_{3max}$	TSAIW	MSTRN
Requirement		< 35		< 21	< 2.7	< 1	< 1
Unit	[-]	[kg]	[mm]	[mm]	[mm]	[-]	[-]
$[\pm 45 \ 0/90 \ 90HM]_s$	10mm WF51	39.8	12.70	10.00	1.76	0.44	0.46
$[\pm 45 \ 0/90]_s$	5mm WF51	19.9	33.70	13.00	16.40	0.38	0.78
$[\pm 45 \ 0/90 \ (90HM)]_s$	5mm WF51	28.9	18.20	11.00	5.19	0.58	0.52
$[\pm 45 \ 0/90 \ (90HM)]_s$	5mm WF110	31	15.96	11.00	3.74	0.56	0.50
$[\pm 45 \ 0/90 \ (0HM)]_s$	10mm WF51	30.8	9.82	3.00	4.57	0.49	0.67
$[\pm 45 \ 0/90 \ (90HM)]_s$	10mm WF51	30.8	14.40	11.00	2.27	0.50	0.54

### Cylinder Drive System Sizing

A system is designed to be able to drive the cylinder, containing the following parts. The first part is the shaft which is driven by the rotor engine, supported by the vertical support and attached to the cylinder. The second part is the shaft which is on the other end of the cylinder. The third part is the bearing system which allows the shaft to rotate while still being supported by the vertical support. The bearing

system design is a complex process, and is therefore described in the separate subsection 3.1.2. The fourth part is the assembly of parts transferring the torque on the shaft provided by the engine to the cylinder, the cylinder end-cap support.

### Cylinder End-Cap Support

To transfer the torque of the shaft to the cylinder a structure is designed to provide such a transfer of the torque. The minimal structure for such a transmission would be a single spoke going from the shaft to the cylinder. The maximum structure would be a sheet covering the entire area between the shaft and the cylinder. The optimal solution is expected to lie somewhere in between these two extremes, in the form of  $n$  spokes going from the shaft to the cylinder. Before a sizing of this structure can be done the loading case on the structure needs to be investigated.

Two different situation can be distinguished for the loading case. The first situation is when the cylinder is rotating at a constant rpm. The load on the end-cap support is then as follows. The torque of the shaft translates to a force perpendicular of the end-cap support on the base of the end-cap support at the driving shaft, and a resultant force to this force is located on the other end of the end-cap support in opposite direction. The end-cap support is deformed at the end that is attached to the cylinder, because the cylinder strains in the direction of the axis of the end-cap support due to the centrifugal force. The cylindrical shape is crucial from an aerodynamic point of view, so the end-cap support cannot be stiff enough to cause a influential limit on that deflection.

The second situation to be considered is when the cylinder is accelerated or decelerated from non-rotating to the rpm required for the maximum lift, or from the maximum rpm to non-rotating. The magnitude of the acceleration is determined in Equation 3.15 by dividing the change in velocity from zero to the maximum rpm and the time it takes to achieve this maximum velocity. The time it takes to achieve this change in velocity comes from the energy required to speed up the cylinder divided by the maximum power that the engine can provide as in Equation 3.16 [24]. The mass moment of inertia  $I_{mass}$  can be determined by using Equation 3.17.

$$a = \frac{dV}{dt} = \frac{d\omega R}{dt} \quad (3.15) \quad dt = \frac{E}{P} = \frac{\frac{1}{2}I_{mass}\omega^2}{P} \quad (3.16) \quad I_{mass} = mR^2 \quad (3.17)$$

During these two different situations the end-cap support is in constant loading perpendicular to the plane of the end-cap support by the deflection of the cylinder due to the lift force. Depending on the stiffness of the end-cap support structure this loading causes a deflection of the end-cap support. Since the end-plates of the cylinder are located at the edges of the cylinder at the same location of the end-cap support, this deflection will cause the end-plates to deflect at an equal angle. Even a deflection of a few degrees will result in a significant deflection at the end of the end-plates, therefore this needs to be minimized. A structure for the end-cap support is therefore chosen that has sufficient stiffness in the outer plane direction. An overview of the loading case of the end-cap support can be found in Figure 3.20.

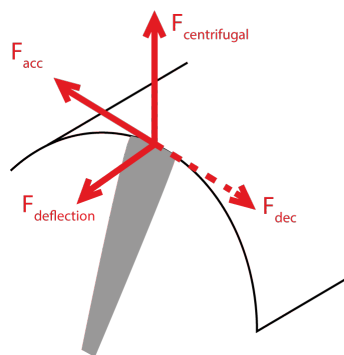


Figure 3.20: Loading case end-cap support

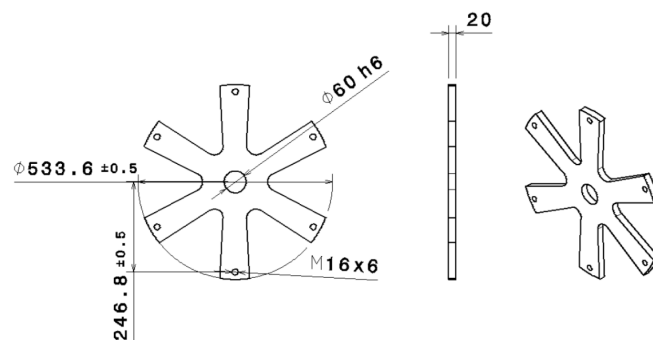


Figure 3.21: End-cap support structure

To withstand the loading cases, a honeycomb with carbon fibre reinforced sheets was selected to provide sufficient stiffness. A symmetric configuration of six relatively wide spokes is chosen as the structure for the end-cap support. An illustration of the configuration can be found in Figure 3.21. The mass of the structure follows from the dimensions as illustrated in Figure 3.21 and the density of the carbon fibre reinforced sheets used. The computed mass is presented in the overview of the masses of the different components in subsection 3.1.4.

### *Cylinder Drive Shafts*

Two shafts of certain dimensions are needed to transfer the torque provided by the engine through the bearings and onto the cylinder and to transfer the loading of the cylinder onto the cylinder support. The second functionality of these shafts is to allow pre-loading on the bearing system, the reason for which will be further explained in subsection 3.1.2. For the sizing of these shafts first the loading case on the shafts is considered.

The end of the shaft on the cylinder side is loaded by half of the total lift force, since the cylinder is supported on two sides. A reaction force to the lift force is found at the position of the vertical support and the bearing system. At the other end of the shaft the torque provided by the engine is applied.

The loading on the shaft by the torque provided by the engine on the shaft is very small compared to the lift force and the reaction force, and can therefore be neglected when sizing the shaft. The largest stress on the shaft is caused by the moment caused by the lift force on the end of the shaft and can be found at the top of the cross-section [16]. The length of the shaft and the position of the reaction force with respect to the lift force determine the magnitude of the moment. The length of the shaft follows from the required space for the parts that are placed on the shaft. The cross-section of the shaft needs to be circular in order to be able to rotate through the bearing system, and the radius of the circular cross-section follows from the maximum allowable stress calculated using Equation 3.18.

The maximum allowable stress  $\sigma_{allow}$  is a material property and thus follows from the selection of the material for the shaft. The material aluminium 7075 T6 was chosen for the shaft based on the preferable density to stiffness ratio [25] of this material. The distance from the centroid  $c$  where the stress is maximum is at the edge of the cross-section, so at the distance equal to the radius. The area moment of inertia of a circular cross-section can be determined using Equation 3.19

$$\sigma_{allow} = \frac{M_{max}y}{I} \quad (3.18) \quad I = \frac{\pi}{4}r^4 \quad (3.19)$$

Rewriting and computing Equation 3.18 and Equation 3.19 gives the radius for the shaft required to withstand the highest loading case.

To achieve the same structural properties with less material, and therefore less weight, a hollow shaft can be used. The above procedure can be used to determine the sizing, but with a different moment of inertia as computed in Equation 3.20.

$$I = I_{outer} - I_{inner} = \frac{\pi}{4}r_{outer}^4 - \frac{\pi}{4}r_{inner}^4 \quad (3.20)$$

The input for the sizing of the cylinder drive shaft are the maximum lift force of 30,000 [N], the required length of 300 [mm], the aluminium 7075 T6 material selected and the pre-loading required. Using the above method for the computation of the sizing, the results of the size of the cylinder drive shaft can be found in Figure 3.22.

The end of the shaft at the side of the cylinder is closed off by a M60 nut. The shaft is pre-tensed by the bolt to ensure all different parts remain in place. Next to the bolt a washer is placed, followed by the hub where the spokes of the end-cap support are attached, followed by another washer. Next to the hub with washers a spacer is placed to ensure enough space for the deflection of the end-plates. Following the spacer, the bearing system with housing is placed, followed by another spacer. This spacer is placed to allow space for possible deflection of the driving band of the engine that is located next to the bearing

and spacer. Next to the driving band a last spacer is placed, followed by a hub which is attached to a cable that runs through the shaft and cylinder all the way to the end of the shaft on the other side of the cylinder. This cable with hubs is to ensure pre-loading on the bearing system, on which will be further elaborated.

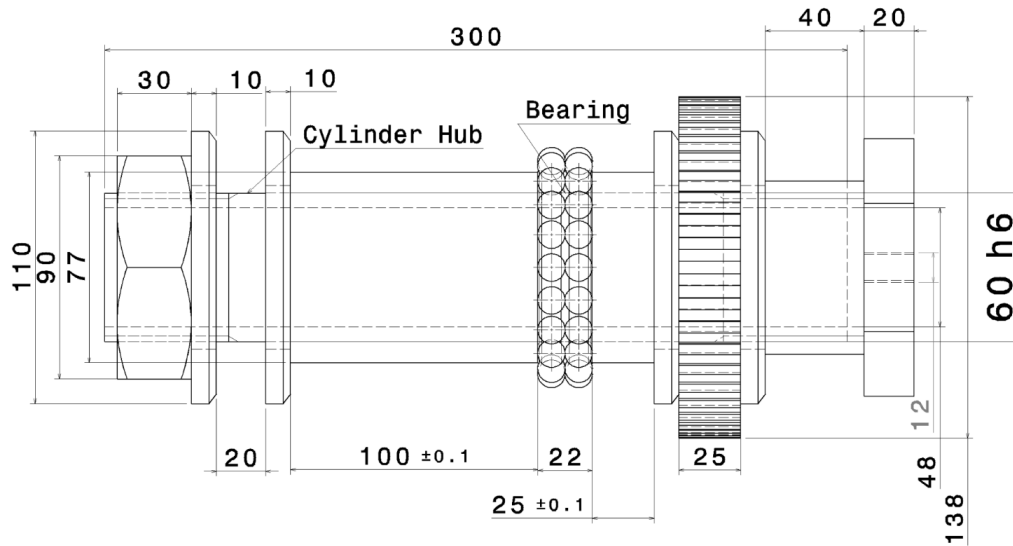


Figure 3.22: Sizes of the cylinder drive shaft

The mass of the shaft and the spacers on the shaft follows from its dimensions as presented in Figure 3.22 and the density of the aluminium 7075-T6 that is chosen for the shaft. The computed mass is presented in the overview of the masses of the different components in subsection 3.1.4.

To ensure the shaft will hold under the loading cases, a stress analysis was done [16]. Using Equation 3.18 the compressive and tensile stress due to the moment by the lift and reaction forces can be found, where  $y$  is at maximum distance from the centroid, in this case the outer radius of the shaft, and  $I$  is computed using Equation 3.20. With Equation 3.21 the maximum shear stress due to the lift and reaction forces is determined, where  $Q$  is the moment area around the neutral axis given by Equation 3.23 and with Equation 3.22 the tensile stress due to the pre-tension in the shaft is determined, where  $P$  is the pre-tensional load and  $A$  is the area of the cross-section of the shaft.

$$\tau = \frac{VQ}{It} \quad (3.21) \quad \sigma = \frac{P}{A} \quad (3.22)$$

$$Q = \frac{4r_{outer}}{3\pi} \left( \frac{\pi r_{outer}^2}{2} \right) - \frac{4r_{inner}}{3\pi} \left( \frac{\pi r_{inner}^2}{2} \right) \quad (3.23)$$

The results of the stress analysis and the comparison to the limits the material allows before failure [25] can be found in Table 3.8.

Stress	Shaft	Allowed	Unit
Maximum compressive stress	335	393	MPa
Maximum tensile stress	381	431	MPa
Maximum shear stress	70	330	MPa

Table 3.8: Stresses on the cylinder drive shaft compared to the allowed stresses before failure

The shaft on the other side of the cylinder has no torque applied on it, since there is only one engine driving the cylinder. The loading caused by the torque however, is negligibly small compared to the

---

loading by the lift force. Therefore when sizing the shaft on the non-driving side of the cylinder the same dimensions and material as the shaft on the driving side of the cylinder will suffice to withstand the loading on this shaft.

### **Bearing System Sizing**

In order to transfer the loads on the cylinder to the payload while still allowing the cylinder to rotate requires a system of bearings. In order to size these bearings, first the loading case on these bearings was assessed. Secondly the rotational speed and diameter of the cylinder were assessed and their influence on the sizing of the bearings was determined. Thirdly the clearance following from the loading case is discussed. Following the discussion on clearance, the operating temperature is assessed and necessary lubrication is considered, and finally the bearing type, material and size are selected.

#### *Loading case*

The loading case most relevant for the bearing system is the resultant force of the pressure distribution on the cylinder, the lift force. This loading case is previously discussed in subsection 3.1.2. The reaction forces determined in that section translate to a radial force on the two bearing systems on both ends of the cylinder.

The lift force causes the cylinder to deflect in the direction of the load, causing a deflection at the bearings would the bearings allow so, or a tilting moment on the bearings. In the case of chosen bearings that allow for a deflection, the maximum deflection angle can be calculated using the formula for the simply supported beam [16] as presented in Equation 3.11. If deflection is allowed, the radial force gets an angle with respect to the axis of the bearing, therefore creating an axial component of the force.

To avoid clearance in the bearing system during operation an axial load is introduced on the bearing, on which will be further elaborated in paragraph 3.1.2. The size of this axial load, the pre-load, is determined as 10 % of the radial load [26].

#### *Rotational Speed and Diameter*

The speed and diameter of the cylinder play an important role in the sizing of the bearing system. Since these parameters are so closely related their multiplication is used as a parameter to determine the feasibility of the bearing system solution. This parameter is referred to as the  $n - d_m$ -value [26], where  $n$  is the rpm and  $d_m$  is the diameter of the bearing system. From a sizing perspective there is a direct relation between this parameter and the weight and complexity of the bearing system, therefore the value of this parameter should be as low as possible. The maximum feasible value for the parameter is around 600,000 [26] and is related to the possibilities of lubrication and the reliability of the bearing system. The rpm of the bearing system is determined by the rpm required by the cylinder and is constrained by the lift required. Changing the rpm is therefore not preferable. To optimize for the  $n - d_m$ -value the diameter of the bearing system will be adjusted accordingly. From the sizing of the cylinder drive shaft follows a minimal inner bore diameter of 60 millimeters. This diameter combined with the maximum rpm of 4110 from the aerodynamic considerations gives an  $n - d_m$ -value of 246,600, a value that is well within the feasible spectrum when bearings are concerned.

#### *Clearance*

Internal clearance is the distance the inner and outer can move with respect to each other, both in radial and axial direction [27]. There is a distinction made between initial internal clearance before mounting and the clearance when the bearing is mounted and reached operational temperatures. Due to thermal expansion and the interference fit the operational clearance will be smaller than the initial clearance. For the optimal performance, especially when selecting ball bearings, virtually zero operational clearance is crucial.

To ensure that there is no clearance during operations the bearing system will be pre-loaded, by putting an axial force on the bearing. For the application of this axial force the shafts with the spacer pressing against the bearing are loaded by having a cable run longitudinally through the cylinder and through

both shafts. The cable will be put in tension and pull the shafts toward each other, putting an axial load on the bearings. A typical pre-load is 10% of the radial load [27], where the radial load for the major part of the bearing system operational life is 5 [kN]. Therefore for each bearing system the required pre-load for this application is 500 [N].

#### Temperature and Lubrication

The temperature has great influence on the behavior of both the bearing material and the lubrication of the bearing. The local temperature is influenced by the environmental temperature and friction between and therefore the rotational speeds of the different parts of the bearing. The environmental temperature for this particular application ranges from 20 to -50 degrees, a temperature range that has no large implications for the selection of the bearing system, since this range provides a large number of feasible bearing system solutions. The high rotation speeds influence the operational temperature of the bearing system, therefore limiting the maximum rotational speed of a certain bearing solution. This speed limit is commonly referred to as the reference speed, whereas the mechanical speed limit is referred to as the limiting speed. When selecting the bearing system solution, both of these speeds are taken into account.

The lubrication for the bearing system can be either oil or grease lubrication. An oil lubrication system can provide higher rotational speeds, but adds more weight and complexity to the bearing system. Since grease lubrication is a feasible solution for the rotational speeds required for this application, grease lubrication is selected as the form of lubrication for this bearing system.

#### Bearing System Type, Material and Size

To allow for the deflection of the cylinder, a bearing needs to be selected that allows for a deflection. Naturally self-aligning bearings are a fitting solution to allow for this deflection. For the relatively high rotational velocity ball bearings are the most optimal solution, since the reliability of other roller bearing solution is lower at high rotational speeds. The material of the bearing and its rolling elements also follows from the requirement of a high rotational speed. The possible solution of polymeric materials is discarded due to their deformation at relatively low temperatures, which leads to a low rotational speed limit. Ceramic rolling element as a solution is discarded due to their explosive failure mode, which leads to failure of the entire bearing system, whereas metallic rolling element failure only leads to a decrease in performance of the bearing system. Since the lift providing system relies heavily on the bearing system, complete failure of the bearing system is not acceptable.

The bearing fitting all the criteria for this particular application is the 1212 ETN9 bearing [26]. This bearing is a self-aligning ball bearing, an illustration of this bearing can be found in Figure 3.23 and the specifications of this bearing can be found in Table 3.9.

Notation	Description	Size	unit
$B$	Width of the bearing	22	mm
$D$	Outer ring diameter	110	mm
$D_1$	Outer ring raceway	97.6	mm
$d$	Inner bore diameter	60	mm
$d_2$	Inner ring raceway	78	mm
$r_{1,2}$	Chamfer dimensions	1, 5	mm
$C$	Basic dynamic load rating	32.2	kN
$C_0$	Basic static load rating	12.2	kN
$V$	Limiting speed	8500	rpm
$m$	Mass	0.9	kg

Table 3.9: Specifications of the 1212 ETN9 self-aligning ball bearing [26]

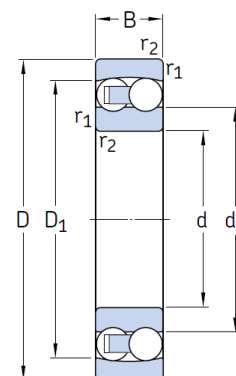


Figure 3.23: The 1212 ETN9 self-aligning ball bearing [26]

## Bearing System Analysis

An analysis is done for the selected bearing system to ensure the bearing system will hold for the loading during the entire operational life of the aircraft. To assess whether the bearing system will hold the basic rating life in operating hours is determined using Equation 3.24 [27], where  $n$  is the rpm of the bearing,  $C$  is the basic dynamic load rating,  $P$  the equivalent dynamic load and the exponent  $p$  is equal to 3 for ball bearings. The equivalent dynamic loading  $P$  is determined using Equation 3.25, where  $F_r$  and  $F_a$  are the radial and axial load on the bearing system and  $X$  and  $Y$  are load factors that depend on the type and size of the bearing. Computing the basic rating life gives an operating life of 640 hours, which complies with the indicated operating life by the manufacturer of the bearing system [26]. With the required operating life of 50 hours, the bearing system meets this requirement by a large margin.

$$L_{10h} = \frac{1}{60n} \left( \frac{C}{P} \right)^p 10^6 \quad (3.24) \quad P = XF_r + YF_a \quad (3.25)$$

### 3.1.3 Rotor propulsion

The cylinder will be powered by the Simonini mini 2 plus (Figure 3.24)<sup>1</sup>, which is an aircraft engine largely used for lightweight personal aerial vehicles. The engine is known for its low fuel consumption, and high power to weight ratio. The engine will sit inside the vertical support. The engine characteristics are as follows, shown in Table 3.10. The maximum power output per rpm can be found in Figure 3.25<sup>1</sup>, where "coppia" is Italian for torque and "potenza" is power.

Characteristic	Value	Unit
Max shaft power	26	hp
Dry weight	14	kg
Rpm for max power	7500	rpm
Est. fuel consumption	145	g/kWh



Table 3.10: Simonini 2 plus characteristics

Figure 3.24: Simonini 2 plus IC-engine<sup>1</sup>

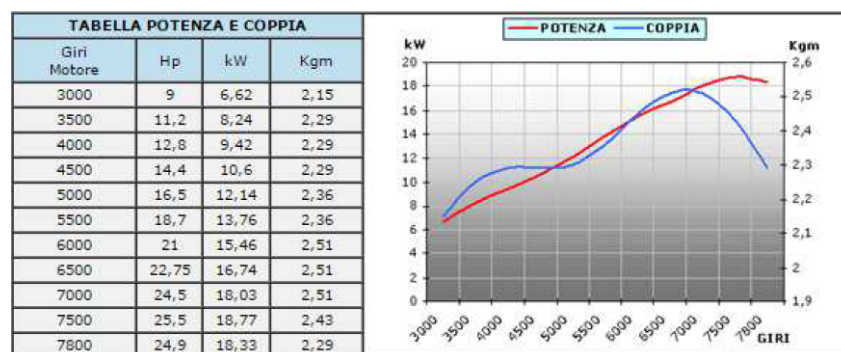


Figure 3.25: Simonini 2 plus performance curve<sup>1</sup>

The Simonini engine, which is placed at the bottom of the vertical tail, has to rotate the cylinder. When buying the Simonini, the engine itself comes with an output shaft and a reduction belt, that runs to the shaft of the propeller attachment. The set-up is slightly changed for this aircraft, instead of having our v-belt running to the propeller shaft, it will run up to the shaft of the cylinder.

<sup>1</sup><http://www.simonini-flying.com/index.php?lang=en>

During cruise the Simonini should spin at its optimum rpm for a certain power during cruise. The optimal rpm is at approximately 80% rpm of max rpm for SI-Engines ([28]), just before the peak of the torque. The rpm for the cylinder at the start of cruise is 2900, which decreases to 2500 for the end of cruise. So the wish of the gearing design is to have a rpm reduction from 6250 to 2700, which is the cruise average. This results in a gearing ratio of 2.3, which is similar to the ratio used for the propeller shaft. The ratio of 2.3 also has to comply with the maximum rpm of the cylinder experienced during flight and the redline of the engine. The engine has a maximum rpm of 7800, with a reduction this leads to 3400. The maximum rpm experienced is 3050 during the take-off phase, which is only for a short time interval. As running on max rpm for a prolonged time will severely harm your engine, but this engine will not exceed the 7000 rpm.

### 3.1.4 Summary rotor

The main characteristics of the rotor support subsystem are summarised in Table 3.11 and illustrated in Figure 3.26.

Table 3.11: Summary of the rotor characteristics

Variable	Value	Unit	Variable	Value	Unit
Span	4.2	m	Mass end-cap & -plate	5.99	kg
Radius	0.27	m	Mass drive shaft	7.9	kg
Aspect ratio	7.8	-	Mass bearing	3.1	kg
Endplate radius	0.68	m	Engine for rotation	Simonini Mini 2 plus	
Lift-to-drag ratio	5.6	-	Operational weight engine	21	kg
Cruise lift coefficient	4.99	-	Max. shaft power $P_{max}$	26	hp
Cruise drag coefficient	0.89	-	Max. cylinder speed	3260	rpm
Lay-up	$[\pm 45 \ 0/90 \ (90HM)]_s$		Core	10 mm WF51	
Cylinder surface	Smooth	-	Fuel consumption (75%)	2.2	l/h
Mass cylinder	30.8	kg			

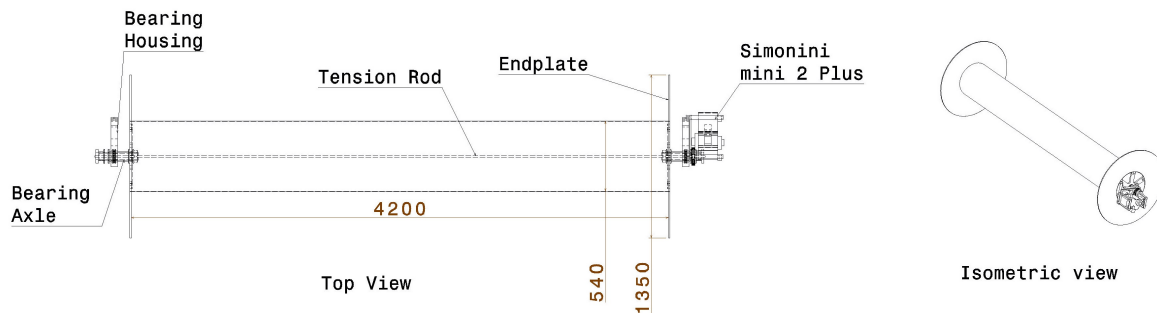


Figure 3.26: Technical drawing of the rotor subsystem

## 3.2 Rotor support

The rotor support consists of two main elements, the vertical support and the horizontal wingbox. This section first discussed the loadcase, design and analysis of the vertical support. Afterwards, the same is done for the wingbox. The minimization of drag for both structural components is subsequently discussed, as well as the operation of the cylinder rotation.

### 3.2.1 Vertical support

The vertical support connect the rotor to the horizontal support. First, the loadcase and the design following from it are explained. Following this, the results are analyzed, verified and validated.

#### Loadcase

The load case of the vertical support and its location are shown on Figure 3.27.

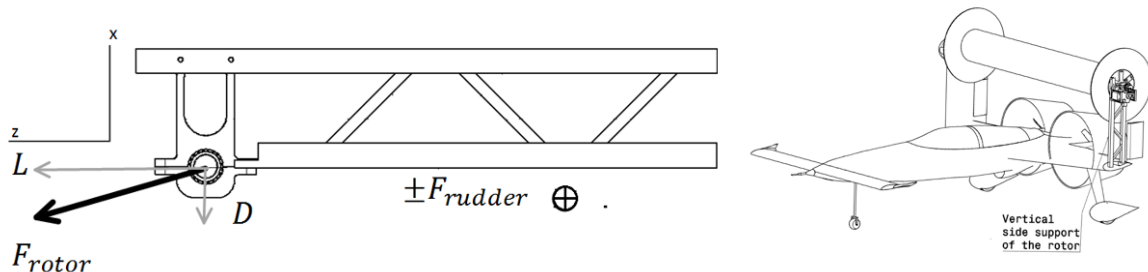


Figure 3.27: Load case on the structure of the rotor vertical side support. The aerodynamic force of the rotor can be translated to lift and drag forces, acting at the bearing. In addition, the moment and force caused by the action of the rudder is distributed over the length. The structure is connected to the spars of the wingbox.

The size of the aerodynamic and rudder forces varies during the flight. The maximum loads expected follow from the reaction loads on the cylinder as discussed in subsection 3.1.2. A lift force  $L$  between 30 and -12 kN is expected, as well as a drag force of maximum 6 kN. Due to the use of self-aligning bearings, no moments are present, which allows for significantly lighter structure. These are the main loads on this support structure and the main drivers on its size. The main function of the vertical support is to transfer the loads on the cylinder to the horizontal support.

Out-of-plane loads and moments also act on the structure, since it functions as a vertical stabilizer and has the rudder attached, and in addition houses the cylinder drive system on the top. The load on the rudder also causes torsion. All of these loads can be considered negligible compared to the main loads. Several reasons justify this simplification.

1. The magnitude of these forces is an order of magnitude smaller than lift and drag forces.
2. The cylinder and horizontal support connect the two symmetric vertical supports. This symmetry boundary condition is much more efficient than the cantilevered boundary condition in the plane.
3. The aerodynamic shape which decreases the drag of this support (see subsection 3.2.3) will need to transfer the aerodynamic loads of the vertical stabilizer and rudder to the internal vertical support structure, and will thus add to the stiffness of the structure.
4. Finally, a certain amount of compliance is welcome in this direction, for reasons discussed below.

The lift force is transferred from the rotor to the vertical support before it reaches the body. Based on aircraft wing structures, the horizontal support would need to be extremely heavy to maintain small displacement. In fact, the load case on the horizontal support is worse than the one on a normal wing as discussed in subsection 3.2.2. If the connection between the vertical support and the wingbox is very

---

rigid, this displacement will cause rotation in the vertical support, and cause displacement at the tip where the rotor is.

The distance on the two ends of the cylinder needs to be properly maintained for clearances of the bearing and endplates. As discussed in subsection 3.1.2, the pretension on the bearing is maintained with a wire, which acts in combination with the cylinder itself. However, the symmetry boundary condition from point 2. would become anti-symmetry and increase the compression loading on the cylinder.

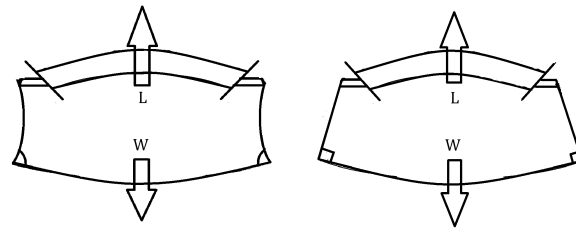


Figure 3.28: The displacement of a more compliant concept (left) for rotor support versus stiffer concept (right). The compliant concept has benefits for both clearance and less compressive load on the rotor, if the vertical displacement of the wingbox is similar. Note: Displacement are greatly exaggerated. The vertical connection is still loaded primarily in tension.

On the other hand, if the connection is compliant, the horizontal support can deflect significantly (order of cm) without causing much rotation of the tip. This concept on the loadcase form the basis of the detailed design of this structure.

## Design

The secondary requirements on the element, in addition to not failing under the highest expected loading, were to allow for mounting of the rotor propulsion (bearing, engine, shaft, etc.), to allow for easy accessibility to both the cylinder and the auxiliary engine and to be easily modifiable after production (see also subsection 4.5.3).

The maintainability and extendability requirement was driving in selecting a modular approach to the assembly of the structure, as well as to aluminium as the material of choice. Reassembly of composite, while possible, is much more labor intensive and decreases the life of the structural elements. Under the chosen design philosophy (Figure 3.28), however, the more flexible connection and vertical support allow for a lighter wingbox. The design consists of a two-part bearing housing and a spar consisting of two C-flanges and truss supported web as shown in Figure 3.29. The bearing is very stiffly attached to the rear flange, to allow the moment caused by lift offset to counteract the bending moment of the drag force.

### *Spar*

For the design optimization, different failure modes were critical to determine various parameters. Column buckling under -1.5g resulted in 50 mm depth dimension and 60 mm flange dimension. The thickness and height of 300 mm resulted from the bending moment caused by the drag. Initially, a swept design was considered to distribute the load between the two spars. However, the bearing housing proved much larger than expected, and customizing its shape to serve this function proved more efficient than sweeping one of the flanges. The attachments suggested the thickness 4 mm for bearing strength, but the combination of thickness and material profile was determine from a set of available off-the-shelf Al 7075-T6 components [29].

### *Bearing housing*

The bearing housing is by necessity a safe-life component, since no alternative load paths are present and inspections are hard to perform conclusively. It is based on existing bearing housing design from [26]. Since off-the-shelf solutions are usually made of cast iron, they are too heavy for aerospace applications.

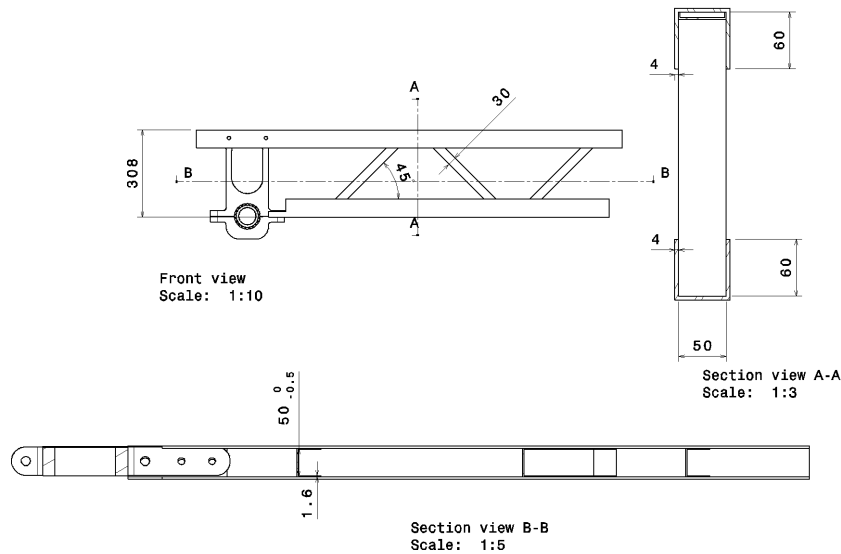


Figure 3.29: Technical drawing of the structure of the vertical support

In this redesigned solution, aluminium was used. As mentioned above, it is a split block housing, allowing for easy mounting of the bearing without complete disassembly of the whole structure. Ideas from both pillow block and flange housings were used to allow for combination of a bearing housing and end truss for the spars.

The 30 kN force to be transmitted from the bearing determined the necessary thickness of aluminium. Large radius and fillets are necessary on the outside to provide for smooth stress field, while the inside needs to be machined to very small tolerances. Detailed dimensions are present on Figure 3.29. The high stiffness in the plane of the spar is necessary to distribute the load between the two flanges, and consequently, between the spars of the wing box.

#### *Attachment*

The attachment points were determined such that they allow the best distribution of the load between the flanges, without initiating unwanted stress concentrations. In addition, the load can be distributed properly to the flanges even if any bolt on the rear side (where the bearing is located), and any two bolts on the front side are loose. This is necessary since high vibrations are expected in the structure, and, in addition, during the prototyping stage, mounting and dismounting of the cylinder and other components will be frequently repeated.

Also, the engine mount for the Simonini auxiliary engine is attached to the port-side vertical support, while housing for the recovery system are housed on the starboard. The load by the engine mount is small compared to the lift, however the vibrations of the engine need to be accommodated by the engine mount. The recovery system attachment point at bearing housings is chosen specifically because it is already sufficiently strong to carry the weight of the whole aircraft.

#### **Analysis**

The spar was modelled similar to a typical crane arrow problem. The two flanges are modelled as deformable Bernoulli-Euler beams, while the cross-members are assumed pin-connected trusses. The validity of modelling similar flange-trusses has been well established in structural analysis, and numerous examples of crane arrows validate the analysis models described in [16]. The dimensions of the structure are well within the assumptions of the theory outlined in this book, and the addition of the tensile loading does not change the failure modes significantly. The model is thus assumed valid for the current analysis.

The code used for determining the stresses was verified against an existing solved problem from [16], reproducing the answer exactly since the same model is used.

The verified and validated analysis tool shows no failure during even the most demanding load case. The design factor of 1.5 and the discrete thicknesses available lead to the structure being capable of carrying significantly more load than necessary. The highest displacement expected due to drag force is of the order of 1 cm, while the maximum displacement of the tip out-of-plane that the structure can withstand without failure under normal operation is approximately 10 cm. In normal operation, at a load factor of approximately 1, the highest von Mises stress in the structure is 50 MPa, which means that the fatigue life of Al 7075 is several orders of magnitude higher than the life time in Requirement **RMEA-SS-LT-8**.

Further development is necessary in determining the exact layout of the engine mount and the connecting structure between the vertical and the horizontal support structure.

### 3.2.2 Wingbox in horizontal support

In order to withstand the loads that go through the rotor support, a structural component is designed within the horizontal support referred to as the wingbox. Like in a regular aircraft, the wingbox transfers the aerodynamic forces to the payload. This section will elaborate on the worst load cases of the wingbox, the failure modes, the input variables and the design criteria. It will be concluded with a full analysis of the structure and a verification of the model used.

#### Loadcase

The wingbox will be analysed for two loadcases, which are shown in Figure 3.30. The first loadcase is from Requirement **RMEA-MIS-2**: a 3.8g turn during cruise at MTOW. The difference with a regular wing is that the lift force is not distributed along the span of the wing. The lift component is concentrated at the tip of the wing, which makes the shear loading constant along the span and the moment distribution linear throughout the wing. An additional constant torsion is added to the wingbox caused by the drag of the cylinder multiplied with the height of the cylinder. This torsion is not present in a regular aircraft. Finally, the lift component adds an additional torsion since the wing is tapered along the y-axis.

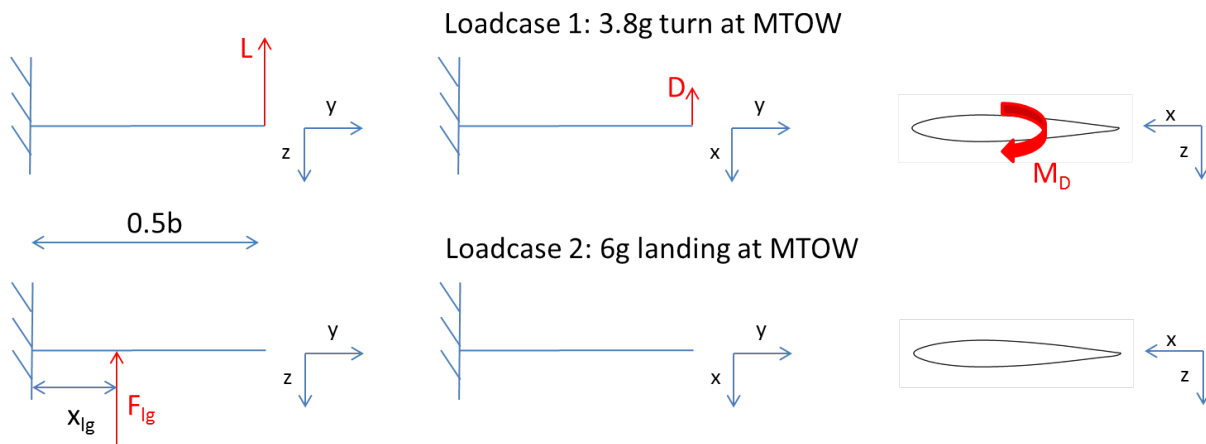


Figure 3.30: Wingbox loadcase: 1ste loadcase - 3.8g turn at MTOW, 2nd loadcase - 6g landing at MTOW. From left to right: front view, top view, side view.

The second loadcase is from Requirement **RMEA-SS-LT-10** a 6g landing at MTOW, which causes a large shear and moment force. In a regular aircraft, a landing at MTOW is not done since fuel is dumped before landing. However, Magnus Aeolus will be an experimental aircraft which means that there is a high risk of failure. This means that the aircraft might return after a short flight already. Dumping the fuel every time a component fails is not sustainable and will add a lot of problems and costs during the

testing phase. Therefore, the landing loadcase is at MTOW, so fuel dumping is not necessary. Any other loadcase will be less severe and is not worth analysing.

### Analysis

The following failure modes will be taken into account for both loadcases: yielding due to von Mises stress (shear loading and bending) and buckling. Additionally, the rotor support assembly houses two self aligning bearings that have a maximum angle they can align. The wingbox should ensure that the deflection of the support does not exceed the allowed bearing deflection. Finally, the wingbox has to accommodate the fuel of the aircraft. The wingbox should have enough volume to accommodate the fuel that is required to be aft of the c.g. for stability purposes. The wingbox has the following design parameters: material choice, location of the spars as percentage of the chord length, root length, number of stringers, stringer geometry and number of ribs. The design will undergo an iterative process to get to the lightest solution shown in Figure 3.31. Between each of the arrows a check is done to see if the design exceeds the failure modes, deflection criteria or volume criteria. The model and the theory used will be discussed in the next paragraphs.

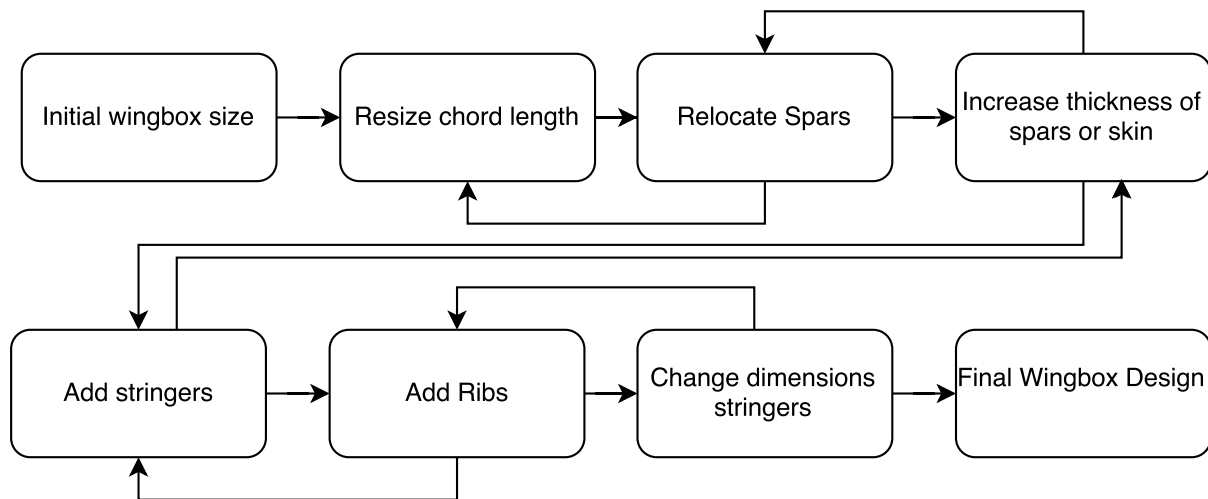


Figure 3.31: Iterative optimization procedure to design the wingbox structure of the rotor support

Table 3.12: Code description wingbox analysis

Step	Description
1	Load airfoil
2	Construct wingbox
3	Calculate geometrical characteristics
4	Deflection calculations
5	Calculate bending stress
6	Calculate & compare buckling load
7	Calculate open shear flow
8	Calculate closed shear flow
9	Calculate torsional shear flow
10	Calculate total shear stress
11	Calculate von Mises stress

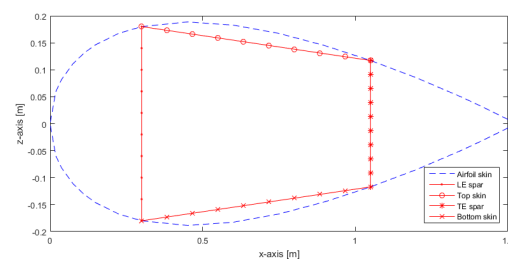


Figure 3.32: Modeling the wingbox structure inside the airfoil of the rotor support

The calculations steps done in the wingbox model can be seen in Table 3.12. The starting point is an airfoil given by the aerodynamics department. The data is imported and scaled to a reasonable size. In

order to transfer the loads, two spars (C-beams) are implemented in the airfoil. To make calculations easier, a skin is placed at the top and bottom between the two spars that varies linear along x. The cross section of the wingbox consists out of these four elements: two spars and two skins. The elements will be referred to as following: leading edge (LE) spar, top skin, trailing edge (TE) spar and bottom skin. The cross section is shown in Figure 3.32. A mesh is created throughout the span, as a base for the future calculations.

Some geometrical characteristics are important for the wingbox. The first calculations include length and heights of the spars and top and bottom skin throughout the wingbox. Next, a centroid calculation has to be done for the x-direction since the structure is asymmetric around the z-axis. Finally, the area moment of inertia around x and z are calculated:  $I_{xx}$  and  $I_{zz}$ . All geometric calculations are a function of the span location.

When the inertia of the wingbox is known, the deflection requirement can be checked. The cylinder is supported by self aligning bearings at the top of the vertical rotor support. These self aligning bearings have a maximum deflection of  $2.5^\circ$ . For a wingspan of 4.4m, the maximum allowable tip deflection is thus 9.6cm. Since the structure is tapered, the inertia varies throughout the span and regular beam theory is not applicable. Therefore, calculating the deflection has to be done with energy methods (Castigliano's theorem) [30] shown in Equation 3.26 and Equation 3.27.

$$C = \int_0^{b/2} \frac{F^2(b/2 - y)^2}{2EI(y)} dy \quad (3.26) \quad \Delta = \frac{\delta C}{\delta F} \quad (3.27)$$

When the wingbox does not exceed the allowed deflection, the stress has to be determined. To calculate the bending stress Equation 3.28 is used. Where  $M_x$  is the moment caused by the lift force or landing gear reaction force and  $M_z$  is caused by the moment around the drag component or zero in case of the second loadcase.

$$\sigma_y = \frac{M_z}{I_{zz}}x + \frac{M_x}{I_{xx}}z \quad (3.28)$$

Next is the calculation of the shear stress. The shear stress will be calculated with shear flow calculations. The shear flow will be calculated in two steps: first a cut is made so an open cross section is created and the shear flow is calculated with Equation 3.30. Next a compensation shear flow has to be added to make sure that the total sum of forces is zero. This is calculated with Equation 3.31. This equation assumes that the forces are applied through the shear center of the structure, so the forces do not apply an additional torque.

$$\tau_{xz} = \frac{q_s}{t} \quad (3.29) \quad q_b = -\frac{F_x}{I_{zz}} \int_0^s tx ds - \frac{F_z}{I_{xx}} \int_0^s tz ds \quad (3.30)$$

$$q_{s0} = -\frac{\int_s pq_b ds}{2A} \quad (3.31)$$

Additional shear stress is created by the torque caused by the drag of the cylinder and the eccentricity of the lift component. This creates a constant shear flow through the walls of the wingbox, which is constant throughout the span. The arm of the drag component is the height of the cylinder with respect to the center line of the airfoil. For the lift it is assumed that the component initiates from a quarter chord length. The arm is the difference between the location of the quarter chord length of the tip with respect to the root. When the additional torque is calculated, the torsional shear flow can be calculated with Equation 3.32. Then, the open shear flow, closed shear flow and torsional shear flow are added together to get the total shear flow (see Equation 3.33). Finally, the shear flow is converted to shear stress with Equation 3.29.

$$q_t = \frac{T}{2A} \quad (3.32) \quad q_s = q_b + q_{s0} + q_t \quad (3.33)$$

When the shear flows are converted to shear stress with Equation 3.29, the final stress can be calculated throughout the cross section with the von Mises stress equation shown in Equation 3.34.

$$\sigma = \sqrt{\sigma_y^2 + 3\tau_{xz}} \quad (3.34)$$

When the structure does not yield, it is still possible that the structure fails due to buckling. Equation 3.35 calculates the critical buckling load. Since the structure is tapered, the critical buckling load varies throughout the span. This is also the case for the compressive force throughout the structure. The compressive force is calculated by multiplying the compressive stresses calculated in Equation 3.28 and multiply it with the total compressive area. First column buckling is checked by taking the total inertia. Next the buckling for each of the elements of the wingbox is checked by taking the individual components.

$$P_{cr} = \frac{n^2 \pi^2 EI}{(\frac{1}{2}b)^2} \quad (3.35)$$

### Verification Strategy

The main challenge of the wingbox model is incorporating the taper in two axes. In order to check whether the values of the design are correct, the following strategy is used. First of all, stress calculation will only be done in the root since there the forces are the largest. This makes the cross-section tapered in one axis. The cross section will have a constant thickness throughout the circumference to make verification easier. Next a minimum and maximum value is calculated for certain parameters to ensure that its value is reliable. This is done by modelling a thin walled box with a square cross section, where the minimum cross section has the height of the TE spar and the maximum cross section has the height of the LE spar. The verification method will be used on: wing box volume, second moment of inertia and maximum deflection. The results are shown in Table 3.13. It shows that the values are within the minimum and maximum values and are therefore reliable.

Table 3.13: Verification of design parameters of the wingbox. The minimum value is a thin walled box with TE spar height and maximum value with LE spar height. The design parameters are within the range and are therefore verified.

Design Parameter	Model value	Minimum value	Maximum value
Volume [ $m^3$ ]	0.26	0.079	0.49
$I_{xx}$ (root)[ $m^4$ ]	$7.74 \cdot 10^{-5}$	$4.55 \cdot 10^{-5}$	$1.13 \cdot 10^{-4}$
$I_{zz}$ (root)[ $m^4$ ]	$2.84 \cdot 10^{-4}$	$2.72 \cdot 10^{-4}$	$3.43 \cdot 10^{-4}$
Max deflection z-axis[mm]	60	32	50

To verify the bending stress, Equation 3.28 is split into two parts: bending due to lift and bending due to drag. For the two components, the correctness of the sign convention is determined throughout the length. This means for the lift component that the top part of the wingbox is compressive and therefore negative and the lower part is in tensile and therefore positive. The same holds for the drag component, right of the centroid is compressive and left of the centroid is tensile. The structure is connected, therefore the stress at the end of the LE spar should be equal to the starting stress of the top skin. As seen in Figure 3.33, the structure has the correct sign convention and has the correct initial and end value throughout the structure. This means that bending stress calculations are verified.

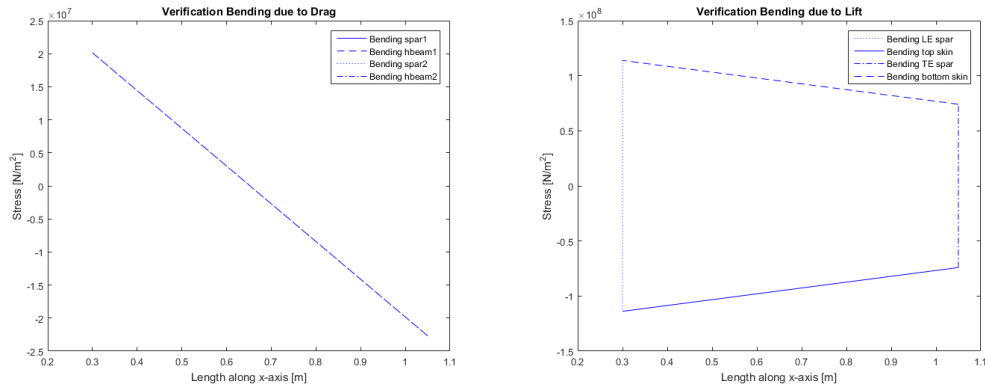


Figure 3.33: Verification of the applied bending equations: left is bending stress due to drag, right bending stress due to lift at the root of the wingbox. The bending stress of the drag force depends on the x-location only. These are constant at the spar locations and equal for the top and bottom skin. This explains why only one linear graph is seen, since the linear behaviour of both skins overlaps. The values of the spars are both one single value (since x is constant), equal to the maximum and minimum bending stress. The lift bending stress however, depends on y which varies along the circumference of the wingbox skin. Both figures are continuous, have a negative value where compression is expected and have zero stress at the centroid. Which means the model is verified.

For the open shear flow, a cut is made at the left bottom corner of the wingbox. At this point the shear flow is zero. When the integration is done over the wingbox, the shear flow should result into zero at the end since the integration arrives at the cut again. Also, continuity should apply throughout the integration and no jumps should appear. Figure 3.34 illustrates that that no jumps appear and that the shear flow goes back to zero. To check the closed shear flow, a moment calculation is done with respect to the centroid. The sum of the shear flows multiplied with the respective length and their respective arm of the closed and open shear flows should result into zero moment. The same method holds for the torsional shear flow, but it should be equal to the external applied moment.

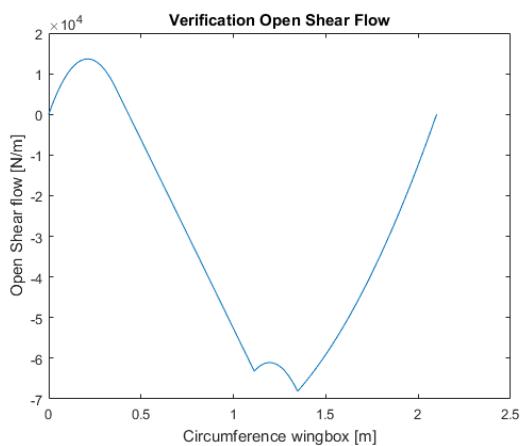


Figure 3.34: Verification of the open shear flow equation. The graph is continuous and returns to zero shear flow, which means that it is verified

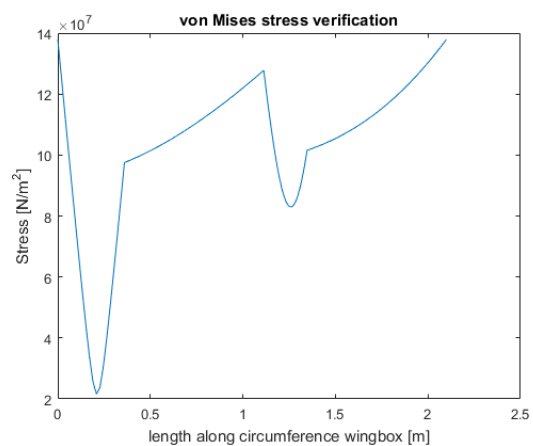


Figure 3.35: Verification of von Mises stress. The graph illustrates the von Mises stress along the circumference of the root of the wingbox, starting from the bottom of the LE spar. It shows continuity and the begin value is equal to the end value. This means the von Mises calculation is correct and verified

Finally the von Mises stress can be verified by checking if the stress is continuous throughout the circumference. For example, the stress at the beginning of the top skin should be equal to the stress at the end of the LE spar as illustrated in Figure 3.35.

## Results

The wingbox final design of the wingbox is shown in Figure 3.36. It is made of aluminium and consists of two C spars placed at 20% and 70% of the chord length. The leading edge spar has a thickness of 1 mm for the web and flanges, the trailing edge spar has 2 mm thickness for both. The diagonal sheets are 1 mm thick and are supported by two L-shaped stringers of 40 x 40 x 2 mm. Halfway through of the wingbox, a rib is placed to prevent buckling.

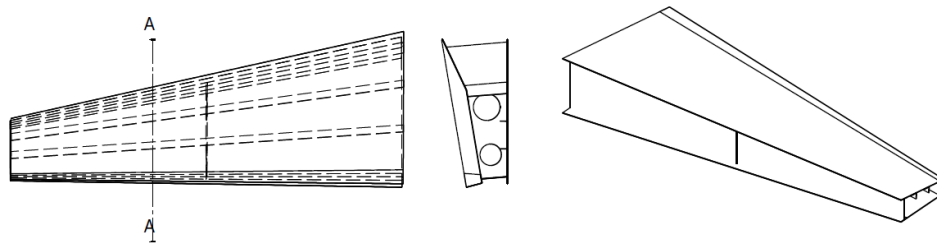


Figure 3.36: Wingbox design of the horizontal rotor support: Top view (left), section view (mid) and geometric view (right).

Figure 3.37 and Figure 3.38 show the failure modes for both loadcases. The figures illustrate that loadcase 1 (a 3.8g turn at maximum take-off weight) is more critical than a 6g landing. The tip loading of the aerodynamic forces cause a larger moment and therefore much higher stresses in the structure. The loading that will be discussed in the remaining part of this section is therefore from loadcase 1.

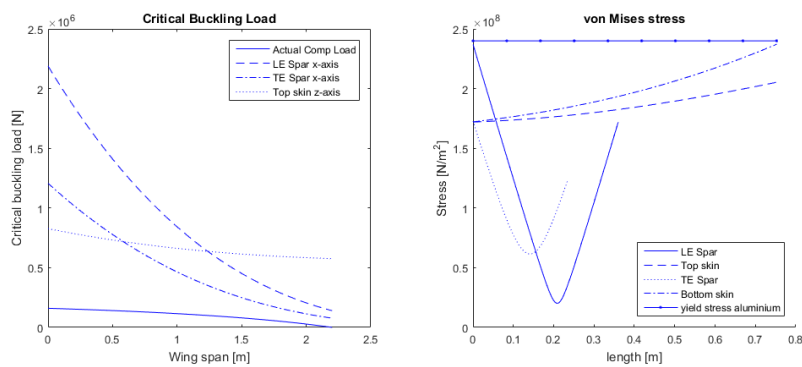


Figure 3.37: Failure modes wingbox: Loadcase 1. Left: Actual compressive load does not exceed critical buckling load of wingbox elements. Right: von Mises stress in the structure is beneath the yield stress. Failure does not occur.

In Figure 3.37, the critical buckling figure from loadcase 1 illustrates that the TE spar is the most critical in buckling at the tip. The stiffness decreases along the span and the TE spar has the smallest stiffness of the four components that make the cross sectional area of the wingbox. Therefore, the thickness of the LE spar and the top en bottom skin could be smaller since their stiffness are higher and buckling is less critical. The thickness is reduced to the point where the stresses are close to yielding. The structure is closest to yielding in the bottom left corner of the wingbox, since the main stresses are caused by the bending, illustrated in Figure 3.39. This section has high bending stresses since both the drag moment force and lift moment force cause tension and it is the furthest from the centroid. Since the skin sections are very thin, additional stringers are placed to the top section to increase the stiffness of the structure to stay within the deflection criteria shown in Table 3.14.

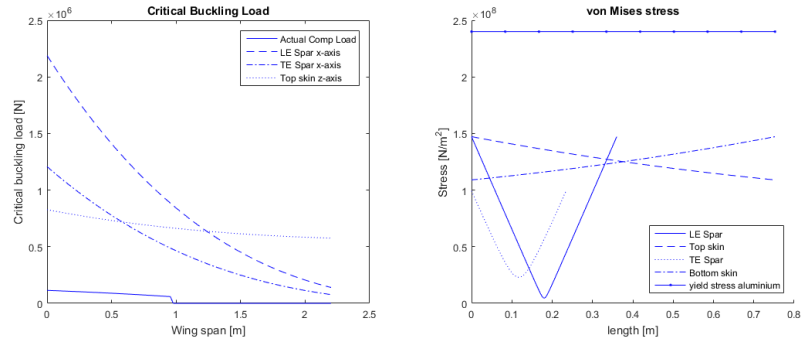


Figure 3.38: Failure modes wingbox: Loadcase 2. Left: Actual compressive load does not exceed critical buckling load of wingbox elements. Right: von Mises stress in the structure is beneath the yield stress. Failure does not occur.

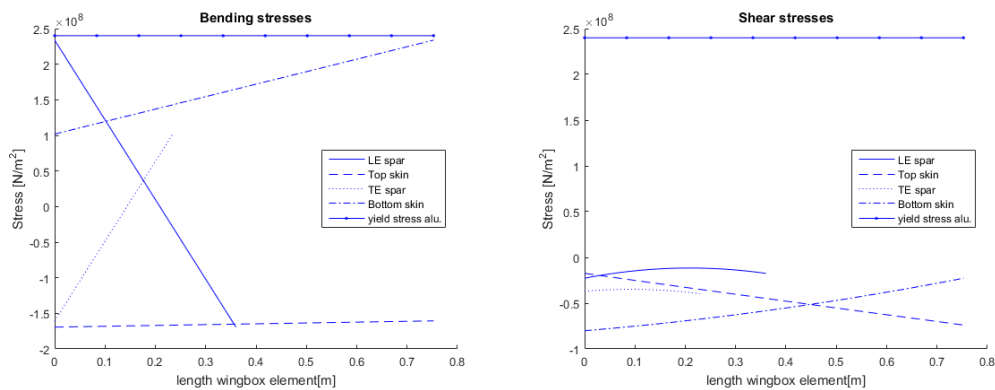


Figure 3.39: Stresses wingbox loadcase 1: Left-Bending, Right-Shear stress. It illustrates that most of the von Mises stresses are bending stresses and therefore the highest stresses are in the top right corner of the construction (beginning of LE spar or end of

Table 3.14: Deflection and stress requirements wingbox

Loadcase	Max. defl. [mm]	Max allowed defl. [mm]	$\sigma_{max}$ [MPa]	$\sigma_{yield}$ [MPa]
1	95,8	96	237.1	240
2	47,9	96	147.2	240

The final design characteristics are shown in Table 3.15. The volume of the wingbox is enough to store all the fuel required for the full range. The total wingbox weight is 28.4 kg. Factors that are not taken into account and will increase the wingbox weight is a rivet analysis and skin buckling. Also, the airfoil shape is not included in the wingbox weight. However, for a first order estimate of the wingbox, the design is within expectations.

### 3.2.3 Aerodynamic considerations

This section evaluates the shape of the cylinder support and its aerodynamic characteristics. The support should be able to fulfill its functions while generating as little drag as possible. From a structural point of view, as well as for the fuel capacity, the support should be as thick as possible. To also comply with the minimum drag wish, the support will be made into a wing like structure. The airfoil for the wing should therefore have a high maximum thickness and a low  $C_D$  at  $\alpha = 0$ , where in this case the  $\alpha$

Table 3.15: Final wingbox characteristics

Wingbox characteristics	Value	Unit
Material	6061	Aluminium
Weight estimation	28.4	kg
Total volume	0.51	m <sup>3</sup>
Max stress	237.1	MPa
Max deflection	95.8	mm

is defined as for a conventional aircraft. The airfoil chosen for the rotor support is symmetrical, meaning that as long as the aircraft flies level, no lift is produced and the cylinder provides the lift of the aircraft.

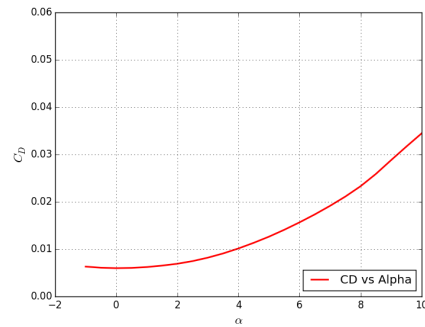
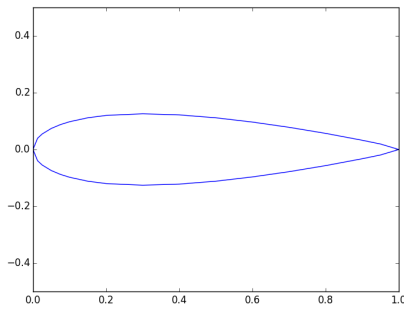


Figure 3.40: Geometry of the GOE-776 airfoil      Figure 3.41:  $C_D$ - $\alpha$  graph for the GOE-776 airfoil

This airfoil chosen for the horizontal support is the Gottingen 776 airfoil (GOE 776)<sup>2</sup>, which is illustrated in Figure 3.40. This is an airfoil with a maximum thickness of 25% chord and a  $C_{D_0}$  of 0.006, as can be seen in 3.41[31]. For the vertical support, the more conventional NACA0012 is used, a thinner airfoil which is also convenient for the rudders. The  $C_{D_0}$  is approximately the same as for the GOE776 airfoil<sup>3</sup>.

### 3.2.4 Summary rotor support

The main characteristics of the rotor support subsystem are summarised in Table 3.16 and illustrated in Figure 3.42.

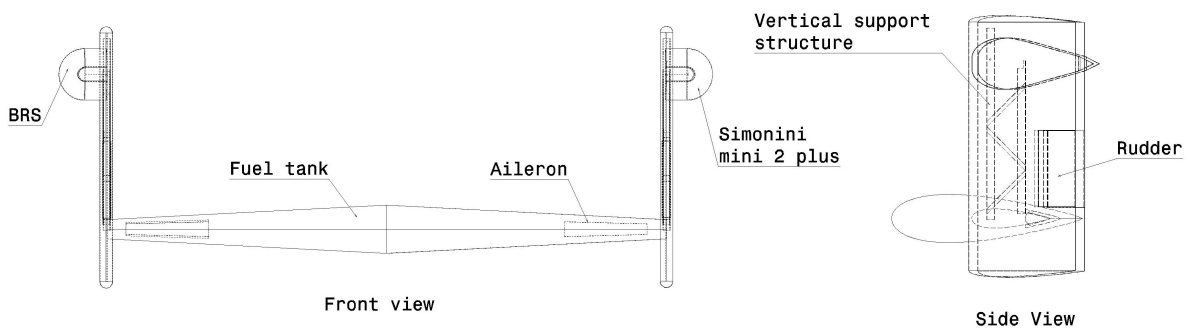


Figure 3.42: Technical drawing of the rotor support subsystem

<sup>2</sup><http://airfoiltools.com/airfoil/details?airfoil=goe776-il>

<sup>3</sup><http://airfoiltools.com/airfoil/details?airfoil=n0012-il>

Table 3.16: Summary of the rotor support characteristics

Variable	Value	Unit
Mass vertical support	45.5	kg
Airfoil vertical support	NACA 0012	-
Assembly vertical support	Fully disassemblable	-
Mass wingbox	28.4	- kg
Mass horizontal support	55.1	- kg
Fuel volume used/available	260/510	L
Airfoil horizontal support	GOE 776	-
Reference area vertical support	1.84	$m^2$
Reference area horizontal support	7.74	$m^2$
Maximum deflection vertical support minus x-direction	10	mm
Maximum deflection vertical support y-direction	100	mm
Maximum deflection horizontal support z-direction	95.8	mm

### 3.3 Propulsion

A very important part of this particular design is to overcome the drag the cylinder generates. Therefore, an efficient yet powerful propulsive system is needed. The design of this system starts by designing the ducted fan. After this, the engine is chosen and analysed. The section continues with the gear box design, the batteries and the alternator. At the end of the section, an analysis of the exhausts of the system is performed, completing the design of the propulsive system.

#### 3.3.1 Ducted fan

##### The Duct

Ducted fans are known for its high efficiencies at low speeds and for their high static thrust at zero speed. The shape of the duct itself adds an extra propulsive force when correctly designed. Also the losses at high tip speed are reduced due to the presence of the duct. When using the boundary layer ingestion, meaning using the boundary layer of the fuselage as an inflow, the fan becomes even more efficient. The diameter of the fan is also lower compared to an open fan, this is a result of the discussed higher efficiency. An extra benefit is less vibrations, noise reduction and increased safety for the passenger. The duct is designed using the book: "Ducted fan Design volume 1", [32], using Python to optimise for the efficiency and size. The design will be optimised for mid cruise to have the highest average efficiency, however the design will be constraint in diameter of the duct. Another constraint is the tip speed of the blades, having too high tangential velocity or flow velocity at the tip can result in supersonic flow over the fan. This phenomena greatly reduces the efficiency of the propeller.

##### *The sizing*

The design of the duct starts with the engine ratings, which are the shaft power output (in horsepower) and the rotations per minute of that shaft, these parameters are discussed in subsection 3.3.4. With these parameters, the torque can be calculated using Equation 3.36. The subscript 0 will be used for the inlet of the duct, 2 for the area just in front of the fan, 3 for the area just after the fan and 4 for the exit area. First, a preliminary size of the fan is selected, taking into account that the center of the fan, the hub radius ( $r_h$ ), should be at least 20 percent of the fan radius ( $r_f$ ). This results in a fan area. Next, the mass flow has to be calculated using Equation 3.37. This mass flow is captured by the inlet area and the inlet area can thus be calculated using Equation 3.38, with  $\rho$  being the density at the altitude and  $v_0$  being the speed of the aircraft. Using the mass flow, which is constant for the complete duct according to the law of continuity, and the fan area the velocity in front of the fan can be calculated using Equation 3.38.

$$\tau = \frac{16500P}{\pi n} \quad (3.36) \quad \dot{m} = \frac{T^2}{2(P - P_t)} \quad (3.37) \quad A_i = \frac{\dot{m}}{\rho v_i} \quad (3.38)$$

Due to the law of continuity and the assumption of incompressible flow, the speed just after the fan is equal to the speed just in front of the fan. This results in only an increase in pressure, the pressure in front of the fan is first calculated with Equation 3.39. Now using Equation 3.40 with having the required thrust and the inlet speed, the exit speed can be calculated. Equation 3.38 can be used again to calculate the exit area of the duct.

$$p_2 = p_0 + 0.5\rho(v_0^2 - v_2^2) \quad (3.39) \quad T = \dot{m}(v_4 - v_0) \rightarrow v_4 = \frac{T}{\dot{m}} + v_0 \quad (3.40)$$

The torque applied to the mass flow by the propeller introduces a swirl in the airfoil, this phenomena will be expressed with the swirl parameter (K), defined in Equation 3.41. The power needed to overcome this swirl can be found with Equation 3.42. With all the current values, the pressure after the fan is calculated using Equation 3.43, with R being the ratio between hub diameter and outer diameter.

$$K = \frac{\tau}{\dot{m}} \quad (3.41) \quad P_{swirl} = \pi\rho K^2 v_2 \ln\left(\frac{r_f}{r_h}\right) \quad (3.42) \quad p_3 = p_0 + 0.5\rho K^2 \left(\frac{\ln(R_4)}{A_4} - \frac{\ln(R_2)}{A_2}\right) \quad (3.43)$$

With all of these calculations, an initial estimate of the size of the duct can be made. The power required for this duct is than calculated using Equation 3.44. For the first iteration power required is not equal to the shaft output power, because the swirl has to be taken into account as a loss. Thus from here, the mass flow will be increased manually until power required is not more than .001% of the shaft output power. The efficiency of the complete system can than be calculated by using the power needed for the drag and the power required by the duct Equation 3.45.

$$P_{req} = A_2 v_2 \Delta p + P_{swirl} \quad (3.44) \quad \eta = \frac{Dv_0}{P_{req}} \quad (3.45)$$

*The design*

The results of the converged solution are summarised in Table 3.17. The design was initially made with only one single ducted fan. However, the large size caused interference with the cylinder and therefore the design was split into two smaller ducts. The two ducts are completely symmetrical.

Parameter	Value	Unit	Parameter	Value	Units
$P_{req}$	42.5	kW	$A_0$	1.2	$m^2$
n	3190	rpm	$A_2$	0.47	$m^2$
$\dot{m}$	41	$kg\ s^{-1}$	$A_4$	0.733	$m^2$
$P_{swirl}$	3.4	kW	$v_0$	37	$m\ s^{-1}$
$P_{Drag}$	30.8	kW	$v_2$	88	$m\ s^{-1}$
$\eta_{duct}$	74	%	$v_4$	57	$m\ s^{-1}$

Table 3.17: Results of the converged solutions for the duct sizing and properties of the ducted fan

## The Fan

The second step is to design the fan in the duct. During the design of the ducted fan a Clark-Y profile was considered [32], for its high critical mach number, which is 0.71. The maximum tip speed that will occur is  $M = 0.69$  during the begin of cruise. The design of the fan starts with dividing a blade in multiple sections using Equation 3.46. This is because the tangential velocity is different for every section and thus every section needs a different pitch angle. For this design 10 sections ( $n$ ) is considered, such that it can be designed in CATIA V5.

$$r_i = \sqrt{\frac{A_2}{n\pi} + r_{i-1}^2} \quad (3.46)$$

In the previous chapter, swirl was already discussed. This phenomena will also be taken into account for the design of the fans. Therefore, a new coefficient is introduced, the swirl coefficient ( $\epsilon$ ) using Equation 3.47. Next, the tangential velocity per section is calculated with Equation 3.48. Using simple pythagoras the absolute velocity experienced by the section can be found with Equation 3.49, as well as the angle of inflow ( $\phi$ ) using Equation 3.50.

$$\epsilon_i = \frac{K}{r_i v_2} \quad (3.47) \quad v_{ti} = \omega r_i - \frac{K}{2r_i} \quad (3.48)$$

$$v_i = \sqrt{v_{ti}^2 + v_2^2} \quad (3.49) \quad \phi = \arctan\left(\frac{v_2}{v_{ti}}\right) \quad (3.50)$$

The following step is to determine the gap ( $s_i$ ) between two blades per section. This gap is used to quantify the solidity of the blades ( $\sigma$ ) defined as the root of the section over the gap. The solidity should not be larger than 1 for all sections. Now that all important factors are defined, the tangential and axial forces can be determined using Equation 3.51 and Equation 3.52. Which is used, just like an airfoil, to calculate the lift in Equation 3.53, and drag in Equation 3.54, of the fan.

$$X_i = \rho v_2^2 s_{av} \epsilon_{av} \Delta r \quad (3.51) \quad Y_i = s_{av} \Delta p \Delta r \quad (3.52)$$

$$L_i = X_i \sin(\phi_i) + Y_i \cos(\phi_i) \quad (3.53) \quad D_i = X_i \cos(\phi_i) - Y_i \sin(\phi_i) \quad (3.54)$$

So lastly, the drag coefficient with Equation 3.55, and the lift coefficient with Equation 3.56, of each blade section can be determined. However, another approach is used. When starting this designing process a constant chord was used for the blades. But now an iteration will be done in order to get the  $C_L$  that is optimal for the chosen airfoil section, which is the Clark-Y. The optimal  $C_L$  for this airfoil is 0.5, the above described process is redone for every section until every section has the same optimal  $C_L$ , which occurs at a different chord. At the end of the design, it was noticed that the root of the fan blade had a solidity, which was larger than 1, such that a smaller chord was needed there which increased the  $C_L$  above optimal at that point. The angle of attack of this airfoil is approximately 2 degrees, adding this to  $\phi$ , the pitch angle of every section can be determined. The number of fan blades is locally optimised to 6. For further developments, this design can be optimised globally, however due to time constraints this is not done for the current design. So with all the parameters the fan blade is designed as a CAD-part.

$$C_{D_i} = \frac{2D_i}{\rho v^2 c_i \Delta r} \quad (3.55) \quad C_{L_i} = \frac{2\epsilon_i \sin(\phi_i)}{\sigma_i} - \frac{\sigma_i C_{D_i}}{\tan(\phi_i)} \quad (3.56)$$

This design has a constant lift coefficient over the whole span, which is the optimal  $C_L$  for the Clark-y profile. This lift coefficient is 0.5, to obtain this the blades have not only a change in pitch, but also a change in chord length over the whole span. The chord length changes from 0.11 m at the chord to 0.076m at the tip. The pitch is the sum of  $\phi$  and  $\alpha$ , where  $\alpha$  is 2 degrees and constant due to the constant  $C_L$ ,  $\phi$  changes from 78° at the chord to 34° at the tip.

### Static Thrust

As the design of the full duct and fan is now done successfully, the last step is to calculate the static thrust it can generate. The static thrust has a major influence on the take-off performance and as a wish it should be as high as possible. However, the static thrust is depended on the max horsepower of the engine, discussed in subsection 3.3.4, and the diameter in inch of the fan. The reference book gives the

---

ACV correlation line to estimate the static thrust using Equation 3.57. The static thrust per fan is 500 Newton, thus totalling to a 1000 N.

$$\frac{T_{static}}{P} = 1.08 \left( D \sqrt{\frac{1000}{P}} \right)^{\frac{2}{3}} \quad (3.57)$$

### 3.3.2 Verification and validation

The design of the ducted fan is done according to the Ducted fan design volume 1 of M. de Piolenc [32]. The book gives an example calculation of a design with every intermediate step given. All these steps are used to verify the program, as this was very elaborate the difference between the analytical model and the numerical model was always less than 1%. Furthermore, the book gives example aircraft which use the same method described to design their ducted fan, thus validating the method. However further validation to see if the ducted fan will operate as designed during actually flight will be done during the testing phase of the aircraft.

### 3.3.3 Propeller

After the design of the initial single duct ducted fan, the inlet and fan area diameters were deemed to be very high. However the design was completely made according the book and the program was verified to the given numbers. So using a verified prop design tool<sup>4</sup> a first estimation of a propeller size was done. At the that current iteration the inlet diameter of the ducted fan was 2.2 meters, the propeller diameter from the design tool was approximately 3 meters. This reassured the choice for the ducted fan and concluded once more that a duct is better at low speed and high thrust. The reasoning behind the immense duct at that point was the L/D of the aircraft, which was lower, because no end plates were used on the cylinder. Needing approximately 2000 Newton of thrust at speeds below 40 m/s is difficult and this resulted in the large sizes.

### 3.3.4 Engine

This section describes the performance and dimensions of the engine, but first starts with the reasoning behind the rotary engine instead of a conventional piston combustion engine.

#### The benefits of a rotary engine

The final design uses a pusher configuration, requiring either having the engine in the front and run a long shaft through the aircraft or having the engine at the back. Having the engine at the back is the better option, to limit the size, efficiency and weight of the output shaft and also to have it close to the c.g.. A small diameter is needed at the end of an aircraft, which asks for a piston in line engine. With the current power required a 6 in line piston engine is required, which is long and tall. Thus a concluding the best option for this design is to have a twin rotary engine. These engine have a high power per volume, beneficial for the shape of the body. The following table contains an overview of all the advantages and disadvantages of a rotary engine. In addition, the request for new rotary engines came during the development of the M400 sky car<sup>5</sup>. One of the most iconic flying cars required a small, light, economical and reliable engine and as a spin-off of the project the company Rotapower started. This once again showed the benefits of the rotary engine. One other example is the Mazda 787B, that won the Le Mans 24 hours race in 1991. The organisation limited the fuel tank size, but because it was a rotary engine the fuel consumption was much lower and they therefore needed less stops. The engine was also more reliable, because it has less parts than the piston engine of the competitors[33].

---

<sup>4</sup><http://propdesign.jimdo.com/download/>

<sup>5</sup><http://www.rotapower.eu/sky car.html>

Airplane Model	Engine Model	MTOW	ICAO Noise limit dB(A)	Noise Level dB(A)	Compliance Margin dB(A)	90% Confidence Interval dB(A)
Glasair Sportsman	Mistral Engines G200	1065	79.7	78.9	0.8	0.47

Table 3.18: Noise level data provided by Mistral Engines.

**Advantages:**

- High power-to-volume ratio
- High output rpm
- High power to weight ratio
- Flat torque curve
- Low vibrations, when using 2 or more rotors
- When 1 rotor fails, the others will still be able to operate

**Disadvantages:**

- High exhaust temperature
- More noise compared to piston engines

**The Mistral G200**

The design of the duct is based on the Mistral G200 IC-engine<sup>6</sup>, which can be seen in Figure 3.45. The characteristics of this engine are described in Table 3.19. As is shown in the table, the max rpm of the Mistral engine is lower than the rpm used to drive the fans in the ducts. A gear is used to decrease torque and increase rpm, which made the duct more efficient. More about the gearing is discussed in subsection 3.3.5. The Mistral engine is chosen because of its low fuel consumption, high power to weight ratio and the fact that it still operates after a rotor fails. Having a low fuel consumption and high power to weight ratio decreases the MTOW. Whereas the latter advantage increases the reliability of the engine. Next to this, the engine has a time between overhaul of 3000 hours, which is about 1.5 times that of an average aircraft engine. The aircraft will be used for only 50 hours, so having a time between overhaul of 3000 hours results in an almost new condition engine at the end of life of the aircraft. Lastly, the noise is a major drawback of this type of engines, however Mistral provided data on the engine noise for a Glasair Sportsman, which is currently using the same Mistral G200. The data shows that the noise level is approximately 79 dBTable 3.18, whereas the noise limit for certification in the Netherlands is 80 dB.

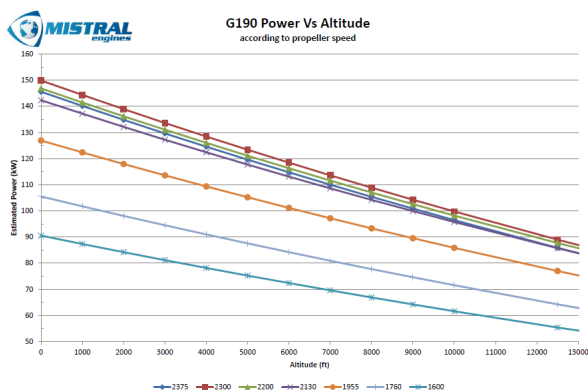


Figure 3.43: Mistral G200 IC-engine power performance versus altitude <sup>a</sup>

<sup>a</sup><http://www.mistral-engines.com/products.html>

<sup>6</sup><http://www.mistral-engines.com/products.html>

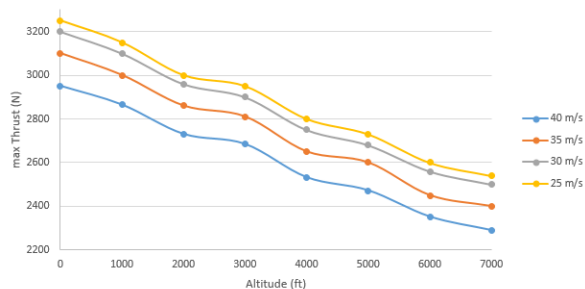


Figure 3.44: Thrust performance versus altitude of the ducted fan

The performance of the aircraft with altitude can be found in Figure 3.43, note that this is data for the G190, the G200 has 5% more power available. During cruise at an altitude of 7000ft the max power is approximately 120kW. The ducted fan requires during mid-cruise approximately 83 kW of shaft power. The power setting of the engine at cruise will be 71%. The maximum thrust which the ducted fans can deliver together at a certain altitude and certain speed is shown in Figure 3.44

Characteristic	Value	Unit
Continuous shaft power	200	hp
Dry weight	132	kg
RPM for max power	2250	rpm
Fuel consumption at sea level	295	g/kWh

Table 3.19: Mistral G200 IC-engine characteristics

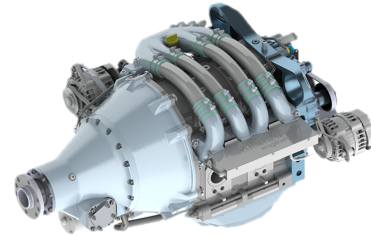


Figure 3.45: Mistral G200 IC-engine<sup>7</sup>

### 3.3.5 Gearing

The Mistral engine is housed at the back of the body, attached to the rear spars of the structural support. The output shaft of the engine has a bevel gear attached to it. This bevel gear has a diameter of 20cm, which spins two smaller bevel gears of 8 cm in diameter placed on either side to get an equal power distribution. This gear is attached to a symmetrical rod running to the axis of the fan, having another bevel gear configuration, however here with equal diameters. At one side this turns the shaft of the fan directly, at the other sides however another gear configuration is installed to get the fans counter-rotating. The rpm of the fan will be 2.5 times the rpm output of the engine, whereas the torque experienced by the fan will be 5 times smaller. The torque is of great importance when considering the swirl in the duct, a lower torque will result in a lower swirl in the duct and thus an increase in the efficiency. There is a limit on decreasing the torque by gearing, because this results in an increase in rotational speed. When the rotational speed becomes too high the tips of the fan blades go supersonic and this gives a drop in efficiency and an increase in noise. The layout can be seen in Figure 3.47.

### 3.3.6 Batteries and alternator

The batteries and alternator provide electrical energy to the electrical systems in the aircraft. The total continuous power required for the electrical systems is 319.9 W and the maximum required power is 474.9 W, see subsection 2.6.2.

Table 3.20: Specifications of the AV016 Lithium battery

Characteristic	Value	Unit
Dimensions	114 x 114 x 112	mm <sup>3</sup>
Voltage	13.6	V
Capacity	28	Ah
Maximum current	500	A
Temperature of the operating environment	-18 to 60	C
Weight	1.61	kg

The main engine (the Mistral G-200 engine) has a dual alternator which generates either 14V at 70A or 28V at 40A<sup>7</sup>. This is enough to recharge the batteries during flight to power the electrical system. Two batteries will be used. One will be continuously charged by the alternator during flight, while the other one is charged before take-off. This second battery serves as a back-up when the alternator or the first battery fail. The battery which was selected is the AV016 Lithium battery<sup>8</sup>. The specifications of this battery are given in Table 3.20. The back-up battery can provide approx. 1 hour of energy when the recharging system fails. This is enough to evacuate to the closest airfield even when crossing the English Channel to London.

### 3.3.7 Engine cooling and exhaust

#### *Cooling*

The Mistral IC-engine will have two radiators attached to the engine, one for the cooling fluid (left) and the other for oil cooling (right) as seen in Figure 3.46. These radiators will be cooled by the air inflow coming from beneath the engine. The radiators lower the temperature of the cooling fluid in order to keep the temperature below 100° C. The temperature of the cooling fluid should not exceed 102° C degrees [34]. The actual sizes of the radiator will not be assessed for this stage, however this is recommended for a further design. Resulting from contact with Mistral resulted in the following coolant power values: coolant fluid cooling power, 58 kW, and oil cooling power, 26 kW. The heat capacity( $c_p$ ) and density( $\rho$ ) of air is approximately 1.0 at cruise altitude. Thus the inlet area needed to cool the radiators can be simply calculated using Equation 3.58 and is 0.022 m<sup>2</sup>. The temperature difference is approximately 100 Kelvin.

$$A = \frac{\dot{Q}}{v c_p \rho \Delta T} \quad (3.58)$$

#### *Exhaust*

The exhausts of the two rotors of the engine are combined in one exhaust. When the gases leave the engine they travel at supersonic speed. Shockwaves will occur at the engine and this will lead to a temperature rise in the exhaust pipe. The temperature of the exhaust gases eventually reaches 850° C degrees Celsius. The same airflow used for cooling of the radiators will be used to create convection for the heat radiated from the exhaust. The exhaust itself will run to the back of the aircraft, where a hole is created for the cooling flow and of the exhaust to exit the aircraft. The skin at the rear of the fuselage over which the exhaust runs, will be made out of GLARE3(Table A.3), because of its good thermal resisting properties [35]. The exhaust gases will be expelled after the two ducts. The emissions of the exhaust are further discussed in subsection 4.1.8.



Figure 3.46: Example of the radiator attachment [34]

<sup>7</sup><http://mistral-engines.com/products.html>

<sup>8</sup><http://www.aircraftspruce.com/catalog/pdf/aerovoltzapp.pdf>

### 3.3.8 Summary propulsion

The dimensions of the duct can be seen in Figure 3.47. All other characteristics of the propulsion subsystem are summarised in Table 3.21

Variable	Value	Unit	Variable	Value	Unit
Main Engine	Mistral G200	-	Duct efficiency	74	%
Fuel consumption at 75%	39	L/h	Static thrust	1000	N
Maximum Power	200	hp	Fan blade profile	Clark-Y	
Maximum rotations	2250	rpm	Number of fan blades	2 x 6	-
Dry weight engine	132	kg	Battery	2x AV016 Li	-
Gearing ratio	2.5	-	Battery capacity	28	Ah -
Exhaust gas temperature	850	°C	Battery Weight	1.61	kg
Total cooling power	84	kW			

Table 3.21: Summary propulsion characteristics

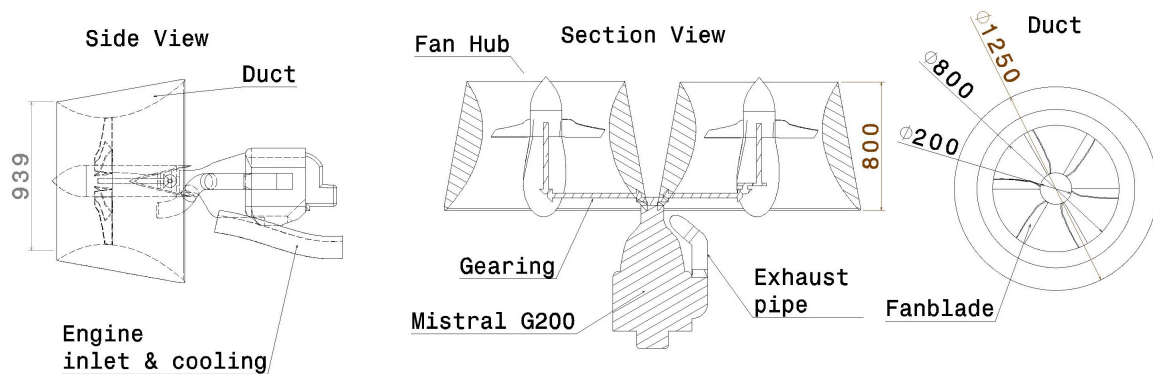


Figure 3.47: Technical drawing of the ducted fan

## 3.4 Stability and Control

The stability and control subsystem is designed next. First of all, the stability surfaces are sized. These include the canard and the vertical tail. The next step is the design of the control surfaces, the ailerons and the rudders. The pilot controls, avionics and instrumentation are also designed. Then the throttle control is evaluated. Next is an explanation of the electronic flight control system, and an explanation of the flight control modes and laws is done. The surface deflection mechanism, control segregation and cockpit elements conclude the design of the stability and control system.

### 3.4.1 Stability surfaces sizing

The first step is to size the stabilizing and controlling surfaces: the canard, vertical tail, ailerons and rudder. The flowchart of the iterative process of the design is presented in Figure 3.48.

#### Canard

Longitudinal stability is provided by the canard. Important to note is that the lift generation of the rotating cylinder does not depend on the angle of attack of the free stream flow. Therefore it is not necessary to actively control the pitch, but rather maintain stability at all flight stages.

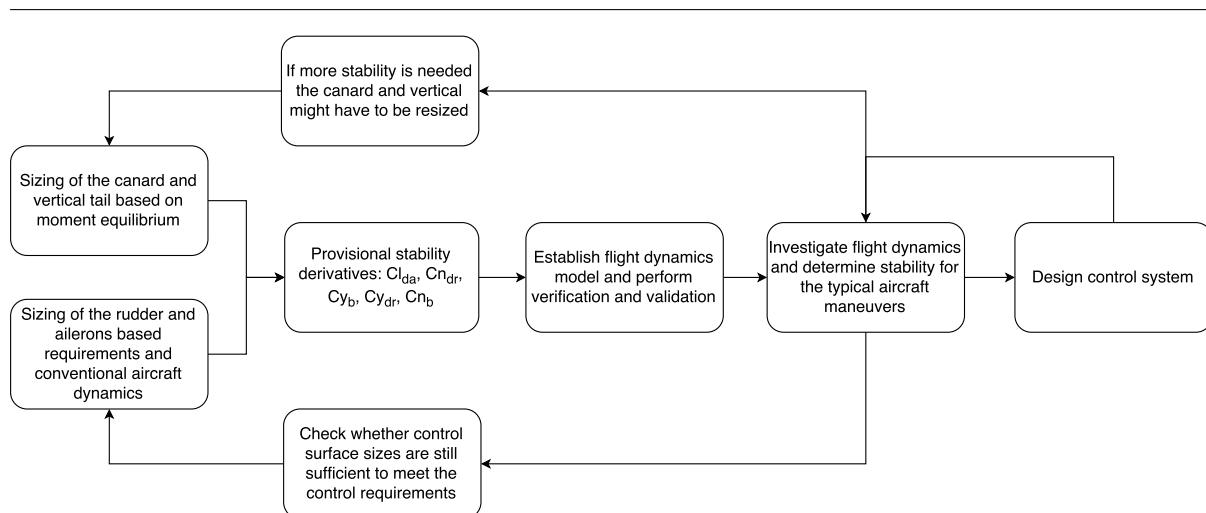


Figure 3.48: Flowchart of the iteration process of the design of the control surfaces

The canard is sized by regarding the moment equilibrium around the c.g. of the aircraft. For all stages of the flight the total moment around the c.g. should be zero. Five aerodynamic forces are taken into account for this calculation: the lift generated by the rotating cylinder, the lift generated by the canard, the thrust produced by the fans, the drag generated by the cylinder and the drag generated by the body. During flight the c.g. location shifts due to the consumption of fuel. Therefore it is necessary to calculate the moment equilibrium for different fuel loads in different stages of flight. It was determined to do this for take-off with a total mass of 1030 kg and for landing with a total mass of 820 kg. The c.g. location was determined according to the component weights and their respective location. The result is shown in Table 3.22. The c.g. is measured with respect to the cylinder measured positively horizontally forward and vertically upward from the centroid of the cylinder. From this table it can be concluded that the landing stage is the most demanding as the c.g. is located far from the wing, which gives the lift of the cylinder a large moment arm.

Flight stage	$c.g.\text{-long}$ (w.r.t. cylinder)	$c.g.\text{-vert}$ (w.r.t. cylinder)
Take-off	0.84	-1.12
Landing	1.05	-1.21

Table 3.22: The c.g. location during take-off and landing, the change in c.g. location is due to the fuel consumption during flight

Because the canard has to produce large amounts of lift for a small speed a highly curved airfoil was used. Different profiles were considered and the NACA6412 was chosen, as sufficient data was available on this profile and its performance excelled for this particular application<sup>9</sup>. It was chosen to operate the canard at an a.o.a. of 5 degrees during cruise condition and at an a.o.a. of 10 degrees for slow speeds close to the minimum speed of the aircraft. After considering the different flight stages and different flight speeds it was found that cruise flight at the end of the mission will be the key requirement for the canard. It was found that the canard has to produce 1200 N of lift for a speed of 35 m/s and an a.o.a. of 5 degrees. Performing the simple lift calculation it was found that the canard needs a reference area of 1.93 m<sup>2</sup> [36].

The canard is fully movable around its hinge point in the aerodynamic center of the wing. Therefore the torque which should be overcome by the actuator mechanism is just the moment of the airfoil. At a maximum deflection of 10 degrees this hinge moment is 86.2 Nm. The decision was made to use 2 separate linear actuators (G-Rock GRA D-5).

<sup>9</sup><http://airfoiltools.com/airfoil/details?airfoil=naca6412-il>

---

## Vertical tail

The vertical tail is needed to maintain both static and dynamic lateral stability. To achieve this the change in lateral yawing moment due to a change in side angle should be positive,  $C_{n\beta} > 0$ . The magnitude of this stability derivative depends on the tail volume coefficient,  $\bar{V}_{vt}$ , shown in Equation 3.59. The value of this coefficient for aircraft with similar size to the Magnus Aeolus is between 0.05 to 0.1 based on data provided in Chapter 8 of [37].

It was decided to use the existing vertical support structure as tail, hence not requiring to introduce additional surfaces to the Magnus Aeolus. These vertical surfaces are 1.5 m in span and 0.8 m wide each however, about one-third of this surface is covered by the rotating cylinder and the endplates. As the effectiveness of the tail in that region is unknown, it was decided to increase the span of the vertical tail downwards by 0.6 m. This result in a tail area of 0.9 m each. The distance of the vertical supports to c.g. is 0.8 m which results in a total tail volume coefficient of 0.15. This means that the area provided by the support structure is sufficient to have a conservative tail volume coefficient, hence being a suitable place to allocate the vertical tail.  $C_{n\beta}$  resulted from this tail volume coefficient and is calculated using Equation 3.59.

$$C_{n\beta} = \frac{2S_{vt}l_{vt}C_{Lv}K_{fuselage}}{S_{ref}b} \left(\frac{V_t}{V}\right)^2 \quad \bar{V}_{vt} = \frac{S_{vt}l_{vt}}{S_{ref}b} \quad (3.59)$$

Using the NACA 0012 airfoil, as well as assuming a destabilizing factor of the fuselage of 0.65 based on Figures in Chapter 8 of [36], a  $C_{n\beta}$  of 0.211 is determined for the aircraft.  $\left(\frac{V_t}{V}\right)^2$  assumed to be 1 as the tails are at the sides, away from the fuselage or wing.

## 3.4.2 Control surfaces sizing

### Ailerons

The ailerons are sized such that Requirement **RMEA-SS-SC-6** is satisfied in the most extreme case conditions, when the aircraft has the maximum moment of inertia and is at its maximum take off weight. At first sizing is done analytically using rotational dynamics without taking the gyroscopic effect into account. Then from the preliminary calculated size, the aileron effectiveness coefficient  $C_{l\delta_a}$  is determined, which is then used to make a model of the aircraft dynamics with the gyroscopic effect. After the model is established and validated, the roll performance of the Magnus Aeolus is simulated and if the ailerons size is not sufficient to satisfy the requirement, the ailerons size is adjusted until the requirement is met.

Equation 3.60 needs to be solved for the stated requirement and it is done by assuming a certain size and iterating its size until the requirement is met.  $C_{l\delta_a}$  is determined by solving the integration in Equation 3.61 which depends on the size of the bottom wing, the span of the ailerons, the airfoil type as well as the wing's taper ratio.

$$\frac{1}{2}\rho V^2 S_w C_{l\delta_a} \delta_a - M_{drag} = I_{xx} \dot{p} \quad (3.60) \quad C_{l\delta_a} = \frac{2C_{L\alpha_w} \tau}{Sb} \int_{y_{start}}^{y_{end}} C_y dy \quad (3.61)$$

The selected airfoil for the ailerons is the same airfoil as the one used for the horizontal support, GOE 776. It is a symmetric airfoil with a stall angle of about 15 degrees [31]. Therefore, the maximum allowed deflection of the ailerons was chosen not to exceed this angle. The parameter  $\tau$  is the chord effectiveness of the ailerons which depends on the ailerons and wing chord ratios. It is extracted from Figure 12.3 in [38]. Moreover, parameter  $M_{drag}$  is the moment by the drag generated by the different aircraft surfaces in a rolling motion is a function of roll rate,  $p$ . Its expression is also extracted from Chapter 12 of [38].

By performing the design iteration it was determined that by allowing a deflection of 15 degrees, a surface area of 0.15 m<sup>2</sup> for each aileron is required to oblige with Requirement **RMEA-SS-SC-6**. It was decided to place the ailerons on the horizontal support as far away as possible from the c.g. for highest effectiveness. Moreover, to avoid interference with the rear spar of the horizontal support wing box and allowing space for the actuator system, ailerons with chord length of 0.24 m with a span of 0.63 m are selected.

## Rudder

The rudders are sized such that Requirement **RMEA-SS-SC-7** is satisfied. Similar to the ailerons, the rudders are sized in the same manner and their size is validated and reiterated using the flight dynamics model. A free body diagram of the aircraft during a crosswind is shown in Figure 3.49. In this situation, the tails push the aircraft towards the wind direction due to the fact that the tails produce lift in the same direction as the wind. The rudders need to generate enough moment in order to keep the aircraft in equilibrium or push it back to its initial position, especially during landing.

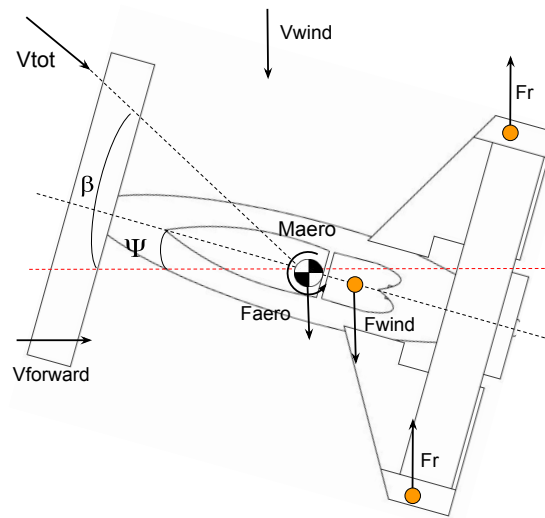


Figure 3.49: Free-body-diagram of the aircraft during a crosswind, the critical flight phase for the rudder sizing.

The equilibrium equations that need to be satisfied are stated in Equation 3.62 and Equation 3.63. The aircraft can allow for a certain crab angle,  $\psi_c$ , but the maximum deflection angle of the rudders is not exceeded to maintain its effectiveness.

$$qS_{ref}b \cdot [C_{n\beta}(\beta - \psi_c) + C_{n\delta_r}\delta_r] = M_{wind} \quad (3.62) \quad qS_{ref} \cdot [C_{y\beta}(\beta - \psi_c) + C_{y\delta_r}\delta_r] = F_{wind} \quad (3.63)$$

By assuming certain dimensions for the rudders and solving the above equations, the maximum deflection and the crab angle can be determined. If the rudder deflection angle is beyond its stall angle, the sizes are reiterated. The stability derivatives required to solve the equations above i.e.,  $C_{n\delta_r}$ ,  $C_{y\delta_r}$  and  $C_{y\beta}$ , are determined similar to Equation 3.59 and are shown in a set of relations in Equation 3.64 to Equation 3.66.

$$C_{n\delta_r} = \frac{-2S_{vt}l_{vt}b_rC_{Lv}\tau_r}{bS_{ref}b_v} \quad (3.64) \quad C_{y\beta} = \frac{-2S_{vt}C_{Lv}K_{fuselage}}{S_{ref}} \quad C_{y\delta_r} = \frac{2S_{vt}b_rC_{Lv}\tau_r}{S_{ref}b_v} \quad (3.65)$$

By iteration it was found that two rudders with a span of 0.6 m and a chord of 0.3 m each are needed. To keep the aircraft in equilibrium during a crosswind, a crab angle of 19 degrees and a rudder deflection

of 15 degrees will be sufficient. Since there are end-plates at the tip of the cylinder, the effect of the end plates on the rudders could not be analysed. Therefore, to be on the safe side, the rudders extend below the end plates. A summary of all control surfaces sizes derived in this section will be given in subsection 3.4.11.

### 3.4.3 Pilot controls

General aviation aircraft of about the same size and weight use in almost every case mechanical controls. Due to the more complicated coupling Magnus Aeolus encounters, the very different flight dynamics of the cylinder, the high lift force dependency on the airspeed, a mechanical system is too complex to operate solely by the pilot. Furthermore an easily controllable aircraft will be an important advantage in the projected market. On this ground it was chosen to use a fully electrical control system.

### 3.4.4 Avionics and instrumentation

First of all the avionics and instrumentation to provide the pilot with information and to operate the aircraft are discussed. These interfaces are selected based on their customizability. The cockpit will embed following systems, the number indicates the location of the system on the cockpit panel in figure Figure 3.50.



Figure 3.50: Cockpit control panel, with instruments indicated as: 1) Sidestick, 2)Throttle ICE, 3) Landing Gear switch + starter panel, 4) Backup cylinder rpm indicator, 5) Backup speed indicator, 6) Backup altitude indicator, 7) Ventilation, 8) Integrated EFIS, 9) Warning/failure panel, 10) Fuel tank indicator, 11) Fuel indicator, 12) Ballistic Recovery System trigger

As EFIS/EMS and gps system, the iEFIS Challenger from MGL Avionics is chosen<sup>10</sup>. The iEfis is designed for experimental aircraft and its tasks are conducted in separate modular multi-processor units. The Airbus EFAN<sup>11</sup> utilized the same system due to its high flexibility, which allows the adaption of the iEFIS to any mission or aircraft. It claims to be the most customizable EFIS on the market and provides enough flexibility to monitor up to 4 engines. Both Cylinder Head Temperature and oil temperature,

<sup>10</sup><http://www.mglavionics.com/html/iefis.html>

<sup>11</sup><http://www.airbusgroup.com/int/en/corporate-social-responsibility/airbus-e-fan-the-future-of-electric-aircraft.html>

---

together with the rpm of both engines will be displayed to monitor them. The iEFIS also comes with an integrated transponder and radio. An artificial horizon is displayed, together with airspeed, altitude and other vital parameters in combination with the overflowed landscape, in effect a synthetic view. The weight of the iEFIS is 3.4 kg and costs approximately 6000 \$. For redundancy, in case of an electrical failure of the iEFIS, a backup airspeed indicator, altimeter and rpm indicator to optimize the rpm of the cylinder, are installed. A slip indicator is installed, in order to provide the pilot with information about the sideslip angle for performing coordinated turns. The installed navigation system consists of a GPS with connection to external navigation systems and radios. VOR, ILS/Glide slope<sup>12</sup> are also present and necessary to perform the departures and approaches at Rotterdam and Heathrow with sufficient accuracy. Another advantage of the EFIS is that it supports external autopilots, that can drive servos (subsection 3.4.8) directly. The supported autopilots can provide up to three axis control, including lateral and vertical control, and is able to fly glide slopes.

A sidestick is installed on the right hand side of the cabin in order to limit the used space and improve the comfort of the pilot. Conventional rudder pedals are installed together with a differential braking system on top of the pedals. On the left hand side, two throttles can be found, the left throttle being the one of the cylinder and the other one is for controlling the fan's engine. A landing gear switch, with indicator of the LG position is installed on the panel. A fuel selector is set up below the fuel indicators. Finally a red handle can be found between the legs of the pilot on the instrument panel to trigger the BRS.

### 3.4.5 Throttle control

The two throttles will be coupled in normal operations, i.e. one throttle can not be moved separate from the other one. The position of the throttles will be translated into the flight computer, optimizing the ratio of rpm of both engines based on the power demanded and flight speed. In case of an electronics or flight control system failure, the throttles can be mechanically decoupled. The rpm of the cylinder is still shown on the backup instrument in case of full electrical failure and can be operated according to optimization tables with flown airspeed as input. The airspeed will be mainly controlled with the right throttle of the pusher engine.

### 3.4.6 Electronic Flight Control System

The aircraft will be controlled fly-by-wire, whereby all control surfaces and the power of both the Mistral and Simonini engine are operated electronically. During normal operations, the computers optimize the performance of the cylinder, provide control and prevent excessive forces. Control inputs are provided throughout two different computers coupled to the control units of both the pilot and first officer, i.e. throttles, sidestick and rudder pedals. Information from other sources, such as an Inertial Reference Unit, a Flight Management Computer and accelerometers are sent to two control computers. These control computers will have different hardware and software for redundancy. They will send deflection signals to the control actuators and control the power of the engines, dependent upon the active control law. The aircraft will feature four different control laws. The selected law (subsection 3.4.7) is based on grounds of the type of failure.

In Figure 3.51 a schematic overview of the build-up of the different elements composing the flight control system is displayed. On the top right, the pilot's input given throughout the sidestick, rudder pedals and throttle setting are translated into an electric signal to both the flight computers. These computers are both different in terms of hardware and software for redundancy. The longitude, latitude, altitude are given by the iEFIS and also provided to the flight computers. Within the flight computers, the signal which will be sent to the actuators is calculated based on the input of the pilot and the flight parameters provided by the different sensors. The FCs also determine the stick force feedback felt by the pilots in order to simulate the loading on the surfaces of the aircraft. Within the FCs an optimization algorithm is implemented to determine the most efficient rpm for both the cylinder and pusher engine,

---

<sup>12</sup><http://www.mglavionics.co.za/iEFIS.htm>

depending on the flight phase as discussed in the flight performance, section 4.1. Multiple sensors for measuring the a.o.a., velocity, altitude will be utilized. Within the FC, the information retrieved from these sensors is compared to the information of the iEFIS, input of the steering system to determine run aways, anomalies. Finally the primary computed order is send to the actuators which deflect the control surfaces and control the power of the engines, which have an aircraft response as a consequence. In case both Flight Computers fail, the servos will be actuated directly without being modulated by the FC's algorithm. In Figure 3.52 a preliminary positioning of the servos, batteries, etc. are given w.r.t. the airframe.

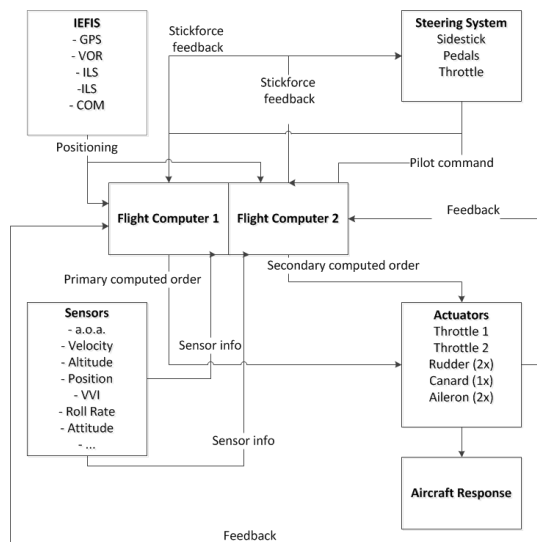


Figure 3.51: S/W diagram: flight control system build-up

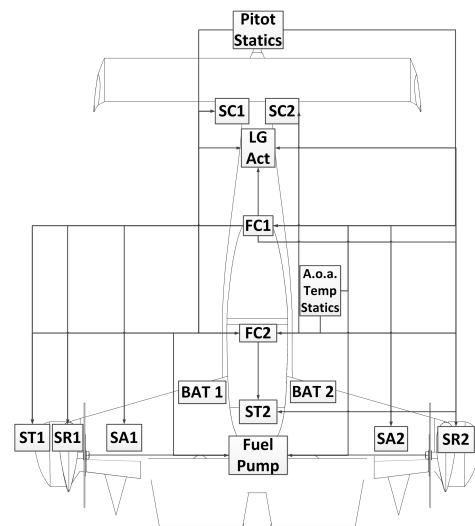


Figure 3.52: H/W diagram: Basic electrical block diagram showing the hardware connections of the avionics system (SC=Servo Canard, LG=Landing Gear, FC=Flight Computer, BAT=Battery, ST=Servo Thrust, SR=Servo Rudder, SA=Servo Aileron)

### 3.4.7 Flight control modes/ laws

The flight control system is based on the fly-by-wire system implemented by Airbus<sup>13</sup>. The major difference is that Airbus aircraft use mechanical back-up systems, being electric and/or hydraulic. This aircraft will only have electrical actuators which are controlled by the flight computers in normal conditions, or are directly controlled by the pilot's input during abnormal operations. Note that this system is also solely electrical, in effect servos which are actuated electrically. The functionality of the control system is explained below, during normal up to extreme anomalous operation and is focused on redundancy.

#### Normal law

Deflection of the sidestick will have normal attitude, bank angle changes as effect, but the pitch attitude, load factor, airspeed and bank angle are protected according to the flight envelope. Here, the control system will have a constant attitude hold on zero a.o.a. Also, the a.o.a. protection guards against stalling of the canard, and effects of for example windshear. The commanded angle of attack of the pilot might be limited by the flight computer. Speed protection will recover the aircraft from overspeed. Because roll, yaw and pitch changes are all coupled, the control system will compensate for this coupling. The bank angle on its own will also be limited to 60, to limit the loading , together with a limit on the

<sup>13</sup>[http://www.airbusdriver.net/airbus\\_fltlaws.htm](http://www.airbusdriver.net/airbus_fltlaws.htm)

---

roll rate for structural protection. According to the flight phase, the control system can switch between modes<sup>14</sup> as follows:

- Ground mode
  - Mode selected while the aircraft is on the ground.
  - Control system switches to flight mode after lift-off.
  - Reactivated after touch-down.
  - Proportional relation between stick deflections and flight controls
  - Throttles are decoupled, to only taxi by using the Mistral engine, and the cylinder is spun up manually.
  - Throttles are coupled again when take-off is initiated and full throttle is demanded.
- Flight mode
  - Activated after lift-off and becomes active during flare before landing.
  - Throttles are coupled and the power setting of the engine is optimized by the algorithm of the flight computers depending on the flight speed.
  - Proportional relation between stick deflections and flight controls becomes independent of the airspeed, by which e.g. the roll rate is the same for all speeds.
  - Turn coordination is computed by the FCs and send to the actuators.
- Flare mode
  - Activated at 50ft above ground level(AGL).
  - In case of an aborted landing/ go-around the flight mode is reactivated at 50ft AGL.
  - The system allows for slightly pitching up the nose of the aircraft just for before touch down.

### **Alternate law**

In case of a single air data reference fault, the control system will enter the alternate law. The inoperative systems depend on the nature of the reference fault. If for example the a.o.a. information in relation with the airspeed and output of the canard actuator seem to be contradicting, the pilot is in control to keep the aircraft at 0° a.o.a. during cruise. Another possibility of entering the alternate law is a flame out of one of the engines. Hereby the auto-throttle, automated attitude hold become unserviceable. The pilot will be informed about the inoperative systems and failures by a failure/ warning panel. Other inoperative systems may be the roll protection, coupled autothrottle. The main idea in the alternate law is that the systems and functions coupled to the single point failure become inoperative and that the pilot's workload increases, but is still limited to the systems coupled to this sole failure.

### **Direct law**

In the direct law, all functions, limitations and protections become inoperative. In this case the pilot is in direct control of all systems by which the workload is increased to a maximum. The pilot in command needs to control the rpm of both engines based on optimization tables, together with directly controlling the attitude of the aircraft. All protections are lost, and all control surfaces can be deflected to their maximum. Direct law becomes active when there are multiple points of failure such as multiple reference unit failures or unserviceable flight computers.

---

<sup>14</sup>[http://www.airbusdriver.net/airbus\\_fltlaws.htm](http://www.airbusdriver.net/airbus_fltlaws.htm)

---

## Final law

This is the simplest law, and is selected in case of uncontrollability due to both software or hardware failure of the EFCS or e.g. structural failures. In this mode all systems will try to position the aircraft in the best possible position for activating the all-saver. This depends on the altitude, velocity and remaining controllability. When the all-saver's parachute is deployed, all systems are shut-off, both engines are turned off, electrical systems disabled and an Emergency Locator Transmitter is activated.

### 3.4.8 Surface deflection mechanism

In stead of push rods, cables and pulleys running through the whole aircraft, electric servos will be used. The movement of the motors of the servos are instructed by the flight control system. These servos provide the mechanical control by linking their control horn, which is coupled to a series of gears to a pushrod which is then coupled to a control horn on the control surface. Two servos per control surface are installed for redundancy, their size depends on the power they need to deliver. In Figure 3.53 the installation of a Dynon servo in a VANS RV4 or RV8 aircraft is displayed<sup>15</sup>. For our aircraft however, it's intended to use the servos for direct control instead of using them for an autopilot. The selected servos are actually used for controlling a general aviation aircraft when its in autopilot mode, while these aircraft use mechanical control when the pilot is operating the aircraft.

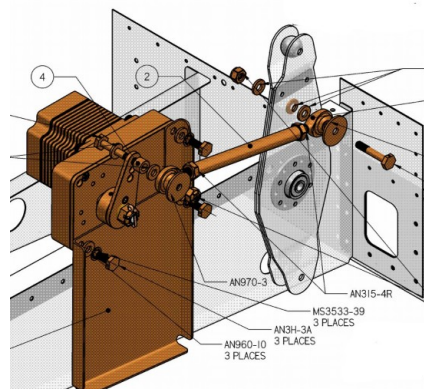


Figure 3.53: Skyview servo installation on a Vans aircraft with push rod as a deflection mechanism<sup>16</sup>

### 3.4.9 Manual and automatic control segregation

The controls the pilot is going to operate are very similar to conventional controls. But the implementation of the fly-by-wire system reduces the workload for the pilot. In the performance section 4.1 it will be discussed what the exact actions of the pilot will be according to the flight stage. The general idea is that the pilot is giving one power input, by which the rpm of both cylinder and pusher engine are optimized according to the flight speed. During turns however, more lift needs to be generated, the flight computers will determine the increase in rpm of both engines. The computers will also take care of the coupling of aircraft's movement, in order for the pilot to not have to compensate for example roll and yaw movement when changing the pitch of the aircraft. During all flight stages, the canard will be controlled by the computers to keep the aircraft aligned with the free stream. Whenever the pilot makes a turn or banks the aircraft, the cylinder rpm needs to increase in order not to loose altitude, which will be done automatically with an automated canard algorithm which is used in the flight computer.

Other, more specific operations will be discussed in the section 4.1, also dealing with the manual and automatic control segregation.

---

<sup>15</sup>[https://www.dynonavionics.com/downloads/Installation\\_Guides\\_Autopilot/RV4,8\\_Pitch\\_Kit\\_Instructions\\_Rev\\_F.pdf](https://www.dynonavionics.com/downloads/Installation_Guides_Autopilot/RV4,8_Pitch_Kit_Instructions_Rev_F.pdf)

### 3.4.10 Cockpit elements

The various constituent elements of the cockpit as described in subsection 3.4.4 were looked up in catalogues which offered data on their purchase prices and links to their technical manuals where their weight and other operational performance characteristics were stated. AircraftSpruce offers a database containing those catalogues and various options in terms of models [29].

Table 3.23 contains data on the various elements constituting the cockpit. The total weight and cost of all the elements (plus a safety margin) is estimated at 25 kg and 20,000 dollars respectively.

Table 3.23: Price and weight for the elementes constituting the cockpit

Element	Quantity	Total Weight [kg]	Total Price [\$]
Integrated EFIS/EMS/Navigator	1	3.4	6000
Backup speed indicator	1	0.29	167.75
Back altitude indicator	1	0.592	395
Backup Cylinder rpm indicator	1	0.168	250
Fuel tank indicator	1	0.1	63.75
Slip indicator	1	0.1	59.75
Sidestick	1	0.34	199.5
Rudder pedals	2	0.3	137
Throttle ICE	1	0.23	179.8
Throttle Cylinder	1	0.23	179.8
Landing gear switch	1	0.1	150
Circuit breaker panel	1	0.36	299
Starter, magneto panel	1	0.1	100
Fuel selector	1	0.1	169.75
Warning/failure panel lights	20	1	379
Servo(s)	6	6.6	5700
Seat(s)	2	2.8	123.5
Seat cushion	2	1.8	165.5
COM antenna	1	0.1	166
VOR antenna	1	0.23	286.5
GPS antenna	1	0.272	579
Final Sum	NA	19.2	16700

### 3.4.11 Summary stability and control

A summary of all control surfaces sizes explained is given in Table 3.24.

Characteristic	Canard	Vertical tail	Aileron	Rudder
Airfoil	NACA6412	GOE 776	GOE 776	NACA 0012
Longitudinal location (w.r.t. cylinder) [m]	4.5	0.3	-	0.3
Lateral Location (w.r.t. center line) [m]	-	2.1	1.8	2.1
Total surface area [m <sup>2</sup> ]	1.93	1.91	0.30	0.35
Span [m]	3.67	1.1	0.63	0.60
Chord length [m]	0.52	0.84	0.24	0.29
Aspect ratio [-]	7.05	1.33	2.62	4.58

Table 3.24: Summary of the dimensions and characteristics of the control surfaces

---

The major decisions on the control system are listed as follows:

- The control of the aircraft will be managed by an automated fly-by-wire control system.
- The pilot will give control inputs with a side-stick, rudder pedals and a coupled throttle system for the engine and the rotor.
- The automated control system will provide stability during all flight operations and translate the inputs of the pilot to optimum deflections for the control surfaces and power settings for the engine and rotor.
- The control surfaces will be deflected by electric deflection mechanisms.
- The total weight and cost of all elements of the avionics are estimated, with the addition of a safety margin, at 25 kg and 20,000 dollars respectively.

## 3.5 Fuselage

The main purpose of the fuselage is to connect the payload to the cylinder and the propulsion system. The fuselage is first designed from a structural point of view. The load cases are analysed and the sizing of the fuselage is determined. Afterwards, a minimization of the drag generated by the fuselage is done by evaluating both the shape and skin of the fuselage. The design of the fuselage is then summarised to provide a clear overview.

### 3.5.1 Structural considerations

#### Purpose and Considerations

The fuselage cabin is defined as the (partly) closed-off space which holds the pilot, the pilot's chair, the avionics, steering system for the pilot and IC-engine. The dimensions of the cabin are determined by the size and shape of the parts it needs to contain. The pilot and its chair are the largest in size and shape, and the way the pilot will need to be placed inside the aircraft determines the arrangement of the steering system and the avionics. For visibility the pilot will be facing forward, and for ergonomics the pilot will be seated. The inclination of the seat is a trade-off between comfort, location of the c.g. of the pilot to balance the aircraft and cross-sectional area of the fuselage. The steering system needs to be reachable for the pilot and the avionics need to be visible for the pilot. From this configuration of the different parts follow the dimensions for the cabin.

A cut-out in the fuselage is made to accommodate a canopy to allow access for the passengers in the aircraft. For the steering of the aircraft it is required that the pilot has forward facing visibility. This is provided by the canopy made of polycarbonate.

The choice of material for the fuselage skin is based on the stiffness of the material needed to ensure it holds the loading, both by the weight of the parts it contains and the loading by the lift surfaces. The choice of material will also be based on fracture toughness, since objects impacting on the cabin cannot influence the safety of the pilot. The crash worthiness of the cabin is the final consideration for the material of the cabin.

#### Bulkhead

Behind the second passenger a bulkhead will be installed. It is located at 3.92m from the nose of the aircraft. This bulkhead will be used to separate the passengers from the engine. During normal operation this will shield the passenger from the engine noise and from heat transfer to the cabin. It also serves as structural component to stiffen the fuselage.

---

### Flame resistance

When engine failure occurs it will use as a firewall to keep passengers from getting severely burned. GLARE is chosen as material for the bulkhead since it has good fire resistance properties [35]. Note that GLARE is also advantageous as lightweight structural material for the bulkhead. It is tested to have a fire resistance of more than  $1100^{\circ}\text{C}$  for over 15 minutes. When an open fire blazes on the GLARE panel, the first layer of aluminium melts. When this happens the first layer of glass fibre with an epoxy resin is exposed. The epoxy carbonizes due to the high heat, which protects the second layer of aluminium. The other parts start delaminating, which increases the space between the aluminium parts. This creates an isolating effect similar to double glass used in buildings. Due to these phenomena there will be no flame penetration, keeping the passenger free of burns, but also leading to a lower temperature due to this isolation. An extra layer of insulation will be added to reduce the noise coming from the engine.

### Thermal insulation

A conservative estimation for the bulkhead thickness, evaluating a worst-case scenario for the heat transfer, is performed here. A sketch of the analyzed is given in Figure 3.54.

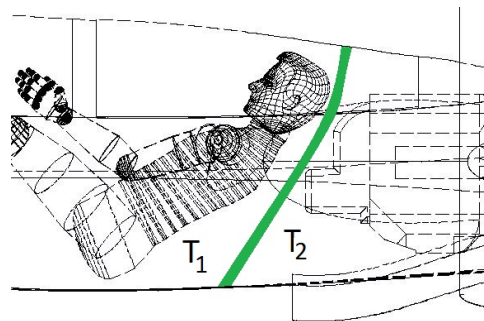


Figure 3.54: Sketch of the location of the bulkhead at the rear of the fuselage including  $T_1$  (cabin temperature) and  $T_2$  (engine room temperature).

Fourier law of conduction is used to size the thickness of the bulkhead. The temperature in the cabin is assumed to be  $T_1 = 25^{\circ}\text{C}$ . The temperature in the engine room is assumed to be the same as the temperature of the engine block, namely  $T_2 = 100^{\circ}\text{C}$ , being the same as the maximum temperature of the cooling fluid in the engine block [39]. The heat flux allowed through the bulkhead is set equal to the cooling flow going through the ventilation holes available for each passenger. Estimating the mass-flow through these ventilation holes to be  $0.01\text{ kg/s}$ , the available cooling power is  $228\text{ W}$ , considering the temperature difference between the cabin and the ambient to be  $25\text{ K}$ . When choosing the glass-fibre reinforced polymer in the GLARE panel as insulator (the glass fibre resin has a heat conductivity of  $0.038\text{ W/mK}$  [40]) a thickness of  $0.003\text{ m}$  is required for the bulkhead panel having a cross-sectional area of  $0.465\text{ m}^2$ .

Radiation of the IC-engine is neglected because the layers of aluminium next to the layers of glass-fibre reinforced polymer in the GLARE panel have a high reflectivity constant ( $\epsilon = 0.1$ [40]). Additionally, the emissivity of the aluminium of the engine block is low ( $\alpha = 0.1$ [40]), making the radiation even more negligible.

## Skin Sizing

### Simplification of Geometry

The shape of the fuselage is simplified to be able to analyze its structure using basic structural analysis tools [30]. The simplification is illustrated in Figure 3.55, indicating the two regions that are analyzed. The first section (1) is at the nose of the fuselage and has a closed cross-section (A). The second section (2) is at the rear of the fuselage and has a C-shaped cross-section (B) to account for the canopy of the cockpit assuming the canopy is not structurally load bearing. For both regions the smallest cross-section

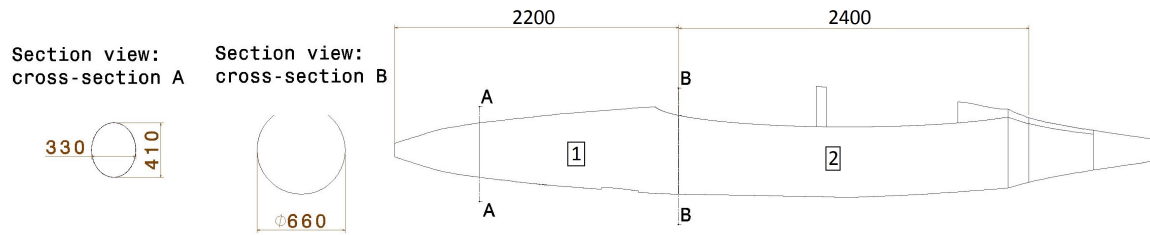


Figure 3.55: Technical drawing of the fuselage including cross-sectional shape of the regions 1 and 2 (dimensions in mm).

is taken as representative cross-section to be conservative in the sizing. For the first cross-section an elliptical shape is simplified with a circular shape of average diameter, namely 370 mm. The second cross-section has a diameter of 660 mm.

### Load Case

The load case includes the sagging load (from the weight of the fuselage structure itself), the passenger weight, the canard lift and the engine weight. The fuselage is supported using two pin supports at the locations of the wing spars in the horizontal supports. The load case is determined using a conservative estimate for the loads. The maximum lift generated by the canard in equilibrium is 12% of the maximum take-off weight, or approximately 1.2 kN. The maximum load encountered is this load, multiplied with the maximum load factor  $n_{max} = 3.8$ . This load is further multiplied with a safety factor  $n_d = 1.5$  get the ultimate design load. The load case is illustrated in Figure 3.56.

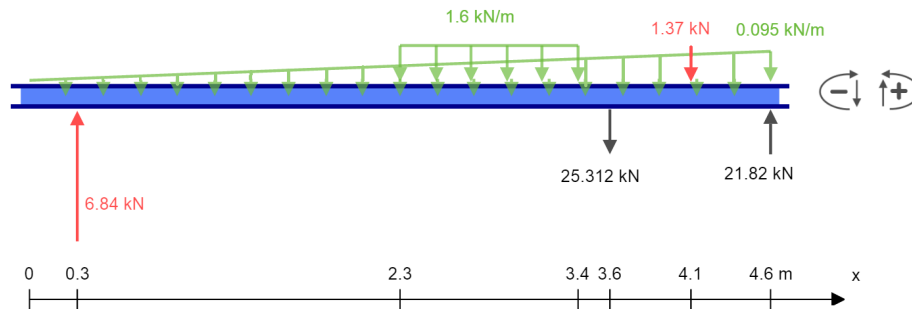


Figure 3.56: Load case on the fuselage. The x-axis points longitudinally and starts at the nose of the fuselage. Loads from left to right: Canard lift, structure sag, pilot weight, engine mount and front spar attachment, engine, rear spar attachment

Looking at [41], the shear stress due to the lift on the canard is considered to not be the driving failure mode. Therefore mainly the bending failure mode is considered critical during the design, in combination with torque loading on the fuselage. The latter can be expected when having e.g. a wind gust on one part of the canard.

### Calculations

The skin is made out of carbon fibre reinforced polymer, with layup  $[\pm 45\ 0/90\ (0IM)]_s$ . Twill weave of 0.3mm thickness is chosen for this lay-up, for aesthetic as well as production reasons. In addition, the intermediate modulus central reinforcement is Toray T700S, 0.4mm. The lay-up is symmetric accompanied by a core in the middle. This core material functions as stabilizing element to counteract buckling of the fuselage skin. Using Appendix A, we get  $E_1 = 95\text{ GPa}$ ,  $E_2 = 36\text{ GPa}$  and  $G_{12} = 13\text{ GPa}$ . Using this lay-up design, having a total thickness of 3.2 mm, a failure assessment is performed to see if the lay-up holds.

---

### *Torque Load*

The torque loading is experienced when a differential lift force acts on the canard surface. A first estimate of the magnitude of the corresponding torque is made as follows. The maximum lift coefficient that can be obtained by the canard is 1.2; one side of the canard surface has a surface area of  $0.95 \text{ m}^2$ , the gust speed considered here is  $20 \text{ m/s}$  [42]. The additional lift force on one side of the canard equals to  $266 \text{ N}$  which corresponds to an induced torque of  $488 \text{ Nm}$ . A safety factor  $n_d = 1.5$  is used to be conservative; corresponding to a torque of  $732 \text{ Nm}$ .

For region 1, having a closed cross-section enclosing an area of  $0.108 \text{ m}^2$ , a shear stress of  $1.06 \text{ MPa}$  occurs in the skin. For region 2, having an open C-shaped cross-section, a shear stress of  $130.7 \text{ MPa}$  occurs in the skin. The torsional stiffness constant is calculated assuming that the length of the section is a lot larger compared to its thickness. This high stress in this region is expected since the cross-section contains a cut-out immensely decreasing its torsional stiffness.

### *Bending Load*

Looking at the load case in Figure 3.56 and converting it into a bending diagram, the maximum bending moment in region 1 and 2 is equal to  $13 \text{ kNm}$  and  $21 \text{ kNm}$ , respectively. Using the bending equation for bending of symmetrical cross-sectional beams, the maximum normal stress in the cross-section is determined.

For region 1, the area moment of inertia is calculated using thin-walled approximation. Noting that the maximum stress occurs at the point furthest away from the neutral line, a maximum compressive stress of  $37.8 \text{ MPa}$  occurs.

For region 2, the area moment of inertia of cross-section is calculated using software (CATIA V5 [43]) considering the complexity of its shape. The corresponding maximum stress due to bending in the cross-section is calculated to be  $340 \text{ kPa}$ . Note that no warping is assumed here.

A summary of the stresses occurring in the fuselage is given in Table 3.25.

Table 3.25: Maximum stresses occurring in the cross-section of region 1 and 2 in the simplification of the fuselage, where region 1 is in front of the canopy and region 2 is at the canopy

Load case	Region 1	Region 2
Torque	$\tau = 1.06 \text{ MPa}$	$\tau = 130.7 \text{ MPa}$
Bending	$\sigma = 37.8 \text{ MPa}$	$\sigma = 0.34 \text{ MPa}$
Combined	TSAIW = 0.01	TSAIW = 0.95

### **Layout of the fuselage**

In the previous discussion the thickness of the fuselage skin thickness is sized. However, although the skin on its own is able to carry the loads, it is not able to maintain its structural rigidity. Therefore to stabilize the skin, stiffeners and frames are installed to support the fuselage shape. The design of these structural elements will be based on conventional aircraft design methods using stiffeners and frames. As already has been said, the stability of the skin is supported by including a core material between the symmetric laminates of the lay-up.

### **3.5.2 Aerodynamic considerations**

The function of the body is to provide space for the passengers and engines, as well as mounting positions for the cylinder support, the canard and the ducted fan. The size of the fuselage is therefore determined by the required length of the body from a control perspective, the ergonomics for the pilots and the structural requirements. Only the detailed and final shape of the body is based on its aerodynamic properties, the approximate sized used will be validated in the rest of this chapter.

---

## Shape

To make the body as efficient as possible from an aerodynamic point of view, the drag should be minimised. It is not required that the body provides lift, which means only the drag coefficient  $C_D$  is considered. The shape of the body is based on the NACA 16-018 airfoil [44]. This is a symmetrical airfoil with a zero-lift drag coefficient  $C_{D_0}$  of  $6.9 \cdot 10^{-3}$  at a Reynolds number of  $10^6$ . The point of maximum thickness is positioned relatively close to the trailing edge. This is beneficial to accommodate the pilots which are also positioned comparably in the back of the aircraft. The basic fuselage shape is accompanied by a canopy to allow the passengers to access the aircraft. Adding this canopy to the fuselage causes the  $C_{D_0}$  to increase. This canopy is divided into two parts; one for the front pilot and one for the rear passenger.

## Skin topology

A potential drag reduction mechanism is the use of advanced coatings in the body of the aircraft. Research was therefore conducted, to investigate such coating solutions.

A promising solution that was recently developed by Stenzel, Wicke and Hage [45], utilizes the same mechanisms as the “sharkskin”. This coating is applied in the form of a paint and contains nanocomposite microstructures (“riblets”) which reduce turbulent skin friction drag. Since the coating has similar characteristics as regular paint and is applied using the same principles, there is neither increase in manufacturing complexity nor in weight. Stenzel, Wicke and Hage [45] claim a total skin friction drag reduction for the aircraft of 3%, although trials conducted by Lufthansa offer a more realistic figure at 1 % [46]. This will help reduce not only fuel consumption and subsequently emissions, but also noise (through the reduction of turbulent vortices).

### 3.5.3 Ergonomics

Ergonomics in aircraft design describes the comfort in the interaction between the people and the aircraft system. This design philosophy was applied when designing the cockpit which houses the two persons.

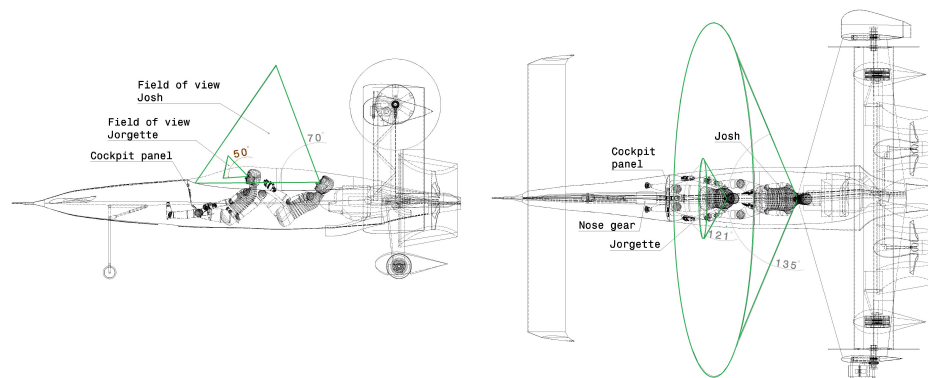


Figure 3.57: Technical drawing of the ergonomics in the fuselage including the field of view of the passengers.

Special attention was paid to the field of view of the pilots. This should provide the pilots with an appropriate all-around sight during all stages of flight. The canopy of the cockpit will be made out of polycarbonate. This gives the front and aft pilot a vertical field of view of respectively  $50^\circ$  and  $70^\circ$ . Furthermore the horizontal field of view of the first pilot is  $121^\circ$  and of the second pilot  $135^\circ$ . These dimensions and a representation of the field of view is shown in Figure 3.57. The most critical flight stage is in general landing, where conventional aircraft have to pitch up to generate enough lift, which reduces the field of view towards the runway. Yet, our aircraft does not require high pitching angles at landing, which facilitates the landing phase.

The pilots will be placed one behind the other. The front pilot will sit between the legs of the aft one, this is done to save space and to keep the c.g. as much aft as possible. One cockpit panel with all avionics and flight monitors will be installed in front of the first pilot. Both pilots, however, can operate the aircraft with their side sticks. These side sticks are common in fly-by-wire aircraft as no large control forces have to be applied. Another feature to save space is the retractable front landing gear which will be located between the legs of the front pilot.

### 3.5.4 Summary fuselage

The main characteristics of the fuselage subsystem are summarised in Table 3.26 and illustrated in Figure 3.58.

Table 3.26: Summary of the fuselage characteristics

Variable	Value	Unit	Variable	Value	Unit
Airfoil	NACA 16-018	-	Length	5.72	m
Material type	Sandwich	-	Location rear bulkhead (w.r.t. nose)	3.92	m
Lay-up	$[\pm 45 \ 0/90 \ (0IM)]_s$	-	Largest radius	0.83	m
Mass	58.60	kg			

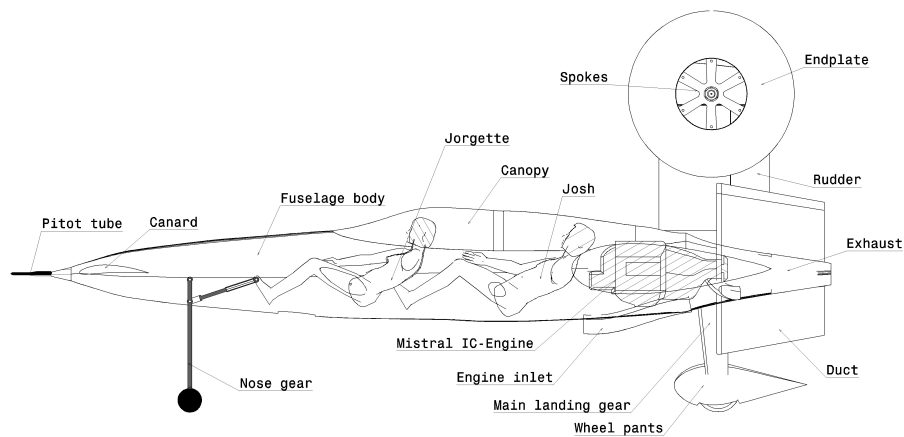


Figure 3.58: Technical drawing of the fuselage including airfoil-shaped body and canopy.

## 3.6 Landing Gear

According to requirement Requirement **RMEA-SS-LT-10**, the aircraft needs to be capable of a rough (6g) landing on its own. This is considered necessary, since the control of the vertical speed can be difficult. Such a rough landing is however considered exceptional, and an inspection and possible minor repairs are expected to take place if it occurs. A normal-operations landing of maximum 3g is expected. As already discussed in [5], a tricycle configuration is chosen for the landing gear, with a non-retractable main gear and a retractable nose gear. In section 4.3, the choice to make the nose gear retractable is discussed. The aircraft is design to land on a type II or III landing surface (paved runway) [47]. The exact position and layout resulting will be currently discussed.

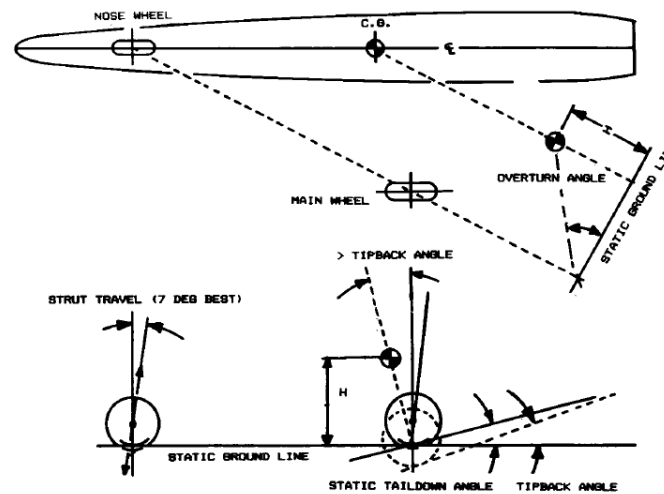


Figure 3.59: Position of the landing gears with respect to the centre of gravity. For the Magnus Aeolus, all of the requirements are satisfied and stability is guaranteed. [48]

### 3.6.1 Location

The locations of the landing gear for normal aircraft are determined from criteria related to balance, tip-over and pitching at take-off [47]. For Magnus Aeolus, the last consideration is of very little importance, since no pitch is required at take-off, and the angle of attack of the fuselage and wing support is kept as close to 0 as possible. Thus, the landing gears need to be positioned far enough from the centre of gravity to ensure the balance of the aircraft on the ground and during taxi. Since this consideration provides an optimization direction, but does not constrain the position, additional reasons are needed to determine the exact location.

A source of such reasons are the structural considerations in transferring the loads from the landing gear to the airframe. To decrease the weight of additional structure to enable landing, such positions for the landing gear are considered that enable the shortest possible load path to existing structure strong enough to support the landing loads. This is especially beneficial for the rear landing gear, which can be placed at the rear spar of the horizontal rotor support. This position is far enough behind the rearmost centre of gravity (full of fuel, no payload) to prevent tipping on the ground. According to [47], a minimum  $15^\circ$  angle is necessary between the line passing through the touching point and the centre of gravity and the vertical. When the landing gear is attached to the rear spar, the maximum allowable height of the landing gear is 2.2 m, which is far above what is necessary for duct clearance.

The constraint for lateral position is usually tip-over during taxi. Again, other considerations constrain the most inner position. In this case, the landing gear strut needs to be attached outside of the duct. This provides an innermost constraint of 1.1 m outboard of the symmetry plane. This is also more than sufficient for tip-over, providing an angle much lower than the maximum  $55^\circ$  [48]. Placing the landing gear further outboard makes the load path longer and is thus not favorable from a structural perspective.

The position of the front landing gear is more flexible, since it is very far from the centre of gravity and carries less loads. It is thus located as much forward as possible without significant changes to the configuration. In this way, the front landing gear can be made lighter at no cost. The most convenient location for its placement is immediately in front of the cockpit. Since only one nose gear is present, it is located in the symmetry plane of the aircraft.

---

### 3.6.2 Struts

The height of the landing gear is mainly determined by the clearance requirement for the duct. FAR 23 requirements [48] 20 cm of clearance between a propeller and the ground at maximum, so similar clearance is used for the duct. In addition, 30 cm are added for shock absorber travel. As a result, the total height of the landing gear is 105 cm.

Since the landing gear is not going to be retractable and passenger comfort is less significant than ease of manufacturing and maintenance, a leaf-spring type landing gear is chosen. Similar landing gears are often used on comparable conventional aircraft. Unfortunately, landing gears that are available off-the-shelf don't completely suit the configuration. Thus, a design was made for the layout of the landing gear, following the approach outlined in [48].

$$S_{stroke} = \frac{V_{land_v}^2}{2g\eta_{ls}N_{land}} \quad (3.67)$$

The required stroke for landing is calculated from Equation 3.67. Then the corresponding bending stiffness  $EI$  and angle of attachment  $\theta_{mgear}$  can be designed for. The efficiency  $\eta_{ls}$  of a leaf spring landing gear is taken as 0.5 [48]. Using a recommended sink speed  $V_{land_v} = 2.6$  m/s (see subsection 4.1.3 and a comfortable 3g landing at maximum landing weight of 1000 kg, (with some margin) one obtains 25 cm of stroke.

$$S_{stroke} = W_{land}N_{land} \frac{\sin^2 \theta_{mgear}}{2} \frac{L_{mgear}^3}{3EI} \quad (3.68)$$

For design at 20 degree incidence angle  $\theta_{mgear}$  made out of Aluminium 7075-T6, this results (Equation 3.68) in a landing gear strut with thickness of 31 mm and average width of 200 mm. The weight of both struts is thus 39 kg.

In a 6g (see Requirement **RMEA-SS-LT-10**) touch-down, corresponding to 5.2 m/s of sink speed, the same shock absorber will stroke 46 cm. The shock absorber itself is still below its maximum stress, however close enough so that inspection after the event is required to check for damage. The duct clearance is barely sufficient, and inspection of the duct for ground damage is also necessary. It must be also noted that a landing at such vertical speed is very impractical, since the aircraft will bounce off the runway several times before settling.

The material of the strut is, as already mentioned, Al 7075-T6. Composite alternatives were deemed too design intensive and unnecessarily complex in terms of production. Finally, a great amount of industry experience with aluminium landing gears and a large number of designs which can be used to verify the current design. The designs Glasair TD , Glasair FT (13 kg per strut, at 70 cm height), Skybolt (18 kg both at 70 cm height) and Starduster (22 kg both per 80 cm) from [49] were compared to the current design to ensure no failure modes or other important considerations were omitted.

The nose landing gear strut length is determined such that the aircraft is perfectly level at maximum take-off weight. It's a rigid design, with all of the stroke coming from the tire. Details on its layout (rake, shimmy dampers, etc. [48]) are dependent on the choice of steering system, which is beyond the current discussion.

### 3.6.3 Wheels

Complete detailed design of the wheel assembly of the landing gear is considered beyond the scope of the current report, since it would be determined mainly on supplier availability and final budgetary constraints. Nevertheless, some initial estimates on the mass added by the wheels are made.

To absorb the expected landing loads, 15x6 tires are selected for the main landing gears [50]. Expected mass for those is 10 kg in total. The corresponding wheels are chosen again from [49]. Since weight

is more important than durability, magnesium wheels are preferred. Taking enough braking power as required by landing, this results in 60-262 wheel provided by [49]. The weight of this wheel is 4.2 kg.

For the front landing gear, a wheel and tire selection is again beyond the scope of the current stage of design.

### 3.6.4 Wheel pants

Since, the main landing gear will not be retractable, a fairing will be used to make the landing gear as aerodynamically efficient as possible. The necessities of an airfoil for the wheel pants are a very big thickness to embed the wheels and a low drag coefficient. The airfoil is selected based on the  $C_d - \alpha$  curve for a Reynolds number of 1,000,000, since their drag contribution will be largest during cruise. The selection of the airfoil was based on the eventual length of the wheel pants which can be translated to structural weight and the drag generated. Eventually the Eppler 863 airfoil<sup>16</sup> was selected out of high thickness symmetrical airfoils. The airfoil is actually developed as strut airfoil, where it would take up structural loadings as for example wing support, for which a high thickness is required. And this while inducing minimum drag. The airfoil's max thickness is 35.7% at 28.5% chord, its drag coefficient for 0 angle of attack is 0.012. Almost all wheel fairings are produced from fibre glass. They should be able to withstand the aerodynamics forces, but do not need to take up structural loads. In general, the weight of a wheel pants is about 1kg.

### 3.6.5 Summary landing gear

The location of the front landing gear is immediately in front of the cockpit. Further details on its layout remain to be determined. The expected mass is about 20 kg, based on reference catalogue parts [49] and statistics [47].

Table 3.27: Summary of values for the main landing gear. For technical drawing, see Figure 3.60

Variable	Value	Unit	Variable	Value	Unit
Location x	Rear spar	-	Height	1.05	m
Location y	Outboard of duct	-	Inclination	20	deg
Rating	6	g	Thickness (avg.)	31	mm
Wheel	15x6	in. <sup>2</sup>	Width (avg.)	20	cm
Total weight	60	kg	Stroke	25	cm

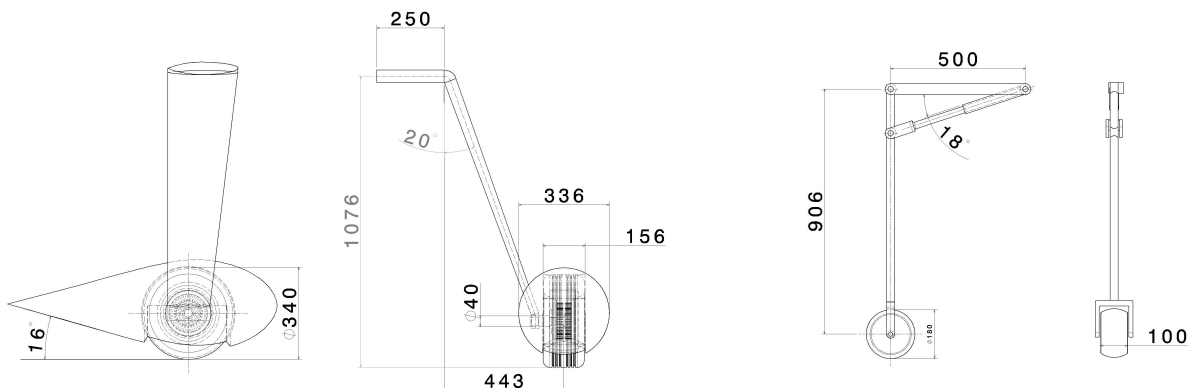


Figure 3.60: Technical drawing of the main landing gear (left) and the front landing gear (right).

<sup>16</sup><http://airfoiltools.com/airfoil/details?airfoil=e863-il>

---

## 3.7 Fuel System

The fuel system contains the 210 kg fuel that the aircraft will carry. It is designed to fuel both engines, where the main engine, the Mistral G200, will be considered first. Afterwards, the fuelling of the Simonini engine, driving the rotor, is designed. The minimum size of the fuel tank and the management system for the fuel are the final elements for this section.

### 3.7.1 Mistral engine fuelling

The basic fuel system for the Mistral engine is displayed in figure 3.61. Mistral engines have an engine-driven fuel pump installed, thus no need for an extra fuel pump for the engines. The fuel will be filtered before injecting it into the engine by multiple filters with a smaller and smaller strainer, excess fuel will be transferred back via a return line. The fuel injection is completely automatized by a Full Authority Digital Engine Control (FADEC)<sup>17</sup>. This FADEC system is designed completely redundant using two Electronic Control Units (ECU), powered by the installed alternators. This system lets the motor runs as efficient as possible, which increases the Time Between Overhaul. It also makes it easier for the control of the pilot, having one thing less to worry about. Lastly, Mistral Engines are what is known as a wet sump engine. The engine is allowed to operate between -0.5g and +4g. If the aircraft exceeds this the oil pump will start to inhale air and this will damage the engine. The aircraft will always be in the limit of the engine operations.

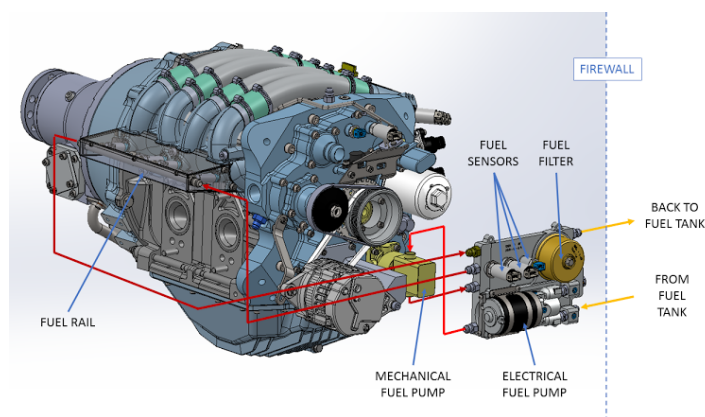


Figure 3.61: Fuel System Mistral G200 IC-engine provided by Mistral Engines

### 3.7.2 Simonini engine fuelling

Since the Simonini engine subsection 3.1.3 is designed to use a gasoline/oil mixture which needs to be premixed, Simonini does not provide a separate oil tank and pump. The gasoline must have an octane number of not lower than 98 to prevent detonation/pre-ignition. The usage of semi-synthetic based oils is recommended, with a mixing ratio of 3%. Because of this very different fuel composition, from the Mistral's engine fuel, a separate fuel tank for this engine is needed.

### 3.7.3 Fuel tank size

The aircraft will have 3 fuel tanks, one for the Simonini engine and two for the Mistral engine. The size of the fuel tank is depended on the power required due to drag, the efficiency of the duct and the specific fuel consumption of the Mistral engine, in combination with the Simonini engine specific fuel consumption and the power required by the cylinder. Table 3.28 gives a quick overview of the numbers during mid

<sup>17</sup><http://www.experimentalaircraft.info/articles/aircraft-engines-fadec.php>

Parameter	Value	Unit	Parameter	Value	Unit
$FC_{Mistral}$ 75%	39	l/h	$\eta_{Duct}$	0.74	-
$FC_{Simonini}$ 75%	2.2	l/h	Cruise time	7.2	h
$P_{maxMistral}$	121	kW	$m_{Mistral}$	169-181	kg
$P_{maxSimonini}$	19.4	kW	$m_{Simonini}$	8.5-9.1	kg
$\rho_{fuel}$	.724-.774	kg/l	$m_{tot}$	203-217	kg
$SFC_{Mistral}$	311-333	g/kWh	$V_{Mistral_{tank}}$	246	l
$SFC_{Simonini}$	109-117	g/kWh	$V_{Simonini_{tank}}$	12.4	l
$\dot{m}_{fmid - cruise}$	28	kg/h	$V_{tank}$	260	l
$P_D$	60.5	kW	$V_{fuel}$	246	l
$P_T$	12.7	kW			

Table 3.28: Overview of fuel system characteristics during mid-cruise

cruise. The fuel mass is then calculated with Equation 3.70, but first the specific fuel consumption is calculated with Equation 3.69.

$$SFC = \frac{FC \cdot \rho_{fuel}}{P_{setting} P_{max}} \quad (3.69)$$

$$m_{tot} = m_{Mistral} + m_{Simonini} = \left( \frac{SFC_M \cdot P_D}{\eta_{Duct}} + SFC_S \cdot P_T \right) \cdot h \quad (3.70)$$

It must be noted that the specific fuel consumption changes per altitude and for this calculation the SFC at 7000 ft is taken, because this is the driving part of the fuel consumption. The engine will be running at an average of 68 % of this max power at cruise altitude. The fuel that will be used for both engines is unleaded 95, note that the Simonini has to be premixed with oil. The density of Unleaded gasoline 95 can vary between batches, the data is taken from Safety Data Sheet from Topaz Energy<sup>18</sup>. All information regarding this fuel can be found here. The fuel tank has an extra 5% of volume to account for expansion during flight [51].

### 3.7.4 Fuel management system

The fuel system consists of three fuel tanks, two in the left wing and one in the right wing. The left fuel tank is split up in two, of which a smaller tank with a volume of approximately 12.4 L at the tip for the Simonini engine<sup>19</sup>.

Fuel to the main ICE engine will be provided by both the left main and right tank. The left engine will have a tank size of 110 L and the right of 123 L. The overflow of Mistral engine will be coupled to the left tank, to compensate for the moment generated by the fuel consumption of the Simonini in the left tank. The Simonini has an approximate fuel consumption of 2 L/h and the main engine consumes 39 L/h mid-cruise, cruise conditions. To maintain the position of center of gravity at the center of the aircraft a fuel selector needs to be installed between the left main tank and right tank as displayed in Figure 3.62. This fuel selector will be coupled to the Mistral engine, due to its considerable higher fuel consumption and can be operated by both the pilot and automated FCS. Moreover, anti-slosh baffles will be used to keep the fuel from uncontrolled transferring from one tank to the other during manoeuvres or turbulence.

<sup>18</sup><https://www.topaz.ie/TOPAZ/media/Topaz/Consumer/PDF/Data/SDS-UNL.pdf>

<sup>19</sup><http://www.simonini-flying.com/index.php?lang=en>

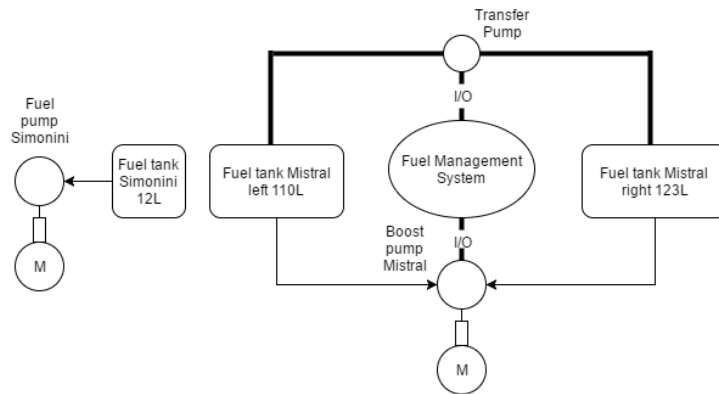


Figure 3.62: Schematic of the fuel system

### 3.8 Ballistic Recovery System

Considering the required innovations involved in the design of the Magnus Aeolus and the experimental nature, safety is a major concern. In case all safety barriers and system backups are breached due to unforeseen circumstances or hazardous situations, a last point of reception is used, in order to save the pilots and airframe. Therefore a Ballistic Recovery System (BRS) will be installed, a parachute connected to the airframe in order to save both pilots and limit the damage to the aircraft and environment.

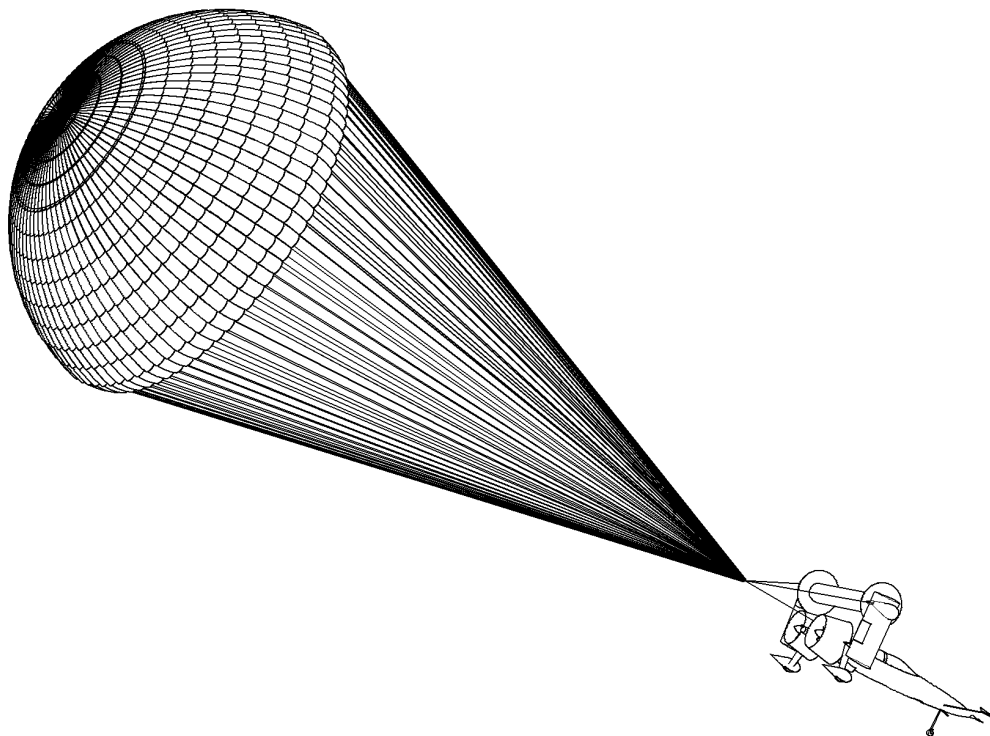


Figure 3.63: The aircraft hanging from the deployed parachute. Lines run to the rotor supports and the engine mounts. Before deployment, the harness straps are covered by aertape.

An off-the-shelf proven design will be used as recovery system. BRS Aviation<sup>20</sup> is one of the main providers of this system and provides close corporation to ensure a solid installation of the recovery

<sup>20</sup>[http://www.brsaerospace.com/experimental\\_aircraft.aspx](http://www.brsaerospace.com/experimental_aircraft.aspx)

---

system. Parachutes of BRS can save aircraft up to 1600 kg, with a significantly higher speed range, such as the Cirrus Sr22 which cruises at 340 km/h. It is expected that the system will cost between \$3,000 and \$12,500. The added weight to the aircraft will be about 40 kg, according to reference aircraft, such as the Cirrus SR22 or Cessna 182 fitted with the BRS. A system for Magnus Aeolus would weigh around 20 kg and would have approximate dimensions of 210x500x220 mm<sup>21</sup>, at a first-order estimate. The sequence of events is illustrated below and on Figure 3.63

1. The pilot pulls firmly on the red handle inside the cockpit
2. The parachute and its deployment are stored in the bulge to the right of the cylinder. When the handle is pulled, the solid rocket booster shoots the parachute out in the free-stream direction.
3. The cabling running along the structure to the three stabilization points rips through its aerotape cover with minimal damage to the rest of the structure.
4. The parachute is attached to the aircraft at three points: at each bearing housing on the sides of the cylinder, and at the engine mount. These points were chosen since they are already strong enough to support the aircraft weight. In addition, the c.g. of the aircraft is always between these 3 points.
5. The aircraft hangs under the parachute, with the lines running below the cylinder. It can land safely, with localized structural damage at the nose and no danger for the lives of the pilot.

The time to fully deploy the parachute depends on the orientation of the aircraft, airspeed and loading. The time is delayed to about 10s for Cirrus aircraft <sup>22</sup>, for full deployment, note that the deceleration of the aircraft starts immediately. If our aircraft would deploy the BRS during cruise at MTOW the expected load induced to the structure is about 4120N, introduced at the attachment points.

## 3.9 Operations and Logistics

Operations and logistics discusses the operation of the aircraft and all of the planning around it. First of all, the operations needed for testing the aircraft are described, after which the actual mission is discussed in detail. Surpassing the mission is a realistic possibility and a short overview of this is also given. Next is an overview of the pilot operations which have to be performed during the mission. Consequently, the ground support around operations is evaluated. Finally, a summary of the mission operations and pilot operations is provided.

### 3.9.1 Aircraft testing

After finishing the production and the assembly, the aircraft has to be readied for the operations. There are a number of steps which have to be performed before the actual mission can be flown. Prior to the final assembly, subsystem-level tests have already been executed. The full integration of the aircraft system has to be tested. There are a number of tests to be executed by a test pilot before the actual mission of flying to Heathrow can be performed. These tests can be used to validate the performance of the aircraft. Also, the control laws described in subsection 3.4.7 can be tested. The main purpose is to determine if indeed the optimal coupling for the engines is used for each of the different flight phases.

First of all, a high speed ground run and stop will be done by the aircraft to test the ground performance of the aircraft. Data is collected to analyse the performance during the ground phase. Parameters to evaluate involve acceleration, braking performance, power, airspeed and fuel consumption. After this test, the aircraft will perform the take-off, turn around and carry out the landing. Similar parameters as for the ground test have to be obtained, while adding the collection of the flight path angle, bank angle and rate of climb. This data can be analysed and compared to the expected data, allowing the possibility of improving the aircraft or its operations. Note that if improvements are made, the same test has to be redone before continuing to the next step. Then the next test is to take-off, turn, do a touch and go, turn again and land. Again, data is collected and analysed to possibly improve the aircraft. The

---

<sup>21</sup>[http://www.brsaerospace.com/advice\\_to\\_owners.aspx](http://www.brsaerospace.com/advice_to_owners.aspx)

<sup>22</sup>[http://cirrusaircraft.com/wp-content/uploads/2014/12/CAPS\\_Guide.pdf](http://cirrusaircraft.com/wp-content/uploads/2014/12/CAPS_Guide.pdf)

---

final test is taking off, climbing to cruise altitude, descent and land again at the same airport. Data for the cruise altitude can now be obtained to review the behaviour of the aircraft. It is expected that most tests have to be executed multiple times to obtain satisfying data and to assess the aircraft's reliability with respect to performing the mission. The maintenance and ground support during this operational phase will be discussed in subsection 3.9.6.

### 3.9.2 Mission operations

The mission operations can be split into three phases, the airfield operations before the flight, the flight operations and the airfield operations at the end of the flight. All of these phases will be discussed in this section. The ground support and maintenance however, will be discussed in subsection 3.9.6.

The actual missions starts by running the pre-flight checklist in the hangar. This test includes for example checking the fuel level, oil level, functioning of mechanics and completing a weight and balance. When completed, the aircraft will be positioned on the apron where the start-up takes place. First the main engine is started, which can be done using the battery carried on board. Once this engine is running, its alternator starts recharging the battery. Also, the cylinder is spun up by the Simonini to take-off rotational velocity. The reason for this is that spinning up the cylinder during the take-off takes too much time and uses a lot of energy. Hereafter, the aircraft taxis to the holding point of the runway in use after asking ATC permission. Subsequently for the actual take-off, the aircraft will be powered up and the cylinder will already be spinning at the appropriate rotational speed for take-off. The main function of the small engine is to maintain the rotation of the cylinder. The aircraft will accelerate at maximum power and thereby take-off at the minimum take-off distance.

After the take-off, a climb is started to reach the height for obstacle clearance. Shortly hereafter Dutch Mil will be contacted to open the filed flight plan and a climb to cruise level is started, which is at 7000ft. When this altitude is reached, the pilot will switch to the cruise setting. During the cruise phase of the flight, a lot of fuel will be burnt. This decreases the weight of the aircraft which means less lift is needed to keep the same altitude. To decrease the production of the lift while maintaining the most efficient  $C_L/C_D$ , the speed of the aircraft has to be adjusted. This decreases both the lift produced and the drag produced, which means the power required also decreases. To keep the ratio between the rotational velocity of the cylinders and the velocity of the aircraft equal, the rotational velocity of the cylinders has to be decreased as well. The pilot therefore has to throttle down to compensate for the decrease in power required for both the cylinder and the main engine.

When nearing the proximity of Heathrow, the descent has to start. Permission has to be granted by the ATC to initiate this descent and loiter may precede this. Because of the experimental nature of the aircraft and the intellectual value of performing the mission the loiter time is assumed to be limited. If loiter is necessary, this has to be done at cruise height since this is the minimum loiter altitude at Heathrow [52]. For the descent, the descent profile preferred by Heathrow will be used. From 3000 ft onwards, a descent angle of  $3^\circ$  has to be maintained. Until this altitude, an unpowered descent will be used to limit the amount of fuel burnt. From the 3000 ft down, a powered descent will have to be used. This flight path greatly decreases the noise for the surroundings of the airfield which makes it preferable. ATC will however guide the aircraft, which may include deviating from this expected descent plan. At 3000 ft, the aircraft will also use its Instrument Landing System (ILS) to be guided to the runway at the same angle of  $3^\circ$ . This angle can then be kept constant while landing the aircraft, completing the mission of flying to Heathrow.

### 3.9.3 Surpassing the mission

The range of the aircraft is high enough to return back to Rotterdam-The Hague airport after delivering the package without refuelling. A pre-flight check will again be executed to make sure the aircraft is fit to perform the mission again. The engines are again started and permission will be asked from the ATC to taxi to the runway. The aircraft takes off at its minimum take-off distance again and will be guided by the ATC to the cruise altitude. The cruise phase will be executed similarly as on the route

---

to Heathrow, the main difference is that since the weight is already below the MTOW, a lower cruise speed for the beginning of cruise is selected. This speed will again decrease during the flight to maintain the most efficient flight. The ATC will guide the descent and landing of the aircraft and the complete mission will have been performed while going back to Rotterdam-The Hague Airport.

### 3.9.4 Pilot operations

The operations of the pilot for different phases of the flight will be discussed here. This includes the handling during take-off, climb, cruise, descent and the landing. These operations are valid both for flying from Rotterdam to Heathrow and from returning to Rotterdam from Heathrow.

#### Take-off

During the ground phase of the take-off, the cylinder has maintain a constant rotational rate which is initiated before the take-off begins. Full power is used for the maximum acceleration, meaning that the throttle has to go all the way forward. As soon as the aircraft lifts off, a number of changes have to be executed. The throttle has to be pulled back while the rotational velocity of the cylinder has to be increased. This allows the aircraft to increase the flight path angle without accelerating. This increasing flight path angle increases the thrust needed and the throttle therefore has to be pushed forward again while keeping the velocity constant. As soon as the maximum thrust needed to keep the speed is constant, the rotational velocity of the cylinder slowly has to be decreased to lower increase of flight path angle and maintain the velocity at full power. The flight path angle will keep on increasing slightly until screen height if the power allows this. This take-off procedure results in a minimum take-off distance because flight path angle is optimized.

#### Climb

The main optimization of the climb is to reach the cruise altitude as efficiently as possible. This starts by accelerations to the most efficient cruise speed of 40 m/s, the flight path angle is kept constant. To achieve this, full thrust is again used until the cruise speed is reached. Besides this, the rotational velocity of the cylinders is again decreased to stop the increase in flight path angle and climb at a constant angle. The angle of attack for the cylinder therefore has to be decreased and then kept constant. This means that the rotational velocity is decreased at first as well. As the airspeed increases and the  $\alpha$  has to stay constant, the rotational velocity has to be increased again until the cruise speed is reached. At this point, all parameters can be kept approximately constant. Because of the influence of altitude on the air density, the rotational velocity of the cylinders has to be slightly increased again over time. Also, because of the decrease in drag with altitude, the thrust can be slightly lower.

#### Cruise

During cruise, the aircraft flies at its optimal  $C_L/C_D$ , which is at a fixed  $\alpha$ . Here,  $\alpha$  is again defined as the ratio between the velocity at the surface of the cylinder and the free stream velocity. Level flight can be obtained by increasing the rotational velocity to the optimal and increasing the thrust. Throughout the cruise, the weight of the aircraft decreases which means that in order to keep on flying at this optimal  $C_L/C_D$ , the airspeed has to be decreased. This means the throttle has to be pulled back allowing the aircraft to decelerate. Because the  $\alpha$  has to stay the same, the rotational velocity has to be decreased as well to maintain this optimal cruise flight. This decrease in power for both engines continuous throughout the cruise flight.

#### Descent

During the descent, the airspeed is kept constant. As the desired speed at screen height is 1.3 times the minimum speed, the aircraft has to decelerate slightly at cruise altitude by reducing the thrust. The first part of the descent is unpowered, which means that the throttle is pulled all the way back. The rotational velocity of the cylinder is increased to slightly above the cruise  $\alpha$ , to prevent stalling at the

lower airspeed. The downward descent is then started and because of the flight path angle this  $\alpha$  can be reduced again as can the rotational velocity of the cylinder. When the instrument landing altitude of 3000 ft is reached, the flight path angle has to be reduced to  $3^\circ$ . This means the throttle has to be pushed forward and the thrust has to be increased again. Also, an increment in the rotational velocity is necessary to change the flight path angle of aircraft. As the aircraft once again flies at the desired flight path angle, the rotational velocity can again be continuously decreased due to the increase in air density. This has to be continued until screen height.

## Landing

As soon as screen height is reached, the thrust is reduced again in order to decelerate the aircraft. It cannot be eliminated entirely however, as the flight path angle of  $3^\circ$  has to be maintained. The rotational velocity of the cylinders has to be increased as the aircraft decelerates to keep the aircraft airborne. At touchdown, the thrust is pulled back entirely and the power on the cylinders is turned off. This gradually decreases the rotational velocity of the cylinders, reducing the lift and therefore making the brakes of the landing gear more efficient. The drag is also reduced by slowing down the cylinder. This means that the difference in landing distance with or without active braking of the cylinder is quite similar. When brakes are added, the wheels contribute more to slowing down the aircraft, while without brakes the cylinder drag remains higher slowing the aircraft as well. As this difference is limited, the weight of the brakes makes the addition less efficient and the cylinder is designed without brakes.

## Operational points

The aircraft will be flown fly-by-wire. In case this fails however, the pilot has to be able to determine the rotational velocity the cylinder has to rotate at to continue safe flight. Figure 3.64 shows the relationship between the rotational velocity of the cylinder in level flight at different altitudes. All lines of constant  $\alpha$  go through the origin, of which three are shown. The optimal is at  $\alpha = 2.1$ , a design point which is shown in the figure. The pilot can use this as an aim for the flight without fly-by-wire.

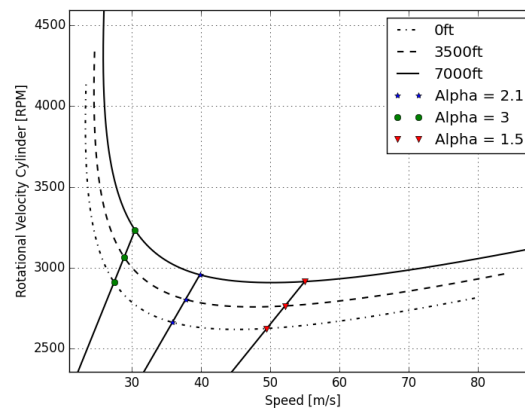


Figure 3.64: Relation between rotational velocity of the cylinder and the airspeed of the aircraft. Lines of constant  $\alpha$  show design point for the aircraft.

## 3.9.5 Logistics

Maintenance is an important aspect of the design because of the unconventional nature of Magnus Aeolus. Spare parts have to be available on a short term, which means the logistics of spare parts is an important consideration. Proper information management ensures knowledge about the actual position of spare parts and the necessity for them at all times. This increases the availability of the aircraft and speeds up the test phase. The second consideration for the logistics is the storage and transport of the aircraft during manufacturing, the test phase and the time in between tasks. A hangar has to be reserved for

this purpose. This hanger will be situated near Rotterdam airport, where the final assembly will also be executed. This is convenient due to the amount of maintenance which has to be performed to the aircraft and for the transport to and from the airport. As the cylinder and the vertical support are detachable, the aircraft fits nose up on a truck for this short distance between the hangar and the airfield.

### 3.9.6 Ground support

The testing phase will require a lot of maintenance. Since the aircraft is quite different from conventional aircraft, the pilot might have some difficulties flying it. This might result in high load factors on the cylinder or canard. Furthermore, take-off and landing is normally the difficult part of flying. As during the test phase these operations are performed a lot, these operations may initiate maintenance or replacement. Also, adjustments following from the collected data might have to be implemented during the maintenance. A number of systems such as the engine, the gearing and the bearings are off the shelf products which have proven their reliability. Moreover, the availability of experienced people who can repair these items is quite high. The complete aircraft will be checked before the actual flight will take place to guarantee the safety of the pilots, as well as in London to ensure a safe flight back home.

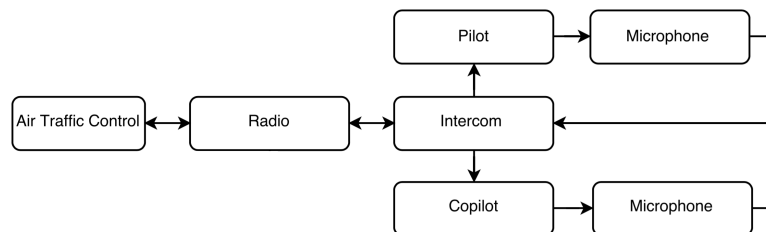


Figure 3.65: Data handling block-diagram of the communication between the pilot, including co-pilot with Air Traffic Control

While flying the pilot also requires ground support, namely from Air Traffic Control (ATC). Permanent communication with ATC has to be available for the pilot. A data handling block diagram of the communication between the pilot, including copilot, and ATC is given in Figure 3.65.

### 3.9.7 Summary operations and logistics

An overview of the operations for the aircraft can be seen in Figure 3.66 as a functional flow diagram. This shows the operations of the aircraft and the sequence of these operations in a summarised matter. These operations are valid both for the flight to Heathrow and for the return to Rotterdam. Similarly, Table 3.29 gives an overview of the pilot operations to be performed in the different flight phases.

Flight Phase	Airspeed	Thrust	Rotation	Cylinders
Take-off Ground	Increased	Full		Constant
Take-off Airborne	Constant	90-100%		Slowly Decreasing
Begin Climb	Increase	Full	Lowered, then	Constant
Steady Climb	Constant	75%		Slowly increasing
Cruise	Decreased	85%		Slowly decreasing
Descent to 3000ft	Constant	No		Slowly Decreasing
Descent from 3000ft	Constant	40%		Slowly Decreasing
Landing Airborne	Decreased	35%		Slowly Increasing
Landing Ground	Decreased	No		Decreasing

Table 3.29: Summary pilot operations during flight

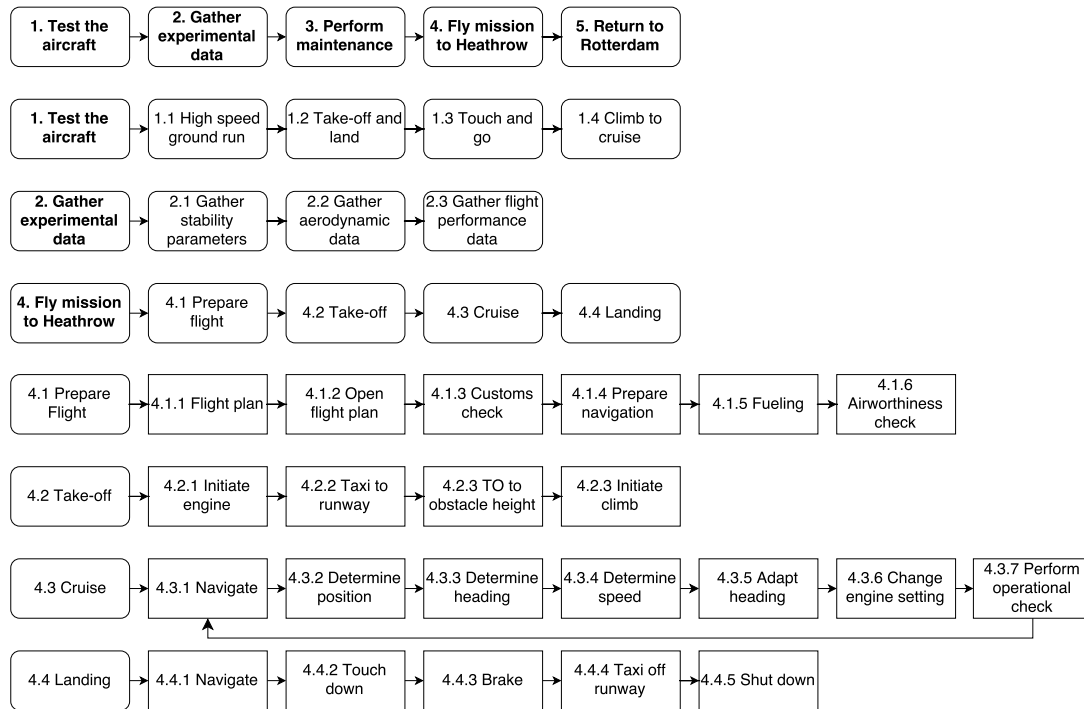


Figure 3.66: Functional flow block diagram giving an overview of operations

### 3.10 Summary Design

The main characteristics of the fuselage subsystem are summarised in Table 3.26 and illustrated in Figure 3.58.

Table 3.30: General characteristics of Magnus Aeolus

General Characteristics				
Passengers	2			
Length	6.2	m	20.3	ft
Height	3.1	m	10.2	ft
Width	5.2	m	17.1	ft
OEW	646	kg	1,424	lb
MTOW	1,030	kg	2,270	lb
Fuel capacity	246	L	65	US gal
Cargo capacity	20	kg	44	lb
Average cruise speed	135	km/h	84	mph
Range	970	km	603	mi
Endurance	7.2	h		
Cruise altitude	2134	m	7,000	ft

Table 3.31: Summary of the most important design parameters of the aircraft

<b>Rotor</b>			<b>Rotor support</b>		
Lift-to-drag	5.60		Vertical support height	1.30	m
span	4.20	m	Vertical support chord	0.84	m
radius	0.27	m	Vertical support airfoil type	NACA 0012	
RPM	3260.00	rpm	Horizontal support span	4.30	m
Engine type	Simonini Mini 2	-	Horizontal support avg chord	1.8	m
Engine power	26.00	bhp	Horizontal support airfoil type	GOE 776	
Mass	62.30	kg	Material type	Aluminium	
Endplate radius	0.68	m	Mass	100.60	kg
Material	Sandwich				
<b>Canard</b>			<b>Vertical tail x2</b>		
Area	1.90	m <sup>2</sup>	Area	1.84	m <sup>2</sup>
airfoil type	NACA 6412	-	Span	1.10	m
Span	3.67	m	chord	0.84	m
Chord	0.52	m	Airfoil type	NACA 0012	
Mass	40.00	-			
<b>Aileron x2</b>			<b>Rudder x2</b>		
Area	0.24	m <sup>2</sup>	Area	0.35	m <sup>2</sup>
Span	0.57	m	Span	0.60	m
chord	0.21	m	chord	0.30	m
Airfoil type	GOE 776		Airfoil type	NACA 0012	
<b>Propulsion</b>			<b>Fuel system</b>		
Duct fan radius	0.40	m	Fuel tank size	260.00	L
Fan engine type	Mistral G200	-	Fuel management system	Auto FADEC	
Inlet area	2.45	m <sup>2</sup>	Fuel type	Gasoline 95	
Max power	200.00	bhp	Mass	30.00	kg
Fuel consumption	39.00	L/h			
Battery type	2x AV016	-			
Mass	216.80				
<b>Fuselage</b>			<b>Landing gear</b>		
Max. radius	0.83	m	Wheel track	3.42	m
Length	5.72	m	Max rating	6g	
Material type	Sandwich		Configuration	Tricycle	
Number of seats	2.00		Landing gear height	1.05	m
Mass	58.60	kg	Mass	80.50	kg

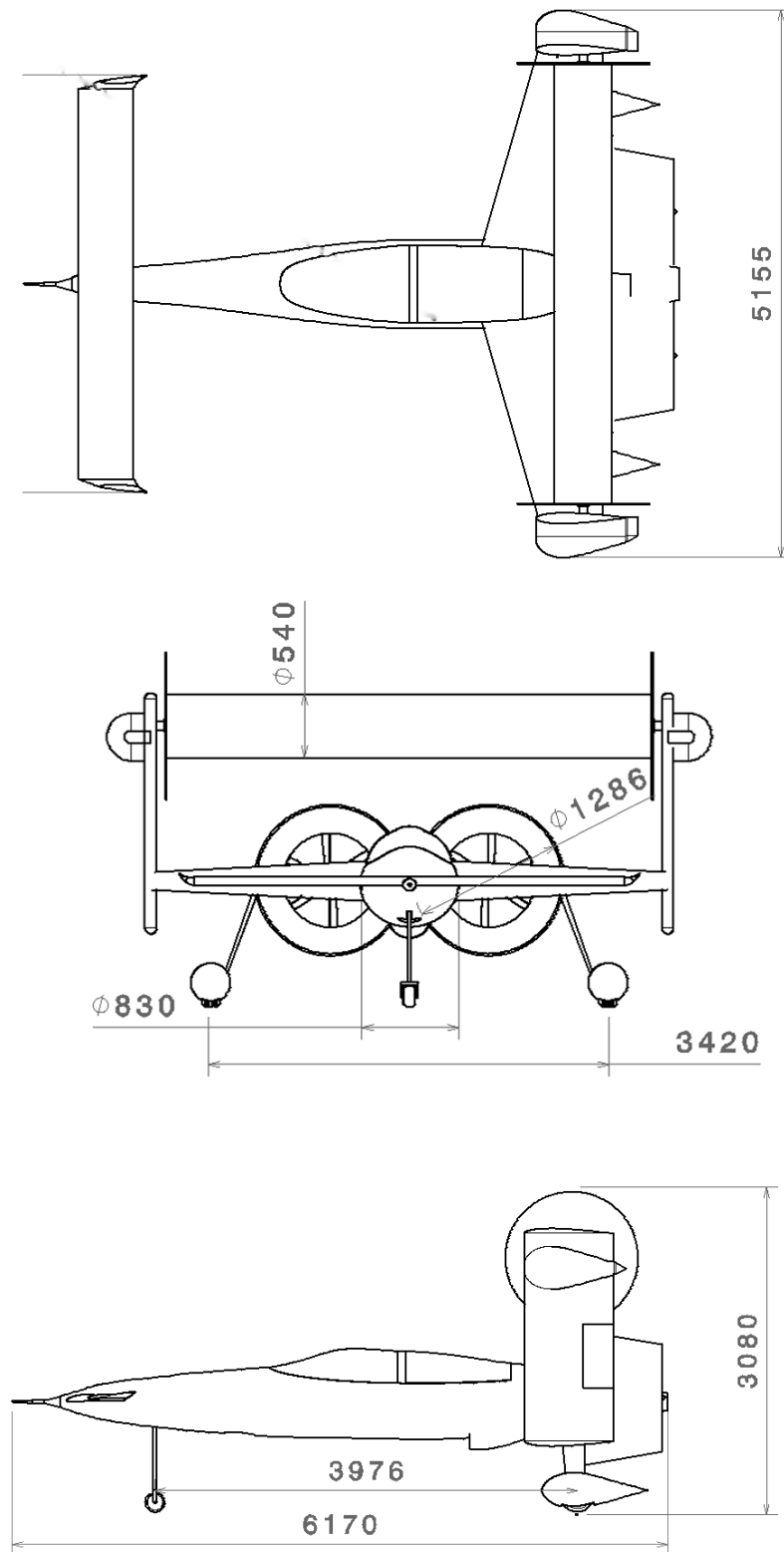


Figure 3.67: 3-view of the complete design of the Magnus Aeolus

---

## Chapter 4

# Design Performance

After having designed the aircraft, the performance of the design can be determined. First of all, the flight performance is analysed, including the mission operations, flight envelope, turn performance and noise and emissions characteristics. Next the flight dynamics of the aircraft are shown. The approach for the sustainability is the next step in determining the performance of the design. Also, the sensitivity of the design, thus the influence of small changes to the properties is evaluated. Then, the reliability, availability, maintainability and safety characteristics are given. The risks and the mitigation of the highest risks is then shown. Finally, the compliance of the design to the requirements set is presented as well as the market analysis, concluding the performance analysis for this design.

### 4.1 Flight Performance Analysis

With the final design and the operations determined, the performance of the aircraft can be analysed. This indicates the properties of the aircraft and the behaviour of the design. First, the consecutive elements of the flight will be discussed. These are the take-off, the climb, the cruise, the descent and the landing. For this analysis, a model was produced which is verified later on in the section. After this, the flight envelope and the turn performance will be considered. The section ends with the noise and emission characteristics.

#### 4.1.1 Take-off performance

The take-off consists of two phases, the ground phase and the airborne phase. The ground phase comprises the distance needed to accelerate until lift-off; the airborne phase comprises the distance to climb to screen height (i.e. 50 ft).

##### Ground run

The take-off speed is set at 1.3 times the minimum speed. For this aircraft at MTOW, the minimum speed is 25 m/s, limited by the cylinder performance. Conventionally, a speed of 1.1 times the stall speed is used[3]. For this aircraft, the  $C_L$  needed for lift off and thus the  $C_D$  generated decrease significantly with increasing airspeed. Therefore, using a higher lift-off speed is more efficient in terms of drag and thus acceleration. This lift-off speed was therefore optimised for minimum total take-off distance, resulting in the take-off speed of 31 m/s, or 1.3 times the minimum speed. For the ground phase, the maximum acceleration is used for the entire ground roll to minimize the take-off distance. This acceleration depends on the excess thrust, which is the thrust with the total drag subtracted. This results in a ground distance of 272m. The cylinder will be spun up before the take-off starts. The reason for this procedure is that spinning up the cylinder until the rotational speed necessary for take-off takes longer than the ground run of the take-off. This means it is better for the take-off distance to spin up the cylinder beforehand. Thereafter all excess power can be fully used to accelerate the aircraft itself.

##### Airborne

For the airborne phase of the take-off, the aircraft has to climb to 50 ft. The thrust, drag and lift determine the optimal flight path for the aircraft to follow. The minimum airborne take-off distance can then be determined by computing this flight path, using [3]. The take-off ends at a flight path angle

of 5° and after 232 m. The total take-off distance therefore is 501m. Figure 4.1 gives an overview of the take-off path of the aircraft at MTOW at Rotterdam-The Hague airport (RTM) and at half the fuel weight at London-Heathrow (LHR) .

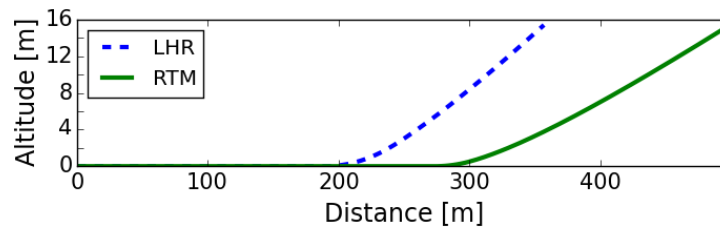


Figure 4.1: Take-off diagram for the final design, both at MTOW (RTM) and half the fuel (LHR).

### Return to Rotterdam

As discussed in subsection 3.9.3, the aircraft is able to return to Rotterdam after landing in Heathrow. For these conditions the same parameters can be determined, considering that about half the fuel has been used. The minimum speed of the aircraft is now lower, as is the weight of the aircraft because of the reduction in fuel. This results in a shorter ground run of 188 m, a higher final flight path angle of 7° and thus a lower airborne take-off distance of 168 m. This results in a final take-off distance of 356 m.

Parameters	Ground RTM	Airborne RTM	Ground LHR	Airborne LHR
Distance [m]	272	232	188	168
Start speed [m/s]	0	31	0	29
Final speed [m/s]	31	31	29	29
Flight path angle [°]	-	5	-	7

Table 4.1: Summary take-off performance characteristics where RTM is at MTOW and LHR is at half the fuel weight

### 4.1.2 Flight profile

The flight profile diagram gives an overview of the flight path of the aircraft while performing the mission. It illustrates the climb, the cruise and the descent distance, as well as the cruise altitude. Figure 4.2 gives an overview of this flight profile for the mission especially. The actual range is longer than the mission range, as will be explained later on in this section. Throughout the flight profile, the angle of attack of the aircraft is assumed to stay at 0°, meaning the aircraft is aligned with the flight path angle at all times. The reason for this is that the cylinder does not need a conventional angle of attack and this decreases the drag of both the body and the support of the cylinder. The flight profile first shows the flight to London and then the flight back to Rotterdam. Both flights will be discussed in this section

#### Climb performance

The climb starts with the flight conditions at the end of take-off. It begins by accelerating to the cruise speed of 40 m/s as fast as possible, continuing the flight path angle of the airborne phase of the take-off. The reason is that the aircraft can then fly at its optimal  $C_L/C_D$ , at its cruise speed of 40 m/s. After the cruise speed has been reached, the thrust is decreased to climb steady until cruise altitude. The climb takes 24.7 km ground distance and 10 minutes to reach cruise altitude. The full consumption at a power setting of 75% is approximately 41 litres per hour. For the climb, the power setting is a 100 percent, thus assumed is an increase of 33% during this phase. After this phase 7 kg of fuel is burnt.

During the flight back to Rotterdam, the weight of the aircraft is less than the MTOW. The conditions while returning to Rotterdam from Heathrow are thus different, as is the cruise speed at which the

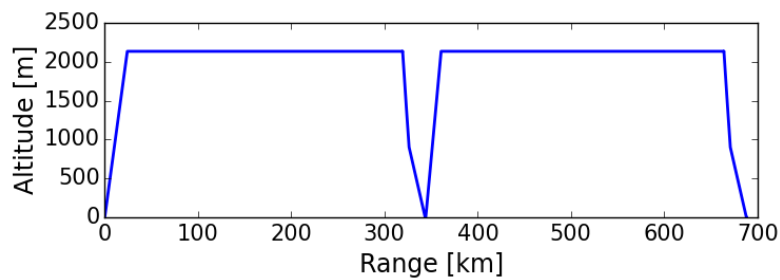


Figure 4.2: Flight profile diagram mission from RTM to LHR and back from LHR to RTM

aircraft flies most efficient. The flight speed is now up to 37 m/s, which is the optimal cruise speed for this aircraft weight. The climb takes approximately 16.5 km and 7 minutes with these climb conditions.

### Cruise analysis

The cruise begins with a mass of about 1030 kg and a cruise speed of 40 m/s. The  $\alpha$  used for the cruise phase of the flight is 2.1, meaning the  $C_L/C_D$  is maximum. As fuel is burnt, the speed at which the aircraft flies at this optimum  $\alpha$  decreases and therefore the cruise speed decreases over time. This gives an end of cruise speed of 37.5 m/s instead of the initial 40 m/s, as half the total range of the aircraft is used to fly to Heathrow. From Heathrow to Rotterdam, at first a cruise speed of 37.5 m/s is used, which is decreased to 35 m/s. The total cruise range is calculated using the fuel for cruise, the airspeed and the fuel consumption. With 7 kg of fuel used for climb, 1.5 kg needed for descent, the fuel available for cruise is 201 kg. With an average power setting of 68% the fuel consumption is 28 kg per hour as described in subsection 3.7.3. This allows Magnus Aeolus to fly 7.2 hours at an average speed of 37.5 m/s. The maximum cruise range is then 976 km. However this is without loiter taken into account. When having a loiter time of 30 minutes, the remaining range is 905 km. As the range is more than 640 km, the aircraft can perform the mission on even surpass it by returning to Rotterdam.

### Descent performance

For the descent, no power will be used at first. To be able to adhere to the procedures at Heathrow, discussed in subsection 3.9.2, the end of the descent will use power. The unpowered descent starts at an airspeed of 1.3 times the minimum speed, which is the standard procedure. The minimum speed is restrained by the minimum speed at which the canard is still able to control the aircraft, which is about 26 m/s when half the fuel has been burnt. The aircraft therefore has to decelerate slightly at the end of cruise before the descent begins. This airspeed is assumed to be kept constant throughout the descent as that is a conventional and easy procedure for the pilot to follow. The descent angle for this unpowered descent is about  $11.7^\circ$ . After an altitude of 3000 ft has been reached, the descent angle is decreased to  $3^\circ$  because of the rules for landing at Heathrow. This means thrust has to be used to maintain the descent angle and the desired airspeed. A total distance of 23.3 km is covered during the descent towards Heathrow. At 40% of thrust and a speed of 33 m/s the power setting is only 10% of full power. This powered descent takes 12 minutes and the fuel consumed in that stage is less than 1.5 kg.

For the descent to Rotterdam, the same procedure is used. The only difference is the weight of the aircraft. At operational empty weight, the minimum speed is 28 m/s at which the canard can still operate properly. This is higher because of the backwards shift in the c.g., meaning the canard has to overcome a bigger moment. The distance covered during the descent is again about 23.8 km with an angle of  $10.5^\circ$  at the beginning and again  $3^\circ$  at the end.

Besides considering descending at the end of flight, the descent performance at MTOW also has to be analysed. In case of engine failure for example, the aircraft still has to be able to descend safely. The aircraft has a lower stall speed at MTOW of 25 m/s because of the convenient location of the c.g., which results in a descending airspeed of 33m/s and a gliding distance of 12 km. Note that for this descent

and entire unpowered descent is assumed because there are no airfield restrictions and thrust may not be available. The average descent angle now is  $10.5^\circ$  covering a total distance of about 11.5 km.

Parameters	LHR descent	RTM descent	MTOW descent
Descent distance [km]	24	24	12
Descent speed [m/s]	33	38	33
Average descent angle [°]	5.2	5.1	10.5

Table 4.2: Summary descent performance, where LHR is partially powered at half fuel weight, RTM is partially powered at empty weight and MTOW is unpowered descent

### 4.1.3 Landing performance

There are three scenarios for the landing which are analysed separately. First of all, the landing performance at the two airports is analysed. A powered landing with part of, or all of the fuel burnt is considered. Secondly, the landing performance of the aircraft at the MTOW in case of an emergency is analysed. Finally, the minimum empty unpowered take-off distance is computed to show the performance of the aircraft. At the end of the section an overview of the landing performance is given.

#### Landing at the airfields

At Heathrow, the angle of  $3^\circ$  is kept during landing. This means power is needed to be able to perform the landing. The speed is kept above the minimum airspeed for the canard to function, which is 26 m/s. The airborne and ground landing distances are then 292 m and 113 m respectively, resulting in a total landing distance of 403 m. The touch-down speed is 26 m/s, of which the vertical contribution is 1.4 m/s which is reasonable considering the load the landing gear then has to withstand. The flight path of the aircraft is shown in Figure 4.3.

The same landing is assumed at Rotterdam, at an angle of  $3^\circ$ . This means again power is needed to be able to perform the landing. The speed is kept above the minimum airspeed for the canard to function, which is 28m/s at empty weight. The airborne and ground landing distances are then respectively 291 m and 148 m respectively, resulting in a total landing distance of 439 m. For these circumstances, the vertical contribution is 1.5 m/s.

#### Landing outside regulations

In case of an engine failure or another emergency, the aircraft has to be able to land at its maximum take-off weight since there is no fuel dispenser. The minimum speed for the canard is then 25 m/s, because of the more favorable location of the c.g. when the fuel is still present.

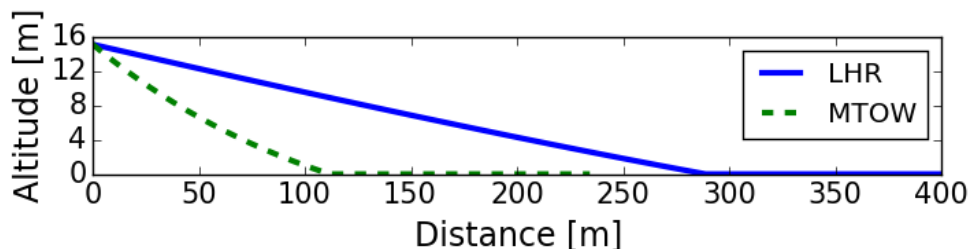


Figure 4.3: Powered landing diagram for the final design at London-Heathrow (half the fuel) and unpowered descent at MTOW.

The descent will be done at a constant speed at the maximum  $C_L/C_D$ , which is 40 m/s. This means the speed at the screen height will be 40 m/s as well, at an angle of  $11^\circ$ . The flight path angle can

be decreased up to  $5.6^\circ$  at touch down while keeping the speed above the 25 m/s for the canard. This results in an airborne landing distance of 112m. With the touch down speed of 28 m/s, it takes 129m to decelerate the aircraft assuming the cylinder can still be braked as fast as for normal landing procedures. The total landing distance is thus 241m and is visualized in Figure 4.3.

A minimum unpowered landing distance can also be obtained for aircraft with all of the fuel burnt. This is very similar to the landing at MTOW and illustrates the actual minimum unpowered landing distance the aircraft can achieve on a regular basis, meaning the vertical velocity does not exceed the maximum set by the landing gear. The results for this landing are show in Table 4.3.

Parameters	LHR landing	RTM landing	MTOW landing	Empty landing
Airborne distance [m]	292	291	112	108
Ground distance [m]	113	148	129	128
Start speed [m/s]	33	34	40	36
Touch-down speed [m/s]	26	28	28	27
Average thrust (air) [N]	1065	933	0	0
Touch-down angle [ $^\circ$ ]	3	3	5.6	5.9

Table 4.3: Summary landing performance characteristics, where LHR is powered landing at half the fuel weight, RTM is powered landing at empty weight and MTOW and empty are both unpowered

#### 4.1.4 Verification flight trajectory performance

The verification of the flight performance ensures that the aircraft is able to perform the mission and the operations. The verification can be split in the different phases of the mission: take-off, climb, descent and landing. First of all, the code itself was checked for mistakes and singularities using unit testing. The verification of the models as a whole will be done using an analytical computation. The analytical method uses average values for the flight from Rotterdam to Heathrow and these are compared to the computed values by the model.

For the take-off, the ground phase is first verified by computing the average acceleration that can be achieved and the desired take-off speed. This results in a take-off distance which is similar to the one from the model. All of the results of the verification can be found in Table 4.4.

Phase	Parameters	Model	Analytical	Difference [%]
Take-off	Ground distance [m]	272	288	5.6
	Airborne distance [m]	232	236	2.1
Climb	Acceleration distance [m]	1041	1135	8
	Distance [km]	24	24	-
	Final flight path angle [ $^\circ$ ]	4.7	4.8	2
Descent	Start flight path angle [ $^\circ$ ]	11.7	11.7	-
	3000ft flight path angle [ $^\circ$ ]	11.0	10.9	1
	Thrust start $3^\circ$ [N]	1140	1132	1
	Thrust end $3^\circ$ [N]	1082	1080	-
	Total distance [km]	23	23	-
Landing	Airborne distance [m]	292	290	1
	Ground distance [m]	113	114	1

Table 4.4: Verification of the performance model with the analytical approximation

For each of the models, one or two important parameters are compared in this table to illustrate the similarities. For the airborne phase, the maximum flight path angle and the average flight path angle are analytically determined resulting in the distance for the take-off airborne phase. For the climb, the acceleration is again approached using the average speed, acceleration, thrust and drag resulting in

the distance. The climb following this acceleration can be checked by computing the distance and the maximum flight path angle at the end of the climb the aircraft can fly at. For the descent, the flight path angle the aircraft needs for unpowered descent at cruise altitude and 3000 ft is computed. Then the powered descent is verified using the power the aircraft needs to follow the predetermined flight path angle. The total distance of the descent is also computed using average flight path angles as a extra verification. Finally, the distances for the landing are computed using the flight path angle of the aircraft and the average deceleration. Table 4.4 also shows the difference of the model with respect to the analytical approximation, indicating the performance can be verified. As all differences are less than 10%, the models can be verified.

#### 4.1.5 Flight envelope

The V-n diagram or flight envelope depicts the performance limits of the aircraft in terms of the maximum load that can be attained/sustained at each velocity for a certain weight and altitude. The “common-practice“ methodology was borrowed by [42] and modified to fit the particularities of this project. Flight envelopes as well as a turn performance analysis (see next section) were presented, using the same methodology, in the midterm report [5], but are now updated for the new design.

A flight envelope normally consists of two curves: one positive for regular flight and one negative for a situation when the aircraft is inverted. Those curves are normally bounded by a set of “constraints“. Up until a certain velocity, the maximum load factors is determined by aerodynamics-namely the maximum lift coefficient that the lifting surfaces can provide. This part of the flight envelope is represented by the (2nd order) polynomial curves and is described by Equation 4.1. From a certain velocity onwards, the load factor that could potentially be attained by aerodynamics, cannot be sustained by the aircraft structure. In the envelope, this translates into horizontal lines at the maximum (structural) load factor. Finally, the part of the graph that is relevant for operations is bounded by two vertical lines: one at the minimum (i.e. stall) velocity and one at maximum velocity.

$$n_{max} = \frac{\rho S C_{L,max} V^2}{2W} \quad (4.1)$$

Figures 4.4, 4.5 and 4.6, present the flight envelopes at take-off, cruise and landing conditions respectively (they also include the gust diagrams, which will be explained at a later stage in the section). A consideration that significantly affects the way those graphs look like, is the power required. At take-off and landing, when the aircraft flies at sea level, dynamic energy cannot be exchanged for kinetic (i.e. the aircraft cannot “lose“ altitude to gain velocity). This means that the load factors that can be attained, are only those that can be sustained by the power available. The load factor at each velocity above the one at which the power required to fly at maximum lift coefficient is equal to the power available, is calculated as follows:

- The power required is equal to the maximum power available.
- At each velocity the maximum drag coefficient that can be sustained is calculated.
- Using interpolation between  $C_L$  and  $C_D$  from the aerodynamic data used in the design, the corresponding lift coefficient is found (approximated).
- This lift coefficient is used to replace  $C_{L,max}$  in Equation 4.1.

It should be noted that, due to the combination of power available and maximum velocity, the maximum sustainable (structural) load factor of +3.8 is never reached in operation, whereas the -1.5 for inverted flight can only be reached at high velocities at cruise and landing. The kink present in all graphs is caused by the change from the curve being driven by only velocity, to velocity and power available, in combination with the (finite) velocity step in the calculations.

The results for the maximum load factor as well as the corresponding velocity and several turn performance parameters are summarized in Table 4.5.

The gust envelope illustrates the loading the aircraft undergoes when a gust is introduced. The gust envelope can be found using Equation 4.2 [42]. Here,  $k_g$  can be found using Equation 4.3 [42] and  $\mu_g$  using Equation 4.4 [42]. The maximum vertical gust speed used is around 20 m/s. When the loading due to the gusts is higher than the one that could be obtained intentionally, it prevails in determining the boundaries of the flight envelope. The gust envelope was determined for take-off in Figure 4.4, for cruise in Figure 4.5 and for landing in Figure 4.6.

$$n = 1 + \frac{k_g V_g V a \rho S_{ref}}{2W} \quad (4.2)$$

$$k_g = \frac{0.88 \mu_g}{5.3 + \mu_g} \quad (4.3)$$

$$\mu_g = \frac{2W}{9.81 \rho \bar{c} a S_{ref}} \quad (4.4)$$

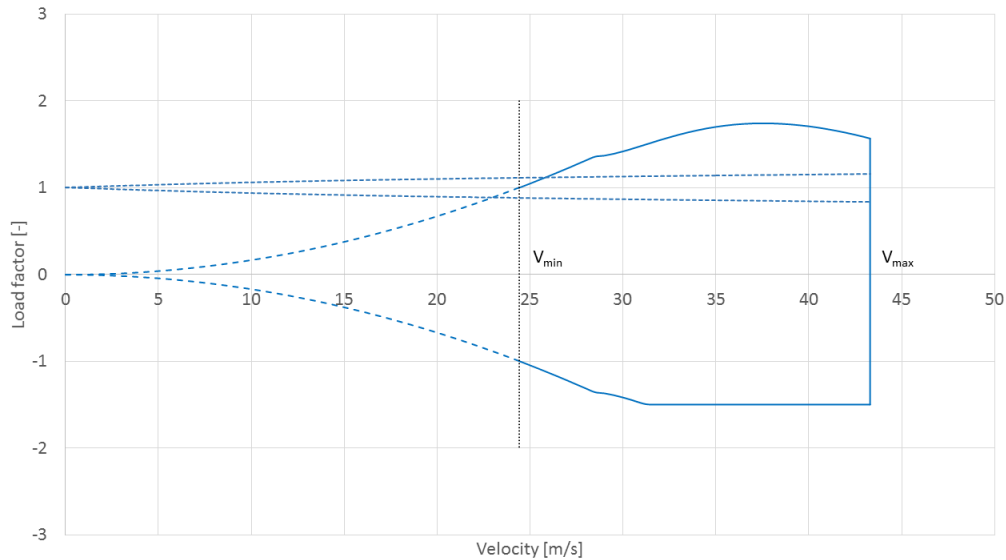


Figure 4.4: The flight envelope at take-off conditions (load factor vs. velocity) for the designed aircraft (the limits are indicated by the solid lines)

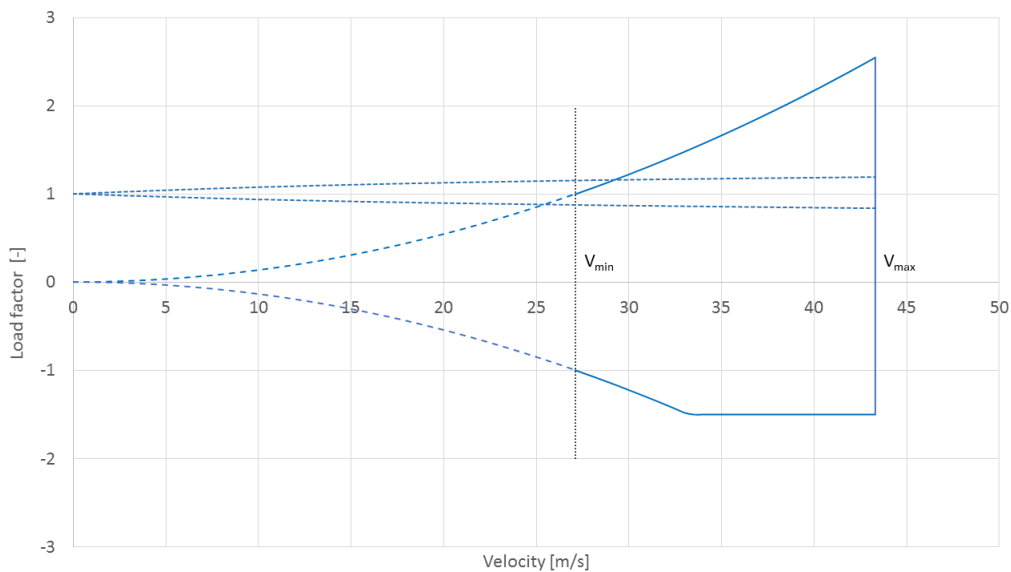


Figure 4.5: The flight envelope at cruise conditions (load factor vs. velocity) for the designed aircraft (the limits are indicated by the solid lines)

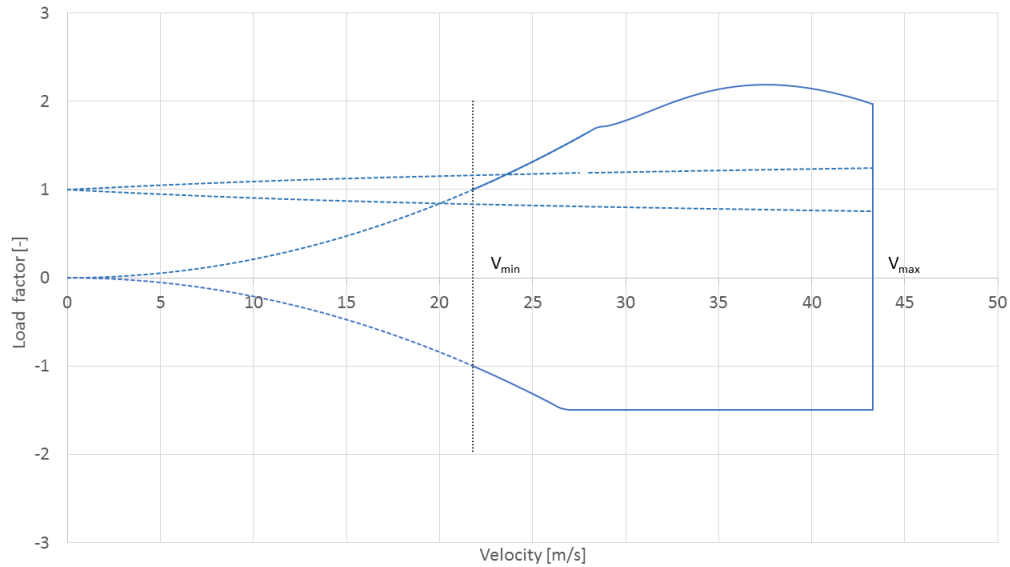


Figure 4.6: The flight envelope at landing conditions (load factor vs. velocity) for the designed aircraft (the limits are indicated by the solid lines)

#### 4.1.6 Turn performance

The turn performance for the aircraft is investigated at each velocity for the flight and aircraft conditions at take-off, cruise and landing. The same assumptions as made for the flight envelope(s) are also made here (e.g. power available is driving after a certain velocity at take-off and landing).

The turn performance is here described using the following parameters:

- Maximum load factor and corresponding:
  - Maximum bank angle (so that the aircraft stays level)
  - Turn radius
  - Airspeed
  - Turn period (time to complete 360 deg. turn)
- Minimum Radius and corresponding:
  - Load factor
  - Airspeed
  - Turn period

Equations 4.5, 4.6, 4.7 give the radius, period and bank angle of the turns [53].

$$R = \frac{V^2}{g\sqrt{n^2 - 1}} \quad (4.5)$$

$$T = \frac{2\pi R}{V} \quad (4.6)$$

$$\phi = \arccos \frac{1}{n} \quad (4.7)$$

The results of the turning performance investigation are summarized in Table 4.5 - Table 4.6, including additional parameters for power required,  $C_L$  required and corresponding velocity ratio.

Table 4.5: Turning performance characteristics at maximum load factor

Phase	Take-off	Cruise	Landing	Units
$n_{max}$	1.74	2.55	2.18	[-]
$R_{nmax}$	100.5	81.6	73.6	m
$\phi_{max}$	55.0	66.9	62.8	deg.
$V_{nmax}$	37.5	43.3	37.5	m/s
$T_{nmax}$	16.8	11.8	12.5	s
$P_{nmax}$	143	143	143	kW
$\alpha_{nmax}$	3	4.3	3.3	[-]
$C_{L,nmax}$	8.9	3.56	4.93	[-]

Table 4.6: Turning performance characteristics at minimum radius

Phase	Take-off	Cruise	Landing	Units
$n_{Rmin}$	1.66	2.55	2.08	[-]
$R_{min}$	76.14	81.6	61.2	m
$\phi_{Rmin}$	53.0	66.9	61.2	deg.
$V_{Rmin}$	31.5	43.3	31.5	m/s
$T_{Rmin}$	15.2	11.8	11.1	s
$P_{Rmin}$	143	143	143	kW
$\alpha_{Rmin}$	3.7	5	3.7	[-]
$C_{L,Rmin}$	10.9	12	10.9	[-]

Finally, Figures 4.7 and 4.8 present the turn radius and load factor versus velocity respectively, for take-off, cruise and landing conditions. The presence of kinks signifies that the power available becomes the driving force for the behaviour (instead of the maximum lift coefficient) and is a consequence of the finite (velocity) step in the calculations. The trends of the presented graphs were verified against the ones expected from theory discussed in [54].

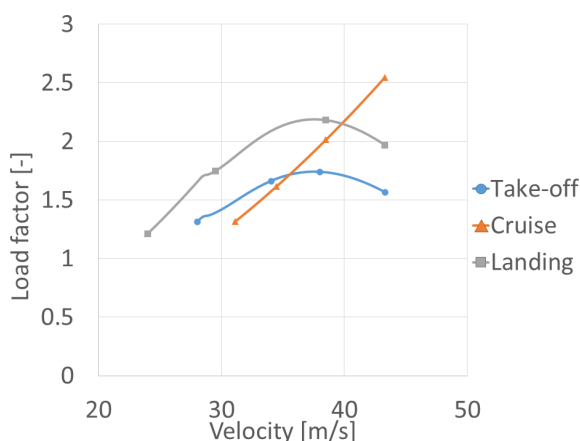
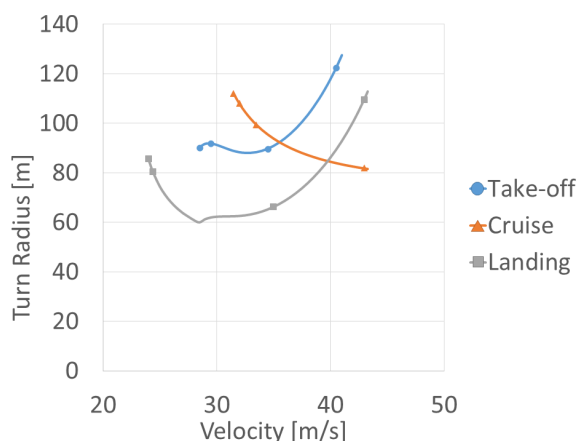


Figure 4.7: Turn radius versus velocity at take-off, cruise and landing conditions

Figure 4.8: Load factor versus velocity at take-off, cruise and landing conditions

#### 4.1.7 Noise characteristics

The noise characteristics is an important consideration for aircraft design. First, the noise sources are identified, after which the quantification of the noise can be performed. At the end of the subsection, mitigation possibilities for the noise are presented.

##### Noise source identification

Different sources of noise generation in the aircraft system are identified below.

- **Turbulence:** Noise is caused by pressure fluctuations. The turbulence caused in the wake of the cylinder, the landing gear, the ducted fan and the supporting wing will be the main contributions to the noise caused by turbulent flow [55].
- **Vibrations:** The rotor is supported by self-aligning bearings and is thus not clamped at the sides, but pinned. This can cause a vibration at a high-frequency. This frequency will be in the range of the high-frequency audible range using the natural frequency of the cylinder. The supporting

---

wing structure below the cylinder also can go into a vibration mode which could generate noise. Its frequency is expected to be in the range of the rotational speed of the rotor. The contribution of the vibration of the wing is assumed to be negligible. The following potential sources of mechanical noise can also be identified: excessive bearing clearance, non-round bearings, rotor unbalance, rotor eccentricity, crooked shafts, misalignment and loose laminations [56].

- **Engine noise:** The main IC-engine and the IC-engines at the sides of the rotating cylinder will contribute to the noise generated. Two noise sources are identified for these IC-engines, namely combustion and exhaust noise.

In order to perform mentioned maneuvers, the control surfaces need to deflect appropriately. The developed flight model will be used to determine the required control surfaces adjustments such that these maneuvers can be performed.

### Noise level quantification

According to Lighthill [57], the noise (sound power) generated by the turbulence in the wake of a (non-rotating) cylinder in a low-mach number flow scales as given in Equation 4.8.

$$W \propto \frac{\rho_0 \cdot V^8 \cdot D^2}{c_0^5} \quad (4.8)$$

This means that, for every doubling of the velocity, the noise increases by 24 dB. Thus, when flying at 40 m/s at sea level, the noise due to the turbulence in the wake of the cylinder is about 120 dB.

As explained in subsection 3.3.4, the engine noise itself is not quantified. It should be noted, however, that a reference aircraft is given, which uses the same engine. A sound level test was executed in the Netherlands and the aircraft passed this.

### Mitigation measures

Limiting noise is a core element of sustainable design. There are several mitigation measures to be taken in order to reduce the noise levels. The mitigation measures can be categorized in the same groups as the noise sources; namely measures to reduce noise due to: turbulence, vibrations and the engines.

Reducing vibrational noise requires mitigating the dynamic response of the structure and especially the cylinder. To achieve this, tuned-mass damper systems could be implemented inside the cylinder [58], thereby reducing vibrations during operation.

Regarding the other two categories, the following solutions are/can be implemented:

#### *Turbulence:*

- A duct will be used to “host” the fans. In this way, tip vortices are reduced and the flow is streamlined before and after the fan.
- The duct also acts like a nacelle, containing the noise. Potential implementation of additional noise abatement mechanisms, such as acoustic liners or (virtual) chevrons, would reduce the noise even further [59].
- The addition of “wheelpants” covering the landing gear will reduce the turbulence (and thus the noise) caused by the wheels.
- The riblets contained in the sharkskin paint used on the fuselage subsection 3.5.2, will reduce the turbulent vortices (and thus the noise due to the turbulence).

#### *Engines:*

- The engines will be shielded to contain both the heat and the noise.

- Mufflers could be used to mitigate the noise cause by the exhaust [60]. This could be combined with the use of multiple exhaust pipes.
- Helmholtz resonators could be used to reduce the (acoustic vibration) noise caused at the engine intake [61].

#### 4.1.8 Emission characteristics

The characteristics of the system related to emissions are subdivided into pollutant emissions and carbon dioxides. Mainly the gasoline IC-engines are considered, but electric motors are also shortly considered.

##### Pollutant Emissions by Spark-Ignition (SI) engines

An internal combustion (IC) engine using gasoline is used as the energy converter to propel the aircraft forward. Gasoline IC-engines burn fuel at an equivalent air-to-fuel ratio around  $\lambda = 1$ , which is a stoichiometric combustion. In the ideal case the fuel (gasoline is mostly modeled by olefin 1-octene  $C_8H_{16}$  [62]) is converted into only  $CO_2$  and  $H_2O$ . However due to fluctuations in air-to-fuel ratio, non-ideal premixing of the fuel and air and non-ideal combustion processes inside the cylinder incomplete combustion takes place [63]. This causes additional reaction product of the combustion. For gasoline spark-ignition engines (SI) these additional products are mainly unburned hydrocarbons (HC), nitrogen oxides ( $NO_x$ ) and carbon monoxides (CO). During combustion the unburned HC are mainly produced at the cylinder walls where the temperature is significantly lower, meaning that combustion of the fuel at these locations is not possible since the fuel cannot ignite at these lower temperatures. At these locations the fuel is absorbed by the oil film covering the cylinder walls. When the pressure in the cylinder decreases, these particles are released into the cylinder.  $NO_x$  gases (mainly NO but also some  $NO_2$ ) are formed during the very high temperature phases during combustion [39].

The equivalent air-to-fuel ratio characterises the operation of the SI-engine. The amount of the three aforementioned pollutant emissions at a certain  $\lambda$  for SI-engines is plotted in Figure 4.9. Note that these values are the ‘engine-out’ emissions, without any exhaust gas after-treatment systems.

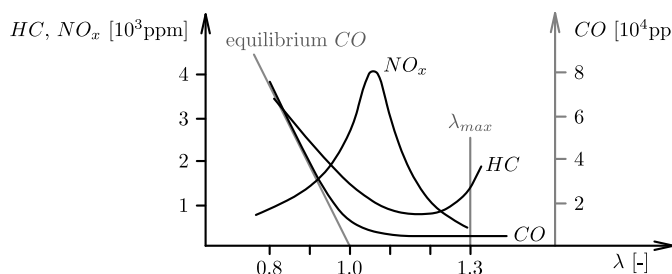


Figure 4.9: Engine-out pollutant emissions for a port-fuel injected SI engine. Note in the graph  $\lambda_{max}$ , the lean limit at which misfires start for the SI-engine [39].

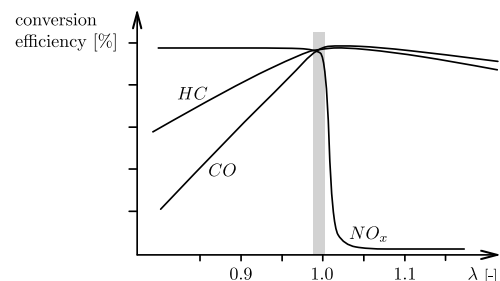


Figure 4.10: Conversion efficiency of a three-way catalytic converter (TWC) as a function of air-to-fuel ratio  $\lambda$  [39]

A special comment has to be made to the type of SI-engines used in the aircraft. The aircraft is propeller using a 2 stroke Wankel-engine provided by Mistral and the cylinder is rotated using a single piston 2 stroke Simonini engine. A considerable amount of lubrication oil has to be used in the engines decrease friction and so have smoother running of e.g. the piston inside the cylinder. Oil is premixed with the fuel to account for this lubrication. This means that oil is present in the combustion charge. At high cylinder temperatures, occurring at high rotation speeds of the engines, most of this oil is combusted. However, at low cylinder temperatures this oil is not combusted causing deposit of oil on the cylinder walls and on the spark plug. This gives rise to e.g. different compression ratios and deviations from the optimal spark timing. It will certainly also influence the engine-out emissions, namely more unburnt hydrocarbons will be emitted. It also has to be noted that during operation these engines will mostly rotate at high rotational speeds reducing these risks.

L. Guzzella and C.H. Onder state that: "... Since 1980, the permitted levels for the concentrations of carbon monoxide (CO), hydrocarbons (HC) and NO<sub>x</sub> (NO, NO<sub>2</sub>) have been reduced significantly. A continuation of this trend is to be expected..." [39]. The European regulations for the emissions of SI engines are listed in Table 4.7. These regulations are difficult to meet by just looking at the 'engine-out' emissions. Therefore exhaust gas after-treatment systems have to be applied to be able to meet the regulations.

Table 4.7: European regulations for emissions of SI-engines. Note that the values <sup>(i)</sup> are only applicable to vehicles using gasoline direct injection [39]. Carbon monoxide (CO), unburnt hydrocarbons (HC), Nitrous Oxides (NO) and Particulate Matter (PM).

Tier		Euro I	Euro II	Euro III	Euro IV	Euro V	Euro VI
Date		1992	1996	2000	2005	2009	2014
CO	[g/km]	2.72	2.2	2.3	1.0	1.0	1.0
HC	[g/km]			0.2	0.1	0.1	0.1
NO <sub>x</sub>	[g/km]			0.15	0.08	0.06	0.06
HC + NO <sub>x</sub>	[g/km]	0.97	0.5				
PM	[g/km]					0.005 <sup>(i)</sup>	0.005 <sup>(i)</sup>

### Carbon dioxide emissions

The carbon dioxide emissions of gasoline IC engine are compared with respect to Diesel and natural gas (CNG) in Figure 4.11. Note that the values are used to compare the individual energy sources and that the energy use (50 MJ/100 km) of a conventional personal vehicle is used as an illustrative example. One can see that the CO<sub>2</sub> emissions of gasoline are about 20-25 % higher compared to the others. One also has to consider the fact that the TWC, as described previously in Equation 4.9, decreases the poisonous emissions at the expense of emitting more CO<sub>2</sub>. Decreasing the CO<sub>2</sub> emissions of the gasoline SI-engines is only possible by decreasing their fuel consumption. A solution to decrease fuel consumption, namely by using a regenerative braking system, is proposed in paragraph 4.3.1.

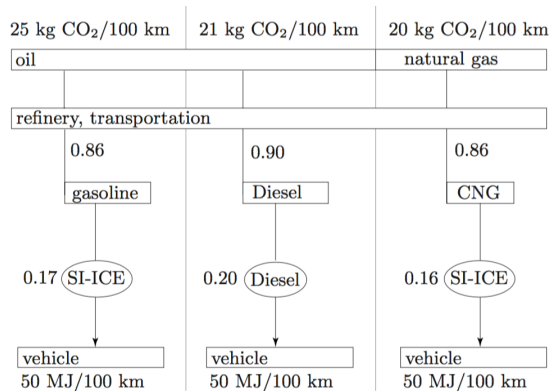


Figure 4.11: "Well-to-miles" CO<sub>2</sub> emission of a conventional gasoline (left), diesel (mid) and CNG (right) powertrain.[28].

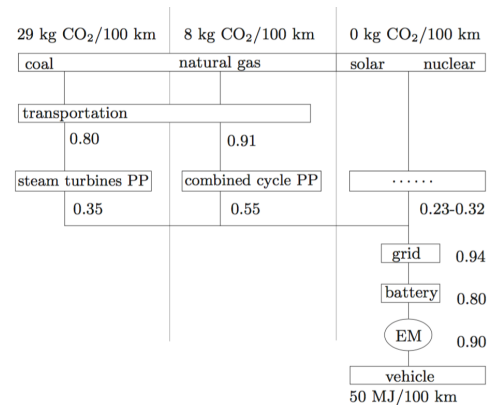


Figure 4.12: "Well-to-miles" CO<sub>2</sub> emissions of a battery electric vehicle [28].

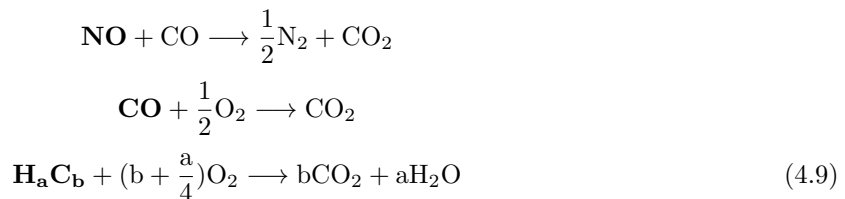
For the energy source of electricity, stored in the battery and used by the electric motors, one has to be careful regarding emissions. Consuming electricity on its own does not emit pollutants such as CO<sub>2</sub>. However, here it is important to consider the upstream process, namely how the electricity was generated. In Figure 4.12 one can see the comparison between different upstream processes to generate electricity. Note that the values are used to compare the individual processes and also that here the energy use (50 MJ/100 km) of a conventional personal vehicle is used as an illustrative example. Producing electricity from coal powerplants (PP) can thus be more polluting compared to just running a gasoline IC-engine.

When using solar or nuclear energy sources, the CO<sub>2</sub> emissions are obviously zero. However, nuclear waste has to be considered for nuclear energy as pollutant [28].

An estimate of the CO<sub>2</sub> emission can be made by looking at the fuel consumption of the two gasoline IC-engines installed in the aircraft. As already discussed, at a power level of 75 % the Mistral engine has a fuel consumption of 39 l/h; the Simonini engine rotating the cylinder has an average fuel consumption of 2.2 l/h. Assuming an ideal combustion of gasoline (modeled by olefin-1-octene C<sub>8</sub>H<sub>16</sub>), per mol of gasoline 8 mol CO<sub>2</sub> is emitted. With a density of 0.75 kg/l, the CO<sub>2</sub> emission of the aircraft equals 97.1 kg/h. .

### Pollutant abatement systems for SI-engines

To have a more sustainable and environmentally friendly solution for propelling the aircraft, pollutant abatement systems are installed on the SI-engines used in the aircraft. The three-way catalytic converter (TWC) is the most used pollutant abatement systems for gasoline port-injected SI-engines [64]. The most advanced TWC are able to remove more than 98% of the pollutants [39]. Their name is derived from the fact that they are able to remove the three most pollutant emissions at once, namely NO<sub>x</sub>, HC and CO. The dynamics of the reactions on the surface of the TWC are modeled using the Langmuir-Hinshelwood kinetics model. The individual reactions are described in Equation 4.9 [39]. Note that the pollutant emissions are mainly converted into carbon dioxides. The TWC and its working mechanism is illustrated in Figure 4.14.



Looking at Figure 4.10 one can see that the conversion efficiency of the TWC converter heavily depends on the air-to-fuel ratio  $\lambda$  and is optimal at a slightly rich ratio. Therefore it is of utmost importance that the equivalent air-to-fuel ratio is kept at a value very close to but smaller than 1, where the conversion efficiency of the three together is optimal. Controlling the air-to-fuel ratio at a slightly rich ratio has to be done by a control system regulated on the electronic-control-unit (ECU) of the engine. The working mechanism of such a control system together with the main specifications of the TWC is described below.

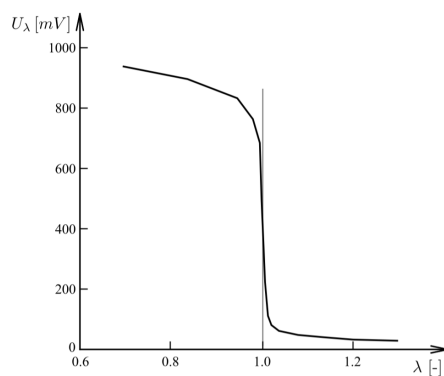


Figure 4.13: Voltage characteristic of a Bosch LSF switch-type air-to-fuel ratio sensor [39].

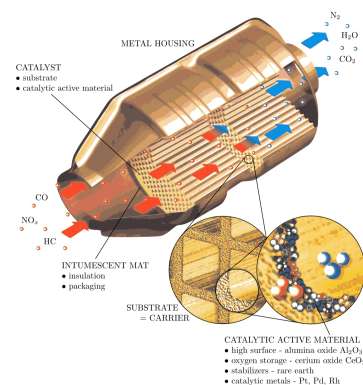


Figure 4.14: Sketch of a three-way catalytic converter indicating its working principle [39].

The proposed control system uses both a feedforward and feedback controller to be able to control the air-to-fuel ratio. The feedforward control loop is used to increase the speed of the controller. The system is rather slow because of the many lags or delays present between the input (=fuel injection) and the output (= air-to-fuel ratio) [39]. The idea of the feedforward loop is to use measurements of e.g. the intake manifold pressure, throttle angle or air mass flow rate into the intake manifold to predict the amount of fuel needed to be injected into the cylinder considering that the required air-to-fuel ratio

has to be slightly below 1. A conventional solution for a feedback controller uses a single switch-type air-to-fuel ratio sensor upstream of the TWC. This sensor gives a voltage signal indicating lean or rich conditions. The voltage characteristics of such a sensor can be seen in Figure 4.13. Using a PI controller on this voltage signal the air-to-fuel ratio can be controlled around the stoichiometric value of 1. However, using this feedback loop only works satisfactory when the emission levels are not too demanding [39].

More complex feedback controllers are available using an  $H_\infty$  design approach [65]. In the conventional solution described above the dynamics of the TWC are not taken into account since it is operated in an open-loop approach (the sensor is installed upstream of the TWC). The  $H_\infty$  feedback air-to-fuel ratio controller uses the capability of the TWC to store oxygen on a so-called catalytic active surface made from e.g. cerium (Ce) [64]. Being able to both store oxygen and release it from the catalytic active surface allows for both lean and rich excursions of the equivalent air-to-fuel ratio of the exhaust gas. When the exhaust gas in the TWC is too lean (meaning excess oxygen is present), oxygen can be stored on the catalytic surface; when the exhaust gas in the TWC is too rich (meaning a deficit of oxygen), oxygen can be released from the catalytic surface. The chemical reaction corresponding to this behaviour is written in Equation 4.10.  $Ce_2O_3$  of the catalytic surface absorbs/releases one oxygen to form a new structure on the surface [39].



The feedback controller has to make sure that the relative oxygen storage level on the catalytic active surface is controller around 50% allowing for both these lean and rich excursions of the air-to-fuel ratio. Therefore the system uses both a wide-range air-to-fuel ratio sensor upstream of the TWC and a switch type sensor downstream of the TWC and so including the storage capability of the TWC into the system. The main advantages of using an  $H_\infty$  feedback controller are its robustness and its ability of decreasing the emissions of the system up to a much higher level[39]. The results of adding such an air-to-fuel ratio control system can be seen in Figure 4.15 illustrating the change in air-to-fuel ratio after a change in operating point of the engine.

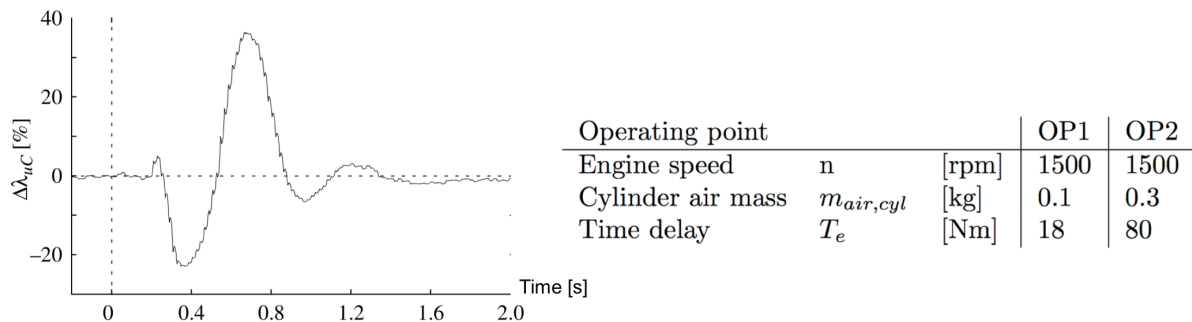


Figure 4.15: Response of the change in air-to-fuel ratio of the complete control system corresponding to a change from operating points OP1 to OP2 [39].

To conclude one can see that adding the TWC as exhaust after-treatment systems on the SI-engines with the appropriate  $H_\infty$  control systems allows for a more sustainable solution regarding pollutant emissions.

## 4.2 Flight dynamics

In this section the dynamics of the aircraft are determined and simulated and modeled. This model is used to predict the behaviour of the aircraft to different motions, gusts or any other disturbance that might happen during the flight. This is useful to see whether the aircraft is stable during the motions. First the dynamics are modelled numerically according to Euler's nonlinear equations of motion and they will then be verified with a linearized state-space system which is derived analytically and validated according to a flight test conducted with a Cessna Citation on March 7. 2016.

## 4.2.1 Dynamic model of the aircraft

The dynamic behaviour of the aircraft is described by the equations of motion. The basic equation for rotational dynamics is given by Equation 4.12[36]. In this equation the gyroscopic effect introduces the final term. As one can see there is a coupling of pitch, yaw and roll due to the cross-product.

$$\begin{bmatrix} \dot{p} \\ \dot{q} \\ \dot{r} \end{bmatrix} = J^{-1} \cdot \begin{bmatrix} L \\ M \\ N \end{bmatrix} - J^{-1} \cdot \left( \begin{bmatrix} p \\ q \\ r \end{bmatrix} \times \left( J \cdot \begin{bmatrix} p \\ q \\ r \end{bmatrix} + \begin{bmatrix} 0 \\ \omega_{cyl} \cdot I_{yy_{cyl}} \\ 0 \end{bmatrix} \right) \right) \quad (4.11)$$

$$\begin{bmatrix} \dot{p} \\ \dot{q} \\ \dot{r} \end{bmatrix} = J^{-1} \cdot \begin{bmatrix} L \\ M \\ N \end{bmatrix} - J^{-1} \cdot \left( \begin{bmatrix} p \\ q \\ r \end{bmatrix} \times \left( J \cdot \begin{bmatrix} p \\ q \\ r \end{bmatrix} \right) \right) \quad (4.12)$$

where

$$J = \begin{bmatrix} I_{xx} & 0 & I_{xz} \\ 0 & I_{yy} & 0 \\ I_{zx} & 0 & I_{zz} \end{bmatrix} \quad (4.13)$$

The next step was to substitute the basic moments ( $L_{roll}$ ,  $M_{pitch}$ ,  $N_{yaw}$ ) with an expression which includes the moments introduced by the control surfaces and the aerodynamic reaction moments of the aircraft. These expressions are given in Equation 4.14 - Equation 4.16.

$$L_{roll} = q_0 S b (C_{l_v} v + C_{l_p} p + C_{l_r} r + C_{l_{da}} da + C_{l_{dr}} dr) \quad (4.14)$$

$$M_{pitch} = q_0 S c (C_{m_\alpha} \alpha + C_{m_q} q + C_{m_u} u + C_{m_w} w + C_{m_{\dot{w}}} \dot{w} + C_{m_{de}} de) \quad (4.15)$$

$$N_{yaw} = q_0 S b (C_{n_v} v + C_{n_p} p + C_{n_r} r + C_{n_{da}} da + C_{n_{dr}} dr) \quad (4.16)$$

The force equations are needed determine the translational motion of the aircraft which is used in parallel with rotational equations of motion. These equations are stated in Equation 4.17 - Equation 4.19[36]. These are used to relate the translational and rotational motion of the aircraft.

$$-W \sin \theta + q_0 S (C_{X_u} u + C_{X_{\dot{w}}} \dot{w} + C_{X_w} w + C_{X_q} q + C_{X_{\delta_e}} \delta_e) = m(\dot{u} + qw - rv) \quad (4.17)$$

$$W \cos \theta \sin \phi + q_0 S (C_{Y_v} v + C_{Y_{\dot{w}}} \dot{w} + C_{Y_p} p + C_{Y_r} r + C_{Y_{\delta_a}} \delta_a + C_{Y_{\delta_r}} \delta_r) = m(\dot{v} + ru - pw) \quad (4.18)$$

$$W \cos \theta \cos \phi + q_0 S (C_{Z_u} u + C_{Z_w} w + C_{Z_{\dot{w}}} \dot{w} + C_{Z_q} q + C_{Z_{\delta_e}} \delta_e) = m(\dot{w} + pvrqu) \quad (4.19)$$

The kinematic relations are stated in Equation 4.20-Equation 4.22 which are used to determine the body angles of the aircraft.

$$\dot{\phi} = p + q \sin \phi \tan \theta + r \cos \phi \tan \theta \quad (4.20) \quad \dot{\theta} = q \cos \phi - r \sin \phi \quad (4.21) \quad \dot{\psi} = \frac{q \sin \phi}{\cos \theta} + \frac{r \cos \phi}{\cos \theta} \quad (4.22)$$

---

### Stability derivatives

The aerodynamic behaviour of an aircraft is described by its stability derivatives. In real life the stability derivatives are found by performing test flights [36]. As this is not possible at this stage of the design a different approach was taken to come up with the stability derivatives of Aeolus. As a basis the derivatives of the Cessna Citation were used. Some parameters ( $C_{l_{da}}$ ,  $C_{n_{dr}}$ ,  $C_{n_{\beta}}$ ,  $C_{Y_{\beta}}$ ,  $C_{Y_{dr}}$ ) were derived from the aileron, rudder and vertical tail sizing. Furthermore some derivatives of the Cessna Citation were adapted to be more representable for our aircraft. This was done by analysing the main contributors on each derivative. Main differences which were concluded are a decreased and  $C_{l_r}$  and an increased  $C_{Y_r}$  and  $C_{m_q}$ . These are due to the smaller reference area of the main wing and the rearward location of the wing compared to the c.g. As no accurate calculations can be done on these derivatives they were determined qualitatively based on reference aircraft. [36]

Stability derivative	Value [-]	Stability derivative	Value [-]	Stability derivative	Value [-]
$C_{x_u}$	-0.028	$C_{m_{\alpha}}$	-0.997	$C_{l_{\beta}}$	-0.103
$C_{x_{\alpha}}$	-0.480	$C_{m_{\dot{\alpha}}}$	0.178	$C_{l_p}$	-0.711
$C_{x_{\dot{\alpha}}}$	0.083	$C_{m_u}$	0.070	$C_{l_r}$	0.180
$C_{x_q}$	-0.282	$C_{m_q}$	-12.630	$C_{l_{da}}$	-0.143
$C_{x_{de}}$	-0.037	$C_{m_{de}}$	1.690	$C_{l_{dr}}$	0.034
$C_{x_{dr}}$	0.0	$C_{m_{dr}}$	0.0	$C_{n_{\beta}}$	0.224
$C_{z_u}$	-0.376	$C_{y_{\beta}}$	-1.253	$C_{n_{\dot{\beta}}}$	0.0
$C_{z_{\alpha}}$	-5.743	$C_{y_{\dot{\beta}}}$	0.0	$C_{n_p}$	-0.060
$C_{z_{\dot{\alpha}}}$	-0.004	$C_{y_p}$	-0.030	$C_{n_r}$	-0.206
$C_{z_q}$	-5.663	$C_{y_r}$	0.560	$C_{n_{da}}$	-0.012
$C_{z_{de}}$	-0.696	$C_{y_{da}}$	-0.040	$C_{n_{dr}}$	-0.0977
$C_{z_{dr}}$	0.0	$C_{y_{dr}}$	0.260		

Table 4.8: Values for the stability derivatives of the aircraft. Determined based on the Cessna Citation, with adaptations made for  $C_{m_{\alpha}}$ ,  $C_{m_{de}}$ ,  $C_{l_{da}}$ ,  $C_{n_{dr}}$ ,  $C_{n_{\beta}}$ ,  $C_{Y_{\beta}}$ ,  $C_{Y_{dr}}$ ,  $C_{l_r}$ ,  $C_{Y_r}$  and  $C_{m_q}$

The stability derivatives used for Aeolus are listed in Table 4.8. One important parameter which should be noted is  $C_{m_{\alpha}}$ . A canard aircraft usually has a positive  $C_{m_{\alpha}}$ , which means that it is longitudinally unstable. So normally an automated control mechanism is then applied to the canard to stabilize the aircraft. Same assumption was made for Aeolus: the canard already has a stabilizing system which, by using a gyroscope, makes  $C_{m_{\alpha}}$  negative. Another difference with a conventional aircraft is a positive value for  $C_{m_{de}}$  due to the canard configuration.

### Solution method

The dynamic model gives a set of coupled differential equations. As decoupling these equations is not preferable, a numerical integration method was used to find the solution.. A simple Euler method gave divergent solutions so the recursive Runge-Kutta method was implemented. This gave much better, converging solutions [66]. A time-step of 0.005s was used for all calculations, this provided accurate results and reasonable computation times. A time-step of higher than 0.1s would deem in a diverging solution so a low enough time-step was needed to get a diverging solution and capture the behaviour of the motion accurately. A time-step lower than 0.005s was also tested, i.e 0.0005s, but that required a longer than 2 minutes computation time with the observed accuracy of the results from 0.005s time-step. So 0.005s was a good compromise with only about 15-30 seconds computational time depending on the duration of the motion.

Any type of desired disturbances or inputs can be simulated and analyzed using the model. However, special attention was given to the 4 characteristic motions of the aircraft. These motions are important as the aircraft can encounter them more frequently during the flight than other motions:

- Dutch roll: rudder input (equivalent to encountering lateral disturbances or a lateral gust)

- Aperiodic roll: aileron input (equivalent to encountering roll disturbances or a diagonal gust)
- Spiral: small aileron input (comparable to encountering roll disturbances)
- Phugoid: elevator input (equivalent to encountering step upward or downward disturbances)

## 4.2.2 Results flight dynamics

The results of the flight dynamics analysis are presented as a combination of graphs which show the characteristic behaviour of the aircraft to various disturbances. In each graph the result will be given of the aircraft with gyroscopic effect and without, by determining a cylindrical rotational speed of 305 rad/s and 0 rad/s respectively.

### Dutch roll

The first characteristic behaviour is the Dutch roll. The pilot gives the aircraft a short, sharp rudder input. This will result in an oscillatory behaviour with coupling between roll and yaw. The gyroscopic effect enhances this coupling by inducing higher roll angle from a rudder input and longer oscillations. With the initial size of the vertical tail the Dutch roll is stable, however the oscillation takes a long time to dampen out. To improve the damping behaviour of this motion, a simple yaw dampening algorithm can be made and fed into servos. The way this algorithm works, is to deflect the rudders in the opposite direction of the disturbances to counteract and dampen the motion quicker. For illustration purposes, a full damping gain is used in Figure 4.16. This means that the rudders are deflected maximally in the opposite direction of the motion to dampen the motion out. In real flight, much lower gain, e.g 50 %, and more slowly will be fed to the servos to reduce the required actuator forces.

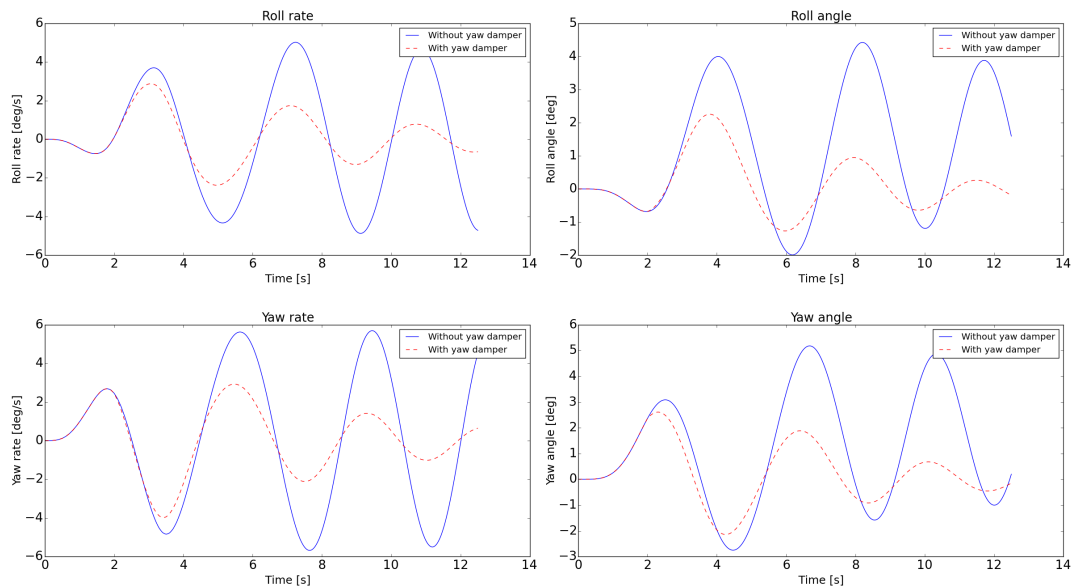


Figure 4.16: Dutch roll: aircraft roll and yaw response to a rudder impulse input

### Aperiodic roll

Aperiodic roll is the aircraft behaviour that results from a constant aileron input. This is comparable to a failure mode when one part of the cylinder generates less lift than the other or a diagonal gust hits the aircraft. So an uneven lift distribution over the cylinder is observed. In the graphs, the aileron input is started at approximately 5 seconds. When reviewing Figure 4.17, the same conclusions can be drawn as for the dutch roll. As can be observed, the gyroscopic effect will induce an oscillatory motion to the

aircraft. The motion can be corrected by applying an inverse aileron input as it is shown in the graphs after 20 seconds into simulation.

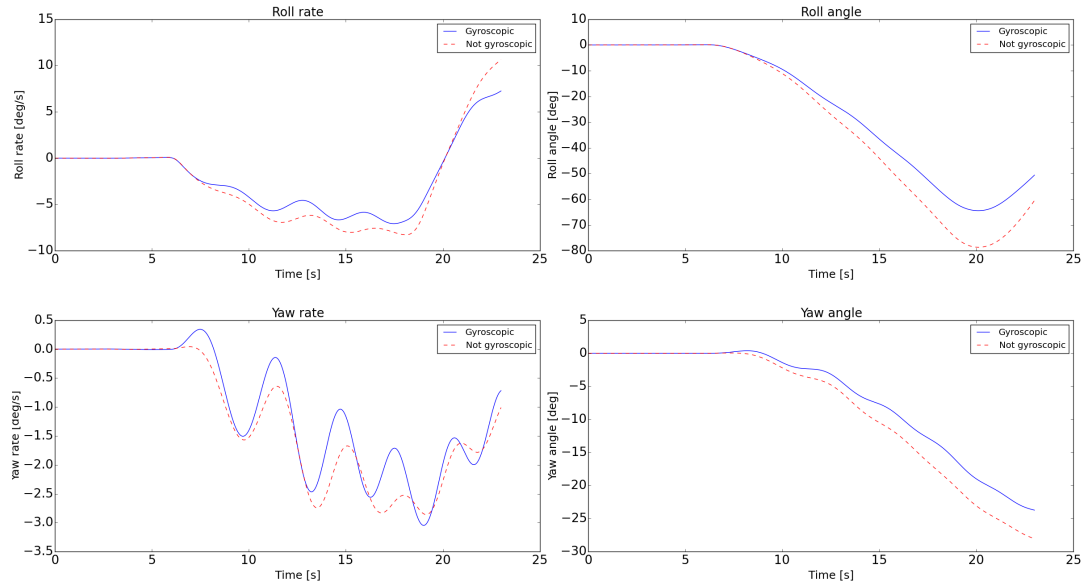


Figure 4.17: Aperiodic roll: aircraft roll and yaw response to a aileron step input

## Spiral

Spiral motion is observed when the aircraft is directed in a slow downward spiralling motion which could be due to a diagonal gust hitting the aircraft. This motion is achieved by giving a small aileron step input. Figure 4.18 presents the roll and yaw motions. As can be noticed, the gyroscopic effect makes the aircraft neutral in spiral motion. So the motion is neither being damped nor is the oscillation getting worse. This is due to the relatively large vertical support structure in the back and the lack of dihedral in the wing. Yet, this behaviour is not severe, since it happens really slowly and the motion can be

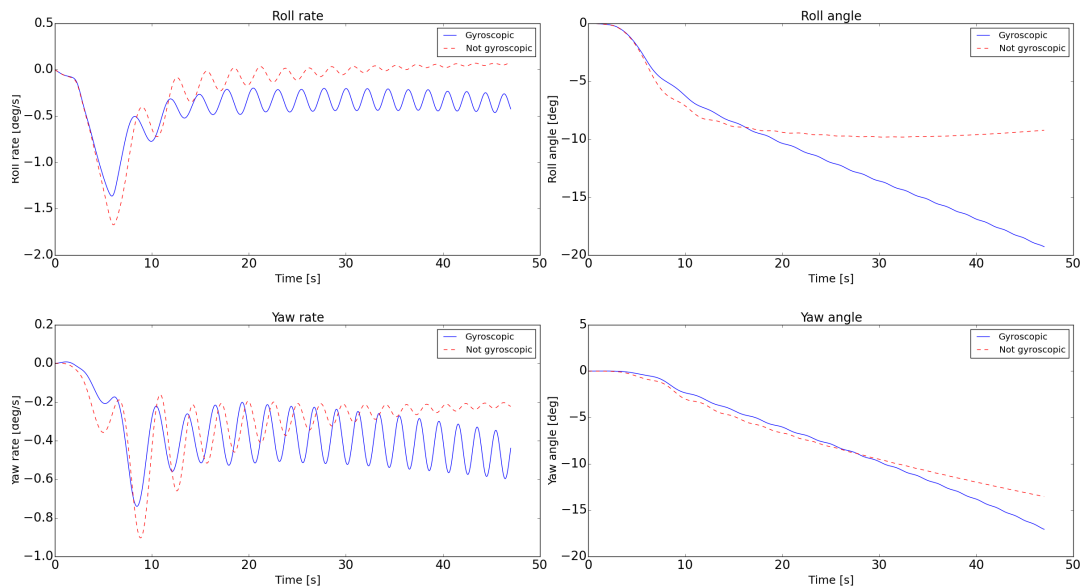


Figure 4.18: Spiral: aircraft roll and yaw response to an initial condition input

easily counteracted by the pilot. Other solution would be to use an automated damper, similar to a yaw damper, which can be used to dampen these oscillations. Many of the conventional, low wing aircraft such as, Cessna Citation are also spirally unstable.

## Phugoid

The only longitudinal motion which will be discussed is the phugoid motion. Such a motion is achieved by giving a negative elevator input. The induced motion does not change the axis orientation of the rotating cylinder, therefore no gyroscopic moment occurs. This means that no rolling or yawing motion is induced either. The pitching response is given in Figure 4.19. One difference with a conventional aircraft is the fact that the aircraft is constantly pitching down rather than oscillating around an equilibrium condition. The reason for this is that the rpm of the cylinder is constant during the motion. In general, by an increase or decrease in angle of attack, the cylinder does not generate excess lift. This causes the aircraft to start pitching down. This motion can be corrected by either adjusting the canard to maintain a constant pitch angle, or by adjusting the rpm during the motion to get the required correcting pitching moment from the cylinder and regain any lost altitude.

Correcting this motion introduces high workloads to the pilot which is preferred to be avoided. This is one reason to use an automated canard to maintain the optimum pitch angle during the flight to reduce pilot's workload and efficient flight. An automated rpm can also be introduced, this system works by capturing the aircraft's airspeed and adjust the rpm of the cylinder accordingly to maintain a constant and optimum velocity-ratio,  $\alpha$  which is also useful during the cruise.

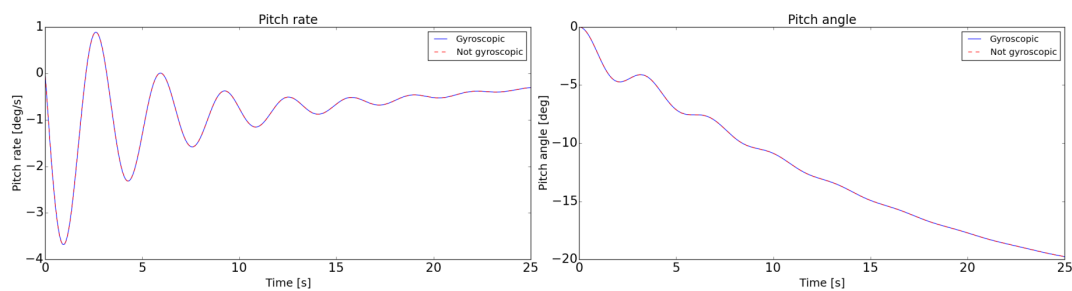


Figure 4.19: Phugoid: aircraft pitching response to a negative canard input

## Influence of gyroscopic effect

Further analysis was conducted regarding the influence of the gyroscopic effect, as this is what makes the flight dynamics of the Aeolus special. In Figure 4.20 a comparison is made for different moments of inertia's of the rotating cylinder. The input which was given, is the same as for the aperiodic roll, so a step aileron input.  $I_{yy}$  of the designed cylinder was 1.5. For an increasing  $I_{yy}$ , one can clearly see the oscillation increases and it becomes harder and takes longer to deviate from the equilibrium condition.

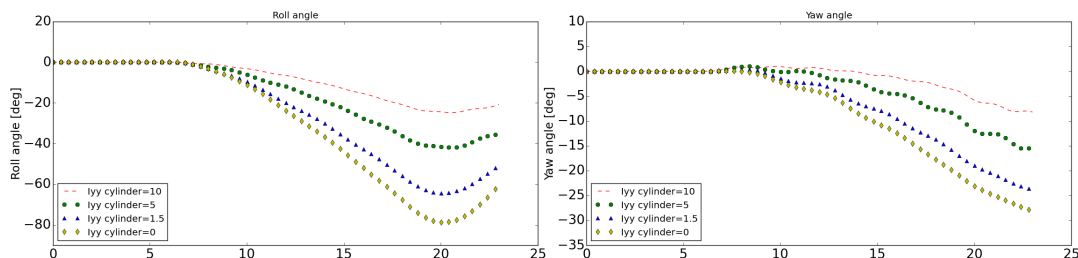


Figure 4.20: Representation of the stabilizing gyroscopic effect of the rotating cylinder on the flight dynamics of the aircraft

### 4.2.3 Verification of dynamic model of the aircraft

The flight dynamics model is verified by comparing with a simplified state-space model. This analytical model made the assumption that longitudinal and lateral motions of the aircraft are decoupled and linearised it around a certain equilibrium condition. This means the state-space model is only valid when the aircraft does not deviate from the equilibrium region too much. First the longitudinal and lateral state-space model is described and then compared to the model for verification. At the end both models are validated using actual flight data.

#### Longitudinal dynamics

This state-space model uses the linearized equations of motion as derived by J.A. Mulder [36]. The following assumptions were introduced for simplification:

- The aircraft is a rigid body with constant mass
- Earth is non-rotating and flat
- Gravity field is constant
- The aircraft has a plane of symmetry and the body-fixed reference frame is chosen such that  $I_{xy}$  and  $I_{zy}$  are zero
- The resultant thrust vector lies in the symmetry plane and thus only affects the aerodynamic forces X,Z and the aerodynamic moment M

The matrices  $C_1$ ,  $C_2$  and  $C_3$  of the longitudinal equations of motion (in the form  $C_1\bar{x} + C_2\bar{x} + C_3\bar{u} = \bar{0}$ ) are given in Equation 4.23 - Equation 4.24.

$$C_1 = \begin{bmatrix} -2\mu_c \frac{\bar{c}}{\bar{V}} & 0 & 0 & 0 \\ 0 & (C_{Z\dot{\alpha}} - 2\mu_c) \frac{\bar{c}}{\bar{V}} & 0 & 0 \\ 0 & 0 & -\frac{\bar{c}}{\bar{V}} & 0 \\ 0 & C_{m\dot{\alpha}} \frac{\bar{c}}{\bar{V}} & 0 & -2\mu_c K_Y^2 \frac{\bar{c}}{\bar{V}} \end{bmatrix} \quad (4.23)$$

$$C_2 = \begin{bmatrix} C_{X_u} & C_{X_\alpha} & C_{Z_0} & C_{X_q} \\ C_{Z_u} & C_{Z_\alpha} & -C_{X_0} & (C_{Z_q} + 2\mu_c) \\ 0 & 0 & 0 & 1 \\ C_{m_u} & C_{m_\alpha} & 0 & C_{m_q} \end{bmatrix} \quad C_3 = \begin{bmatrix} C_{X\delta_e} & C_{X\delta_t} \\ C_{Z\delta_e} & C_{Z\delta_t} \\ 0 & 0 \\ C_{m\delta_e} & C_{m\delta_t} \end{bmatrix} \quad (4.24)$$

The numerical linear model is based on the state-space representation of the system of equations of motion, given by Equation 4.25. The form of the equations of motion  $C_1\bar{x} + C_2\bar{x} + C_3\bar{u} = \bar{0}$  can be transformed into a state-space system using Equation 4.26. Note that matrix C is used to make the output state vector dimensional.

$$\dot{\bar{x}} = A\bar{x} + B\bar{u} \quad \dot{\bar{y}} = C\bar{x} + D\bar{u} \quad (4.25)$$

where the matrices A, B, C and D are the following:

$$A = -C_1^{-1} \cdot C_2 \quad B = -C_1^{-1} \cdot C_3 \quad C = \begin{bmatrix} V & 0 & 0 & 0 \\ 0 & 1 & 0 & 0 \\ 0 & 0 & 1 & 0 \\ 0 & 0 & 0 & \frac{V}{\bar{c}} \end{bmatrix} \quad D = \bar{0} \quad (4.26)$$

## Lateral dynamics

The state-space of the lateral flight dynamics was also derived from [36]. Yet, an addition had to be made to include the gyroscopic moment in this system. This model incorporates the gyroscopic effect by adding a term to the stability derivatives  $C_{N_r}$ ,  $C_{N_p}$ ,  $C_{L_r}$  and  $C_{L_p}$ . This approach was presented by J.Seifert in his analysis of the flight dynamics of a MAV with a rotating cylinder. [67] The result is presented in Equation 4.27-Equation 4.30.

$$C_{n_r} = \frac{b}{4\Delta V_0}(I_{xz}C_{l_r} + I_{xx}C_{n_r}) - \frac{1}{\Delta q_0 S b} I_{xz_{cyl}}(I_{xx_{cyl}} - I_{yy_{cyl}} + I_{zz_{cyl}})\omega_{y_{cyl}} \quad (4.27)$$

$$C_{n_p} = \frac{b}{4\Delta V_0}(I_{xz}C_{l_p} + I_{xx}C_{n_p}) + \frac{1}{\Delta q_0 S b} I_{xz_{cyl}}(I_{xx_{cyl}}^2 - I_{xx_{cyl}} \cdot I_{yy_{cyl}} + I_{xx_{cyl}}^2)\omega_{y_{cyl}} \quad (4.28)$$

$$C_{l_r} = \frac{b}{4\Delta V_0}(I_{zz}C_{l_r} + I_{xz}C_{n_r}) - \frac{1}{\Delta q_0 S b} (I_{zz_{cyl}}^2 - I_{zz_{cyl}} \cdot I_{yy_{cyl}} + I_{xx_{cyl}}^2)\omega_{y_{cyl}} \quad (4.29)$$

$$C_{l_p} = \frac{b}{4\Delta V_0}(I_{zz}C_{l_p} + I_{xz}C_{n_p}) + \frac{1}{\Delta q_0 S b} I_{xz_{cyl}}(I_{xx_{cyl}} - I_{yy_{cyl}} + I_{zz_{cyl}})\omega_{y_{cyl}} \quad (4.30)$$

Making the coefficients non-dimensional and combining them with the expressions for the other coefficients [36], the state-space system is set up as can be seen in Equation 4.31 and Equation 4.32,6 with matrix  $[\bar{I}]$  being the identity matrix.

$$\begin{bmatrix} \dot{r} \\ \dot{\beta} \\ \dot{p} \\ \dot{\phi} \\ \dot{\psi} \\ \dot{y} \end{bmatrix} = A \cdot \begin{bmatrix} r \\ \beta \\ p \\ \phi \\ \psi \\ y \end{bmatrix} + B \cdot \begin{bmatrix} \xi \\ \zeta \end{bmatrix} \quad \text{and} \quad y = C \cdot \begin{bmatrix} r \\ \beta \\ p \\ \phi \\ \psi \\ y \end{bmatrix} + D \cdot \begin{bmatrix} \xi \\ \zeta \end{bmatrix} \quad (4.31)$$

where

$$A = \begin{bmatrix} C_{N_r} & C_{N_\beta} & C_{N_p} & 0 & 0 & 0 \\ C_{Y_r} - \cos(\alpha_0) & C_{Y_\beta} & C_{Y_p} - \sin(\alpha_0) & \frac{g}{V_0} \cdot \cos(\alpha_0) & 0 & 0 \\ C_{L_r} & C_{L_\beta} & C_{L_p} & 0 & 0 & 0 \\ \tan(\theta_0) & 0 & 1 & 0 & 0 & 0 \\ \frac{1}{\cos(\theta_0)} & 0 & 0 & 0 & 0 & 0 \\ 0 & V_0 \cdot \cos(\psi_0) \cdot \cos(\gamma_0) & 0 & 0 & V_0 \cdot \cos(\psi_0) \cdot \cos(\gamma_0) & 0 \end{bmatrix}$$

$$B = \begin{bmatrix} C_{N_\xi} & C_{N_\zeta} \\ C_{Y_\xi} & C_{Y_\zeta} \\ C_{L_\xi} & C_{L_\zeta} \\ 0 & 0 \\ 0 & 0 \\ 0 & 0 \end{bmatrix} \quad C = \frac{b}{2 \cdot V_0} \cdot [\bar{I}] \quad D = \bar{0} \quad (4.32)$$

## Results verification & validation

The results in this section are generated for the Cessna Citation aircraft from two different models: one is the simplified state-space model and the other if the numerical Runge-kutta model. In both of these models, the Gyroscopic effect is “turned-off” to represent the Cessna Citation as closely as possible. Moreover, all the dimensions, stability derivatives and flight conditions used for verification and validation are from Cessna Citation’s aircraft again, to make the validation and verification process valid.

---

## Verification

The results of the verification are combined in the graphs of Figure 4.21. It can be seen that the numerical Runge-Kutta model corresponds closely to the linearized state-space model. The main difference is a small lag of the state-space model and a different curve for the yaw rate. This difference can be attributed to the, less accurately modelled, coupling in the linearized state-space model.

## Validation

Flight data of an aircraft using the Magnus effect as main lift provider is not available, since no such aircraft has actually flown yet. So validation is made by result comparison with a flight test which was performed with the Cessna Citation aircraft of the TU Delft on March 7 2016. The flight data from this test is used to validate the results from the dynamic model of the aircraft. The models are used to simulate exactly the pilot's input during the flight and then the simulated results are compared with the actual aircraft behaviour for validation. The validation results are also presented in Figure 4.21. One can see that the Runge-Kutta model corresponds perfectly for the roll rate and roll angle. Some deviation can be seen in the yaw rate and yaw angle, yet the same overall behaviour can be observed. It should be noted that the models are validated with the Gyroscopic effect "turned-off" as Cessna Citation does not have a rotating cylinder.

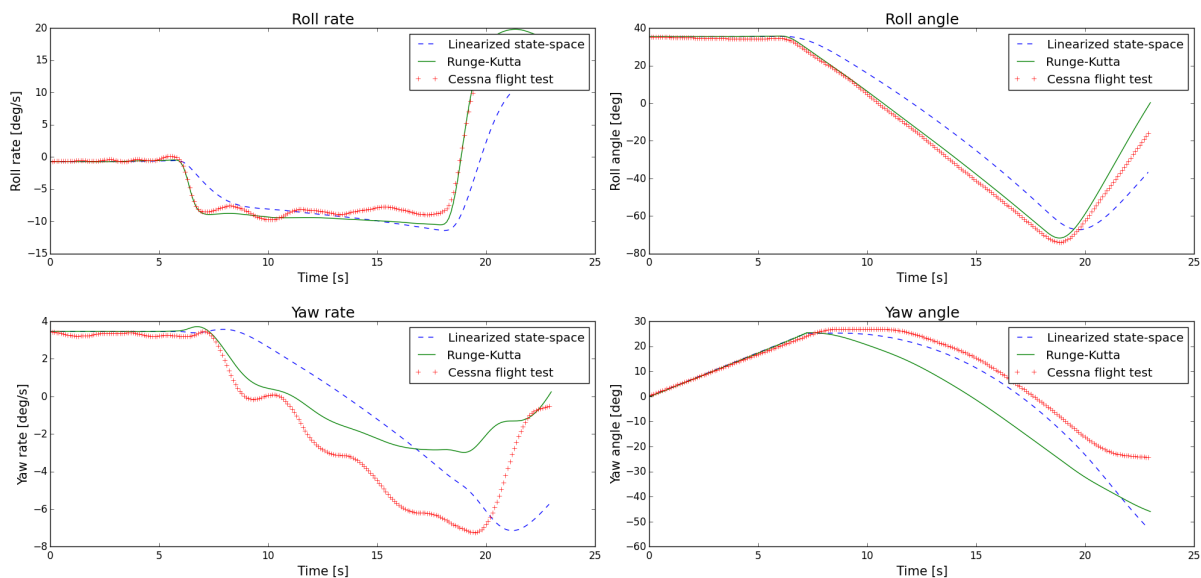


Figure 4.21: Verification and validation of the flight dynamics model

### 4.2.4 Summary flight dynamics

The verified and validated flight dynamics model gives insight in the stability and control of Aeolus. The aircraft is stable for most disturbance inputs. Only the spiral motion is slightly divergent, which is common in aircraft and easily correctable by the pilot.

The gyroscopic effect acts has a stabilizing effect for most motions, yet its effect is not as significant as expected for Aeolus. Therefore the control will be fairly similar to conventional aircraft. The control surfaces are given enough control authority to control and perform all projected maneuvers. Hence performing the turn maneuvers requires similar control inputs to the ones of a conventional aircraft with the addition of controlling the rpm of the cylinder to maintain the pitch and altitude.

---

## 4.3 Sustainability Analysis

Sustainability is an important aspect of modern engineering. It evaluates the impact of the design on its environment and tries to limit it. First, the sustainability characteristics of the design during its lifetime are described. Thereafter, an end-of-life solution for the aircraft is presented, discussing the solutions for different components and for the aircraft system as a whole.

### 4.3.1 Lifetime characteristics

The following design evaluations illustrate the implementation of a sustainability design philosophy throughout the detailed design phase.

#### Material for supporting structures

Based on prior experience in the aerospace industry the material selection for supporting structures in general came down to a choice between aluminum or carbon fibre reinforced polymers (CFRP). Some of the advantages and disadvantages of using CFRP instead of aluminum alloy are shown below:

- Advantages
  - Weight reduction
  - Simple manufacturing of narrowly curved shell shape
  - High stiffness
  - Good characteristics for unilateral loading cases
- Disadvantages
  - Poor recyclability characteristics
  - Poor assembly characteristics

In fact this evaluation translates to a choice between having a negative impact on the environment during or after the lifetime of the aircraft. Furthermore Requirement **RMEA-SYS-1** gives that at least 50% of the supporting structure has to be recyclable. For each supporting component separately the magnitude of these advantages and disadvantages was estimated and evaluated. It was found that most of the inner supporting structure will be made out of recyclable aluminum alloy, because of the recyclability requirement and because of the easy assembly characteristics. Three structures were made out of CFRP. First of all the rotor because of the high stiffness requirements. Furthermore the fuselage because of the required narrowly curved shell shape. And finally the duct because of the unilateral loading case of the duct. A total list of the elements and used material is given in Table 4.9. A more in depth description of the load cases and the material selection is described in chapter 3.

#### Regenerative braking

During flight operations and especially after touch down, the rotational speed of the cylinder needs to be decreased. Using normal brakes, such as, for example, disk or rim brakes would converse the kinetic energy of the cylinder to heat that is dissipated to the environment. In order to increase the range and sustainability of the aircraft, regenerative braking could be used. All information provided in this section is based on Tesla's blog on regenerative braking <sup>1</sup>.

##### *Operation*

During flight, the pilot will mainly change the altitude of the aircraft by changing the rotational speed of the cylinder, since the speed range of the aircraft is very limited and changing the rotational speed of the cylinder will have a lower lag compared to changing the velocity. To lower the rotational speed of the cylinder fast enough, brakes are necessary. A system based on regenerative braking used in hybrid and electric cars could be used, which can store a part of this energy.

Since only electric engines could be used to spin the cylinder, algorithms of the engine controller would be used to control both the spinning and braking of the cylinder. The torque requested is derived from

---

<sup>1</sup>[https://www.teslamotors.com/nl\\_NL/blog/magic-tesla-roadster-regenerative-braking](https://www.teslamotors.com/nl_NL/blog/magic-tesla-roadster-regenerative-braking)

---

the throttle position. The controller will transform this request into the appropriate amount of voltage and current to deliver the torque in the motor. This value can be both positive or negative. The torque can thus also serve to slow the cylinder down and so regenerate the energy stored in the cylinder.

### *Efficiencies and power*

When the chemical energy of the battery is used to spin the cylinder, the energy first needs to pass through an inverter which inverts the energy from DC to AC, which is provided to the engine. In the engine, the electrical energy is transformed to mechanical energy. In the planetary gearing the torque generated by the engine is transformed to a force, by which the cylinder is spun. All these conversions of energy cause a loss of energy and their efficiencies are equal when the process is reversed for the regenerative braking.

### *Disadvantages*

Powering the electric motor requires power supplied by a battery pack. For cars these days this is the major drawback of going electric. Moreover, the batteries should be constantly charged by an alternator attached to the main engine. An average brushless alternator has an efficiency of 60-70%. In combination with the efficiency of the main engine, this has a negative effect on the fuel consumption, thus actually being less sustainable by burning more fuel. Furthermore, the increase in weight due to the extra batteries and the alternator system, which is currently approximated to be an extra 50kg with respect to the current configuration with the Simonini engine. Increasing the weight by 50kg, not only requires larger structures, but also more power which results again in more fuel according to the snowball effect.

According to L. Guzella in [28], the additional weight of the mechanisms to allow for regenerative braking is only advantageous when braking is applied repeatedly. For example it is suitable for city driving with a car and not for cruising on the highway. Considering the mission of Magnus Aeolus, it is concluded that regenerative braking will not be more sustainable. Therefore it is decided to rotate the cylinder using an IC-engine.

## **Retractable nose gear**

An investigation is made whether a retractable nose gear can prove to be a sustainable design option. A retractable nose gear adds weight to the aircraft structure for the mechanism to make the gear retractable. First, both the main and rear landing gear cause drag, which is preferably mitigated in order to reduce fuel consumption. The front landing gear is loaded less heavily than the main landing gear, which means that making it retractable has less influence on the weight gain. The second reason is that the front landing gear trips the boundary layer of the airflow over the body. The boundary layer becomes turbulent and this propagates over the full lower side of the body. The turbulence creates drag due to skin friction. This drag decrease becomes favorable at higher speeds when looking at fuel consumption<sup>2</sup>. Lower fuel consumption has the two main advantages of both less CO<sub>2</sub> emissions and also less pollutant emissions. However, the weight gain requires more lift and thus an increase in drag from the cylinder. At this stage both a fixed and a retractable nose landing gear have their disadvantages and this needs to be tested in a wind tunnel or examined with a computational fluid dynamics model for quantification.

However, when looking at the mechanism of the retractable main landing gear of the Silence Twister (having a MTOW of 375kg)<sup>3</sup>, one can see that it weighs only 2kg. This aircraft is a taildragger, meaning that most of the weight will be carried by this main landing gear. Knowing that the mechanisms for a nose gear will definitely be lighter than a main gear and considering that - because the c.g. is so much aft - the load on the nose gear will also be small, the weight addition of this retractable nose gear will be limited and is estimated to be below 2kg. Therefore this solution is preferred over a fixed landing gear.

---

<sup>2</sup>[https://www.faa.gov/regulations\\_policies/handbooks\\_manuals/aircraft/amt\\_airframe\\_handbook/media/ama\\_Ch13.pdf](https://www.faa.gov/regulations_policies/handbooks_manuals/aircraft/amt_airframe_handbook/media/ama_Ch13.pdf)

<sup>3</sup><http://silence-aircraft.de/en/aircraft/>

---

### 4.3.2 End-of-life solution

The end-of-life solution is divided in two parts. First a solution is found for the prototype. Next a preliminary end-of-life analysis is made for the aircraft if it would be mass produced (+10 aircraft).

#### Prototype

The prototype would be a one of a kind aircraft. Being able to fly using the Magnus effect as main lift providing force is an important step in aviation history. This makes that the aircraft would be a great addition to a museum. The aircraft could, for instance, be donated to the TU Delft Faculty of Aerospace Engineering. However, this only concerns the outer shape of the aircraft.

An end-of-life solution for the rest of the aircraft is proposed based on the PAMELA approach launched by Airbus [68]. The end-of-life aircraft still has value, which needs to be recovered. By reusing or recycling parts, natural resources can be spared which otherwise would have been required to make them. This also includes the resources and pollutants emitted during the production of those parts. Finally, it also leads to a reduction of the amount of waste material.

The PAMELA approach, as proposed by Airbus, consists of three phases, namely decommissioning, dis-assembly and smart dismantling which allow for a proper end-of-life solution for retired aircraft.

#### *Decommissioning*

The first steps in the end-of-life process of the aircraft comprise inspection, cleaning and decontamination. Afterwards, drainage of all operating liquid tanks should be done, including fuel (gasoline of the IC-engines), the hydraulic fluids (for the brakes), oil and cooling fluids (for the engine). These operating fluids can be resold directly (e.g. fuel) or be disposed using regulated recovery channels [68].

#### *Dis-assembly*

The dis-assembly process starts with making a dis-assembly planning to optimize the amount of material recovery. After the process has been carried out, re-usable parts have to be selected. These parts should be ordered and sorted into different groups to allow for the next stage.

#### *Smart dismantling*

Smart dismantling means disassembling parts for re-using or reselling purposes. First of all, there are parts which can directly be reused in other aircraft and therefore are resold. These components comprise the Mistral IC-engine, the Simonini IC-engine, the avionics, the actuators including control systems, the fans, parts of the landing gear, canopy, seats, etc. Secondly, as already described there are re-usable operating liquids.

This end-of-life solution for the prototype aircraft allows for recovering most of the value of the aircraft after the mission is performed. An overview of end-of-life solution for each aircraft component is given in Table 4.9.

#### Mass production

An end-of-life solution also had to be given to the design if it is mass produced. In this case more consideration has to be given to the recyclability of all aircraft components. An overview is given in Table 4.9. It can be seen that 112 kg of CFRP material will be used which is not recyclable. On the other hand most of the inner supporting structure is made out of aluminium alloy. This sums up to a total of approx. 400 kg recyclable aluminium. Other components like avionics, actuators or control system will not be reused after a full lifetime and will therefore be waste. This results in a total recyclability of the Magnus Aeolus weight of 73%.

Table 4.9: End-of-life solutions for all aircraft elements

Element	Material	Mass [kg]	Prototype	Mass Production
Cylinder shell/Hubs/Endcaps	CFRP/foam/honeycomb	32	museum	waste
Bearings/bearing housing/axle	Aluminium alloy/Steel	30	museum	recycled
Vertical side support	Aluminium alloy	45	recycled	recycled
Wing box	Aluminium alloy	55	recycled	recycled
All saver	Nylon	20	reused	reused
Fuel tanks	Aluminium alloy	30	recycled	recycled
Fuselage shell/Canopy	CFRP/Poly carbonate	49	museum	waste
Batteries	Lithium	3	reused	recycled
Mistral G200 engine	Mainly aluminium alloy	140	reused	recycled
Simonini engine	Mainly aluminium alloy	14	reused	recycled
Avionics/cockpit elements	N.A.	12	reused	waste
Actuators	N.A.	7	reused	waste
Control system/computers	N.A.	11	reused	waste
Canard	Aluminium alloy	40	museum	recycled
Ducted fan	CFRP/foam	31	museum	waste
Landing gear structure	Aluminium alloy	80	museum	recycled

## 4.4 Sensitivity Analysis

For the final design a different approach is taken towards this sensitivity analysis compared to the sensitivity analysis performed during the preliminary design. There is a lot more consideration going into the detailed design, therefore the magnitude of the changes will be smaller. A 5% increase in mass and drag and a forward translation of c.g. by 2% of the total length will be explored. Furthermore, the subsystems are designed and all of their elements are chosen or designed. Therefore, for each change in parameters, it should be investigated whether the subsystem has to be redesigned or whether it is more designated to decrease the mission target. In contrast to what was done during the preliminary design, iterations will be done to investigate the severity of parameter changes in better detail. All numbers and the flow of the sensitivity analysis is given in Figure 4.22. The following sections give extra information on this flowchart.

### 4.4.1 Increase in mass

The increased mass will require a higher lift generation, which in its turn requires a bigger cylinder and more fuel. The main drawback of resizing the cylinder is the redesigning of the horizontal supporting structure. The mass increase of the cylinder and the supporting structure will require a new iteration of the total mass. The lift increase of 5% will result in an equal drag increase of 5%. This assumption is justified since the L/D will remain constant and because the cylinder is the main source of the drag.

Another approach is to keep the same design and adjust the mission. This can be done by spinning the cylinder at a higher rpm or by increasing the flight speed, since a higher lift has to be produced. If these measures are applied separately, the efficiency of the cylinder will decrease. Therefore it is better to increase both these parameters to maintain the efficiency. The margins applied on the supporting structure are large enough so the support structures do not have to be redesigned to handle the increased loads. The result of this change is, however, that the engine has to produce more thrust, which will decrease the range. Furthermore, the take-off performance will also be negatively affected.

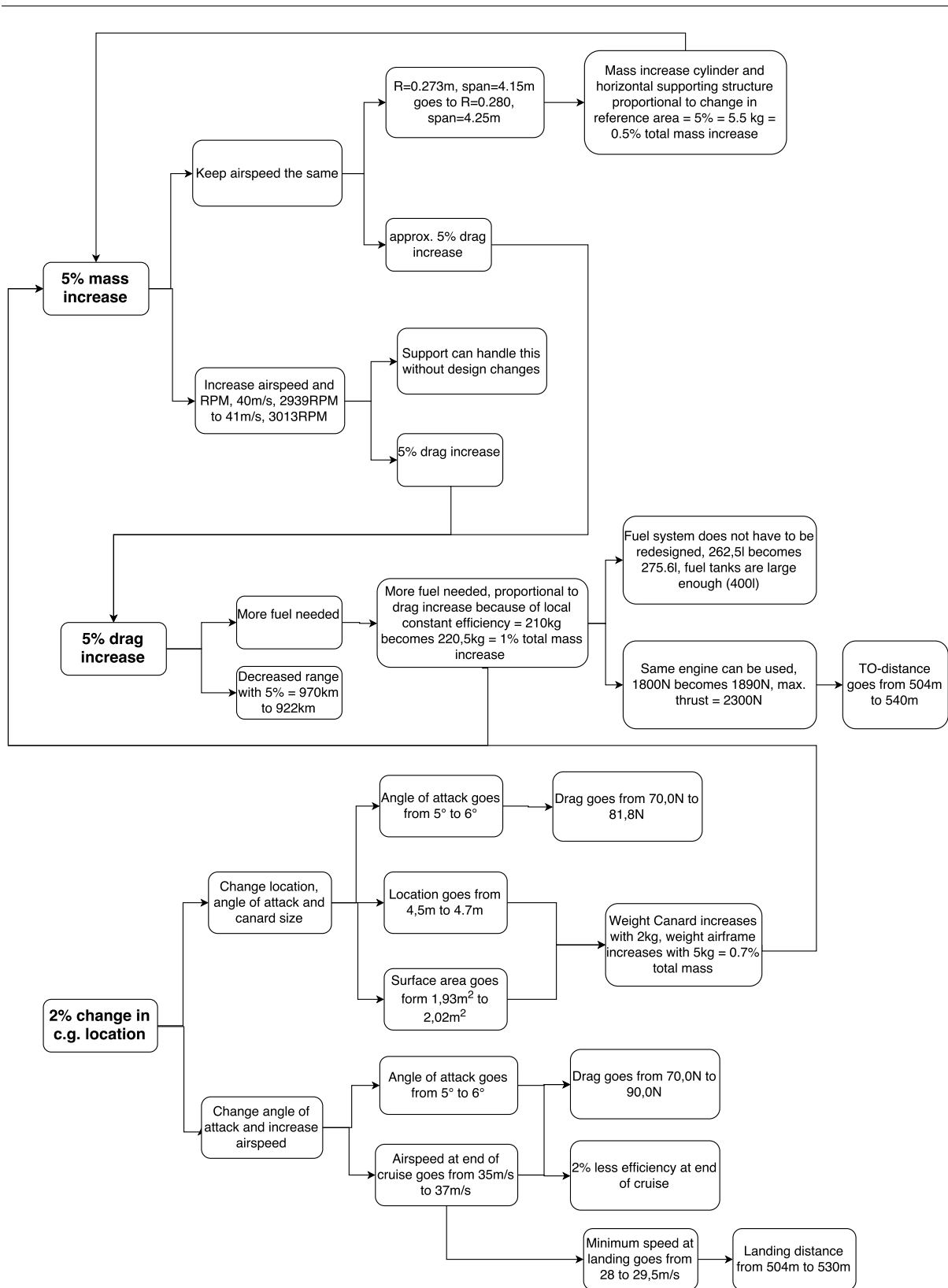


Figure 4.22: Sensitivity analysis on the final design. A presentation of the effect of a change in one of the major design parameters: mass, drag and c.g. location

---

#### 4.4.2 Increase in drag

More thrust will be needed, which results in more fuel to reach the same range. It is assumed that the efficiency of the engine is locally constant. Therefore the fuel weight increases proportionally to the drag increase. The additional weight causes an increase of 1% of the total mass, which has to be iterated. The additional fuel does not require an extensive redesign of the fuel system. The space available for fuel in the supporting wings is large enough. The engine has to deliver extra thrust, yet this can be delivered by the same engine. Using the same engine will decrease the excess thrust however, which will increase the take-off distance by 7%.

If the design remains the same, two options can be applied. The airspeed can be decreased to fly with the same thrust or the airspeed can be kept the same, which will require thrust increase. Both will result in a lower range, but to generate the same lift at a lower airspeed the rpm has to be increased. This will result in less efficiency and even more drag and, therefore, it is preferred to keep the airspeed the same. In this case the take-off distance also increases by 7%.

#### 4.4.3 Change in center of gravity location

Three measures can be taken to counteract the change in c.g. location. The surface area of the canard can be increased, the angle of attack can be increased or the canard can be moved forward. During the preliminary design these measures were analysed separately. Now these measures are applied together. This will result in a drag increase of the canard from 70.0 N to 81.8 N. This will not be iterated because it is negligible compared to the drag of the cylinder. The additional weight of the canard and the airframe, result in an increase of 0.7% of the total mass of the aircraft.

Two possible solutions to keep the design the same are to either change the angle of attack of the canard or increase the speed of the aircraft, which will make the canard more effective. The increased angle of attack and higher speed, increase the drag from 70.0 N to 90.0 N. Furthermore, the increased airspeed at end of cruise will result in 2% less efficiency (L/D) at end of cruise. This is an overall reduction of the efficiency of less than 1%. The stall speed will also increase. Therefore, the landing distance will increase from 504 m to 530 m. The take-off distance will not increase, because take-off will be done at a speed higher than the minimum one.

#### 4.4.4 Conclusion

Based on the sensitivity analysis a strategy can be chosen for a change in design parameters. The consequences are listed below for the 3 major changes in parameters. For these results, iterations were performed to come to the most detailed and precise results.

- Increase in mass (5%)
  - Airspeed increases from 40.0 m/s to 41.3 m/s
  - Rotational speed increases from 2939 rpm to 3035 rpm
  - Fuel weight increases from 210 kg to 224 kg
  - Landing distance increases from 504 m to 551 m
- Increase in drag (5%)
  - Airspeed increases from 40.0 m/s to 40.2 m/s
  - Rotational speed increases from 2939 rpm to 2954 rpm
  - Fuel weight increases from 210 kg to 223 kg
  - Landing distance increases from 504 m to 543 m
- Change of c.g. location (2% total length)
  - Angle of attack cruise increases from 5° to 6°
  - Drag of the canard increases from 70.0 N to 90.0 N
  - Airspeed at end of cruise increases from 35 m/s to 37 m/s

- 
- Efficiency at end of cruise decreases with 2%
  - Minimum speed at end of cruise increases from 28.0 m/s to 29.5 m/s
  - Landing distance increases from 504 m to 530 m

## 4.5 RAMS Characteristics

The Reliability, Availability, Maintainability and Safety characteristics (RAMS) were discussed in the preliminary design phase and were based on similar products. As this is a new and experimental aircraft, the most similar products are never actually built on this scale. The preliminary RAMS analysis for the Magnus Aeolus and its mechanisms is therefore based on estimations, whereas other subsystems which are still similar to existing products can be analysed by comparison. In this phase of the design process, the characteristics will be analysed more extensively. The characteristics of the preliminary design can be analysed in more detail and with respect to the subsystems instead of the system as a whole.

### 4.5.1 Reliability

To implement the Magnus effect, the wing is substituted by a fast-rotating cylinder. This not only changes the method of lift generation, but also influences the other major subsystems like control, structures and power and propulsion. The reliability analysis will be performed for all of these subsystems separately, as well as for the system as a whole to ensure the mission can be performed.

The reliability of the cylinder used in the lift subsystem can be examined by testing it in a wind-tunnel under predetermined flight conditions (thus in fact validating it). As this is a prototype, there are no data on the performance of such a cylinder and the reliability or the failure modes. Another way to determine the reliability before conducting a wind tunnel test is to use a scale model and analyse the performance of the cylinder. At this moment, all of the expected failure modes have been evaluated and mitigated. At this point in the project development of an entirely new concept, the reliability of the cylinder can not be guaranteed. Because of this, a safety system is implemented in the aircraft discussed later in the section.

A lot of off-the-shelf products are used during the production of the aircraft, which increases the reliability of those components and thus the aircraft. Examples of these off-the-shelf elements are both the engines, alternator, batteries, bearings, wheels, actuators, avionics and control computer. Only the exhaust temperature of the engine may pose a threat to the reliability of the aircraft as a whole. A cooling system for the exhaust is therefore designed, as is the material usage around the exhaust. This keeps the reliability of the airframe surrounding the exhaust high.

The control surfaces are the canard, the rudder and the aileron. The canard uses a conventional airfoil and sizing, which means that the reliability does not deviate from conventional aircraft. The ailerons are positioned on the horizontal winglike cylinder support, which means that they can also function similarly to conventional aircraft. The reliability of the rudders does deviate from the reliability of conventional aircraft. Downwash of the endplates on the rudders might influence their performance. This is an unknown interaction and it cannot be analytically determined. The solution is first to fly a model aircraft with control systems at the same position and evaluate the controllability of the aircraft. If the interaction does not pose any threats to the reliability in the model test, a full scale test will be conducted in the testing phase of the aircraft. The control surfaces are therefore deemed reliable enough to test them first on a small scale and then on full scale.

Finally, the reliability of the aircraft as a whole is evaluated. Failure of the main engine does not pose a big problem for the aircraft as a whole, as it can safely descent and land even if the aircraft is still at MTOW. Failure of the cylinder however, poses the only big problem. In order to create a reliable system this failure mode has to be considered. To this purpose, an all saver is added to the design, as is explained in section 3.8. This means that even in case of failure of the cylinders, the pilots still have a alternative to descent safely. Because the aircraft is saved as well, the failure cause and its consequences can be analysed, allowing improvements for future implementations of the aircraft.

---

## 4.5.2 Availability

Availability is primarily the result of the reliability of the system and the maintainability. It concerns the probability that a system is ready for use when that is required. The availability of the aircraft is assumed to be lower than for conventional aircraft. The reason is that a lot about the concept is unknown yet. This means the reliability is probably slightly lower, while the maintenance also takes more time and is performed more frequently. This increase in maintenance is also linked to the more frequent changing of the oil, because of the two engines which are used. Also, the availability currently can not be guaranteed during certain weather conditions, mainly because of the design being a prototype which is not designed for all possible conditions. As at this moment the aircraft is an experimental prototype and not a commercial aircraft, this lower performance with respect to availability is expected and can be taken into consideration during the planning of the operations. Something which increases the availability is the number of off the shelf products used. This increases not only the reliability of these parts, but also makes it easier to attain spare parts decreasing the time needed for maintenance. This increases the availability.

## 4.5.3 Maintainability

The experimental side of the mission brings some requirements on maintainability with it. The product will be tested and then used for the flight from Rotterdam-The Hague to London Heathrow airport. After this, it would be the end of life of the experimental aircraft and it could be donated to the TU Delft. When testing the aircraft, problems will arise, which could require a redesign of some subsystems. Thus, most of the parts of the aircraft should be replaceable. However, the prototype itself has a short operational life, as per Requirement **RMEA-SS-LT-8**, and the time until overhaul will not be reached for the engines and require little maintenance.

Nevertheless, the engines need to be and are designed to be accessible for other reasons, e.g. tuning, installation, oil replacement and so on. The rear top of the fuselage between the cabin and the fans can be removed to provide easy access to the G200 engine. The cowling for the Simonini engine can also be opened. Unfortunately, due to the location of this engine, it requires some facilities (e.g. a ladder) to be reached. Next to this location are also some of the most important parts from a maintenance point of view. The bearings and the rest of the rotor drive system need to be easily accessible during the prototyping phase. Moreover, the current design allows for easy removal of the entire rotor from the aircraft, even without dismounting the engine. The part that needs to be accessed most often is most likely the pretension screw for the bearings. Although the Kevlar material of the pretension wire doesn't exhibit a lot of relaxation with time, it might be expected that tightening the screw will happen often, especially in the early testing.

Another important aspect for maintainability, is the modular nature of the side support structure. As already mentioned, it was designed such that the cylinder can be removed if it proves inadequate to lift the aircraft or if endplates need to be removed, special surface coverings added, etc. The most likely reason for repeated removal of the cylinder however, is balancing. Although the cylinder can be re-balanced without any disassembling, by moving the balancing weights along the spokes, accurate determination of its balance might require measurement tools for which separating the rotor from the aircraft is necessary. In addition, balancing on the sides of the cylinder is limited and adjusting the balance in case of damage is by necessity done in disassembled state.

Other parts of the aircraft that require easy access and should be replaceable are all actuators, the fuel system tubing, electrical wiring, hydraulic tubing for the brakes, etc. Access to all electronic components, such as gyroscopes, accelerometers or other sensors, as well as the control units and the connections between them, is also necessary. To ensure this, openings are present at key locations, and the above listed items are grouped together, as well as mounted in a way such that their removal doesn't damage the rest of the structure. For example, when an item is mounted to a sandwich structure, suitable metallic inserts are present to protect the brittle core and fibres.

---

#### 4.5.4 Safety

The safety characteristics for this aircraft are considered for both the pilots and the aircraft. The airframe and frame of the rotor is designed fail safe; the structure has multiple elements carrying the same loads, in case one fails. However, the connection between the rotor and the airframe is designed safe life. First of all, the placement of the two ducted fans is behind the engines, which means that the passengers are not in danger when a blade detaches. As for the safety of the cylinder, the ducts contain the fan blades in case of detachment and in case this does not work, fans are also placed slightly behind the cylinder. The blades can therefore hurt neither the passengers nor the cylinder.

Another important matter to discuss with respect to safety is the noise for the pilots. Both the cylinder and the engine produce noise and the pilots have to be protected from this. The fuselage protects the passengers from the noise of the cylinder, but for the engine a separate measure has to be taken. Behind the passengers, there is a bulkhead shielding them from the engine. This protects the passengers from the noise and the heat of the engines. Earplugs and headphones will be used by the pilots to minimize the noise interference. Additionally, if engine failure occurs the bulkhead also acts as a firewall protecting the passengers from the fire. More about this bulkhead can be found in subsection 3.5.1.

To increase the safety of the aircraft and considering that it is an experimental mission, there will be a parachute system, as discussed in section 3.8. This means that in case the cylinder fails, both the pilots and the aircraft as a whole can descend safely. An alternative in case of parachute failure would be to fly the aircraft at a high angle of attack and glide using the canard and the winglike horizontal support as lift providers. The efficiencies of this gliding flight can be determined using the reference areas of the canard, body and horizontal support and their lift coefficients. Preliminary calculations indicate engine power is necessary in order to perform this gliding flight. The aircraft is able to glide between 10 and 15 km if the rotor is not functioning while the main engine still is, using the horizontal support to provide most of the lift. Full power is needed however, which can also provide part of the lift. This possibility could be further analysed in the next phase of the project.

### 4.6 Risk Evaluation

The risk evaluation consists of two parts, the risk map and the risk mitigation. The risk map considers the risks for different components and aircraft systems. Afterwards, the risk mitigation solves the high and noticeable risks to make Magnus Aeolus as a whole more reliable.

#### 4.6.1 Risk map

During the start of the design multiple risks were presents and this number increased when going more detailed into the design. The following subsystems are considered in the risk: Cylinder (Cyl), Power and propulsion (P&P), Control (Cont), Structural (Struc), Operations (Ops), Manufacturing (Man), Repairability (Rep), Materials (Mat), Airport (Airt), Market (Mark), Sustainability (Sus) and Design process (Des). The first column of Table 4.10 states the subsystem and its event. Then the following three columns state: the probability that the event occurs, the impact the event has on the mission and lastly the risk, which is the product of the impact and the probability. The first three columns describe the potential risks at the start of the detailed design and the last three after risk mitigation.

To come up with the initial values for the risk mitigation a baseline has to be set. This was determined as follows. For probability, the scale is 0 (proven flight design), 25 (extrapolated from existing flight design), 50 (based on existing non flight engineering), 75 (working lab model) and 100 (feasible in theory), whereas the scaling for impact is 10 (negligible), 40 (marginal), 70 (critical) and 100 (catastrophic). Catastrophic is defined as that the system will not be able to perform its mission, which is proving the Magnus effect. Whereas critical means that the secondary mission is questionable, which in this case in actually flying from the Hague to London. When the risk was 70 or larger, serious mitigation actions needed to be defined, when the risk exceeded 30 some slight mitigation was done. The mitigation of the risky events is discussed in subsection 4.6.2

Table 4.10: Risk assessment: before (mid) and after (right) mitigation. For probability, the scale is 0 (proven flight design), 25 (extrapolated from existing flight design), 50 (based on existing non flight engineering), 75 (working lab model) and 100 (feasible in theory), whereas the scaling for impact is 10 (negligible), 40 (marginal), 70 (critical) and 100 (catastrophic).

Subsystem: Event	Prob.	Impact	Risk	Prob.	Impact	Risk
Cyl.1: Downwash of the cylinder interferes with duct	100	100	<u>100</u>	25	70	18
Cyl.2: Experience a too high load/low load factor	75	70	<u>53</u>	25	70	18
Cyl.3: Cylinder does not provide any lift	50	100	<u>50</u>	0	100	0
Cyl.4: The end plates will reach supersonic speed	100	40	<u>40</u>	25	40	10
Cyl.5: Large deflection of the end plates	75	40	<u>30</u>	50	40	20
Cyl.6: Bearings are loaded incorrectly	75	40	<u>30</u>	25	40	10
P&P.1: Engine failures	50	70	35	25	40	10
P&P.2: Blade detachment due to e.g. bird strike	25	40	10	25	40	10
P&P.3: Gearing failure	25	40	10	25	40	10
P&P.4: Fuel depletion	0	40	0	25	40	10
Cont.1: Controllability too difficult or too minimal	100	100	<u>100</u>	25	70	18
Cont.2: Rudder might not be effective due to endplates	100	100	<u>100</u>	25	70	18
Cont.3: Dynamic stability insufficient	75	100	<u>75</u>	50	40	20
Cont.4: Control surface failure	25	40	10	25	40	10
Cont.5: Autopilot failure	25	40	10	25	40	10
Cont.6: Avionics failure	0	40	0	0	40	0
Struc.1: Aircraft weight too high for efficient flight	50	40	20	50	40	20
Struc.2: Structural failure of any component	25	70	18	25	70	18
Ops.1: Hypoxia	25	70	18	25	70	18
Ops.2: Environmental conditions, e.g. corrosion	25	70	18	25	70	18
Man.1: Producibility of the components is too difficult	50	70	<u>35</u>	25	40	10
Man.2: Duration of production is too long	50	10	5	50	10	5
Rep.1: Product not repairable	75	70	<u>53</u>	25	70	18
Rep.2: No spare parts available	25	10	3	25	10	3
Mat.1: Material failure or material imperfections	25	70	18	25	70	18
Airp.1: Does not comply with airports regulations	100	70	<u>70</u>	25	70	18
Airp.2: Runway too harsh for the system	0	70	0	0	70	0
Airp.3: Runway too short for the aircraft	0	70	0	0	70	0
Mark.1: Does not suit any market	75	10	8	75	10	8
Sus.1: Noise system do not meet regulations	75	40	<u>30</u>	50	40	20
Sus.2: Emissions system does not meet regulations	75	40	<u>30</u>	50	40	20
Des.2: Inconsistencies in the design	100	100	<u>100</u>	25	100	25

---

## 4.6.2 Risk mitigation

### High risks

- Cyl.1: The duct was split into two smaller ducts to decrease the diameter. This resulted in a larger distance between the cylinder and the top of the duct. Also the duct is conically shaped in order to have a slope similar to the downwash of the cylinder. These changes were simulated in Ansys and after a few iteration, this risk was decreased significantly.
- Cont.1: The maneuverability of the design shall be simulated and tested in a with a mathematical flight model to assess possible difficulties. When difficulties arise the design shall be adjusted accordingly.
- Cont.2: The rudder was first the full length of the vertical support and the rudder could only deflect outwards due to the presence of the endplates. However due to possible interference the vertical tail was extended downwards below the horizontal wing and the rudder was downsized to fit under the endplates. This also resulted in the rudder being able to deflect inwards and outwards.
- Cont.3: Firstly, the stability characteristics should be thoroughly simulated for the verification of the stability. A scale model shall be made to further validate the characteristics. Lastly, the final design shall have multiple flight tests before the mission from Rotterdam The Hague to Heathrow shall be performed.
- Airp.1: An assessment shall be done of the airport regulations and when possible the design shall be adjusted according to the airport regulations.
- Des.2: Again proper project management is performed here. The consistency of the design is managed by the chief engineer, that has log book of every engineering departments. He also makes sure that everyone has access to the information of every department.

### Noticeable risks

- Cyl.2: The load factor is the ratio between the lift and the weight of the system. Therefore, two factors need to be taken into account. The management of the weight shall be done by means of close monitoring of whether or not it divergences during the design phase and taking proper action when it does, and by means of contingency management. The lift shall be managed during the design phase, taking into account the negative lift of a Magnus rotor that occurs at certain lower Reynolds Numbers. The aircraft shall be designed that it does not have to operate in these Reynolds Number conditions.
- Cyl.3: A scale model will be tested before the actual aircraft is built, to prove the that the cylinder will actually provide lift. When the actual aircraft is built, the cylinder is made detachable in order to make changes to the cylinder such that it will actually provide the lift required.
- Cyl.4: During the design this was taken into account by sizing the endplates properly. The maximum rotational speed that the cylinder will experience is 3100 rotations per minute. With the current dimensions this is still far from going supersonic.
- Cyl.5: Due to the endplates being close to the vertical support, there was a probability of the endplates actually hitting this support. This was firstly taken into account by creating a gap between the end plates and the support. Secondly, the stiffness of the material and the shape was selected such that under load the plates' deflection is always less than this gap.
- Cyl.6: Normally bearing are not loaded under a moment, however with the cylinder producing lift this is the case. The selected bearings are self aligning in order to mitigate this problem
- P&P.1: When a piston of an IC-Engine fails, the complete engine will stop working. However a Wankel engine was selected for this aircraft, which uses a rotor instead of pistons. The selected engine has two rotors, with having the benefit of when one rotor fails the engine will just work on half power. This power is enough to safely descent.

- 
- Man.1: Manufacturing can be simplified by using off-the-shelf components and in-house production methods.
  - Rep.1: Split some of the integrated designs, such that at failure only a small component needs to be replaced. Have multiple spare parts for every components, depended on the risk and the cost of the component.
  - Sus.1: Noise mitigation is done by: firstly, using ducted fans to contain fan noise. Secondly, the wheelpants decreases the drag of the landing gear, which also mitigates its noise. Thirdly, the engine manufacturing is currently working on an improved design of their current engine line, with main focus to largely reduce the noise.
  - Sus.2: Predictions shall be made on the level of sustainability of the use of the system and where possible the most sustainable design choices shall be made, for example in the choice of fuel.

## 4.7 Market Analysis

After discovering the strengths and uniqueness of Magnus Aeolus, three market spaces have been developed that the aircraft can fit into. These are the Scientific Market, the Unconventional Personal Aerial Vehicle (PAV) market and The Remote Controlled (RC) Aircraft market.

### 4.7.1 Scientific Market

Nasa's X-plane program is a program funded by NASA to investigate experimental aircraft that have the potential to provide improvement to current aviation or to investigate new technology and new ways of flying <sup>4</sup>. Many concepts such as supersonic or hypersonic aircraft, ramjets, thrust vectoring etc. were developed as X-planes before they, or a variation of them, made their way to aviation.

The Magnus Aeolus aircraft perfectly fits NASA's X-plane program, mainly because it acts as a great research tool to push for improvements in aeronautics. NASA can use this concept to investigate whether the use of this concept in aeronautics can result in improvements of the next generation aircraft. NASA can also provide the required funds to explore some of the previously dropped concepts. A prototype can be made to explore the feasibility of the design and gather actual flight data to confirm theoretical researches. Moreover, the results can be used by NASA to implement a variation of Magnus aircraft to current aviation designs.

Other than the X-plane program, the contribution of this project to general scientific market is worth mentioning. The information, experimental data, etc. on the subject are very limited. Hence, this project together with its special features such as the Remote Controlled aircraft, Computational Flow Dynamics simulations, state space flight dynamics simulation will have a contribution to the scientific market. Experimental and analytical data together with aerodynamic characteristics of an aircraft with major gyroscopic procession will add a lot of value in the scientific aviation market.

On top of that, the model is constructed in such a way that it gives the capability to remove or replace the cylinder with any other shape of interest. This is specifically done for experimental purposes in order to test different cylindrical configuration and test their performances. This gives the possibility to e.g. test tapered cylinders, Thom rotors, augmented wings, etc. without making major changes to the design and shape of the Magnus Aeolus aircraft. This shows the flexibility of the design, which is important when gathering experimental data about using the Magnus effect in a sustainable manner.

### 4.7.2 PAV market

Although Magnus Aeolus fits best in the scientific market. It is possible that when further research is done, the Magnus effect has a future in the aviation market. In the baseline report [69], the Personal

<sup>4</sup><http://www.nasa.gov/feature/nasa-aeronautics-budget-proposes-return-of-x-planes>

Aerial Market was considered suitable for Magnus Aeolus. The PAV Market is a future market created by NASA that wants to promote aerial vehicles for personal use for the general public [70]. Requirements include a door-to-door transportation, flyable with only a driver's licence and as affordable as a car. Currently, there is no such product that fulfills these requirements, because for flying an aircraft amongst others a drivers license is not sufficient. However there is a wide variety of products that transport a payload of between 1-4 people, shown in Figure 4.23 which include all the unconventional solutions like a flying car, jetpack, helicopters and ultralight aircraft.

The customers that will buy these PAVs, are wealthy individuals with a pilot license of at least an ultra-light aircraft. They are very adventurous and innovation oriented. They are looking for products that are eye-catching, are one of a kind and offer a unique experience. Magnus Aeolus fits this profile perfectly. Its unique design allows for an one of a kind flight experience and can be used for long range personal transportation.

When comparing the aircraft with its PAV competitors, shown in Table 4.11, it shows that Magnus Aeolus fits quite well in this market. It has a high fuel consumption, comparable with the R22 helicopter, and has a take-off distance of approximately a regular aircraft. The range is just short of a regular 2-seater aircraft, like the TECNAM P2002 JF. It can be best compared with the Icon A5, an amphibious 2-seater aircraft, with foldable wings for transportation. It is an unconventional aircraft that is for fun outdoor entertainment, that has its price-tag, but is less of a problem for the more wealthy investors. The purchase price might be higher than those in the table but this is due to the fact that this configuration is unique and the methods for building it is not yet developed to an extent of a conventional aircraft.



Figure 4.23: Competitors in the PAV market, named from top left to top right, bottom left to bottom right: Airborne XT-912 Ultralight [71], The Icon A5 [72], Cobalt Co50 Valkyrie [72], Tecnam P2002JF [72], Robinson R22 [73], Terrafugia Transition [74] and Martin Jetpack [75]

Magnus Aeolus would be then for the PAV market, which contain wealthy aviation enthusiasts. To specify further, The aircraft is made for pilots that want an one-of-a-kind flying experience. Its long range means that you can travel across Europe with multiple stops at interesting locations. The low stall speed allows for the passenger to make beautiful pictures of the environment, while the pilot enjoys a unique flying experience. If Magnus Aeolus has the same popularity as the Icon A5, an annual production of 40 aircraft can be expected [72].

### Entry barriers

Following section is based on the EASA aircraft certification<sup>5</sup>. In order for a newly developed aircraft concept to enter operation, a type certificate needs to be obtained. This type certificate is delivered by the responsible aviation regulatory authority, being the EASA for Europe and the FAA for the United States of America. The above mentioned type certificate evidences that the aircraft meets the safety requirements set by the regulatory authority. As a first indication of a certification process, the EASA

<sup>5</sup><https://www.easa.europa.eu/easa-and-you/aircraft-products/aircraft-certification>

Table 4.11: 7 type of the competitors to Magnus Aeolus. Note \*: This not the cost of the first prototype and certification cost was assumed to be an initial investment.

Model	Magnus Aeolus	Airborne XT-912 [71]	The Icon A5 [72]	Cobalt Co50 Valkyrie [72]
Purchase costs-[\$]	340,000*	50,000	189,000	700,000
Fuel consumption-[L/h]	37	11	22	60
Capacity	2	2	2	47
Range-[km]	970	690	790	1,900
Cruise Speed-[km/h]	135	130	175	480
Take off distance-[m]	300	235	220	550
Model	TECNAM P2002 JF [72]	Robinson R22 [73]	Terrafugia Transition [74]	Martin Jetpack [75]
Purchase cost	133,000	288,000	279,000	300,000
Fuel consumption-[L/h]	17	36	6.7-18.9	90
Capacity	2	2	2	1
Range-[km]	1090	460	640	50
Cruise Speed-[km/h]	220	160	160	56
Take off distance-[m]	320	Vertical	518	Vertical

was chosen as certification basis. Note that the certification of an aircraft is a very expensive and time consuming process. Only an indication about a Primary Category certification for the FAA has been estimated at about \$1million, which is in fact an aircraft for pleasure and personal use. The type-certification process of new aircraft consists of 4 steps:

1. Technical Familiarisation and Certification Basis: The project is presented to EASA at the point at which a sufficient mature design is reached. The certification team, and the set of regulations that will be employed are established, i.e. the Certification Basis.
2. Establishment of the Certification Programme: The means of demonstrating compliance of the aircraft with each requirement is agreed upon by the aircraft manufacturer and EASA.
3. Compliance demonstration: The product demonstrates its compliance with the set of requirements, all different aspects such as the structure, engines, control systems, electrical systems and flight performance are analyzed. Tests are performed both on the ground as during flight and are analyzed by EASA experts.
4. Technical closure and issue of approval: In case EASA is satisfied with the compliance demonstration, the investigation is completed and finalized by the issuing of the certificate. Note that the primary certification delivered by the EASA can be in parallel validated by foreign authorities (e.g. FAA).

Another entry barrier might be the innovative and experimental nature and look of the aircraft. A great deal of logical skepticism and hesitancy by a large part of the public together with a lot of bias of the product is expected, having the necessary familiarization and a slow introduction as a consequence.

### 4.7.3 RC model market

The last possible market is to sell small scale remote controlled version of the aircraft. An example is provided in Figure 5.19, Aeolini RC model. Aeolini RC model is completely unique with a very unconventional configuration which is a great point of interest to anyone interested in RC model aircraft. The price of conventional RC aircraft ranges between \$ 150 to more than \$ 500 while the Aeolini costs about \$ 200 dollars to make and it can be sold for about \$ 400 with the transmitter, batteries and including its uniqueness factor. This model can be used to raise awareness about the Magnus aircraft and show that it really works so clients and buyers can gain trusts on feasibility of the full scale aircraft, Magnus

Aeolus. It is also can be used to partially fund Magnus Aeolus’s design optimization and exploration phase. The market space goes beyond just individuals buyers and to universities or companies who want to do experimental or wind tunnel studies on small scale Magnus aircraft.

## 4.8 Compliance Matrix

The compliance matrix gives an overview of all of the requirements and whether the requirements are fulfilled by the design. First, the requirements for the mission and aircraft as a whole are shown in Table 4.12. Afterwards, the subsystem requirements and their compliance is illustrated using Table 4.13. Together, the table provide a full overview of the adherence of the design to the requirements.

Identification	Requirement	Yes/No
RMEA-MIS-1	The range shall be at least 350 km	Yes
RMEA-MIS-2	The aircraft shall withstand load factors between 3.8 and -1.5g	Yes
RMEA-MIS-3	The Magnus effect shall be the main lift provider	Yes
RMEA-SYS-1	The load transferring subsystem shall be 50 percent recyclable	Yes
RMEA-SYS-2	An end-of-life solution for all of the aircraft components shall be formulated	Yes
RMEA-SYS-3	The aircraft shall be able to descent and land safely in case of engine failure	Yes
RMEA-SYS-4	The aircraft shall ensure the safety of the pilots	Yes
RMEA-SYS-5	The aircraft shall be able to adhere to the noise mitigation procedures at LHR	Yes
RMEA-SS-LG	The system shall contain a lift providing system.	Yes
RMEA-SS-SC	The system shall accommodate a control system.	Yes
RMEA-SS-LT	The system shall accommodate a load transferring subsystem.	Yes
RMEA-SS-PP	The system shall accommodate a Power & Propulsion system.	Yes

Table 4.12: Compliance matrix of the design. Compliance indicated in rightmost column (yes/no).

As Table 4.12 shows, all of the mission requirements are met. Similarly, the requirements for the aircraft system are almost all fulfilled, which means the design contains a lift generating, stability and control, load transferring and propulsion and power subsystem. The other requirements for the system as a whole which are primarily focused on sustainability and safety, have been achieved as well.

As for the subsystem requirements, the compliance is shown in Table 4.13. This indicates that again most of the requirements have been met. For the lift generating subsystem, all of the requirements have been fulfilled. For both the stability and control subsystem and the load transferring system this is also the case. Finally, the power and propulsion subsystem fulfills six out of seven requirements. The requirement on the  $CO_2$  has not been reached. An explanation is that the requirement was based on car emissions and because of the higher fuel consumption of aircraft this was an unrealistic goal. Overall, the aircraft is able to fulfill all of the mission requirements set by the stakeholders and most of the other requirements determined based on the functions of the different subsystems. The requirement which is not yet met by the subsystems will be discussed and evaluated in section 5.6, where recommendations for the future of the project will be given.

<b>RMEA-SS-LG-1</b>	The lift providing system shall use the Magnus force as primary lift vector	Yes
<b>RMEA-SS-LG-2</b>	The minimum $\alpha$ shall be above 0.2 for Reynolds numbers between 99000 and 501000	Yes
<b>RMEA-SS-LG-3</b>	The downwash of the cylinder shall not hinder the capabilities of the control surfaces	Yes
<b>RMEA-SS-LG-4</b>	The torque of the cylinder shall be within the range of propulsion systems	Yes
<b>RMEA-SS-LG-5</b>	The rotational rate of the cylinder shall be within the range of propulsion systems	Yes
<b>RMEA-SS-LG-6</b>	The relative Mach number on any point of the lift providing system shall be lower than 1	Yes
<b>RMEA-SS-SC-1</b>	The control system shall make the aircraft longitudinally stable during cruise, ascending, descending, take-off and landing	Yes
<b>RMEA-SS-SC-2</b>	The control system shall make the aircraft laterally stable during cruise, ascending, descending, take-off and landing	Yes
<b>RMEA-SS-SC-3</b>	The control system shall allow a rate of turn of 26.6 deg/s	Yes
<b>RMEA-SS-SC-4</b>	The longitudinal control system shall have a trim drag of less than 10% of the total drag during cruise	Yes
<b>RMEA-SS-SC-5</b>	The control system shall eliminate cross control during maneuvering	Yes
<b>RMEA-SS-SC-6</b>	The aircraft shall be able to roll from a steady 30 degrees bank through an angle of 60 degrees within 5 seconds	Yes
<b>RMEA-SS-SC-7</b>	The aircraft shall be able to carry out landing for 90 degrees cross-winds of up to a wind velocity of 10 knots	Yes
<b>RMEA-SS-LT-1</b>	The load transferring subsystem shall be capable of transferring 60 000 N aerodynamic load from the LGS to the airframe	Yes
<b>RMEA-SS-LT-2</b>	The load transferring subsystem shall be capable of transferring -20 000 N downward load from the LGS to the airframe	Yes
<b>RMEA-SS-LT-3</b>	The subsystem shall enable the rotation of the rotor	Yes
<b>RMEA-SS-LT-4</b>	The subsystem shall transfer power from the rotor engine to the rotor	Yes
<b>RMEA-SS-LT-5</b>	The subsystem shall be capable of transferring the loads generated by other subsystems to the airframe	Yes
<b>RMEA-SS-LT-6</b>	The subsystem shall be capable of accommodating the pilot and their luggage at total mass of 100 kg	Yes
<b>RMEA-SS-LT-7</b>	The subsystem shall be capable of accommodating the pilot in comfort	Yes
<b>RMEA-SS-LT-8</b>	The subsystem shall have an operating time of 100 hours	Yes
<b>RMEA-SS-LT-9</b>	The subsystem shall have an operating temperature range from -20 to 50 degrees Celsius	Yes
<b>RMEA-SS-LT-10</b>	The subsystem shall be able to carry a maximum load of 6 g during landing operations	Yes
<b>RMEA-SS-LT-11</b>	The subsystem shall have a service life of 1 year accommodating an environment containing salt water, ice, rain and hail	Yes
<b>RMEA-SS-PP-1</b>	The P&P system shall emit less than 100 grammes per kilometres of CO2 per engine	No
<b>RMEA-SS-PP-2</b>	The P&P system shall have a noise level below 82 Decibel	Yes
<b>RMEA-SS-PP-3</b>	The P&P system shall have a to-be-overhauled time of at least 1500 hours	Yes
<b>RMEA-SS-PP-4</b>	The P&P system shall be able to use more than one fuel	Yes
<b>RMEA-SS-PP-5</b>	The P&P system shall be maintainable	Yes
<b>RMEA-SS-PP-6</b>	The propulsion fuel shall not release toxic gases	Yes
<b>RMEA-SS-PP-7</b>	The propulsion engine shall be able to provide a max power of 140 kW	Yes

Table 4.13: Compliance Matrix of the subsystems. Compliance indicated in rightmost column (yes/no).

---

## Chapter 5

# Project Implementation

The project implementation shows the next steps of the project. It uses the design discussed in this report as the starting point, refines the design and goes into the production, certification and the mission. This is discussed in the project development and design. A production plan is provided, as well as a cost breakdown of this phase of the project. The planning for the next project stages is also shown using a Gantt chart. The future of the project is then considered with respect to the markets and possible implementations.

### 5.1 Project Development & Design Logic

This section gives an overview of the activities that have to be executed and the next phases of the project. In Figure 5.1 an overview of the different phases is given. These are all separately discussed throughout this section. The design discussed throughout this report is the starting point for these activities. First, extra experimental data is gathered to explore additional modifications for the current design. These modifications may then be implemented during the design optimization, taking into consideration the interaction between different systems. Then the design is validated, before the product can be manufactured. During the manufacturing, unit and assembly tests are performed. Also, the aircraft as a whole is tested and these data together with the test data from the production and validation can be used for the certification. Parallel, the operations are prepared. Finally, the aircraft is ready to perform the mission and fly to Heathrow.

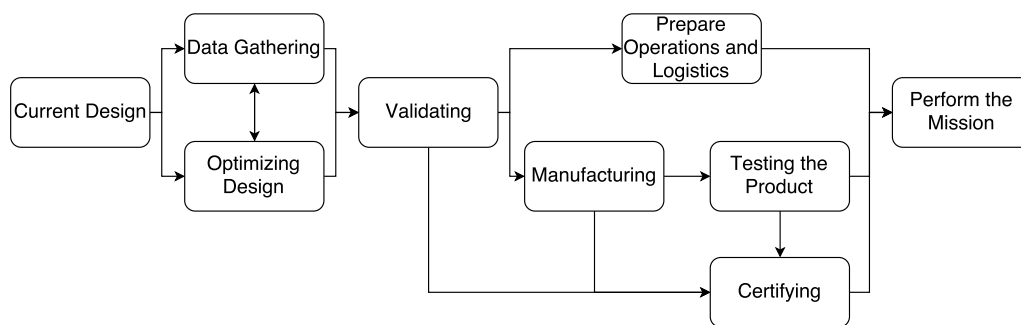


Figure 5.1: Project Development & Design overview project phases

#### 5.1.1 Experimental data gathering

Additional improvements to the design can only be realised if data about these improvements can be obtained. These tests include wind tunnel tests to explore modifications to the cylinder. These modifications include the varying of the endplates, addition of airfoils and the addition of spanwise discs. Also, the downwash and aeroelasticity of the cylinder can be determined. Besides this, also the gyroscopic effect of the cylinder and an actuator will be tested. This data can then be compared to the data of the current design, and possibly design changes can be implemented. An overview of the flow of the tests is shown in Figure 5.2. A more extensive discussion on possible experimental testing is given in section 5.3.

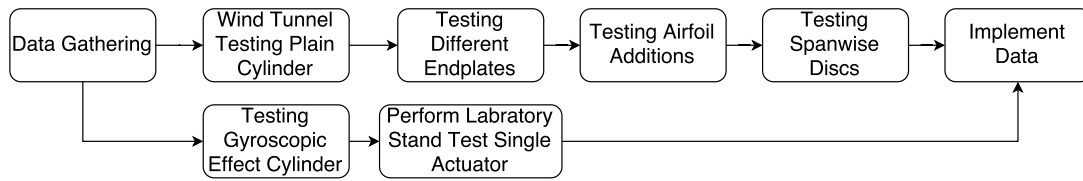


Figure 5.2: Project Development & Design experimental data gathering phase

### 5.1.2 Design optimization

Most changes to be implemented influence the whole design. Figure 5.3 shows the flow of the optimization process. Test data may initiate changes to the cylinder, the structure or the control surfaces. These changes might influence other components as well, which means the influence has to be quantified and adjusted. Besides this, the duct and the ergonomics have to be optimized to finalize the design.

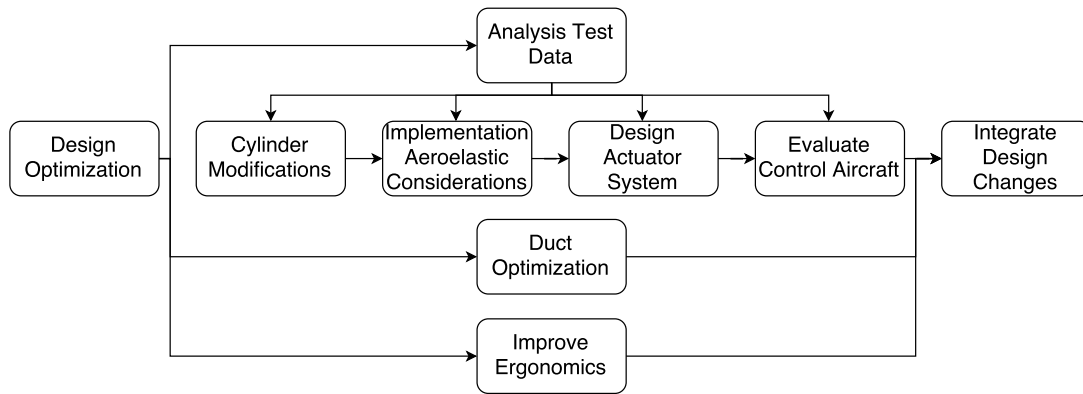


Figure 5.3: Project Development & Design optimization design phase

### 5.1.3 Validation of the design

The validation of the design is the next big step in the design process. For the different components, different validation methods will be used. Table 5.1 shows the major components and the validation method that will be used. There are a number of different ones which can be used for the validation of the design. The methods used are testing, simulation, relying on documentations and predictions based on similarities. The validation of the aircraft will be executed later during the aircraft test phase.

Component	Validation Method	Component	Validation Method
Cylinder	Wind tunnel test	Engine Shield	Material heat test
Simonini mini 2 plus	Documentation		Analysis
Mistral G200	Documentation	Materials Structures	3 point bending test
Ducts	Simulation flow		Coupon test
Control Surfaces	Flightgear simulation		Perimeter shear test
Ergonomics	Similarities		Lap shear joint test
Landing Gear	Similarities		

Table 5.1: Validation methods for subsystem design validation

---

### 5.1.4 Prepare operations and logistics

There are a number of operational considerations which have to be considered before the aircraft can be tested and the mission can be performed. These preparations include the reservation of a hangar for the aircraft to stay in when it is inoperative. Similarly, transportation for the aircraft from the production facilities to the hangar and from the hangar to the airfields has to be arranged. A test pilot and a pilot for the actual mission have to be found, preferably the same pilot. Then, arrangements have to be made with the airfields to be able to test the aircraft and to be allowed to use the airfields during the mission. Finally, fuel has to be bought. Arrangements have to be made at Heathrow in case loiter time exceeds the predictions to be able to return to Rotterdam. An overview of these preparations is shown in Figure 5.4.

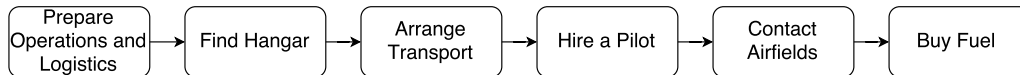


Figure 5.4: Project Development & Design preparation operations and logistics phase

### 5.1.5 Production and assembly

The next phase for the project is manufacturing the design. An extensive production plan for this phase of the project is produced to illustrate the procedures and can be found in section 5.4. A short overview of this phase in terms of actions is shown in Figure 5.5. One of the tests to perform during the sub-assembly tests is the Iron bird test, discussed in subsection 5.3.3. First, parts are manufactured and separately tested. Then, the sub-assemblies are produced and tested as well. After this, the total assembly can be executed to generate the aircraft as a whole. The integration phase then tests the interaction of the different sub-assemblies and whether production has been completed successfully.

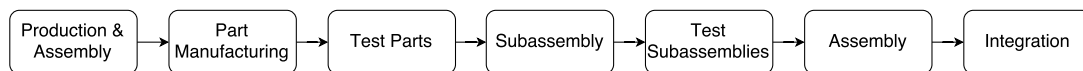


Figure 5.5: Project Development & Design manufacturing phase

### 5.1.6 Testing the product

An extensive plan for the tests of the aircraft is provided in subsection 3.9.1. A summary of these tests is also shown in Figure 5.6. These test results can be used to improve the aircraft and certify it, before the actual mission is performed. These tests include ground tests, take-off and landing tests and tests at cruise altitude. Data are gathered throughout the test phase to analyse the performance and possibly adjust the aircraft.

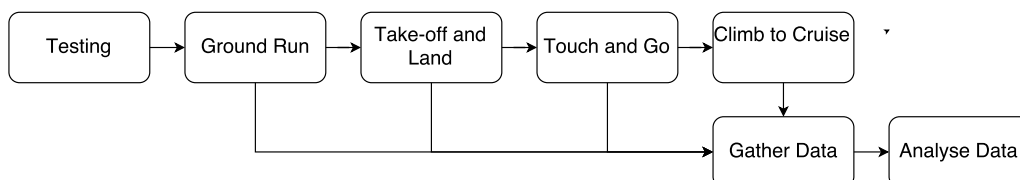


Figure 5.6: Project Development & Design Test phase

### 5.1.7 Certification

The certification of the aircraft is an important step towards performing the mission. The certification the aircraft will have to adhere to is given in section 4.7. The EASA was chosen as the basis for the

certification. The results from the validation, unit and assembly tests and aircraft tests are used to complete this certification.

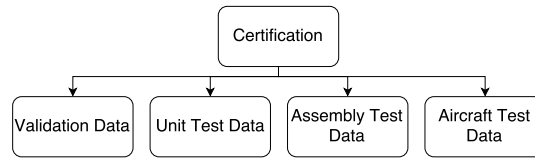


Figure 5.7: Project Development & Design certification phase

### 5.1.8 Performing the mission

The final phase of the project is performing the actual mission. The execution of the mission can be done after the certification and testing of the aircraft. First, a final check is performed for the aircraft as a whole. Then the flight plan is submitted before the flight can be initiated. The actual flight will be performed according to the operations discussed in section 3.9. After the flight to Heathrow has been completed and the stroopwafels have been delivered, the aircraft can fly back to Rotterdam if there is sufficient fuel left. An overview of this project phase is shown in Figure 5.8.

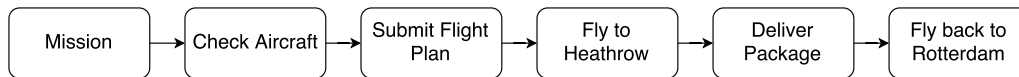


Figure 5.8: Project Development & Design mission performance phase

## 5.2 Project Gantt Chart

The Gantt chart in Figure 5.9 gives an overview of the planning for the next phase of the project. It consists of the different phases discussed in section 5.1. As the chart shows, there are a number of project phases executed simultaneously. The optimization of the design and the implementation of the design modifications begins after the first test results are obtained. Also, the operations are prepared parallel to the validation of the design, as both have to be finished prior to starting the manufacturing. The certification is an ongoing process, beginning with the validation of the design, continuing during the manufacturing and ending with the testing of the aircraft. Finally, approximately two years from now the mission is expected to be performed and the package can be delivered to Heathrow.

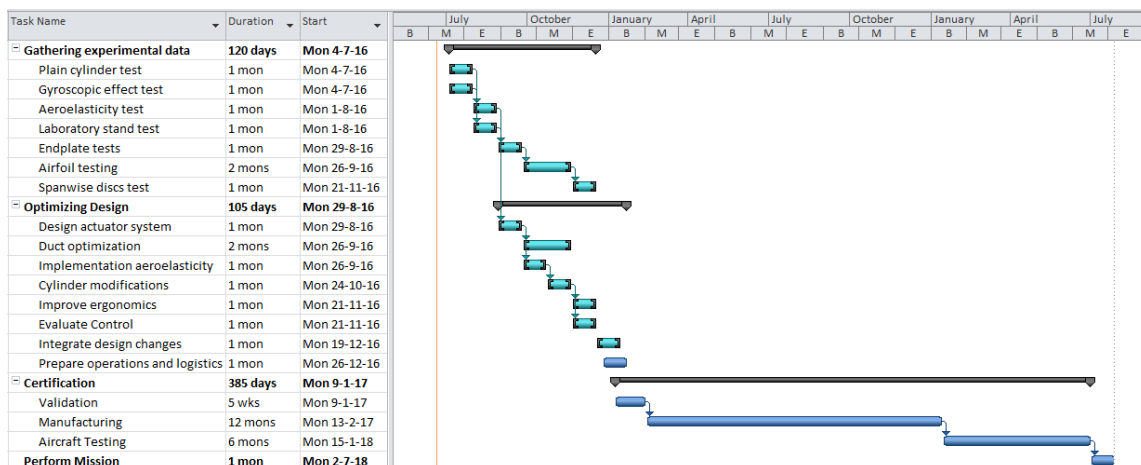


Figure 5.9: Project Gantt chart for the next phases of the design and implementation of the project.

---

## 5.3 Experimental testing

As discussed there are a number of tests which preferably are executed before finalizing the design phase of the project as a whole. This consists of tests which can already be executed and tests for which the facilities are currently not available. Both are discussed in this section. First of all, an outline of the test which would preferably be executed later on in the design process, consisting primarily of wind tunnel tests. Then, testing with and RC model is discussed. Finally, a simulation of the flight of the aircraft as a whole is discussed.

### 5.3.1 Exploration of cylinder modifications

As discussed before, in the next phase of the project data gathering will play an important role. The main motivation for this is that there are a number of disadvantages of the current design with respect to other aircraft. The most important disadvantage is the high drag of the aircraft, which is related to the low lift to drag ratio. This section describes a number of modifications for the cylinder which may increase this ratio by either increasing lift or decreasing drag. The effects of these modifications can be explored using a number of different wind tunnel tests, an overview of which will be provided in this section. Besides optimizing the design, gathering more knowledge about the behaviour of the cylinder in conditions more specific to the operations will increase the reliability of the aircraft.

#### Testing the plain cylinder

First of all, it is important to test a plain cylinder. The data obtained, including the different coefficients and the downwash direction and severity, can be used as baseline for all of the cylinder modifications. There, the influence of the aspect ratio is an interesting test to execute. Furthermore, the aeroelasticity of the cylinder is important to determine from a structural point of view.

- Reference data:  $C_L$ ,  $C_D$ ,  $C_T$
- Aspect ratio effect,  $AR = 5$ ,  $AR = 8$ ,  $AR = 11$
- Determine: Aeroelasticity cylinder
- Determine: Downwash cylinder

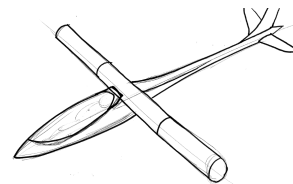


Figure 5.10: Design with plain cylinder

#### Further exploration of endplates

The first modification for the cylinder to reduce the drag is the addition of endplates. Literature indicates an increase in lift and torque and a decrease in drag. These changes in lift, drag or torque indicate the advantages and disadvantages for this design option. Evaluation of different sizes for the endplates can lead to an optimized design in terms of lift, drag and torque. Also, the influence of the aspect ratio of the efficiency of the endplates should be evaluated.

- Diameter endplates 1.5, 2, 3 times cylinder diameter
- Aspect ratio effect,  $AR = 5$  and  $AR = 8$
- Measure:  $C_L$ ,  $C_D$ ,  $C_T$
- Determine: Downwash endplates

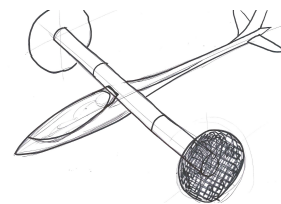


Figure 5.11: Cylinder with endplates

#### Spanwise discs

If the endplates show significant improvements in terms of lift to drag ratio, it would be interesting to add more plates over the span of the cylinder. These spanwise discs should be investigated for different spacings between the discs to accurately predict the behavior. Again,  $C_L$ ,  $C_D$ ,  $C_T$  and the downwash of the cylinder with its modifications should be determined, to compare to the plain cylinder and to

---

facilitate designing the aircraft. However, yaw performance is expected to decrease when the number of discs increase. This should be simulated and validated

- Number of midplates: 2, 4, 6
- Aspect ratio = 8
- Measure:  $C_L$ ,  $C_D$ ,  $C_T$
- Determine: Downwash midplates
- Determine: Effect of yaw

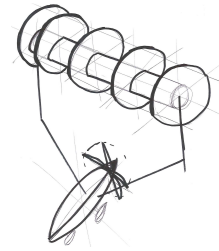


Figure 5.12: Cylinder with spanwise discs

### Surfaces around the cylinder

The addition of surfaces around the cylinder is a different modification to the cylinder, but not less promising. To this regard, both simple plates and airfoils are added to the cylinder. They will be placed in front of the cylinder, behind the cylinder and both in front of and behind the cylinder. The effect with respect to  $C_L$ ,  $C_D$ ,  $C_T$  and downwash angle can then be determined.

- Position: In front, behind, around
- Surface: Airfoil, flat plate
- Measure:  $C_L$ ,  $C_D$ ,  $C_T$
- Determine: Downwash surfaces

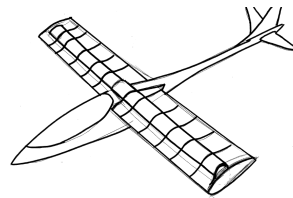


Figure 5.13: Cylinder with surfaces around it

### Additional test options

There are a number of additional test options which would be interesting to consider if time and resources allow it. A short reasoning for testing these options is included in this section, the options are:

- Different cylinder shapes
- Autorotation
- Interference two or more cylinders
- Surface roughness
- Movable surfaces around cylinder
- Tapered cylinder outward/inward
- Effect thickness endplates and spanwise discs

Additional investigation into the shape of the cylinder could lead to a higher efficiency of the cylinder, and possibly allow for autorotating. This shape investigation includes both the surface roughness of the cylinder and the overall shape. Autorotation might decrease the power the aircraft needs as the extra engine would become unnecessary. An important part of investigating autorotation is to evaluate the applicability to the mission and design.

The interference between two cylinders can be derived from the downwash, but determining the influence of a second cylinder experimentally is also interesting, as it might give a better overview of the advantages and disadvantages. Investigating movable surfaces could improve the efficiency of the surfaces around the cylinder discussed before, but would be difficult to both analyse and implement in the design. Tapering the cylinder changes the lift distribution of the cylinder, but the extent of this option is currently unknown and could lead to a performance increment. Overall, the investigation of the plain cylinder, endplates, spanwise discs and surfaces is deemed more realistic options to improve the lift to drag ratio than these design options, but they may prove to be interesting adaptations improving the design.

Finally exploring the effect of thickness of the efficiency of the endplates and spanwise discs implies evaluation of the vortices which are formed over them. No record was found of experiments in this

---

direction, which is why the plates are currently sized from a structural point of view. The thickness, however, may influence the shape and size of the vortices thereby influencing the lift and drag increment of the endplates.

### 5.3.2 Laboratory stand test

In a paper on electro-mechanical actuators for general aviation fly-by-wire aircraft<sup>1</sup>, a laboratory test for the actuators is described. The stand allows to test an actuator at numerous load conditions and driving inputs. The servo will be tested for its responses to step, harmonic and other inputs. The data retrieved from this testings allows for optimizing the control algorithm. According to the paper, their servos were able to establish static precision of 0.1 degrees, and were tested to full load conditions both in the positive as negative direction. Special attention should be payed to the reactive speeds of the servos, to limit the lag of the control system.

### 5.3.3 The Iron Bird

The Iron bird<sup>2</sup>, is utilized by Airbus to optimise and validate vital aircraft systems, for both electronics and hydraulics. It is a ground-based system integration test bench, in which the physical systems are installed in the same position as they would be on the real aircraft. It is utilized as a tool to assess the characteristics of the systems and to determine if any modifications are necessary. Here all adverse effects and unwanted phenomena can be analyzed and recorded in detail. This way of testing allows for a high level of development maturity in a safe and cost effective way. The Iron bird is coupled to a flight simulator, which is controller from a flight deck as similar as possible as the real aircraft. A computer is then generating the aerodynamic model and simulating the environmental conditions. For a design as innovative and complex to control as the Magnus Aeolus, using an Iron bird on a smaller scale could be a very effective way to achieve a high development maturity and adequate validation of the control system. The system to be tested would mainly be all the servos and flight computers. This test would be executed during the manufacturing phase of the project, shown in section 5.1.

### 5.3.4 Remote-Controlled Magnus Aeolus model

Halfway the Midterm report, it was decided to start the development of a Remote Controlled version of our design so far, as can be seen in Figure 5.19, to validate the performance of the concept. The project was lead by T. Cappuyns and accomplished by the great help of I. Cappuyns and J. Huygen. The aircraft was designed to have dimensions of about 1m to 1m and a weight of 1.2kg. Note that the design of the RC-model does not entirely resembles the full-scale design. This is mainly due to the design changes made after the midterm report. However, the sizing of the cylinder and canard Figure 5.17 are performed in the same way as the full-scale design. The RC-model does not feature a supporting wing, since the full scale model only uses this wing for structural reasons and for fuel storage, which is not necessary for the model.

The structure of the aircraft is mainly built up out of carbon rods and noma plan of 3 and 5mm. The cylinder has a diameter of 18cm and span of 96cm, which provide enough lift for a 1.5kg aircraft at a velocity of 4.3m/s and rotation of the cylinder of 2000rpm. The cylinder is built up around a circular carbon spar Figure 5.16, with 8 circular ribs of 5mm noma plan. It was than covered with pre-formed with 3 mm noma-plan and attached by specific noma plan contact adhesive. The smooth running of the cylinder is provided by 2 micro bearings and statically balancing by using paper tape. The supporting structure of the cylinder is built-up out of a carbon frame to which the engine support for the cylinder and landing gear is attached.

The cylinder is belt driven and a pusher propeller was used for the propulsion. The rotation of the cylinder is regulated by a rubber belt coupled to a brushless outrunner, shown in Figure 5.18. The

---

<sup>1</sup><http://www.tandfonline.com/doi/pdf/10.1080/16487788.2005.9635892>

<sup>2</sup><http://www.airbus.com/innovation/proven-concepts/in-design/iron-bird/>

transmission ratio is 4:1 for the pulley used on the cylinder and it is able to rotate well over 2000rpm. The belt however tends to wear, thus regular replacement becomes necessary.

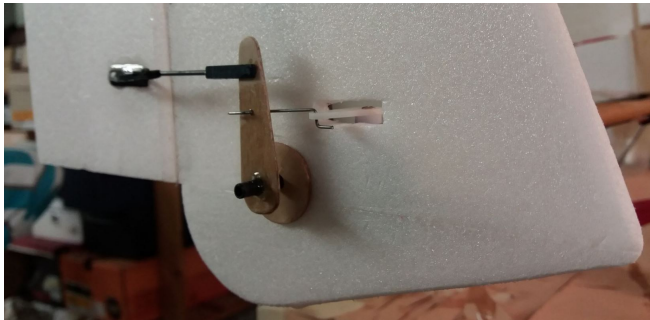


Figure 5.14: Rudder and aileron coupling deflection mechanism

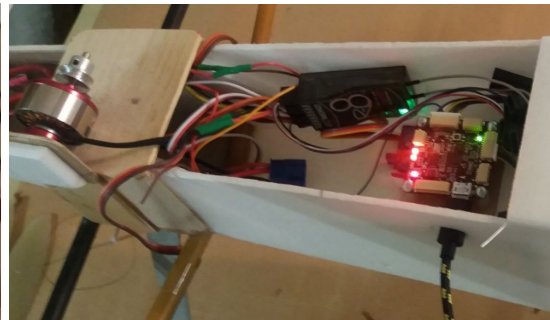


Figure 5.15: Flight controller, receiver and brushless outrunner of cylinder



Figure 5.16: Structure of cylinder with carbon spar and noma plan ribs, reinforced with multiplex



Figure 5.17: Canard with carbon spar and nose gear installment

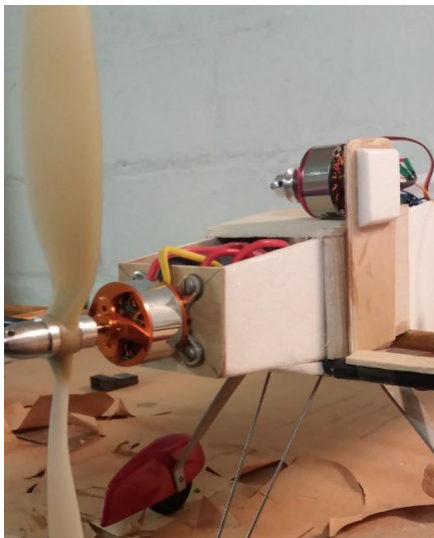


Figure 5.18: Brushless outrunners



Figure 5.19: Full aircraft model with transmitter

For weight considerations, ailerons and rudders shown in Figure 5.14 are deployed by only two servos instead of one servo per surface. Also, a micro sized flight controller and autopilot with leads was used to aid in the control of the canard. The flight controller shown in Figure 5.15 is programmed to keep the aircraft level around the lateral axis during operation, i.e. to limit the pitching of the aircraft to a

---

minimum. The configuration of the flight controller was performed by the use of Mission Planner<sup>3</sup>. A differential for the rudder and aileron deflection of 90/10 was used, since the rudder moving inward are limited by the placing of the cylinder.

Once finished, the aircraft weighs just below 1 kg, the costs of the material add up to around 250 euros and the estimated time input for the manufacturing adds up to about 100 hours. The first tests of the aircraft were performed on the 19th of June 2016. The propulsion system performed normally, directional control on the ground was present and the functionality of the canard was satisfactory. The flight controller, however performed too slowly for being adequate for controlling the aircraft in take-off. The RC-model did lift off for a very short time in a peculiar way, which was presumably due to a too critical c.g. location, too high torque input of the pusher engine and an adverse input of the canard. After the crash, one of the engine controllers caught fire due to blockage of the cylinder after impact, but the damage was limited. The aircraft was restored in its former condition for the next test. A new, more robust controller was soldered, the c.g. is moved forward and the zero position of the canard is adapted to generate negative lift during the ground roll, to allow for a more controllable take-off.

This next tests took place on the 25th of June 2016. At the beginning, the aircraft was not able to lift off, indicating that the lift off from the previous test was possibly primarily caused by the lift of the canard. To facilitate the flight of the RC model, endplates were added to the model which should increase the lift production of the cylinder. This addition of endplates increased the vibrations at the bearings which allowed the cylinder to get loose from the model when the cylinder was spun up. This indicates the importance of the pretension of the bearings, which is used for the actual design. Spinning it up while providing this tension by hand eliminated the problem and facilitated an actual test flight with endplates. The aircraft was less controllable and deviated from the control input given. Eventually, the aircraft was able to take-off. It back flipped and landed on its nose, which was the end of the test flights. There are a number of possibilities for this crash, these include the lift of the body, the slow reaction of the canard orientation and the center of gravity.



Figure 5.20: RC Model after the addition of endplates

There are a number of design choices for the actual design which are confirmed by the RC model. First of all, the flight proves that adding endplates to the cylinder increases the lift production of the cylinder. Also, putting pretension of the bearings is included in the design and would have improved the design of the RC model. The instability of the model also confirmed that an extensive control system and auto pilot is key to a successful mission, which have been implemented in the design of Magnus Aeolus.

<sup>3</sup><http://ardupilot.org/planner/index.html>

### 5.3.5 Simulation

Eager to see how the flight behaviour of the aircraft would look like, it was decided to make a simulation of its flight dynamics. This project was lead by T. Cappuyns and L. Voet.

A Matlab Simulink [18] model was set up starting from a Joystick input up to the FlightGear visualization. This model is illustrated in Figure 5.21. The model starts with the Joystick input. This input comprises pitch, roll, yaw and throttle input. These inputs go to the state-space systems for both longitudinal and lateral motions. The output of these blocks are the longitudinal and lateral states of the equations of motion. These states come together into the FlightGear visualization block. This block writes a “Run script file” for FlightGear. The CAD-model of the aircraft is converted into an AC-model and is inserted in FlightGear. This model allows to visualize the flight dynamics of the aircraft.

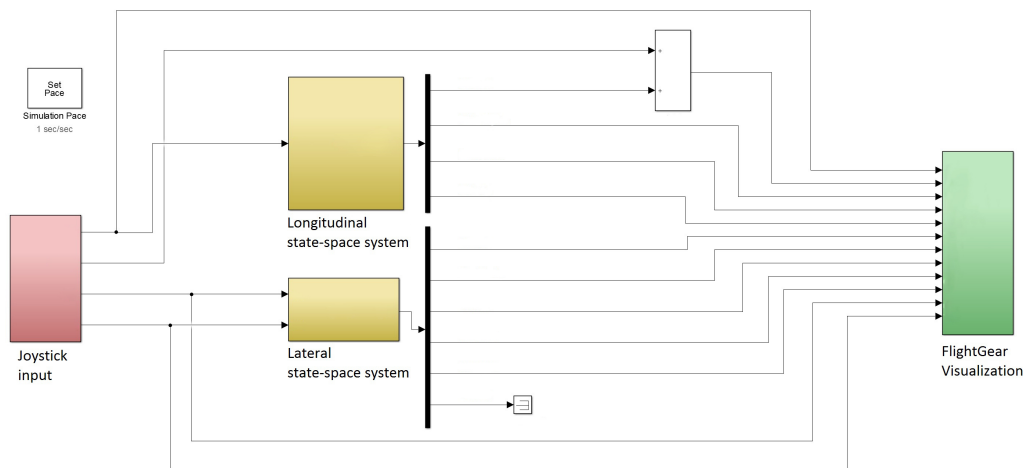


Figure 5.21: Matlab Simulink model of the flight dynamics

Attempting to in fact make a complete flight simulator proved too demanding considering the available time frame. Therefore, it was decided to focus on illustrating the eigenmotions of the aircraft. Having obtained the eigenmotions from the already designed flight dynamic model, explained in section 4.2, the simulation could serve best as an illustration of that on the Design Synthesis Exercise Symposium on June 30, 2016. Still effort is put in to take out the bugs in the program and revising the link between the Simulink model and the FlightGear to finally obtain an illustration of the five main eigenmodes describing the flight dynamics of the design. An illustration of the FlightGear Simulation is given in Figure 5.22.

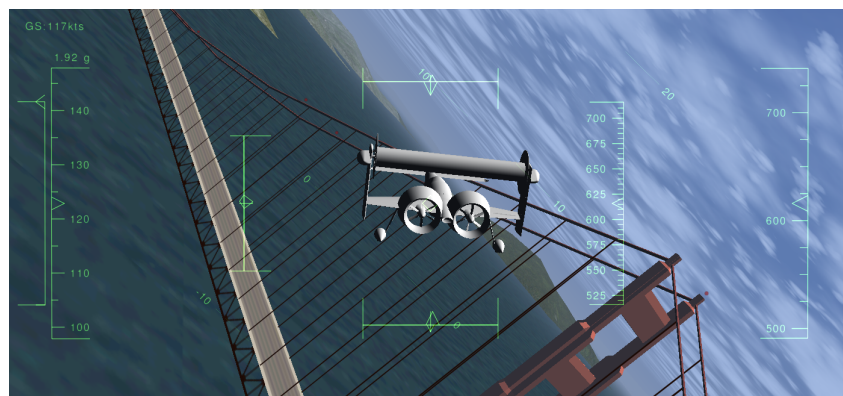


Figure 5.22: FlightGear illustration the model of the Magnus Aeolus aircraft

---

## 5.4 Production Plan

The production plan covers three different aspects of the production process: the manufacturing plan, the assembly plan and the integration plan. The manufacturing plan will elaborate on the custom made parts for the detailed design, organized by the different materials and mention the off-the shelf parts. The assembly plan will contain descriptions of the assembly of different subsystems of the aircraft. Finally implementation of the different assemblies will lead to the complete configuration of the system.

### 5.4.1 Manufacturing

#### Composite parts

Considering the prototyping nature of this endeavour, the best choice for manufacturing of composite part is undoubtedly vacuum bag curing of pre-impregnated composite plies. Despite its higher price and somewhat stricter demands on schedule, due to the limited shelf-life of the prepregs, this method requires very little facilities, but can still produce very high-quality results. To keep the cost further down, one-time molds are planned to be used. The production method will be the same for all composite parts. The main difference between all the carbon fiber components are the complexity of the moulds and whether or not core is used during laminating.

For the cylinder, this will be a mandrel-type positive mold, on which the CFRP plies and the foam will be laid. This mandrel can be easily manufactured from thick sheet steel. One limitation of having the mandrel inside the cylinder is that the outside is laminated in a vacuum bag, which will decrease its surface quality. To account for this issue, the last external ply of the cylinder will be very thin quasi-isotropic layer of glass fibre, which can be sanded and polished to the desired surface finish. In Figure 5.23, the glass fiber is referred to as surface finish layer.

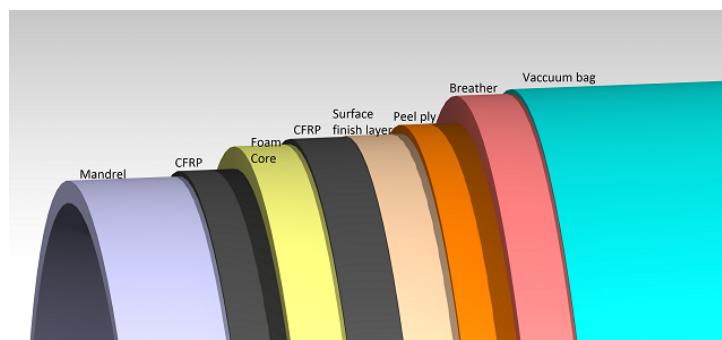


Figure 5.23: The different layers in the laminating in the cylinder. After the vacuum is applied, the whole assembly is put in an oven at 130 degrees.

Manufacturing the fuselage body in one piece is unnecessary and also unwanted in case of modifications. Several different pieces can be much more easily manufactured and then mechanically joined together at the locations of the bulkheads (before the pilot, between the pilot and passenger, between the passenger and engine). Details remain to be determined.

The duct consists of carbon fibre with a foam core. A large negative mould will be used to laminate the duct. First a layer of carbon pre-impregnated carbon fiber is cured, then the core is placed and the inner layer is placed and cured. Since the diameter of the fan is large, producing it from a single block of foam will be very inefficient. Therefore the ring will be milled in sections and put in the final mould. After curing and remeasuring the size of the duct, the trailing edge of the horizontal support has to be cut into duct, so that the duct can slide over the rotor support.

The end-caps and endplates are easy 2D shapes so curing can happen on a flat plat with a vacuum bag. As a core aluminium honey comb can be used.

---

## Aluminium

The vertical support consist an aluminum alloy truss support structure assembled with a bearing housing. The truss elements are off the shelf extruded beams and are connected with nuts and bolts. The bearing housing has tight tolerances due to the bearings press fit. The bearing housing will be milled with a 5-axis CNC out of a block aluminium. This method allows very accurate milling which is necessary for the tolerances of the press fit that have to be within nanometers accuracy

The aluminum alloy wingbox consists of C-beam spars, l shaped stringers, sheet metal rib and sheet metal skin. The parts will be custom made out of sheet metal. The tapered C-beam spars will be manufactured from a single sheet of aluminum and bended twice at an angle to make the taper. Excess material is cut from the flanges to create the C-beam. The stringers will be made with the same method but without the taper. Computer guided stamping will be used for the (airfoil shaped) ribs and a connection element will be bended into the cross section. The skin will be riveted to the airfoil shape. The same methods will be used for the canard and the vertical support.

## Polymeric parts

The canopy will be made from transparent polycarbonate and produced with thermoforming. The polycarbonate will be heated and folded over a mould with the help of a vacuum. When hardened the excess material is trimmed.

## Off-the-shelf parts

Parts that will be off the shelf are (but not limited to): bearings for the rotor, motors and gearbox, engine mount, avionics instrumentation, seats and safety gear. These are parts that require specialties that are not available to the engineers of Magnus Aeolus or components that are light weight and applicable for the design.

### 5.4.2 Assembly & integration

The top level assembly is explained in Figure 5.24. Much like a car, a structure has to be maneuverable to make the logistics easier. Therefore the first phase is a rolling airframe, explained in Figure 5.25. Magnus Aeolus has to go to paint before everything is installed so nothing has to be covered and protected coatings connect with the complete aircraft.

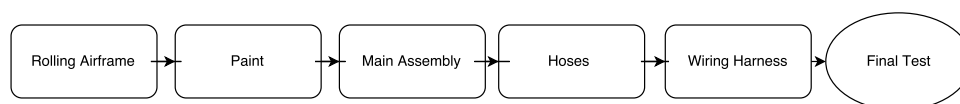


Figure 5.24: Flow diagram in top level about the assembly phase of Magnus Aeolus

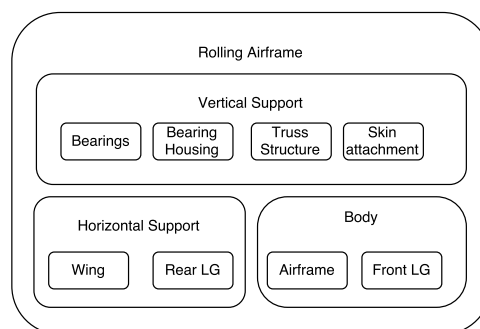


Figure 5.25: Elements of a rolling airframe assembly

Next is the main assembly phase, where most of the subsystems are installed. The aircraft is divided into 6 sections that can work parallel, when enough employees are available. This phase is illustrated in Figure 5.26. When all sub-assemblies are done, the hoses and wiring still have to be installed. When everything is assembled, some integration tests are done.

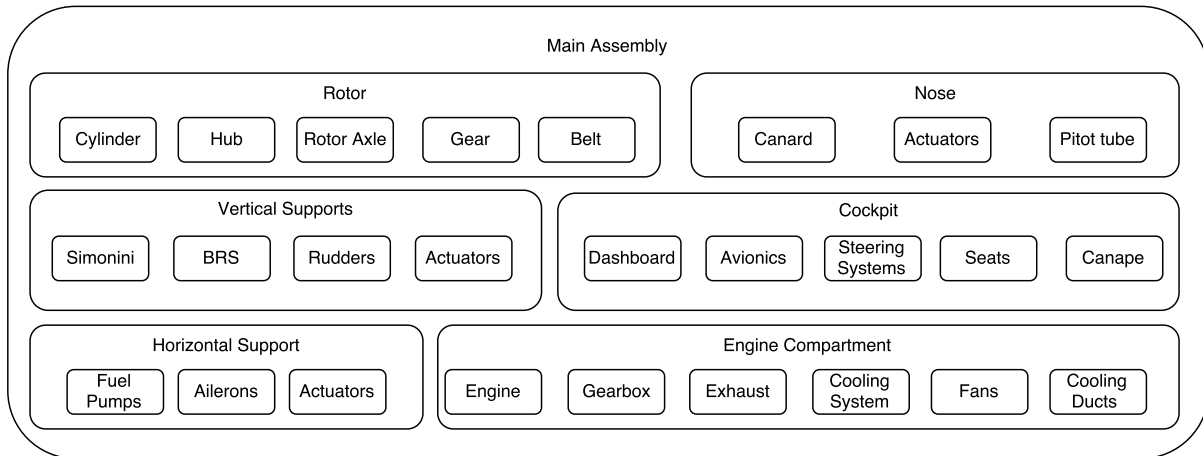


Figure 5.26: Elements of the main assembly phase

To test the integration of each sub-assembly it is important that each sub-assembly is tested on its own. For example: the electrical system can already be checked on a dummy, where all sensors are installed on the wiring harness and check if they work. The same can be done with actuators, engine and gearbox, fuel pumps etc. When everything is assembled, a check is done if everything is successfully integrated by doing the pre-flight checks like: accelerating the cylinder, turning fans and deflect control surfaces.

## 5.5 Cost Analysis

The cost analysis consists of the cost breakdown structure and a cost estimation of the aircraft. The cost breakdown structure gives an overview of the cost elements for the project phases discussed in the previous section. An overview of this cost breakdown is given in Figure 5.27. For all of the costs, a short description will be provided in this section. The cost estimation for the aircraft gives an overview of the costs for the different subsystems and their source.

### 5.5.1 Cost breakdown

An important group of costs shown in Figure 5.27 contains the costs for the different tests. These costs return in a number of project phases, like data gathering, validating, manufacturing and testing. The costs include the set-ups, and the facilities for the test procedures. Another returning cost group is labour, during all of the project phases wages will have to be paid for the people performing the work. Mentioned separately is the pilot, who also has to be hired. Operational costs include the hanger rental, the transport for the aircraft, but also the airfield fees, fuel and maintenance to ready the aircraft. Production costs are the final group of costs, including the costs for the materials, the machines and tools, the facilities and the resources used.

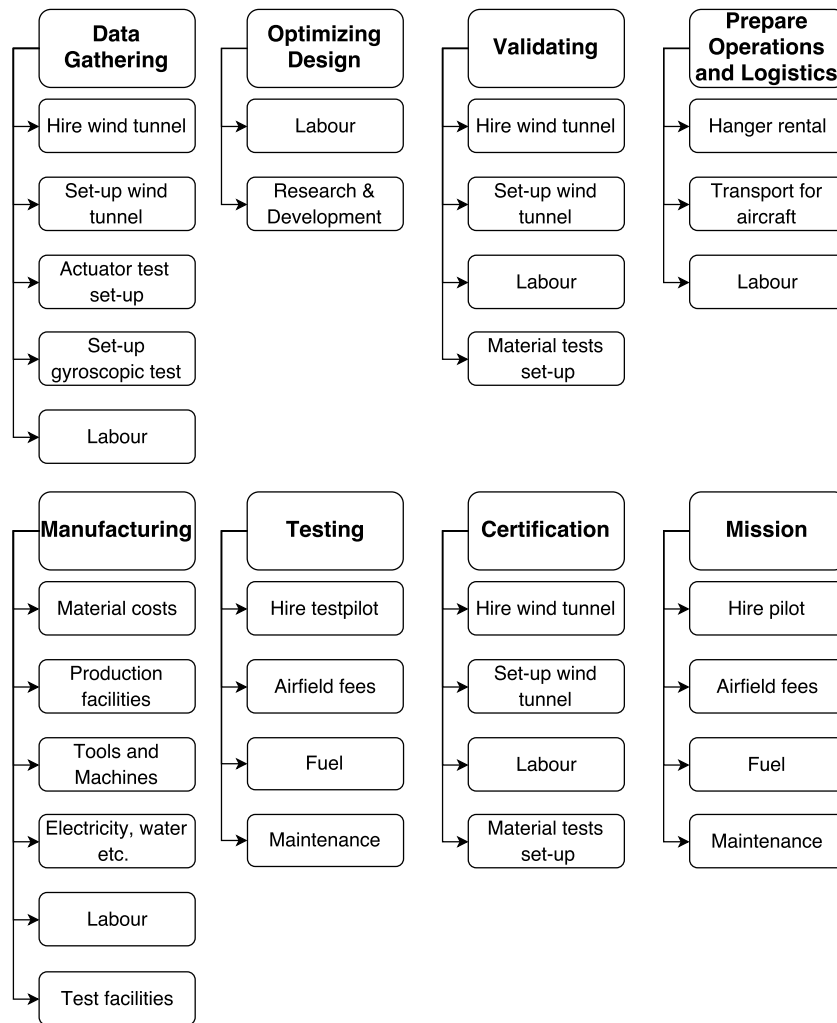


Figure 5.27: Cost Breakdown Structure

### 5.5.2 Cost estimation aircraft

A cost estimation of different elements of the aircraft are given here. These are roughly estimated and are there just to give an indication of how much some of the aircraft components will cost.

#### Control system and avionics costs

As it was shown in Table 3.23 cost of most of the elements of the control system and avionics are given and explained in detail. The cost of control surfaces are determined in material and manufacturing costs.

Total estimated cost: \$16,700.

#### Power and propulsion costs

The engines that are used in the aircraft are Mistral G200 for the ducted fan and a Simonini Mini 2 Plus for the rotor. The price of a Mistral G190 which is very similar to G200 is about \$31,500 <sup>4</sup> and Simonini Mini 2 Plus is about \$ 3,900 <sup>5</sup>. The cost of duct design and material is determined in material and manufacturing costs.

<sup>4</sup><http://kitplanes2.com/blog/2010/03/mistral-rotary-moves-closer-to-certification/>

<sup>5</sup><https://aerolight.com/A/index.php/products/powered-paragliding-engines-parts/simonini-mini-2-plus/simonini-mini-2-plus-detail>

---

Total estimated cost: \$35,400

### Materials and structure costs

The materials used in the aircraft and their costs per unit kilogram are given in Table 5.2. This is based on the rough estimation provided by the structural requirements. Carbon Fibre Reinforced Polymer (CFRP) and Core are used in end plates, cylinder and fuselage and Aluminium is mainly used in the support structures, canard and landing gear.

Table 5.2: Materials used in the aircraft and their raw costs

Type of material	Weight used [kg]	Total cost [\$]
Aluminium	192.6	5,600
CFRP	27	28,300
Core	7.2	2,800

Total estimated cost: \$ 36,700

### Manufacturing and labour costs

The dominating costs of the aircraft will be the manufacturing and production costs which are difficult to estimate. As this aircraft has unique design, the manufacturing costs cannot be estimated using existing statistical methods. Therefore, one way to get a very rough estimate of cost would be to determine the labour costs per month and the number of months that is needed to produce different components. As is shown in the Gantt-chart in Figure 5.9, it takes 12 months for 10 people to manufacture the aircraft. The yearly salary of an aircraft mechanic on average is about \$ 49,000 to 54,000 based on different sources<sup>6 7</sup>

Total estimated cost: \$490,000 to 540,000

### Operational costs

One part of the mission cost is the fuel cost. As was explained, a maximum of 56 gallons of fuel will be used for the mission which translates into 84 \$ of fuel costs according to latest fuel cost per gallon<sup>8</sup>. Other part of operational costs could relate to maintenance, repair, pilot and payload which are variant and unexpected but it is expected to be less than \$ 1,000

Total estimated cost: less than \$ 1,000

### Other subsystem costs

Systems such as landing gear and all saver should also be included in the overall airplane costs. Landing gear costs is determined from retailers<sup>9</sup> Total landing gear cost of \$4,000 was estimated based on required components for the landing gear. The total cost of all-saver parachute is between \$3,000 to \$12,000<sup>10</sup>.

Total estimated cost: \$7,000 to \$16,000

### Certification costs

As this is an experimental and a totally new aircraft, it needs to be certified based on EASA aircraft certification as was explained in section 4.7. This cost is expected to be \$1,000,000. This is a one-off cost so once the first one is certified, all the follow-ups will be in certified category.

Total estimated cost: \$1,000,000

**Overall cost of the first certified aircraft:** \$1,586,800 to \$1,645,800

---

<sup>6</sup><http://www.indeed.com/salary/Aircraft-Mechanic.html>

<sup>7</sup>[http://www.payscale.com/research/US/Job=Mechanic\\_Aircraft/Hourly\\_Rate](http://www.payscale.com/research/US/Job=Mechanic_Aircraft/Hourly_Rate)

<sup>8</sup><http://www.indexmundi.com/commodities/?commodity=gasoline>

<sup>9</sup><http://www.skygeek.com/landinggear.html>

<sup>10</sup>[http://www.brsaerospace.com/experimental\\_aircraft.aspx](http://www.brsaerospace.com/experimental_aircraft.aspx)

---

## Effect of mass production on total costs

If the aircraft is to be mass produced in the future, the number of labour hours required for manufacturing reduces exponentially as the number of aircraft build increases. This is illustrated in the manufacturing learning curve which shows, as the tasks becomes more repetitive, it becomes easier to complete each work package [76]. In Aerospace industry the learning effectiveness is about 85%.<sup>11</sup> If 10 units of the aircraft is to be produced, then the cost of the 10th aircraft will be reduced to about \$ 265,000 (assuming the first aircraft costs 586,000) and the total cumulative manufacturing cost of 10 of them aircraft will be about \$ 3,400,000 plus the one million required for certification. These calculation were done using the Wright's learning curve model<sup>12</sup>.

**Overall cost of 10 certified aircraft:** \$4,400,000 to \$4,760,000

## 5.6 Future of the Magnus effect

The purpose of this project has been to determine the feasibility of utilizing the Magnus effect in aviation. The conclusion that this is indeed feasible, now bears the question: what place could the Magnus effect have in the future of aviation? To attempt an answer to that question, an analysis will be presented in the following section, based on two pylons: examining the strengths and weaknesses of the Magnus effect and evaluating its potential with respect to the markets. Despite having the same functionality as conventional wings (i.e. providing lift), a rotating cylinder has significant differences. An overview of the advantages and disadvantages of the Magnus effect as main lift provider are given hereafter.

### Aerodynamics

- + Maximum lift coefficient of 12 (with the endplates), which is 5-6 higher than current conventional aircraft. This means that it has a higher lifting capacity for a smaller reference area.
- + There is no alpha stall. Lift (but also drag) increases with alpha.
- Very high drag which leads to very low lift-to-drag ratios. The maximum for the cylinder only (with endplates) is 5.6. This is 2-3 times lower than what is typical for conventional aircraft.
- The rotation means that the effective velocity at the lower tip of the cylinder will become supersonic relatively fast. For example, a cylinder with a 1 m radius and an endplate to cylinder diameter ratio of 2.5 (the one used in the present design), will reach supersonic conditions at the lower tip of the endplates at a speed of 48.3 m/s during cruise (alpha=2.4).
- Significant downwash.

### Control

- + Increased stability for short period motions.
- More oscillatory for long period motions.

### Structures

- + High stiffness. A circular cross-section is inherently stiffer per surface area unit than an airfoil.
- Interference. The rotation of the cylinder severely constricts placing structure inside it.
- High rotational speed. A large amount of friction and centrifugal forces to be dealt with, as well as vibrations.

---

<sup>11</sup><http://fas.org/news/reference/calcl/learn.htm>

<sup>12</sup><http://maaw.info/LearningCurveSummary.htm>

---

## Propulsion

- The cylinder needs power to be operated (in contrast with conventional wings)

Based on the analysis presented above, several recommendations for further research can be made, in order to overcome the weaknesses and enhance the strengths. Part of these recommendations, the first 7, are already incorporated in the plan for the continuation of this project, discussed in section 5.1, with the modifications for the cylinder and a test proposition is given in subsection 5.3.1. The most important recommendations are:

- Determination of the downwash for different velocities and velocity ratios. There is little information available about this, but from sporadic information in literature and CFD simulations the effect is significant and cannot be neglected.
- Further investigation on the endplates. This would include further exploration of the lift, drag and torque increments, as well as the vibrations and stresses in the endplates.
- Further investigation on the effect of spanwise discs. Although there has been some research on their effect, the results are inconclusive and not sufficient for such a solution to be included in the design.
- Investigation of the effect of adding surfaces in front of the leading edge and/or behind the trailing edge of the cylinder. This could lead to drag reduction by shielding the cylinder and offering a surface for the wake to re-attach, respectively.
- Research on other drag reduction mechanisms.
- Investigation on the possibility of autorotation
- Interaction between several cylinders
- Flight tests of the prototype or wind-tunnel experiments, which would allow the determination of the stability coefficients.
- Vibrational testing of the rotating cylinder in the flow.
- Investigation on the possibility of electromagnetic propulsion (i.e. using the entire cylinder as an electric motor). Alternatively, research on methods of power (re)generation from the rotating cylinder.

With this research concluded and many of the weaknesses mentioned previously mitigated and/or the strengths enhanced, the market analysis for the suitability of the Magnus effect can be re-evaluated.

The prototype Magnus Aeolus can be implemented as is, into the scientific market. Introducing the aircraft for the commercial market is a different story though. Assuming that the drag is mitigated and the stability characteristics of the long period motions are improved, the concept would then offer significant potential for General Aviation and especially for the Personal Aerial Vehicle market, due to its very high lifting capacity and its increased short period stability. However, it seems that the drag is an inherent characteristic of the Magnus effect. Thus, it can be more safely said, that the Magnus effect could have a future in combination with existing solutions. For example, it could be used in parallel together with wings and only during take-off and landing, in order to reduce the stall speed and thus also the required runway length. Using a different approach, it could be integrated into the wing. This has, in fact, already been investigated and is called an “augmented wing”, offering twice the lift coefficient with respect to the airfoil [77]. However, no effect on the drag coefficient was mentioned/investigated.

All-in-all, the Magnus effect is certainly a concept that deserves more attention in the field of Aerospace. Despite its drawbacks, further research with a focus on applications could turn it into a design option capable to supplement or potentially even replace conventional lift-providing mechanisms in certain functions.

---

## Chapter 6

# Conclusion

Reintroducing the Magnus effect in the aviation industry by using it as main lift provider: a challenge enterprise demanding perseverance and an innovative attitude. A design for this experimental aircraft has been made and the outcome and process are presented in this report. The different components of the aircraft were all designed, taking into consideration all of the subsystem requirements. The main purpose of this design was to achieve and preferably surpass this mission. The report continues from the preliminary design, but extends not only the detail but also the capabilities of the aircraft.

The design features a cylinder positioned above the rear end of the body with rotating endplates on both ends to get the maximum L/D with the minimum influence of the downwash on the body. A separate engine, the Simonini mini 2 plus, is used to rotate this cylinder. The main engine, the Mistral G200, was chosen for its high power to weight ratio and low fuel consumption. It drives two ducted fans, chosen to optimize the thrust generation even more while keeping the clearance for the cylinder. The configuration is stable because of the canard at the front of the aircraft and the two vertical supports functioning as vertical tails, as well as the possibility to pump fuel from one side of the aircraft to the other. A full fly-by-wire system will be used to control the aircraft because of the coupling between the different motions and engines. For the safety of the passengers, a parachute system is implemented in the design in case the cylinder fails.

The performance of the aircraft shows that this mission can be fulfilled, and that it can even be surpassed by returning back to Rotterdam. The aircraft can adhere to the descent and land procedures set by the airfields and is able to do an unpowered landing at MTOW in case of engine failure. Additionally, the sustainability analysis proves an end-of-life solution for up to 73% of the aircraft elements by either recycling or reusing them. The sensitivity analysis then indicates that there are no significant parameter changes which have to be prevented at all costs, as the consequences are limited for all changes. The RAMS characteristics indicate that the reliability and availability is slightly lower than for conventional aircraft, but the experimental nature of the aircraft makes this expected. The safety of the pilots is ensured by the all saver parachute system. The risk map shows all of the significant risks can be mitigated, primarily by testing and project management. Finally, the compliance matrix concludes the performance analysis of the design and indicates that most of the requirements have been met. The project implementation then continues with giving an overview of the next phases for this project. There are a number of possible modifications for the cylinder which can be explored with wind tunnel tests and it is recommended to execute these tests in the next design phase. Final adaptations can also be made to achieve compliance to all of the requirements. Without these adaptations however, the requirements set by the stakeholders can all be achieved, proving the design is feasible. Even better, further research in the application of the Magnus effect may supplement or even substitute current lift-providing methods in certain applications.

Overall, a detailed subsystem design has been provided and analysed. This design explores the possibilities of the Magnus effect and implements them to its full potential. The mission set for the aircraft has not only been achieved, but it can be surpassed as well. The payload has been doubled, the range is over 970km and the speed is about three times higher than required. The design has exceeded the expectations and has shown that this unconventional way of flying is actually feasible. Once again, the aviation industry experiences innovation.

---

# Bibliography

- [1] Flettner, A., *Mein Weg zum Rotor*, Köhler & Amelang, Leipzig, 1926.
- [2] Seifert, J., “A review of the Magnus effect in aeronautics,” *Progress in Aerospace Sciences*, Vol. 55, 2012, pp. 17–45.
- [3] Ruijgrok, G., *Elements of Airplane Performance*, Delft University Press, Delft, 1990.
- [4] Hamann, R. and van Tooren, M., “Part 2,” *Systems Engineering & Technical Management*, TU Delft, Faculty of Aerospace Engineering, 2004.
- [5] DSE Group 18, “Rediscovering the Magnus Effect in Aeronautics - Midterm report,” Tech. rep., TU Delft, apr 2016, Unpublished.
- [6] Swanson, W., “The Magnus Effect: A summary of Investigations to Date,” *Journal of Basic Engineering*, Vol. 83, 1961, pp. 461–470.
- [7] Anderson Jr., J. D., *Fundamentals of Aerodynamics*, McGraw-Hill, 2001.
- [8] Bickley, W., “The Influence of Vortices Upon the Resistance Experienced by Solids Moving Through a Liquid,” *Proceedings, Royal Society*, Vol. 119, 1928, pp. 146–156.
- [9] Thom, A., “Experiments on the Air Forces on Rotating Cylinders,” Reports and memoranda, no. 1018, Aeronautical Research Committee, 1925.
- [10] Badalamenti, C. and Prince, S., “The Effects of Endplates on a Rotating Cylinder in Crossflow,” *26th AIAA applied aerodynamics conference, American Institute of Aeronautics and Astronautics*, August 2008.
- [11] Ansys<sup>®</sup> Inc., “Fluent 16.1,” Cecil Township PA, USA, 2015.
- [12] Carstensen, S., Mandviwalla, X., Vita, L., and Paulsen, S., “Lift of a Rotating Circular Cylinder in Unsteady Flows,” *Journal of Ocean and Wind Energy*, Vol. 1, No. 1, 2014, pp. 41–49.
- [13] Gerasimov, A., *Modeling Turbulent Flows with Fluent*, Ansys Inc., 2006.
- [14] Schlichting, H. and Kestin, J., *Boundary-layer theory*, McGraw-Hill Book Company, 1960.
- [15] E.G.Reid, “Tests on rotating cylinders,” *NACA Technical Notes*, Vol. 1, No. 209, 1924.
- [16] Hibbeler, R., *Mechanics of Materials*, Pearson Prentice Hall, New Jersey, USA, 2011.
- [17] Brazier, L. G., “On the Flexure of Thin Cylindrical Shells and Other ”Thin” Sections,” *Proceedings of the Royal Society of London A: Mathematical, Physical and Engineering Sciences*, Vol. 116, No. 773, 1927, pp. 104–114.
- [18] MathWorks<sup>®</sup> Inc., “Matlab R2012b (8.0.0.783),” Natick, MA, USA, 2012.
- [19] Peterson, J. P., “Buckling of stiffened cylinders in axial compression and bending - A review of test data,” Tech. rep., National Aeronautics and Space Administration, 1970.
- [20] Weingarten, V. I., Seide, P., and Peterson, J. P., “Buckling of thin-walled circular cylinders,” Tech. rep., National Aeronautics and Space Administration, 1970, [ntrs.nasa.gov/archive/nasa/casi.ntrs.nasa.gov/19690013955.pdf](https://ntrs.nasa.gov/archive/nasa/casi.ntrs.nasa.gov/19690013955.pdf).
- [21] Kassapoglou, C., *Design and Analysis of Composite Structures with Application to Aerospace Structures*, Aerospace Series, Wiley, 1st ed., 2010.
- [22] Dassault Systmes Simulia Corp., “Abaqus/CAE v6.11,” Providence, RI, USA, 2011.
- [23] Dassault Systmes Simulia Corp., *Abaqus 6.11 Verification manual*, Dassault Systmes, 2011.
- [24] Hibbeler, R., *Engineering Mechanics: Dynamics*, Pearson Prentice Hall, New Jersey, USA, 2011.
- [25] Granta Design Ltd., “Cambridge Engineering Selector v16.1.22,” Cambridge, UK, 2016.
- [26] SKF<sup>®</sup>, *Rolling bearings catalogue*, SKF, Gothenburg, Sweden, 2012.
- [27] van Beek, A., *Advanced Engineering Design*, [www.engineering-abc.com](http://www.engineering-abc.com), 2012.
- [28] Guzzella, L. and Sciarretta, A., *Vehicle Propulsion Systems: Introduction to Modeling and Optimization*, Springer-Verlag Berlin, Heidelberg, 3rd ed., 2013.

- 
- [29] Aircraft Spruce & Specialty Co. <sup>®</sup>, *Aircraft Spruce Catalogue*, Aircraft Spruce, Corona CA, U.S.A., 2016.
- [30] Megson, T., *Aircraft Structures for Engineering Students*, Elsevier, Oxford, UK, 2007.
- [31] Drela, M. and Youngren, H., “XFOIL - Subsonic airfoil analysis,” MA, USA, 2006.
- [32] de Piolenc, M. and Wright, G., *Ducted fan design volume 1*, Mass flow, 2001.
- [33] Squatriglia, C., “A rotary will wail at le mans once again,” *Autopia*, 2011.
- [34] Janssens, P., “More Mistral Magic,” *Kitplanes*, december 2014.
- [35] Fokker, S., “GLARE and Bonded Repairs,” Tech. rep., 2007.
- [36] Mulder, J., *Flight Dynamics Lecture Notes*, Delft University Press, Delft, 2013.
- [37] Roskam, J., *Airplane Flight Dynamics and Automatic Flight Controls*, Vol. II of *Airplane Design*, Darcorporation, Kansas, USA, 2001.
- [38] Sadraey, M., *Aircraft Design: A Systems Engineering Approach*, Wiley Publications, 2012.
- [39] Guzzella, L. and Onder, C., *Introduction to Modeling and Control of Internal Combustion Engine Systems*, Springer-Verlag Berlin, Heidelberg, 2nd ed., 2010.
- [40] Giancoli, D. C., *Physics*, Pearson, 4th ed., 2003.
- [41] Niu, M., *Airframe Stress Analysis and Sizing*, Hong Kong Conlimit Press Ltd., Hong Kong, 1999.
- [42] Sadraey, M., *Aircraft Performance Analysis*, VDM Publishing, Saarbrücken, 2009.
- [43] Dassault Systmes, “CATIA<sup>®</sup> V5R21 SP6,” Providence, RI, USA, 2013.
- [44] Jacobs, E., Ward, K., and Pinkerton, R., “The characteristics of 78 related airfoil sections from tests in the variable-density wind tunnel,” Tech. rep., National Advisory Committee for Aeronautics, 1935.
- [45] Stenzel, V., Wilke, Y., and Hage, W., “Drag-reducing paints for the reduction of fuel consumption in aviation and shipping,” *Progress in Organic Coatings*, Vol. 70, No. 4, 2011, pp. 224–229.
- [46] Balmer, E., “Aviation industry dons ‘shark skins’ to save fuel,” *Phys.org*, Feb. 2013.
- [47] Roskam, J., *Layout Design of Landing Gear and Systems*, Vol. IV of *Airplane Design*, Darcorporation, Kansas, USA, 2003.
- [48] Raymer, D. P., *Aircraft Design: A Conceptual Approach*, AIAA Education Series, American Institute of Aeronautics and Astronautics(AIAA), 3rd ed., 1999.
- [49] Grove Inc., *Aircraft landing gear systems catalogue*, Grove Inc., El Cajon, CA, USA, 2014.
- [50] The Goodyear Tire & Rubber Co. <sup>®</sup>, *Aircraft tire data book*, Goodyear, Akron, Ohio, USA., 2002.
- [51] ir. D. Steenhuizen, “Wing Design Part 4,” TU Delft Faculty of Aerospace Engineering, Unpublished. Available on Blackboard.
- [52] Jeppesen, *EGLL (Heathrow) Airport Information*, SMA, jeppview 3.7.5.0 ed., 11 2015.
- [53] Voskuijl, M., “Lecture 11-12: Cruise flight (lecture slides),” *Flight & Orbital Mechanics*, TU Delft Faculty of Aerospace Engineering, 2015, Unpublished. Available on Blackboard.
- [54] Voskuijl, M., “Lecture hours 5, 6, 7, - Turning performance,” *Flight and Orbital Mechanics*, TU Delft Faculty of Aerospace Engineering, 2015-2016, Unpublished. Available on Blackboard.
- [55] Gerges, S. N., Sehrndt, G. A., and Parthey, W., “Noise sources,” *Occupational exposure to noise: evaluation, prevention and control*, edited by B. Goelzer, C. H. Hansen, and G. A. Sehrndt, World Health Organization, 1995, pp. 103–124.
- [56] Everest, F. and Pohlmann, K., *Master Handbook of Acoustics*, Mc-Graw Hill, 4th ed., 2001.
- [57] Lighthill, M. J., “On sound generated aerodynamically. I. General theory,” *Proceedings of the Royal Society of London A: Mathematical, Physical and Engineering Sciences*, Vol. 211, The Royal Society, 1952, pp. 564–587.
- [58] Connor, J. and Laflamme, S., “Tuned mass damper systems,” *Structural Motion Engineering*, Springer, 2014, pp. 199–278.
- [59] Leylekian, L., Lebrun, M., and Lempereur, P., “An overview of aircraft noise reduction technologies.” *AerospaceLab*, , No. 6, 2014, pp. p–1.
- [60] Davis Jr, D. D., Stokes, G. M., Moore, D., and Stevens Jr, G. L., “Theoretical and experimental

- 
- investigation of mufflers with comments on engine-exhaust muffler design,” 1954.
- [61] Kostun, J. D., Goenka, L. N., Moenssen, D. J., and Shaw, C. E., “Helmholtz resonator,” 2004, US Patent 6,792,907.
  - [62] Boulouchos, K., “Lecture 3 – Thermodynamics of IC-engines,” *IC-engines and Propulsion Systems*, ETH Zürich Faculty of Mechanical Engineering, p. 12, Unpublished. Available on MyStudies.
  - [63] McCartney, K., “Catalytic converter theory, operation and testing,” 1997.
  - [64] Auckenthaler, T., “Modelling and Control of Three-Way Catalytic Converters,” Jul. 2005, pp. ix.
  - [65] Vogel, A., *The  $H_\infty$  control problem: a state-space approach*, University of Michigan Department of Electrical Engineering and Computer Science, Ann Arbor MI, US, Feb. 2000.
  - [66] Butcher, J., *The numerical analysis of ordinary differential equations*, Wiley, 1987.
  - [67] Seifert, J., “Micro Air Vehicle lifted by a Magnus Rotor A Proof of Concept,” *50th AIAA Aerospace Sciences Meeting including the New Horizons Forum and Aerospace Exposition*, American Institute of Aeronautics and Astronautics, Nashville, Tennessee, 2012.
  - [68] Ribeiro, J. and de Oliveira Gomes, J., “Proposed framework for End-Of-Life aircraft recycling,” *Proceedings of 12th Global Conference on Sustainable Manufacturing*, Vol. 26, CIRP, 2015, pp. 311–316.
  - [69] DSE Group 18, “Rediscovering the Magnus Effect in Aeronautics - Baseline Report,” Tech. rep., TU Delft, apr 2016, Unpublished.
  - [70] Harrington, M. B., “Requirements for the PAV challenge,” .
  - [71] Company, A., “XT912-Tundra specifications,” 2016, <http://www.airborne.com.au/pages/microlights-2014-xt912-tundra-specs.php>.
  - [72] IHS<sup>®</sup> Jane’s, “Jane’s All the World’s Aircraft,” *Jane’s All the World’s Aircraft*, Jan. 2016.
  - [73] Company, R. H., “R22 BETA II Helicopter,” 2016, [http://www.robinsonheli.com/rhc\\_r22\\_beta\\_ii.html](http://www.robinsonheli.com/rhc_r22_beta_ii.html).
  - [74] Terrafugia, “The Transition,” 2016, <http://www.terraffugia.com/aircraft/transition>.
  - [75] Jetpack, M., “Martin Jetpack,” 2016, <http://www.martinjetpack.com/>.
  - [76] Sinke, J., “Organization of the production process-Production reader,” Accessed 2016.
  - [77] von König, F., *Windkraft vom Flettnerrotor*, Udo Pfriemer Verlag, München, 1980, Chapter 4.
  - [78] Torayca<sup>®</sup>, “Technical datasheet No. CFA-018 M60J,” 2016, <http://www.toraycfa.com/pdfs/M60JDataSheet.pdf>.
  - [79] Torayca<sup>®</sup>, “Technical datasheet No. CFA-008 T1000G,” 2016, <http://www.toraycfa.com/pdfs/T1000GDataSheet.pdf>.
  - [80] Torayca<sup>®</sup>, “Technical datasheet No. CFA-005 T700S,” 2016, <http://www.toraycfa.com/pdfs/T700SDataSheet.pdf>.
  - [81] Gurit<sup>®</sup>, “General datasheet - Carbon & Glass SparPreg<sup>™</sup>,” 2016, <http://www.gurit.com/files/documents/sparpregpdf.pdf>.
  - [82] Gurit<sup>®</sup>, “General datasheet - ST 95 Structural sprint,” 2016, <http://www.gurit.com/files/documents/st-95v0pdf.pdf>.
  - [83] Hexcel<sup>®</sup>, “Product data - Hexply<sup>®</sup> M20,” 2016, [http://www.hexcel.com/Resources/DataSheets/Prepreg-Data-Sheets/M20\\_global.pdf](http://www.hexcel.com/Resources/DataSheets/Prepreg-Data-Sheets/M20_global.pdf).
  - [84] Wu, F. and Yang, J., “The mechanical Behavior of GLARE Laminates for Aircraft Structures,” Tech. rep., University of California, Department of Materials Science and Engineering.

# Appendix A

## Material Characteristics

The materials used for structural applications are discussed here, together with their relevant properties. A summary of numerical constants for the materials used is presented in Table A.1 and Table A.2. The material used in each specific element or subsystem is specified in its corresponding chapter.

Table A.1: Material properties of metals used in the design

	Specific gravity [g/cc]	Young's modulus [GPa]	Yield strength [MPa]	Ultimate strength [MPa]
Al 7075-T0	2.81	72	140	280
Al 7075-T6	2.81	72	503	572
4130 Steel	7.81	190-210	410-480	590-760
52100 Steel	7.81	190-210	2034	2241

Table A.2: Material properties of pre-impregnated CFRP systems used in the design

Fibre/Resin	Specific gravity [g/cc]	Young's modulus [GPa]		0° strength [MPa]		90° strength [MPa]		Ref.
		$E_1$	$E_2$	Tens	Comp	Tens	Comp	
Toray M60J 60%/Toray 250F (HM)	1.6	365	10	2010	785	80	80	[78]
Toray T1000G 60%/Toray 250F (HS)	1.6	165	10	3040	1570	80	80	[79]
Toray T700S 60%/Toray 250F (IM)	1.6	135	10	2550	1470	80	80	[80]
Gurit TC35S 60%/Sparpreg (SP)	1.6	140	8	2234	1183	83	83	[81]
Gurit RC200T 59%/ST-95 (twill)	1.6	70	70	796	670	796	670	[82]
Hexcel G904 60%/M20 (spread-tow)	1.6	65	65	870	840	870	840	[83]

Table A.3: Material properties of GLARE

Composite	Specific gravity [g/cc]	Young's modulus [GPa]	0° strength [MPa]		90° strength [MPa]		Ref.
			E	Tens	Comp	Tens	
GLARE2 Unidirectional	2.52	66	1214	390	317	253	[84]
GLARE3 0°/90° cross-ply	2.52	66	717	319	716	318	[84]